MC 68-3001-R1 (BNY)

PROPULSIVE RE-ENTRY AERODYNAMICS

BY

PHILIP O. JARVINEN
RICHARD W. LUCE
EMMANUEL WACHSLER

INTERIM REPORT

JUNE 1968

PERIOD COVERED: 1 JUNE 1967 – 1 JUNE 1968
CONTRACT NO. NAS 7-576

PREPARED FOR

NATIONAL AERONAUTICS AND SPACE ADMINISTRATION
LIQUID ROCKET RESEARCH AND TECHNOLOGY CODE RPL
WASHINGTON, D. C.

MITHRAS, A DIVISION OF SANDERS ASSOCIATES, INC.

701 CONCORD AVENUE, CAMBRIDGE, MASS. 02138

MITHRAS
a division of sanders associates, inc.,
701 Concord Ave., Cambridge Mass. 02138

MC 68-3001-R1 (BNY)

PROPULSIVE RE-ENTRY AERODYNAMICS

by

Philip O. Jarvinen
Richard W. Luce
Emmanuel Wachsler

INTERIM REPORT

JUNE 1968

Period Covered: 1 June 1967 - 1 June 1968
Contract No. NAS 7-576

Prepared for

National Aeronautics and Space Administration
Liquid Rocket Research and Technology Code RPL
Washington, D. C.

FOREWORD

This report was prepared by MITHRAS, a division of sanders associates inc., for the National Aeronautics and Space Administration, Liquid Rocket Research and Technology Branch, Washington, D.C. Mr. Hartwell Long of the Jet Propulsion Laboratory, California Institute of Technology was the Technical Manager.

The investigations whose results are reported here, represent the work accomplished during Phase I of contract NAS 7-576 during the period 1 June 1967 to 1 June 1968. Phase II of this contract is presently underway and will be completed June 1, 1969.

The research reported here was performed in the Aeroscience Department of MITHRAS under the direction of the department manager, J.A.F. Hill. Mr. P.O. Jarvinen was project engineer and wrote the interim final report. Mr. Norbert Durando contributed substantially to the development of the entrainment along the inner and outer interfaces and to the location of the inner interface.

SUMMARY

This report discusses the progress accomplished during the first year of a two-year contract to study Propulsive Re-Entry Aerodynamics. Analytical methods were developed during the first year to predict the flow field in the immediate vicinity of a planetary entry system composed of an aeroshell with a single retrorocket which exhausts into a subsonic or supersonic counterflowing planetary atmosphere. In the second year a digital computer program will be developed for the analytical solutions, and the analytical model will be tested by performing an experimental test program and comparing the experimental results with the analytical predictions.

The analytical investigation considers the flow field due to a single supersonic retrorocket exhausting from an aeroshell into oncoming subsonic, transonic, or supersonic streams in the large thrusting coefficient regime, $0.5 < C_T = T/q_\infty A_m < 15$, which is the range of thrusting coefficients encountered during the terminal landing phase for planetary landing on Mars or Venus.

Analyses are provided for all the geometrical features of the flow field such as the location of the terminal shock, jet boundary, and the profile for the interface between the jet and atmospheric gases. In addition, analyses are developed which describe the growth of the mixing layers along the interface and at the edge of the jet boundary and dead-air region and the reattachment of the shear layer to the aeroshell or the recompression of the shear layer in wake type flow.

A comprehensive discussion of the experimental wind tunnel test program to be accomplished in Phase II is presented.

TABLE OF CONTENTS

TABLE OF CONTENTS (Continued)

TABLE OF CONTENTS (Continued)

NOMENCLATURE

		Defined
A^*	Nozzle throat area	Page 14
A_{e_j}	Jet exit area	" 33
A_m	Aeroshell base area	" 33
a_{o_j}	Chamber velocity of sound	" 40
C	Mass concentration of foreign gas	" 57
$\overline{C}$	"Average" concentration in merged shear layer	" 57
C_D	Drag coefficient	" 14
C_d	Dead air concentration	" 61
C_{D_W}	Hemispherical wave drag coefficient	Fig. 35
C_F	Thrust coefficient	Page 14
C_T	Retrothrust coefficient, thrusting coefficient	" 4
C_q	Entrainment coefficient	" 45
D	Drag	" 33
d_{e_j}	Jet exit diameter	" 29
d_f	Blunting sphere diameter	" 28
h	Altitude	Fig. 13
H	Atmospheric scale height	Page 12
$\overline{H}$	"Average" total enthalpy	" 56
h_o	Ignition altitude	" 13
I_s	Specific Impulse	" 11
M'	Mach Number behind reattachment shock	Fig. 14

NOMENCLATURE (Continued)

		Defined
$\dot{m}$	Mass flow in merged shear layer	Page 49
M_∞	Free stream Mach Number	" 20
M_{e_j}	Jet exit Mach Number	" 27
$\dot{m}_j$	Jet mass flow	" 29
$\dot{m}_\ell$	Flow in jet layer	" 29
M_ℓ	Average Mach Number in jet layer	Fig. 30
P_∞	Free stream pressure	Page 31
P_c	Chamber pressure	" 14
P_d	Dead air pressure	" 18
P_{e_j}	Jet exit pressure	" 20
P_{o_f}	Total pressure behind bow shock, free stagnation point pressure	Page 20
P_{o_∞}	Free stream total pressure	" 21
P_{o_j}	Jet total pressure	" 18
q_∞	Free stream dynamic pressure	" 4
$R_{e_{D_\infty}}$	Free stream Reynold's number	" 20
r_f	Blunting sphere radius	" 39
s*	Nondimensional distance along shear layer	" 51
T_{o_∞}	Free stream total temperature	" 20
T_{o_j}	Jet total temperature	" 20

NOMENCLATURE (Continued)

		Defined
T_{t_∞}	Free stream total temperature	Page 20
T_{t_j}	Jet total temperature	" 20
u_1	Velocity just inside first interface	" 44
$\overline{u}$	"Average" velocity in merged shear layer	" 48
u_2, u_e	Velocity just outside first interface	" 44,45
V_e	Entry velocity	" 12
V_{e_j}	Jet exit velocity	" 29
V_ℓ	Average velocity in jet layer	Fig. 30
V_o	Velocity at ignition	Page 12
x_1	Axial coordinate of intersection of jet boundary and terminal shock	" 36
x_c	Location of blunting sphere center	" 36
x_s	Axial distance to terminal shock	" 38
y_1	Lateral coordinate of intersection of jet boundary and terminal shock	" 36
α	Complement of ϕ	" 28
β	Ballistic coefficient	" 12
γ_∞	Free stream specific heat ratio	" 20
γ_j	Jet specific heat ratio	" 20
δ	Width of annulus from edged jet to interface	" 34
δ_d	Location of inner edge of mixing layer	" 48
δ_e	Location of external edge of mixing layer	" 48

NOMENCLATURE (Continued)

		Defined
δ_r	Location of separation streamline	Page 59
η	Self similar shear layer parameter	" 54
η_o	External edge of mixing layer	" 55
θ_v	Aeroshell half cone angle	Fig. 1
λ	Parameter in nozzle flow	Page 22
ρ'	Density behind reattachment zone	Fig. 14
ρ_1	Density just inside first interface	Page 45
ρ_2, ρ_e	Density just outside first interface	" 40,45
ϕ	Angle measured from centerline	" 28

LIST OF FIGURES

LIST OF FIGURES (Continued)

LIST OF FIGURES (Continued)

LIST OF FIGURES (Continued)

LIST OF FIGURES (Continued)

LIST OF FIGURES (Continued)

LIST OF TABLES

1. INTRODUCTION

1.1 BACKGROUND

Studies[1-6] of the exploration of the planet Mars have indicated a need to augment the aerodynamic decleration of the lander vehicle with a deployable aerodynamic decelerator, and/or retrorocket system which operates in the terminal descent phase (the last several thousand feet of altitude above the surface) and slows the lander vehicle to assure a safe landing. Lander vehicles without terminal deceleration systems have excessive velocities at the surface of the planet due to the low atmospheric density which exists on Mars. All systems considered, in the references cited, for the terminal descent phase, employ a retrorocket system for the entire or concluding landing sequence with the aeroshell providing the main deceleration from atmospheric entry to the beginning of the termal descent phase. Aeroshell vehicles are typically members of the blunted-sphere-cone family, with included half angles of sixty degrees. Parachutes and ballutes have been suggested as possible deployable aerodynamic decelerators, and retrorocket systems with from single to six engine configurations have also been considered. Lander vehicles with three or four retrorockets appear more attractive than the other alternatives.

Aeroshell, deployable aerodynamic decelerator and retrorocket systems have been joined in various combinations and used in various staging sequences. One system that has been proposed consists of a combination of the aeroshell-retrorocket systems. Propulsive deceleration is used from the beginning of the terminal descent phase until the vehicle reaches a few feet above the surface with aeroshell separation occurring near the surface. Because the lander vehicle with a retrorocket system is passing through an atmosphere as it

descends to the surface, the flow of exhaust gases from the retrorocket motors is modified by the interaction with the atmosphere. The atmosphere causes the retrorocket exhaust gases, which are being discharged forward into an oncoming stream to turn and flow back over and about the lander vehicle. The lander vehicle is immersed in a bath of atmospheric and retrorocket gases which will influence the heating, the deceleration and the vehicle control. Thus, a prerequisite for a Mars lander design which employs a retrorocket system is the understanding of the interaction of a retrorocket with a countercurrent flow.

The general features of the flow field about vehicles with a single rocket or jet exhausting through the aeroshell into a supersonic counterflowing gas stream are shown in Figures 1 and 2. The retrojet issues into a region of separated flow and expands laterally to a maximum diameter determined by the ratio of the jet exit pressure to separated (dead air) flow pressure. The upstream extent of the retrojet is bounded by a terminal or jet shock which adjusts its pitot pressure to balance that of the free stream. The free stagnation point at which the pitot pressures are actually balanced is somewhat upstream of the terminal shock, and defines the apex of the interface between the jet and atmospheric gases. The thickness of the inner shock layer, between the jet shock and the interface, is fixed by the requirement that it contain the flow passing through the jet shock. If the flight speed is supersonic, a bow shock forms ahead of the interface, as sketched in the figures, and defines an outer shock layer. Its thickness and the flow within it are the same as for a solid body defined by the profile of the interface. The bow shock is, of course, absent at subsonic flight speeds but the external flow may still be calculated as if the interface were the surface of a solid body. For the retrojet flow the shape of the interface is determined by a local balance everywhere between the pressure distribution corresponding to the external flow and the internal pressure generated by the jet.

The velocities on either side of the interface between the retrojet and atmospheric gases are different and viscous forces are generated which form a shear layer spreading out into both gases. Gases in this shear layer merge with those at the Inner Interface and they then flow downstream together as shown in the figures. The scale of this flow pattern is determined by the thrust of the retrorocket gases acting on the counterflowing atmosphere. If the aeroshell is large with respect to this scale, the shear layer attaches to its surface as shown in Figure 1. If, on the other hand, the aeroshell is small relative to the flow pattern, the annular shear layer converges behind the aeroshell in a wake-like flow, as shown in Figure 2.

1.2 OBJECTIVES OF THE STUDY

This report discusses the progress accomplished during the first year of a two-year contract to study Propulsive Re-entry Aerodynamics. The objectives of the first year of study are to develop the analytical means required to predict the flow field in the immediate vicinity of a planetary entry system composed of an aeroshell with one or more retrorockets in sub or supersonic flight through a planetary atmosphere and to determine the forces, moments and heating conditions on the aeroshell. In the second year a digital computer program will be developed for the analytical solutions, and the analytical model will be tested by performing an experimental test program and comparing the experimental results with the analytical predictions.

The analytical description of the flow field generated by a rocket exhausting into a counterflowing gas stream must include calculation procedures for the jet flow, including the location of its terminal shock, the jet boundary, the profile of the interface between the jet and atmospheric gases, the growth of the shear layers along the interface, and along the edge of the jet boundary and dead-air region, the reattachment of the shear layer to the aeroshell or the recompression of the shear layer in wake-type flow.

In the analysis, we have taken a balanced approach to a problem in which the properties of free jets, regions of separated flow, and reattaching or recompression shear layer all interact to determine a very complex flow pattern. This balance has two aspects: one consists in using mutually consistent degrees of approximation in treating the various features of the flow; the other consists in using a method for one feature which yields information in a form acceptable to the method used in treating another feature of the flow which interacts with the first. The completely analytical methods which resulted were developed without recourse to method of characteristic solutions. We have used a degree of approximation which provides results with acceptable engineering accuracy.

1.3 SUMMARY OF WORK ACCOMPLISHED DURING THE FIRST YEAR

A literature search was made to locate previous analytical and experimental work on how a rocket or jet exhausting through an aeroshell and into a counterflowing gas stream affects the aeroshell. Allied fields such as thrust-vector control and attitude control were canvassed for relevant information that could aid the investigation. The results of the literature survey are discussed in the Summary of Previous Investigations, Section 2, and the references are documented in Appendix A.

In the analytical investigation, we have considered only the flow field due to a single supersonic retrorocket exhausting from an aeroshell into oncoming subsonic, transonic or supersonic streams so far. The large thrusting coefficient regime, $0.5 < C_T = T/q_\infty A_m < 15$ is considered. This is the range of thrusting coefficients encountered during the terminal landing phase for planetary landing on Mars when values of retrorocket ignition altitude and vehicle velocity at ignition are considered which are represented of direct entry or entry from a parking orbit (Section 3 and Appendix B). The analysis is general and also applies to the terminal landing phase for landings in Earth or

Venus atmospheres. All the main features of single jet flow field are described in this report. Two regimes of flow are distinguished on the basis of whether the returning shear layer reattaches to the aeroshell, or passes around it to a point of confluence which marks the beginning of a wake. Analyses for the jet flow, jet boundary and terminal shock location are developed without need for method of characteristic solutions (Section 4.2.2). The jet flow model utilizes the Hill-Draper[7] approximation for the flow from a nozzle into a vacuum. The jet boundary locations are determined from Charwats approximate method.[8] A momentum balance analysis, similar to that of Finley [9, 10], is used to locate the interface between the free stream and jet flow (Section 4.2.3). A convenient relationship between the diameter of the blunting sphere, the ratio of the jet total pressure to free stream pitot pressure and the ratio of dead air to free stream pitot pressure is found. Fluid entrainment and mixing in the aeroshell-single jet flow field is considered and the rate of growth of the exhaust and interface mixing layer are determined (Section 4.2.4).

The recompression and recirculation conditions for reattachment of the shear layer to the forward face of the aeroshell vehicle or recompression of the shear layer at the wake neck region are discussed in Section 4.2.5. Concepts for the dividing streamline and stagnating streamline are considered. Conservation equations are developed to describe the foreign gas recirculation and enthalpy balance in the recirculation region. The overall flow field for the jet exhausting into an oncoming stream is determined in an iterative manner (Section 4.3). After assuming a recirculation region pressure, the jet flow, jet surface location, location of the terminal shock on the jet centerline, and the interface geometry and mixing layer inclination to the aeroshell surface are calculated. The dividing streamline location in the shear layer is found and the recompression conditions are evaluated. The manner in which the solution is to be iterated until the pressure rise and conservation of foreign gas recirculation and enthalpy at reattachment or recompression are satisfied simultaneously is discussed.

A comprehensive discussion of the experimental wind tunnel test program to be accomplished in Phase II is presented in Section 5.0. The purpose of the experimental program is to substantiate simplifying assumptions made in the analysis as well as establish the practical capabilities of the analytical method itself.

2 REVIEW OF PREVIOUS WORK

The existing literature on the effects of jets projected upstream from the nose of bodies in supersonic flows is considerable, dating back at least 15 years. However, not all previous work has been dedicated to the use of forward facing jets for deceleration. References 11 and 12 describe some early investigations by the NACA with small jets on slender bodies. Their purpose was to reduce the drag but, since the magnitudes of the reduction achieved were less than the thrust which could have been obtained by directing the jets aft, they were not really successful.

In the middle 1950's a program was begun at the MIT Naval Supersonic Laboratory to develop the forward-facing jet, or "aerospike", as a means of shielding infrared guidance systems from the aerodynamic heating associated with the flight of high-performance missiles (References 13 and 14). Wind tunnel tests were run on both single and multiple jets covering a range of supersonic nozzle-exit Mach numbers. The measurements included pressure distributions, drag and heating rates. At about the same time a more basic investigation of sonic jets, using interferograms to measure density fields, was conducted at the University of Toronto (Reference 15).

In the period since 1960 NASA has conducted several investigations (References 16-21) which extend significantly the range of variables previously covered. References 18 through 20 contain many fine photographs of the interaction of sonic and supersonic jets exhausting counter to supersonic and hypersonic main streams. In these tests the jet flow exhausted forward from tubes or flat faced cylinders and did not reflect the interactions of interest in this study where the jet is exhausting from a sphere-cone aeroshell.

In Reference 17, Peterson and McKenzie made experimental measurements of the forces and moments for a semi-ellipsoid body shape which had four simulated retrorockets on the forward flat face which operated countercurrent to subsonic and supersonic airstreams. Experiments were performed at stream Mach numbers ranging from 0.25 to 1.90 and for total thrusting coefficients $C_T = T/q_\infty A_{ref}$ up to 10.

In connection with a classified project,[22] forward-facing jet tests were conducted in a hypersonic tunnel (M_∞=9) with a number of jet gases and analytical models were developed to account for the observed experimental results. Charwat and Faulman[23] conducted some experiments under roughly the same conditions as the MIT work[13,14] and developed a more detailed analysis than had hitherto been available. More recently, Good and Hill in connection with a program of chemical releases from sounding rockets, has developed analytical models and conducted experiments for the previously unexplored regime of very large (C_T = 100) thrusting coefficients. (Reference 24) In this regime the jet plume is much bigger than the vehicle from which it issues and the flow pattern is quite different from that previously investigated.

The most recently published study of the retrojet is that of Finley[9] who again covers the range of conditions explored by MIT and Charwat. He considers, both analytically and experimentally, the exhaust of a sonic jet from an orifice at the nose of a body in a direction countercurrent to a supersonic main stream. It is an excellent piece of work and his main contribution is an analytical method for sonic jets which predicts the flow pattern and pressures on the body for thrusting coefficients up to about C_T = 0.5. The predictions of his analytic model for the location of bow shock, interface and jet shock are in excellent agreement with the data. Related discussions of this investigation are presented in References 10, 25, 26. The experiments of Reference 26 consider the reattachment of an axisymmetric free

shear layer to a spherical surface and the Chapman-Korst reattachment model is shown to correlate the results very well.

An investigation of retrojet flow with multiple nozzles has been reported in Reference 19. The interaction of the individual jet plumes is similar to that observed in other investigations (References 27 and 28) of multinozzle flows issuing into still air. As the individual plumes merge, a portion of the flow is reversed and impinges on the aeroshell, again in a manner similar to that reported by Göethert (Reference 29) in connection with his investigation of base heating of cluster-nozzle rocket exhausts. It seems that the only previous investigation of aeroshell heating by a retrorocket plume is reported in Reference 30. The recovery, or equilibrium temperature was found to be closer to the chamber temperature of the rocket than to the stagnation temperature of the airstream.

A complete list of references for forward facing jets into oncoming free streams is contained in Appendix A.1. References for the interaction of a transverse jet with a free stream and the use of jets for thrust vector control are listed in Appendix A.2. The interactions of jets with surfaces are considered in Appendix A.3. Of all the references contained in Appendix A.1, the works of Finley are most applicable to the present investigation. The experiments and theories for transverse jets, thrust vector control and interaction of jets with surfaces, though they are interesting and informative, are not directly useful to the present investigation.

From the preceding analyses and experiments, some general conclusions may be formed about the interaction of a forward facing jet with a countercurrent free stream.

1. Four distinct flow regimes have been identified of which the first three are illustrated by schlieren photographs in Figure 3-5 in the order of increasing C_T. For low thrusting coefficients, the jet penetrates forward a short distance from the nozzle exit plane.

(Regime 1 $C_T = .04$ Figure 3). If the thrusting coefficient is increased to the point where the nozzle exit pressure and dead air pressure are equal, the jet penetrates far upstream into the oncoming flow (Regime 2 $C_T = 0.12$ Figure 4). Regime 1 and 2 flow fields are unsteady. The upstream penetration of the jet decreases with further increases in the thrusting coefficient and a steady flow field is formed closer to the vehicle. The flow field is approaching this condition in Figure 5 (Regime 3 $C_T = 0.28$). As the thrusting coefficient is increased still further, the steady flow field increases and size and the diameter of the flow field becomes large with respect to the nozzle exit diameter. (Regime 4). Photographs of this regime are shown in References 19 and 20. An example of Regime 4 flow is shown in Figure 6 for $C_T = 109$.

2. The behavior of the total drag of the body plus retrorocket as C_T increases is illustrated in Figure 7 based on Reference 13. The sharp drop in the curve at $C_T \approx 0.1$ corresponds to the transition from Regime 1 to Regime 2. The subsequent transition to Regime 3 is by contrast very gradual, occurring approximately at the minimum in the curves. As C_T increases in Regime 3 the drag rises with it linearly and is offset an approximately constant amount from the curve corresponding to the retrothrust alone. As noted elsewhere (References 16, 17, and 19) the value of C_T required to achieve an actual increase in total drag (over the value without retrothrust) is quite large. For the case illustrated, this requirement, is approximately, $C_T > 1.6$. Similar values have been reported for all other tests with the exception of Reference 21. If the objective of the retrojet system is to provide braking over and above that obtainable from the vehicle drag alone, it follows that the only flow regimes of interest are 3 and 4. The anomalous results of Reference 21 should be investigated further, however. The results obtained for multiple retrorockets in Reference 17, both with respect to bow shock displacement and drag variation are similar to those observed with a single jet.

3. RETROJET OPERATING CONDITIONS

The main conclusions of an analysis of retrorocket braking during the terminal landing phase are reviewed here. The process is considered in greater depth in Appendix B. We assume that the trajectory is vertical before retrorocket firing and that the forces of gravity and aerodynamic drag acting on the vehicle may be neglected during retrorocket firing. It is assumed that a deceleration force of constant magnitude is applied from retrorocket ignition to landing. The variation with time of the mass of the lander vehicle is considered in the analysis. The thrust magnitude is chosen such that the vertical velocity of the lander is reduced to zero at the surface. The manner in which the analysis may be applied to nonvertical landing trajectories is discussed in Appendix B. Low m/C_DA vehicles in dense Martian atmospheres have nearly vertical trajectories during the terminal landing phase, while the same vehicles in the VM 8 atmosphere[2, 31] (lowest density atmosphere - Figure 8) follow terminal landing trajectories which initially (at retrorocket ignition) make shallow angles with the surface. Reference 2 (pp. 2-125, 2-126). The thrust-to-weight ratios for reasonable lander vehicles are sufficiently high so that neglecting the force of gravity in the analysis is reasonable. The analysis is intended to supply a preliminary feeling for the magnitude of certain parameters affecting the terminal landing phase and is not exhaustive in scope.

The required propellant mass fraction versus retrofire velocity is shown in Figure 9, while the required thrust to earth weight ratio, T/W, versus the same parameter is shown in Figure 10 for various retrofire altitudes. In Figure 9 the required propellant weight is multiplied by a factor of 1.15 to allow for propulsion hardware. A specific impulse, I_s, of 310 sec. was assumed for the rocket. In general the amount of propellant expended for a rocket of specified

specific impulse depends only on the landers initial velocity while the thrust-to-weight ratio required to reduce the lander velocity to zero at zero altitude is a function of the initial velocity and altitude at retrofire only (Appendix B).

At retrofire altitude, we may write the thrusting coefficient $C_T = T/q_\infty A_m$ in the general form

$$C_T = \frac{2gC_D\beta}{\rho V_o^2} \left(\frac{T}{W}\right) \qquad (1)$$

where

g is the acceleration due to gravity,

C_D is the lander-aeroshell drag coefficient,

β is the lander-aeroshell ballistic parameter $m/C_D A_m$,

V_o is the initial velocity at retrofire,

and ρ is the density of the atmosphere at the retrofire altitude and is obtained from a suitable model of the Martian atmosphere.

T/W is described by Equation B-8, Appendix B.

Lines of constant vehicle ballistic parameter, β, are also shown in Figure 10 and were obtained from calculations of atmospheric entry in Reference 6. The lines of constant β are shown for a typical set of entry conditions and the VM-8 atmosphere.

V_e = 3.8 km/sec,

γ_e = 15^o,

P_o = 5 mb surface pressure,

and H = 10 km atmospheric scale height.

For those cases of interest where the propulsion system mass expenditure is small (i.e., less than twenty percent), a constant mass analysis may be used. In this case the thrusting coefficient at retrofire is simply

$$C_T = \frac{\beta C_D e^{h_o/H}}{\rho_o h_o} \tag{2}$$

where

ρ_o is the surface density,

H is the atmospheric scale height,

and h_o is the initial retrofire altitude.

To derive this expression, we have assumed an exponentially varying atmosphere density

$$\rho = \rho_o e^{-h/H} \tag{3}$$

The variation of thrusting coefficient with altitude after ignition is found from the expression

$$C_T = \frac{\beta C_D e^{h/H}}{\rho_o h} \tag{4}$$

where h is the altitude of the lander vehicle. The variation of thrusting coefficient with altitude for this approximate case is independent of ignition altitude, h_o, and initial velocity V_o.

The variation of thrusting coefficient with altitude, determined from the preceding equation, is shown in Figure 11 for a particular set of vehicle and atmospheric parameters. The vehicle β is chosen as 0.50 slugs/ft^2 and the surface density, ρ_o, and the scale height, H,

are chosen as $\rho_o = 1.32 \times 10^{-2}$ kg/M^3, corresponding to a surface pressure of 5 mb, and H = 10 kilometers (VM-8 Martian atmosphere, Figure 3).

A drag coefficient slightly larger than unity is typical for blunted conical shapes in the transonic-supersonic region[32]. If C_D is assumed to be unity, then the thrust coefficient would increase with decreasing altitude as shown in Figure 11. For an ignition altitude of 5 kilometers, the initial thrusting coefficient would be 2. The thrusting coefficient C_T increases to 6.5 at an altitude of one kilometer. The thrusting coefficients in Figure 11 are representative for cases of low propulsion mass expenditure. For larger propulsion mass expenditure, the thrusting coefficient may be determined from Equation B-8, Appendix B.

The nozzle area may also be computed from the thrust/weight ratio, since

$$\frac{T}{W} = \frac{C_F P_c A^*}{\beta g C_D A} \tag{5}$$

We get the simple result

$$\frac{A^*}{A} = \frac{\beta g C_D}{P_c C_F} \frac{T}{W} \tag{6}$$

In Figure 12 we have plotted d^*/d_m (where d^* is the nozzle throat diameter and d_m is the vehicle diameter) versus the ballistic parameter. This has been done for the particular conditions

$P_c = 200$ psi,

$C_D = 1.0$,

and $C_F = 1.8$

but the results may, of course, be generalized very simply according to Equation (6).

Certain conclusions may be reached from the preceding analysis.

1. If the propulsion system weight is limited to a reasonable fraction of the vehicle weight, say less than 25 percent, the retrofire velocity must be less than about 0.7 km/sec.

2. In turn, if we use the nominal aerodynamic braking trajectories of Reference 6, this sets an upper limit on the allowed ballistic parameter of $\beta = 0.7$ slugs/ft^2 (Figure 10).

3. Given a value of β, it is obvious that the propulsion system required will become lighter as retrofire is delayed and more use is made of aerodynamic braking. It is also true, though less obvious, that the thrust/weight ratio is also least for the lowest retrofire altitude. (At least for the re-entry trajectory data of Reference 6 which is shown in Figure 10.)

4. Retrorockets having thrusting coefficients substantially greater than unity may be encountered during the final retrorocket braking phase of a Mars entry mission (Figure 11). In fact, the thrusting coefficient approaches infinity in the limit of small velocity. Since the thrusting coefficient is proportional to the ballistic parameter, β, of the lander, lander vehicles with small β will require lower thrusting coefficients during landing. In the two Voyager studies[1-5], the aeroshell ballistic parameters were chosen as $\beta = 0.3$ slugs per square foot and $\beta = 0.2$ slugs per square foot in an effort to maximize the velocity decrease produced by the aeroshell vehicle from entry to the beginning of the terminal phase, and thus, to minimize the propulsion propellant requirements.

5. The engine size required is a strong function of ballistic parameter, and depends less strongly on retrofire altitude (Figure 12).

6. The following limitations of these typical results must be kept in mind:

a) The rocket performance analysis is approximate, neglecting gravity and aerodynamic forces. It will be shown later in the report that at large thrusting coefficients the aerodynamic forces acting on aeroshell are indeed small, since the aeroshell is immersed in a constant pressure bath. As far as the thrust-to-weight ratio, T/W, is concerned, the assumption of a vertical trajectory yields an upper limit. If the flight path angle during retrofire is γ, these values should be multiplied by $\sin\gamma$.

b) The aerodynamic calculations[6] which were used to define initial conditions for retrofire are specifically restricted to a certain entry velocity, entry angle and assumed Martian atmosphere. Page 12.

4.0 THEORETICAL ANALYSIS

The flow field about an aeroshell vehicle with a single retrorocket which exhausts countercurrent to an oncoming stream will now be discussed. Thrusting coefficients from about 0.5 to 15 or greater will be considered. We have seen previously that this is the range of thrusting coefficients which may be encountered during a planetary landing on Mars and which produces a retrorocket-aeroshell drag which is near or greater than the drag coefficient of the aeroshell without retrorockets. The magnitude of the thrusting coefficient has been shown to be an indicator of the flow regime present. In the present analysis, it will be shown that the overall dimensions of the flow field are determined by the magnitude of the thrusting coefficient and that the diameter of the interface or blunting sphere and the jet-shock standoff distance scale as the square root of the magnitude of the thrusting coefficient. Thus the thrusting coefficient is a good parameter with which to describe the flow field. The subsonic, transonic and supersonic free stream speed ranges (as opposed to the hypersonic range) are emphasized since the aeroshell itself will be used for deceleration at higher speeds. Supersonic retrorocket nozzle flow will be considered.

4.1 GENERAL FEATURES OF THE FLOW FIELD

The general features of the overall flow field are shown in Figures 1 and 2 for the cases of shear layer attachment at the aeroshell shoulder and recompression of the shear layer in the wake neck region for wake type flow respectively. The retrorocket jet expands from supersonic velocity at the nozzle exit plane to a high Mach number, experiences a normal shock on the axis (jet shock or terminal shock) and decelerates subsonically to a mutual stagnation point (free stagnation point). The supersonic free stream flow also encounters a normal shock on the axis (bow shock) and the recovered stagnation pressure for both flows,

$P_{o_{f,\infty}}$ and $P_{o_{f,j}}$ for the mainstream and jet respectively, must be equal regardless of the jet pressure. The Mach number (M_j) of the jet flow just before the jet shock occurs is of such a value that it will satisfy the free stagnation point pressure as the jet total pressure, P_{o_j}, is varied. The terminal shock to a good approximation is a portion of a spherical surface whose center is located at the nozzle exit plane (see Figure 1 Reference 20 for sonic jets and Figure 9 Reference 23 for supersonic jets). The location of the jet boundary is dependent on the ratio of the jet exit pressure P_e to the dead air pressure P_d. An interface separates the free stream gas from the jet gases. The free stream gas which passes through the bow shock wave turns and flows outward between the bow shock wave and interface while the jet flow which passes through the jet terminal shock flows outward between the jet terminal shock and interface. Mixing between the free stream gases and the jet gases occurs along the interface because properties such as the velocity and density of the two fluids are different. Mixing occurs in the region which separates the free stream-jet layer from the dead air region (recirculation region) too.

Two modes of flow are distinguished on the basis of whether the returning shear layer reattaches to the shoulder of aeroshell or passes around it to a point of confluence which marks the beginning of the wake. Aeroshells from the blunted sphere-cone family are considered with a typical aeroshell vehicle having an included half-angle of 60 degrees.

It is postulated that reattachment of the shear layer at the shoulder of the aeroshell vehicle (Figure 1) occurs in the same manner as observed by Wood[33] on spiked cone-cylinders in hypersonic flow. Reattachment at the shoulder is depicted in Figure 13. Wood noted that, although the dividing streamline must meet the face of the body, the outer part of the shear layer may pass outside of the shoulder. By this mechanism, the deflection of the shear layer and the associated reattachment pressure rise can be very much less than the values

required to turn the flow parallel to the face of the body. Recompression of the shear layer in the wake region (Figure 2) is assumed to take place in the classical Chapman[34] - Korst[35] manner in which recompression occurs along the separation streamline in an isentropic manner. In Figure 14 the angle that the shear layer in the wake type flow case makes with the axis of symmetry is such that the mass flow reversed into the recirculation region by the pressure rise through the reattachment region is balanced by the mass scavenged from the recirculation region along the jet boundary and along the inside of the free stream-jet flow shear layer. The mass returned to the recirculation region when reattachment occurs at the areoshell shoulder is balanced in the same manner.

It is possible that wake type flow will not close for subsonic free stream conditions and the subsonic wake may approximate a three dimensional Kármán Vortex street. Also, there may be a region of flow instability in passing from the mode where reattachment occurs at the aeroshell shoulder to the mode where a wake type recompression occurs. No data is available to confirm or deny these possibilities.

In the following material, the details of the single jet flow pattern are discussed. The jet flow within the jet boundary, the location of the jet boundary and terminal shock, the position of the interface, the mixing along the interface and dead air region, the reattachment or recompression conditions and the iterative manner in which a complete solution is obtained are described.

4.2 THE SINGLE JET FLOW PATTERN

4.2.1 Flow Interaction Diagram

The elements required in the solution of the single jet flow field are noted in Figure 15. The atmospheric and retrorocket exhaust gases are treated as chemically frozen perfect gases in the analysis. The

principal parameters in the solution are:

1) the gas properties; molecular weight M, specific heat C_p, and ratio of specific heats γ;

2) the geometric parameters; aeroshell shape, and for the retrorocket, the ratio of exit area to the aeroshell frontal area and internal area ratio Ae_j/A^*;

3) the flight parameters; Mach number M_∞ and Reynolds number Re_{D_∞}:

4) the retrorocket operating parameters; the total temperature ratio T_{t_j}/T_{t_∞} and the thrusting coefficient $T/q_\infty A$, based on flight dynamic pressure and aeroshell reference area.

The magnitudes of the various variables encountered during the solution of the flow field of a single jet exhausting into an oncoming free stream are noted in Figures 16-18. The equations appropriate to these Figures are discussed in Appendix C.

Figure 16 shows that total jet pressure to shocked ambient pressure ratios P_{o_j}/P_{o_f} from 20 to 350 are required to produce thrusting coefficients, C_T, from 1 to 10 for the case of a M = 3.0 jet exhausting into a supersonic free stream from a aeroshell with a diameter to nozzle exit diameter ratio of 5.

The variation of jet exit to dead air pressure ratio P_{e_j}/P_d with changes in the dead air to shocked ambient pressure ratio P_d/P_{o_j} and total jet pressure to shocked ambient pressure ratio P_{o_j}/P_{o_f} is shown in Figure 17. A Mach three, γ = 1.4, jet is assumed in the calculation. Values of P_{e_j}/P_d from 5 to 100 are encountered for the conditions of interest in this study. The location of the jet boundary is determined directly by the magnitude of this ratio, P_{e_j}/P_d. Specification of the free stream Mach number, M_∞, and specific heat ratio γ_∞ and

P_{o_j}/P_{o_f} determines the total jet pressure to total free stream pressure ratio, P_{o_j}/P_{o_∞} (Figure 18).

4.2.2 Jet Plume

Since the velocities in the dead air recirculating region are small, the retrorocket exhausts essentially into still air which is at the dead air pressure level P_d. The jet boundary location is determined by the ratio of the retrorocket exit pressure, P_{e_j}, to the dead air pressure, P_d, i.e., P_{e_j}/P_d. The jet flow inside of the jet boundary (inner jet flow) is not affected by the external flow and expands into the region bounded by the jet boundary and terminal shock wave as if into a vacuum. For a jet exhausting into a vacuum, the gas, upon exit from the jet, quickly accelerates to within a few percent of its limiting velocity. The farfield of the jet is essentially radial flow, with straight streamlines appearing to originate from a common source near the exit plane of the retrorocket.

4.2.2.1 Inner Jet Flow

The inner jet flow can be described without recourse to method of characteristic solutions by the approximate method of Hill and Draper.[7]

Hill and Draper developed an analytical analysis for the flow from a nozzle into a vacuum which may be used to specify the spatial variation of parameters such as density, temperature, Mach number, etc. in the inner jet flow. A schematic of the flow pattern of a nozzle exhausting into a vacuum is shown in Figure 19. The method replaces the tedious and costly method of characteristics approach with a simple analytical model which allows many calculations to be performed quickly and cheaply.

Hill and Draper noted that published method of characteristic solutions exhibit a very rapid decay of $(\dot{dm}/d\Omega)_\theta$, the mass flow/sec/unit solid angle in the θ direction, away from the axis and that this decay could be closely approximated by the members of the one-parameter family

$$\frac{(\dot{dm}/d\Omega)_\theta}{(\dot{dm}/d\Omega)_0} = \frac{r^2(\theta)}{r^2(0)} = f(\theta) = \exp\left[-\lambda (1-\cos\theta)^2\right] \qquad (7)$$

where λ is a parameter determined by satisfying the conservation of mass and momentum flux in the jet. λ is a function only of the Crocco number, $c = v/v_\ell$ and C_F and C_{Fmax}, the nozzle thrust and maximum thrust coefficient respectively. Specification of the jet specific heat ratio, γ_j, and area ratio Ae_j/A^* fixes C_F and C_{Fmax}.

The variation of density along the centerline of the jet was found to be given by

$$\frac{(\rho r^2)_0}{\rho_c r^{*2}} = \left[\frac{2}{\gamma+1}\right]^{1/\gamma-1} \frac{\lambda}{\sqrt{\pi}} \frac{c^*}{c} \qquad (8)$$

where the density is normalized with respect to its chamber value.

Once the point on the axis corresponding to any given density is located with the above equation, the rest of the curve along which the density has this value may be determined from Equation 7. Parameters such as velocity, temperature and Mach number are also constant along the constant density contours and can be determined from gas flow tables.

A comparison between the Hill-Draper analytic approximation and a typical set of constant property contours calculated numerically by the method of characteristics[36] is made in Figure 20. A comparison of the predictions of the Hill-Draper theory for the mass

flux distribution in the inner jet flow with method of characteristic solutions of Piesik[37] et al is shown in Figure 21. The agreement is good. The Hill-Draper model may be used to calculate the flow from a number of nozzle types using different gases since variations in these parameters simply affect the value of λ used in the computation. Sonic and supersonic nozzle flows may be handled with this method. The Hill-Draper Method can be used for solid propellant rocket motors by utilizing the methods discussed in References 38-39. This flow model is used to obtain the locations of the terminal jet shock (Section 4.2.2.3).

4.2.2.2 The Jet Boundary

The jet boundary may also be located with an analytical method instead of using the method of characteristics approach. In the region of thrusting coefficients of interest, $0.5 < C_T < 15$, the jet expansion from the nozzle is equivalent to the case of a jet expanding into a constant pressure reservoir, where the pressure is equal to that in the recirculating region.

During our literature search, the analysis of A. F. Charwat entitled 'Boundary of Underexpanded Axisymmetric Jets Issuing into Still Air'[8] was found and upon examination appeared to be a simple approximate method which gave satisfactory results, at least for the single comparison with a method of characteristics solution made in his article, and suited to the pressure levels of interest. It should be noted that there are other approximate analyses available for locating the jet boundary, for instance references 40 and 41, but reference 8 appeared to be especially well suited to low pressure ratios.

Comparisons of Charwats' approximate method with available method of characteristics solutions[42-43] were made to ascertain the accuracy over a wide pressure range of the method for exhaust jets with supersonic exit Mach numbers.

A comparison of jet boundary shapes calculated with Charwats' approximate method and method of characteristic solutions[42] is shown in Figure 22 for $M_{e_j} = 2.5$ and $M_{e_j} = 3.0$ jets with nozzle divergence angles of zero degrees. The jet boundary location is a function only of the ratio of the nozzle exit to dead air pressure ratio. The approximate method is found to be in good agreement with the characteristic solutions for nozzles with zero divergence angles for jet exit to dead air pressure ratios from 2 to 20. Method of characteristic solutions were not available in reference 42 above $P_{e_j}/P_d = 20$. To test the approximate method at higher pressure ratios P_{e_j}/P_d, for nozzles with zero divergence angle, a comparison was made with method of characteristic solutions contained in reference 43. The solutions selected for comparison were those for a $M_{e_j} = 5.35$ jet, with $\gamma_j = 1.24$ and zero nozzle divergence angle. The boundary shape at a pressure ratio, P_{e_j}/P_d, of 188.1 is shown in Figure 23. The approximate method is within 15 percent of the method of characteristic solution at $P_{e_j}/P_d = 188.1$. Comparisons at other pressure ratios could not be made due to a lack of method of characteristic solutions. A discussion of Charwats' method and further comparisons with method of characteristic solutions are contained in Appendix C. In Summary, we found that the approximate method is suitable for calculations over the pressure ratios of interest and the desired degree of accuracy for nozzles with zero divergence angle, and properly accounts for variations in nozzle divergence angle at low pressure ratios. The jet boundary locations for a Mach three retrojet exhausting air are shown in Figures 24 and 25 and were calculated using Charwats' method.

4.2.2.3 Jet Terminal Shock

The terminal shock wave position may be determined analytically. The terminal shock is located so that it will increase the jet pressure to that of the decelerated free stream at the free stagnation

point. The jet flow Mach number before the normal shock is such that the normal shock compresses the exhaust flow back to a pressure level which is equal to the pressure level of the free stream gas after passing through the bow shock wave (for supersonic free stream conditions). The balance of pressure determines the location of the free stagnation point in the flow field.

For a specified free stagnation point pressure, the jet shock location can be determined using the jet flow model of Hill and Draper for the centerline density and Mach number decay and equations for conditions across a normal shock. The Mach disc location is found by iterating on the difference between the desired pressure and the pressure behind the normal shock until this difference is zero (Appendix E).

A similar technique was used with good results to locate the Terminal Shock location for underexpanded jets issuing into a still atmosphere. (Ref. 44). Those results differ from the ones to be discussed here in that for underexpanded jets issuing into a still atmosphere, the terminal shock may be located by assuming the normal shock recompresses the centerline exhaust flow to ambient pressure. For the case of a jet expanding into a separated flow region countercurrent to an oncoming stream, the jet boundary is located by the separated or dead air pressure but the terminal shock location is located so that it will increase the pressure to that of the decelerated free stream at the free stagnation point.

The analysis of Appendix E was solved in order to locate the terminal jet shock position on the jet centerline for the case of a jet opposing a supersonic stream. To test the accuracy of the approximate analysis for the location of the terminal shock wave, a comparison was made with experimental data available for a single supersonic jet into an oncoming stream.[18]

A comparison of theoretical predictions for the location of the jet shock with experimental data of Hayman and McDearman[18] is made in Figure 26. The experimental data and theoretical

calculations shown are for a M = 3.00 jet exhausting into a M = 2.91 counterflowing stream. It appears that the experimental data fairs into the theoretical predictions for ratios of jet-to-shocked ambient pressure greater than twenty. No data is available for this supersonic jet with P_{o_j}/P_{o_f} ratios larger than thirty. To place this comparison in perspective, we should note that at $P_{o_j}/P_{o_f} = 20$, with a nozzle exit to diameter ratio, d_{e_j}/d_m, of .2, $C_T = 0.56$ where

$$C_T = \frac{T}{q_\infty A_m} = \frac{C_F A^* P_{o_j}}{q_\infty A_m} \tag{9}$$

Since we are to consider C_T's to 15 in the present study, we will be interested in the larger jet to shocked ambient pressure ratios where the theoretical predictions appear to be reasonably good. Though a more complete comparison than that made above of the analytical method with experimental results is desireable, the absence of appropriate experimental data at this time does not allow such a comparison to be made. Since the Hill-Draper Model for exhaust flow was shown to be in good agreement with method of characteristic solutions for the inner exhaust flow (i.e. the exhaust flow bounded by the jet boundary and terminal shock), was shown to accurately locate the terminal shock wave in underexpanded plumes which are exhausting into still air[44] and provides reasonable predictions for the location of the jet shock for a jet into an oncoming flow (Figure 26), it is used for predicting the terminal shock location in the present investigation. The location of the jet terminal shock is shown in Figure 27 for a Mach 3 jet exhausting air with a specific heat ratio, γ, of 1.4 as the total jet pressure to shocked ambient pressure is varied from 10 to 350. For the pressure ratios, P_{o_j}/P_{o_f}, of interest, the jet shock is located, from six to twenty nozzle exit radii, upstream from the nozzle exit plane.

4.2.2.4 Plume Shoulder Locations

As noted earlier, the terminal shock may be represented by a portion of a spherical surface whose center of curvature is located at the retrorocket nozzle exit plane. The intersection between the terminal shock wave and jet boundary is a circle centered about the axis of symmetry of the jet and will be designated at the plume shoulder location. The lateral and longitudinal coordinates of the plume shoulder location as measured from the jet centerline and retrorocket exit plane respectively are presented in Figures 28 and 29 for γ_j=1.4, M_{e_j}=3.0 jet. The jet terminal shock depends only on the ratio of the total jet pressure to the shocked ambient pressure while the jet boundary is a function only of the ratio of the jet exit pressure to the dead air pressure.

4.2.3 Interface

4.2.3.1 Blunting Sphere Diameters from Momentum Balance

The interface (first interface) between the shocked free stream gases and retrojet gases is determined using a momentum balance analysis which is similar to that used by Finley.[9] The control surface used for the momentum balance is shown in Figure 30 as a broken line. The control volume is located about the interface which separates the jet flow from the mainstream flow. The interface is taken to be a spherically blunted cone with cone semi-apex angle α and the diameter of the blunting sphere d_f. The choice of a blunted cone shape is supported by previous experimental results.[9] The pressure on the conical portion of the interface and the dead air region is constant at P_d, the dead air pressure. The pressure on the spherical portion of the interface decreases with increasing polar angle, θ, until the dead air pressure level is reached.

The momentum theorem states that the net force acting instantaneously on the fluid within the control volume is equal to the time rate of change of momentum within the control volume plus the excess of outgoing momentum flux over incoming momentum flux.

The net force acting on the control volume was obtained by integrating the pressure forces over the control volume. For a supersonic free stream, the pressure acting on the spherical portion was assumed to be that given by modified Newtonian theory; i.e.,

$$P/P_{o_f} = \sin^2 \phi + (P_\infty/P_{o_f}) \cos^2 \phi \qquad (10)$$

where ϕ is the local inclination of the surface to the free stream (Figure 30), P_∞ the free stream static pressure and P_{o_f} the pitot pressure of the free stream. A comparison of modified Newtonian theory with experimental data [45] is shown in Figure 31 and indicates that this is a suitable choice for Mach numbers greater than M = 1.5. Finley's experimental data [9] showed good agreement with modified Newtonian flow for a free stream Mach number of 2.5.

We will first develop an analysis for free stream Mach numbers greater than M = 1.5 utilizing modified Newtonian theory for the pressure on the blunting sphere. The analysis is extended over the range from M = 1.5 to subsonic free stream condition by another analysis which starts on page 31.

The horizontal component of the net force attributable to the spherical portion of the control surface was determined by integration of the local pressure forces. We find that

$$\sum F_H = \frac{\pi d_f^2}{8} \cos^4 \alpha (P_\infty - P_{o_f}) + \frac{\pi d_f^2}{4} \cos^2 \alpha P_{o_f} \qquad (11)$$

The total force acting on the control surface, including the dead air contribution on the conical and rearward portions of the control surface and the exhaust jet pressure contribution at the nozzle exit plane was

found to be

$$F_H = \frac{\pi d_f^2}{8} \cos^4 \alpha \, (P_\infty - P_{o_f}) + \frac{\pi d_f^2}{4} \cos^2 \alpha \, P_{o_f} \qquad (12)$$

$$- \frac{\pi d_f^2}{4} \cos^2 \alpha \, P_d - \pi r_{e_j}^2 P_{e_j} + \pi r_{e_j}^2 P_d$$

where r_{e_j} is the nozzle exit plane radius. The contributions to the horizontal force balance of the portion of the conical surface and rearward facing control surface above $r = \frac{d_f}{2} \sin \alpha$ cancel.

Upon substitution of the dead air pressure

$$P_d/P_{o_f} = \sin^2 \alpha + (P_\infty/P_{o_f}) \cos^2 \alpha \qquad (13)$$

the net force on the control volume is found to be

$$\sum F_H = \frac{\pi d_f^2}{8} \cos^4 \alpha \, (P_{o_f} - P_\infty) - \frac{\pi d_j^2}{4} (P_{e_j} - P_d) =$$

$$+ \dot{m}_\ell V_\ell \cos \alpha + \dot{m}_j V_{e_j} \qquad (14)$$

The terms on the right represent the momentum flux in the jet layer and nozzle flow respectively.

Equation (14) provides a convenient relationship between the diameter of the blunting sphere d_f, the ratio of jet total pressure to free stream pitot pressure, P_{o_j}/P_{o_f} and the ratio of dead air to free stream pitot pressure P_d/P_{o_f}. Dividing both sides of equation 14 by P_{o_f} and recognizing that

$$\dot{m}_j = \dot{m}_\ell = \rho_{e_j} V_{e_j} A_e = \rho_{o_j} \left(\frac{\rho_e}{\rho_{o_j}}\right) a^* \left(\frac{V_{e_j}}{a^*}\right) \frac{\pi d_{e_j}^2}{4}$$

we find that

$$(d_f/d_{e_j})^2/(P_{o_j}/P_{o_f}) = \frac{1}{1/2\cos^4\alpha\left(1-\frac{P_\infty}{P_{o_f}}\right)}\left[\left(\frac{P_{e_j}}{P_{o_j}}\right) - (P_d/P_{o_f})/\right. \tag{15}$$

$$\left.(P_{o_j}/P_{o_f}) + \frac{2\gamma}{\gamma+1}\left(\frac{\rho_{e_j}}{\rho_o}\right)\left(\frac{V_e}{a^*}\right)^2 + \sqrt{\frac{2\gamma}{\gamma+1}}\left(\frac{\rho_{e_j}}{\rho_p}\right)\left(\frac{V_{e_j}}{a^*}\right)M_\ell\sqrt{\gamma\frac{T_\ell}{T_o}}\right]$$

The term $\dfrac{\left(P_{e_j}/P_{o_j}\right)}{1/2\cos^4\alpha\,(1-P_\infty/P_{o_f})}$ represents the contribution due to the nozzle exit plane pressure.

The second term, $\dfrac{\left(P_d/P_{o_f}\right)\left(P_{o_j}/P_{o_f}\right)}{1/2\cos^4\alpha\left(1-P_\infty/P_{o_f}\right)}$ is due to the dead air pressure and will be shown to be negligible, for supersonic free streams, in comparison with other terms in expression 15 for the conditions of interest in the present study; i.e., $P_{o_j}/P_{o_f} >> 1.0$. The third and fourth terms arise from the inward and outward momentum fluxes respectively. The manner in which equation 15 is solved is discussed in Appendix F.

The magnitude of the diameter of the blunting sphere was evaluated from expression 15 for a M= 3.0 air jet exhausting into a supersonic counterflowing air stream. The results are shown in Figures 32 and 33 for free stream Mach numbers of M = 2.5 and 1.5 respectively. In each case the total value as well as the individual contributions due to nozzle exit pressure, dead air pressure, inward jet momentum flux and outward jet layer momentum flux are noted.

For $M_\infty = 2.5$, the dead air pressure term is shown for pressure ratios, P_{o_j}/P_{o_f}, equal to 35, 175 and 350 which correspond to C_T's, where

$$C_T = \frac{T}{q_\infty A_m} = \frac{C_F A^* P_{o_j}}{q_\infty A_m} = \frac{C_F A^* P_{o_j}}{\frac{\gamma}{2} M_\infty^2 P_\infty A_m}, \tag{16}$$

of 1.0, 5.0 and 10.0 if a nozzle exit to vehicle diameter ratio, $d_{e_j}/d_m = .20$ is assumed. For these pressure ratios the dead air pressure term is of negligible size in comparison to the other contributions and may be neglected in the computations.

The dead air pressure term is also negligible at $M_\infty = 1.5$, Figure 33. The pressure ratios of $P_{o_j}/P_{o_f} = 30$, 150 and 300 at $M_\infty = 1.5$ correspond to C_T's of 1.0, 5.0 and 10.0 respectively if a nozzle exit to vehicle diameter ratio, $d_{e_j}/d_m = .20$ is assumed.

The foregoing calculations were limited to supersonic (i.e. $M > 1.5$) flow wherein the external pressure distribution was assumed to be of the modified Newtonian form:

$$P/P_{o_f} = \cos^2\theta + (P_\infty/P_{o_f}) \sin^2\theta \tag{17}$$

The following analysis discusses how these calculations may be extended over the range from M=1.5 to the subsonic external flow regime. In this connection, it is noted that the flow model inside the interface is completely independent of whether the external flow is subsonic or supersonic (except possibly from mixing considerations). The problem is thus reduced to one of expressing the subsonic pressure distribution in a suitable analytic form, and integrating the expression in an analogous

way to the modified Newtonian distribution. In the subsonic case, of course, there will be no bow shock, so that P_{o_f} is simply P_{o_∞}.

Reference 45 gives a compilation of data on the pressure distribution on a spherical surface, covering both the subsonic and supersonic ranges. The subsonic data from Figure 4 of Reference 45 has been correlated in the following form:

$$P/P_{o_f} = \cos^2 \theta + f(M_\infty) \sin^2 \theta \tag{18}$$

where:

$$f(M_\infty) = \cos^2 \left(\frac{\pi M_\infty}{2}\right) + 0.38 \sin^2 \left(\frac{\pi M_\infty}{2}\right) \tag{19}$$

The correlation is shown in Figure 34 where the solid lines represent data from Reference 45, and the dotted lines are calculated from equation (18). It can be seen that the maximum error is less than 5 per cent. Comparison of equations (17) and (19) shows them to be identical when P_∞/P_{o_f} is replaced by $f(M_\infty)$. The subsonic analysis is thus identical to the supersonic analysis when $f(M_\infty)$ is substituted for P_∞/P_{o_f} in equation (15).

The blunting sphere diameter for subsonic and transonic free stream conditions may be determined by integrating the pressure distributions of Figure 34 over the spherically blunted cone control volume. The variation of the blunting sphere diameter with Mach number may be obtained from a somewhat simplified but equivalent calculation. The interface is assumed to be a hemisphere so that the hemispherical drag coefficients of Reference 45 (Figure 35) may be used to evaluate the forces on the control volume. The integrations mentioned above were done in Reference 45 to evaluate the drag coefficients for a

hemisphere. In this case,

$$\sum F_S' = D = C_D q_\infty A_m \tag{20}$$

and

$$\sum F_S' = \dot{m}_\ell V_\ell + \dot{m}_j V_{e_j}; \tag{21}$$

For

$$\dot{m}_\ell = \dot{m}_j = \rho_{e_j} V_{e_j} A_{e_j} = \rho_{o_j} \left(\frac{\rho_{e_j}}{\rho_{o_j}}\right) a^* \left(\frac{V_{e_j}}{a^*}\right) A_{e_j} \tag{22}$$

the blunting sphere diameter is found to be

$$\left(\frac{d_f}{d_m}\right)^2 = \frac{C_T}{C_D} \left[1 + \frac{V_{e_j}/a^*}{\dfrac{v_j/a^*}{1 + \dfrac{1}{\gamma_j M_j^2}}} \right] - \frac{A_{e_j}}{A_m} \frac{2}{C_D} \gamma_\infty M_\infty^2 . \tag{23}$$

The derivation of the preceding equation and the definition of various parameters are found in Appendix F. In the preceding calculations, the jet layer is assumed to exit in a rearward direction parallel to the jet axis of symmetry. ($\alpha = 0^\circ$). To use the drag coefficients of Reference 45 we have assumed that the pressure on the shoulder of the hemispherical control volume and across the plane at the rear of the control volume is equal to the free stream static pressure. Recent experimental data[46] on blunt entry shapes has shown that the dead air or base pressure is slightly less than P_∞, so that our assumption is reasonable. The variation of the blunting sphere diameter with Mach number is shown in Figure 36 for thrusting coefficients of one, five and ten respectively. The calculations are made for specific

retrorocket engine and aeroshell area ratios. $A_{e_j}/A^* = 10.$ $A_j^*/A_m = 0.0013$ and $\gamma_j = 1.4$.

4.2.3.2 Location of Center Of Blunting Sphere

The magnitude of the blunting sphere diameter is determined from the preceding analysis, but the location of the center of the blunting sphere must also be determined. The location of the blunting sphere is found by determining the interface standoff distance, δ (i.e. the distance between the jet terminal shock wave and the interface) from a conservation of mass balance. The geometry used in the mass balance is shown in Figure 37.

The fluid downstream of the terminal shock wave (i.e. the fluid between the interface and the terminal shock) is assumed to be uniform with total pressure P_{o_f}, and is assumed to be chocked in an annulus of width δ running from the edge of the jet to the interface as shown in Figure 37. The mass flux, $\dot{m}_\delta$, flowing through the annulus of width δ is equal to the mass flux, $\dot{m}_j$, from the nozzle located in the aeroshell. Therefore

$$\dot{m}_j = \dot{m}_\delta \tag{24}$$

but

$$\dot{m}_j = \rho_{o_j}\left(\frac{\rho_{e_j}}{\rho_{o_j}}\right)(a^*)\left(\frac{V_{e_j}}{a^*}\right)\frac{\pi d e_j^2}{4} \tag{25}$$

and

$$\dot{m}_\delta = \rho_{o_j}\left(\frac{\rho_\delta}{\rho_{o_j}}\right) V_\delta A_\delta \tag{26}$$

where

$$V_\delta = M_\delta a_\delta = a_\delta \text{ since } M_\delta = 1.0 \tag{27}$$

$$A_\delta = \pi d_s \delta$$

$$\left(\frac{\rho_\delta}{\rho_{o_j}}\right) = \left(\frac{\rho_\delta}{\rho_{o_f}}\right)\left(\frac{\rho_{o_f}}{\rho_{o_j}}\right) = \left(\frac{2}{\gamma_j + 1}\right)^{1/\gamma_j - 1}\left(\frac{P_{o_f}}{P_{o_j}}\right) \tag{28}$$

and

$$a_\delta = \sqrt{\gamma_j R_j T_\delta} = \sqrt{\gamma_j R_j T_{o_j}\frac{T_\delta}{T_{o_j}}} = a_{o_j}\sqrt{\frac{T_\delta}{T_{o_j}}} \tag{29}$$

Substituting equations 27, 28 and 29 into 26, we find

$$\dot{m}_\delta = \rho_{o_j}\left(\frac{2}{\gamma_j+1}\right)^{1/\gamma_j - 1}\left(\frac{P_{o_f}}{P_{o_j}}\right) a_o\sqrt{\frac{T_\delta}{T_{o_j}}}\ \pi d_s \delta \tag{30}$$

where

$$\left(\frac{T_\delta}{T_{o_j}}\right)^{1/2} = \left(\frac{2}{\gamma_j+1}\right)^{1/2}$$

Equating formulae 25 and 26, and solving for δ, we find

$$\left(\frac{\delta}{r_{e_j}}\right) = \frac{\left(d_{e_j}/d_s\right)}{2}\,\frac{\left(\frac{\rho_{e_j}}{\rho_{o_j}}\right)\left(\frac{V_{e_j}}{a^*}\right)}{\left(\frac{2}{\gamma_j+1}\right)^{1/\gamma_j-1}\left(\frac{P_{o_f}}{P_{o_j}}\right)} \tag{31}$$

where d_s is the lateral diameter of the terminal shock measured at the intersection of the jet boundary with the jet terminal shock wave.

The center of the blunting sphere is determined from the triangle composed of the radius vector from the center of the blunting sphere to the intersection of the jet terminal shock and jet boundary, the lateral radius, $d_s/2$, from the jet centerline to the intersection and the segment of the jet centerline between the longitudinal location of the intersection and the center of the blunting sphere. Hence

$$\left(\frac{x}{d_{e_j}}\right)^2 + \left(\frac{d_s/d_{e_j}}{2}\right)^2 = \left(\frac{d_f/d_{e_j}}{2} - \frac{\delta}{d_{e_j}}\right)^2 \tag{32}$$

Solving for x/d_{e_j};

$$\frac{x}{d_{e_j}} = \left[\left(\frac{d_f/d_{e_j}}{2} - \frac{\delta}{d_{e_j}}\right)^2 - \left(\frac{d_s/d_{e_j}}{2}\right)^2\right]^{1/2} \tag{33}$$

Since the longitudinal coordinate of the intersection of the jet terminal shock and jet boundary is x_I/d_{e_j}, the center of the blunting sphere is located at

$$\frac{x_c}{d_{e_j}} = \frac{x_I}{d_{e_j}} - \frac{x}{d_{e_j}} \tag{34}$$

The determination of the lateral and longitudinal positions of the intersection of the jet boundary and terminal shock, $\frac{y_I}{r_{e_j}} = \frac{d_s/2}{r_{e_j}}$ and $\frac{x_I}{r_{e_j}}$ respectively, is discussed in section 4.2.2.4.

In the preceding calculation, it was assumed that the flow through the annulus of width δ was choked ($M_\delta = 1$). Additional calculations were made where this assumption was relaxed by assuming that the flow in the annulus is uniform but not chocked. These calculations showed that the location of the blunting sphere is effected only slightly by the new assumptions for the flow in the annulus. See Appendix G.

4.2.3.3 Scaling Laws for Blunting Sphere Diameter and Terminal Shock Standoff Distance

It was shown in Section 4.2.3.1 that in the momentum balance which defines the blunting sphere diameter, d_f, certain terms may be neglected. If this is done, we may write

$$\left(\frac{d_f}{d_m}\right)^2 = \frac{2T}{A_m q_\infty} \frac{q_\infty}{\cos^4\alpha\left(P_{o_f} - P_\infty\right)} \left[1 + \frac{V_{e_j}\cos\alpha}{V_j\left(1 + 1/\gamma_j M_j^2\right)}\right] \quad (35)$$

Finley (Reference 9) has shown that the factor in the brackets does not vary very much with γ_j or M_j. It may be useful, then, to correlate the available solution in the form

$$\left(\frac{d_f}{d_m}\right)^2 \Big/ C_T \approx A^2\, f(M_\infty)/\cos^4\alpha \quad (36)$$

where

$$f(M_\infty) = 2q_\infty/\left(P_{o_f} - P_\infty\right) \quad (37)$$

and is graphed in Figure 38.

Figure 39 shows the values of A obtained from the complete solutions given in Section 4.2.3.1 as well as from Finley (Reference 9). All these data are within ±8 percent of the value

$$A = 1.25$$

for $P_d/P_{o_f} \leq 0.5$.

Note that the value of d_m is really arbitrary in relating d_f to the rocket thrust. Equation (36) may be written

$$q_\infty \, d_f^2/T \approx 2f(M_\infty)/\cos^4\alpha \tag{38}$$

In all of these expressions, T is the vacuum thrust of the retrorocket. Therefore at a fixed flight condition, the blunting sphere diameter, d_f, scales as $\sqrt{T}$.

Jarvinen[44] et al have shown that the axial distance to the Mach disc for a wide range of jet conditions may be correlated approximately by the expression

$$x_s/d_j \approx 0.69(P_{e_j}/P_{o_f})^{1/2} M_{e_j} \tag{39}$$

or

$$x_s^2 \approx 0.607 \left(\frac{\pi}{4} d_{e_j}^2 P_{e_j} \gamma_j M_{e_j}^2\right)/P_{o_f}$$

$$\approx 0.607 \, (T/P_{o_f})/(1 + 1/\gamma_j M_{e_j}^2) \tag{40}$$

In a non-dimensional form analogous to Equation 38, we may write

$$q_\infty \, x_s^2/T \approx 0.30 \, g(M_\infty)/(1 + 1/\gamma_j M_{e_j}^2) \tag{41}$$

or, in terms of C_T

$$\left(\frac{x_s}{d_m}\right)^2 \Big/ C_T \approx 0.24\, g(M_\infty)/(1 + 1/\gamma_j M_{e_j}^2) \qquad (42)$$

where $g(M_\infty) = 2q_\infty/P_{o_f}$ which is shown in Figure 38. Therefore at fixed flight conditions, the distance to the terminal shock scales as $\sqrt{T}$.

The blunting-sphere radius is generally considerably larger than the shock standoff distance, by the approximate ratio

$$(r_f/x_s)^2 \approx (5/3)\left(1 - P_\infty/P_{o_f}\right)^{-1}\left(1 + 1/\gamma_j M_{e_j}^2\right)\cos^{-4}\alpha \qquad (43)$$

The preceding approximate formulas should be adequate for parametric studies if not specific calculations.

4.2.3.4 Second Interface Location - Supersonic Free Stream

The stream surface separating the jet gas from the shocked air is referred to as the first interface. The stream surface which separates the jet gas from the recirculating flow about the vehicle will be called the second interface. The main purpose of this analysis is to describe the shape of this second interface, assuming that the first interface is a sphere-cone (Section 4.2.3.1).

Since all the mass exhausting from the nozzle must flow between the first and second interfaces, a mass balance condition will be used to determine the shape of the second interface. The relevant geometry is shown in Figure 40.

Mass balance requires:

$$\dot{m}_j = 2\pi \int_{y_d}^{o} r\rho u \, dy \tag{44}$$

Dividing both sides by $\rho_{o_j} \; a_{o_j}$,

$$\frac{\pi d_{e_j}^2}{4} \quad \frac{\rho_{e_j} V_{e_j}}{\rho_{o_j} a_{o_j}} = 2\pi \int_{y_d}^{o} r \left(\frac{\rho u}{\rho_{o_j} a_{o_j}} \right) dy$$

Dividing through by d_f^2, where d_f denotes the diameter of the blunting sphere ($d_f = 2r_f$) the above becomes:

$$\left(\frac{d_{e_j}}{d_f} \right)^2 \left[M_{e_j} \left(\frac{P_{e_j}}{P_{o_j}} \right) \sqrt{\frac{T_{o_j}}{T_{e_j}}} \right] = 2 \int_{\bar{y}_d}^{o} \bar{r} \left(\frac{\rho u}{\rho_{o_j} a_{o_j}} \right) d\bar{y} \tag{45}$$

where:

$$\bar{r} = \frac{r}{r_f} \tag{45a}$$

$$\bar{y} = \frac{y}{r_f} \tag{45b}$$

$$\bar{x} = \frac{x}{r_f} \tag{45c}$$

From Figure 40, $\bar{r}$ may be expressed as a function of $\bar{x}$ and $\bar{y}$

$$\bar{r} = (1 + \bar{y}) \sin \bar{x} \text{ , for } 0 \leq \bar{x} \leq \theta_s \tag{46a}$$

$$\bar{r} = \sin\theta_s + (\bar{x} - \theta_s)\cos\theta_s + \bar{y}\sin\theta_s \text{, for } \bar{x} \geq \theta_s \tag{46b}$$

θ_s is the angle measured from the jet centerline to the sphere-cone juncture. Now, on $\bar{y}_d(x)$

$$\frac{\rho_d u_d}{\rho_{o_j} a_{o_j}} = \left(\frac{p_{o_f}}{p_{o_j}}\right) M_d \left(\frac{p_d}{p_{o_f}}\right) \sqrt{\frac{T_{o_j}}{T_d}} \cos \omega \tag{47}$$

where ω is the angle between the tangent to $y_d(x)$ and the perpendicular to the radius vectors and p_d/p_{o_f} (and consequently M_d and T_d/T_{o_j}) is assumed to be constant. It will also be assumed that ω is everywhere small, so that cos ω is everywhere approximately equal to unity. Along the first interface

$$\frac{\rho_1 u_1}{\rho_{o_j} a_{o_j}} = \left(\frac{p_{o_f}}{p_{o_j}}\right) \left(\frac{p_1}{p_{o_f}}\right) \sqrt{\frac{T_{o_j}}{T_1}} M_1 \tag{48}$$

where $\frac{p_1}{p_{o_f}}$ is given by the Newtonian expression

$$\left(\frac{p_1}{p_{o_f}}\right) = \cos^2 \bar{x} + \left(\frac{p_\infty}{p_{o_f}}\right) \sin^2 \bar{x}$$

At a given $\bar{x}$, ρu will be assumed to be equal to the average value between ρ_1, u_1, and $\rho_d u_d$

$$\frac{\rho u}{\rho_{o_j} a_{o_j}} \simeq \frac{1}{2} \left[\frac{\rho_1 u_1}{\rho_{o_j} a_{o_j}} + \frac{\rho_d u_d}{\rho_{o_j} a_{o_j}} \right] \tag{49}$$

Using Equations (47), (46) and (49), Equations (45) may be written

$$\left[\frac{p_{o_j}}{p_{o_f}}\left(\frac{d_{e_j}}{d_f}\right)^2\right]\left[M_{e_j}\frac{p_{e_j}}{p_{o_f}}\sqrt{\frac{T_{o_j}}{T_{e_j}}}\right] = \left\{M_d\frac{p_d}{p_{o_f}}\sqrt{\frac{T_{o_j}}{T_d}} + M_1\frac{p_1}{p_{o_f}}\sqrt{\frac{T_{o_j}}{T_1}}\right\}\int_{\bar{y}_d}^{o}\bar{r}\,d\bar{y} \tag{50}$$

and using Equation (46)

$$\int_{\bar{y}_d}^{o}\bar{r}\,d\bar{y} = -\sin\theta\left[\frac{\bar{y}_d^2}{2} + \bar{y}_d\right] \tag{51a}$$

$$\text{for } \bar{x} \leq \theta_s$$

and

$$\int_{\bar{y}_d}^{o}\bar{r}\,d\bar{y} = -\left[\sin\theta_s + (\bar{x}-\theta_s)\cos\theta_s\right]\bar{y}_d - \frac{1}{2}\sin\theta_s\,\bar{y}_d^2 \tag{51b}$$

$$\text{for } \bar{x} \geq \theta_s$$

The parameter

$$\frac{p_{o_j}}{p_{o_f}}\left(\frac{d_{e_j}}{d_f}\right)^2 \tag{52}$$

was calculated in Section 4.2.3.1 as a function of (p_d/p_{o_f}).

For a specified interface location, free stream Mach number, M_∞, retrojet exit Mach Number, M_{e_j}, total jet to free stream pitot pressure ratio P_{o_j}/P_{o_f} and dead air pressure ratio P_d/P_{o_f}, the

location of the second interface, $\bar{y}_d(x)$, may be determined from equations 50 and 51a for the case $\bar{x} \leq \theta_s$ and from equations 50 and 51b for the case of $\bar{x} \geq \theta_s$. The results of a sample calculation are shown in Figure 41, where the magnitudes of certain parameters are: $M_\infty = 2.5$, $M_{e_j} = 3.0$, $P_d/P_{o_f} = .20$, $P_{o_j}/P_{o_f} = 147$.

4.2.4 Jet Layer and Entrainment

Though the retrorocket flow field has been considered to be inviscid up to this point, important viscous effects are occurring and must be accounted for in any general theory. Since the total temperature of the free stream gas will be substantially lower than the stagnation temperature of the retrorocket exhaust gases, a substantial velocity difference will exist across the interface (first interface). The velocities on the inner side of the interface will be higher than those on the outside. This means that a mixing layer will develop which will entrain air from the outer side and jet gas from the inner side. A mixing layer will also form along the second or inner interface between the jet gases and the recirculating region. Jet gas will be entrained into the mixing layer from the outer side of the second interface while recirculation region gas will be entrained along the inner side (Figure 42).

The formation of these mixing layers raises the following questions.

1. How much mass is entrained along the first interface and how does that compare with the mass entrained along the second?

2. Is a point reached where all the mass (total jet flow) initially flowing in the jet gas layer between the first interface and the terminal shock, is entrained into the outer and inner mixing layers?

3. If a position is reached where a completely merged mixing layer exists, what are its characteristics (such as velocity, enthalpy and concentration profiles across the mixing layer)?

4. How does this completely merged mixing layer grow as it passes downstream along the edge of the dead air region?

In this section, these questions will be answered. It will be shown that:

a) the mixing layer along the first interface entrains a majority of the gas in the jet layer,

b) the total jet mass flow is entrained by the time the mixing layer reaches the position corresponding to a polar angle of sixty degrees,

c) the mixing layer has properties that are both shear layer and jet like, and

d) these properties persist even though the formation of the completely merged mixing layer is followed for large distances downstream.

4.2.4.1 Entrainment from the Outer Interface

In general, the velocities on the inner side of the interface will be higher than those on the outer side, since the jet total temperatures will be higher than T_{o_∞}. This means that a shear layer will develop which will entrain air from the outer side, and jet gas from the inner side. A typical value of the total temperature ratio is 1/9*, so that for $\gamma_j = \gamma_\infty$

$$V_1 - V_e = V_1 \left(1 - a_{o_e}/a_{o_j}\right) = \frac{2}{3} V_1 \qquad (53)$$

where V_e is the velocity of the shocked free stream gas on the exterior side of the interface, and V_1 is the velocity of the jet gas on the inside of the interface.

*See Appendix L, JET MOLECULAR WEIGHT EFFECT

Considering two parallel incompressible streams with velocities and densities u_1, ρ_1 and u_2, ρ_2 respectively, there is a self-similar solution of the shear layer equations in the form

$$\begin{aligned} \rho &= \rho(\xi), \\ u &= u(\xi), \\ v &= v(\xi), \end{aligned} \tag{54}$$

and

$$\xi = \sigma y/x$$

where σ must be determined experimentally. If the mass entrainment coefficient for the upper stream is defined as

$$C_{q_1} = \frac{1}{\rho_1 u_1} \frac{d\dot{m}_1}{dx} \tag{55}$$

the upper and lower edges of the layer are defined as those for which either

$$u_u = u_1 - .05\,(u_1 - u_2) \tag{56}$$

and

$$u_\ell = u_2 + .05\,(u_1 - u_2)$$

or

$$\rho_u = \rho_1 + .05\,(\rho_2 - \rho_1)\,, \tag{57}$$

and

$$\rho_\ell = \rho_2 - .05\,(\rho_2 - \rho_1)$$

whichever is larger, and a mass entrainment coefficient for the lower stream is defined as

$$C_{q_2} = \frac{1}{\rho_1 u_1} \frac{d\dot{m}_2}{dx} \tag{58}$$

Then Appendix H shows that

$$C_{q_1} = \left(\frac{1-\Gamma}{1+\Gamma}\right) \left[\frac{1}{2\sigma\sqrt{1+\lambda}}\right] \left(\frac{\rho}{\rho_2}\right)_u \left[\eta_u - \eta_o - \alpha\right], \tag{59}$$

and

$$C_{q_2} = \left(\frac{1-\Gamma}{1+\Gamma}\right) \left[\frac{1}{2\sigma\sqrt{1+\lambda}}\right] \left(\frac{\rho}{\rho_2}\right)_\ell \left[\left(\frac{1-\lambda}{1+\lambda}\right)\left(\eta_e - \eta_o\right) - B\right] \tag{60}$$

where

$$\lambda = \frac{u_1 - u_2}{u_1 + u_2},$$

$$\Gamma = \frac{\rho_1 - \rho_2}{\rho_1 + \rho_2},$$

and

$$\eta = 2\sqrt{1+\lambda}\ \xi$$

Figure 43 shows C_{q_1} and C_{q_2} plotted versus ρ_2/ρ_1 for λ=0.8. Figure 44 shows them plotted against λ for Γ=0. The results show that over the velocity range of interest, C_{q_1} and C_{q_2} are approximately equal to .05 when Γ=0 and in general C_{q_1} can then be approximated by the formula

$$C_{q_1} = .05\,(\rho_2/\rho_1)^{1/2} \tag{61}$$

The entrainment of jet air into the outer interface (the surface separating the shocked free stream gas from the jet gas) is similar to the two dimensional mixing just discussed with the exception that the flow area is constantly increasing as the fluids progress along the spherical surface. Assuming the mixing to be locally two-dimensional, this effect can be accounted for by defining

$$\frac{d\dot{m}_1^*}{2\pi r(x)} = d\dot{m}_1 = \rho_1 u_1 C_{q_1} dx \tag{62}$$

where x is a coordinate in the flow direction, and

$2\pi r(x)$ is the local circumference.

The fraction of the jet flow which has been entrained is then

$$\dot{m}_1^*/\dot{m}_j = \frac{2\pi}{\dot{m}_j} \int_o^x r(x)\, \rho_1 u_1 C_{q_1} dx \tag{63}$$

The details of the evaluation of this integral are carried out in Appendix I

4.2.4.2 Entrainment into the inner Interface

Similar to the analysis of the outer interface, the mixing along the inner interface (the surface that separates the jet gas from the recirculation (dead air) region) is assumed to be two dimensional locally. The shear layer has a velocity of u_1 on the outer side and zero velocity on the inside, so that

$$\lambda = 1.0$$

Analogous to the outer layer, the fraction of jet flow entrained can be expressed as:

$$\frac{\dot{m}}{\dot{m}_j} = \frac{2\pi}{\dot{m}_j} \int_o^\xi r(\xi)\, \rho_1 u_1 C_{q_1} d\xi \tag{64}$$

where ξ is distance along the shear layer. The starting point ($\xi = 0$) is the intersection of the jet boundary and the terminal shock. The evaluation of the integral is more cumbersome than the previous case, since the interface is not a spherical surface. In Section 4.2.3, it was shown that y_d, the distance between the two interfaces continually decreases as the flow proceeds downstream. This variation in y_d was used in evaluating the integral as discussed in Appendix (J). The results of the two entrainment calculations are shown in Figure 45, which shows the fraction of the jet flows which has been entrained into each of the interfaces as a function of the angle θ. The curves show two significant facts. First, the great majority of the jet flow is entrained in the outer interface shear layer. This is physically due to the fact that $\rho_e >> \rho_d$. Secondly, at a value of $\theta \simeq 60^\circ$, all of the jet flow has been entrained. Beyond this point, it is not valid to consider the flow as two separate layers. It is rather one merged layer with some of the characteristics of a free shear layer and some of a free jet into still air. The analysis also indicates that the result that complete entrainment of the jet flow occurs by $\theta \cong 60$ degrees is independent of the thrusting coefficient.

4.2.4.3 Velocity Distribution in the Merged Shear Layer

A mean velocity across the shear layer is defined so that when multiplied by the mass flux, it yields the momentum flux, i.e.

$$\bar{u} = \frac{\int_{\delta_d}^{\delta_e} \rho^2 u \, dy}{\int_{\delta_d}^{\delta_e} \rho u \, dy} \tag{65}$$

For the limiting cases of a pure shear layer and a pure jet into still air, this reduces to

$$\bar{u}_{S.L.} = u_e/2 \tag{66}$$

$$\bar{u}_j = 2/3\, u_{max} \tag{67}$$

For the pure shear layer case, it has been shown that

$$\frac{1}{b}\frac{d\dot{m}}{dx} = .05\,(\rho_e\rho_l)^{1/2}\,u_e \tag{68}$$

$$= 0.1\,(\rho_e\rho_l)^{1/2}\,\bar{u}_{S.L.}$$

where

$$b = 2\pi r\ . \tag{69}$$

Reference (49) shows that for the entrainment from one side only of a two-dimensional jet.

$$\frac{1}{b}\frac{d\dot{m}}{dx} = 0.1\,\rho\bar{u} \tag{70}$$

These two expressions are combined for the mixed merged layer as follows

$$\frac{1}{b}\frac{d\dot{m}_e}{dx} = 0.1\left[\rho_e\left(\bar{u} - \frac{u_e}{2}\right) + (\rho_e\rho_d)^{1/2}\,\frac{u_e}{2}\right] \tag{71}$$

and

$$\frac{1}{b}\frac{d\dot{m}_d}{dx} = 0.1\left[\rho_d\left(\bar{u} - \frac{u_e}{2}\right) + (\rho_e\rho_d)^{1/2}\,\frac{u_e}{2}\right] \tag{72}$$

Note that for the pure shear layer ($\bar{u} \rightarrow u_e/2$) and the pure jet ($u_e \rightarrow 0$), and these expressions approach the correct values.

From Reference (47), the momentum equation is

$$\frac{d(\bar{u}^2)}{\bar{u}^2} + \frac{2}{\dot{m}} \left[\left(1 - \frac{u_e}{\bar{u}}\right) d\dot{m}_e + d\dot{m}_d \right] = 0 \tag{73}$$

Substituting we get

$$\frac{d(\bar{u}^2)}{\bar{u}^2} + \frac{0.2b}{\dot{m}} \left\{ \left(1 - \frac{u_e}{\bar{u}}\right) \left[\rho_e \left(\bar{u} - \frac{u_e}{2} \right) + (\rho_e \rho_d)^{1/2} \frac{u_e}{2} \right] \right. \tag{74}$$

$$\left. + \left[\rho_d \left(\bar{u} - \frac{u_e}{2} \right) + (\rho_e \rho_d)^{1/2} \frac{u_e}{2} \right] \right\} ds = 0$$

The continuity equation can be written in similar form as

$$\frac{d\dot{m}}{ds} = \frac{d\dot{m}_d}{ds} + \frac{d\dot{m}_e}{ds} \tag{75}$$

$$= 0.1b \left[(\rho_e + \rho_d) \left(\bar{u} - \frac{u_e}{2} \right) + (\rho_e \rho_d)^{1/2} u_e \right]$$

The two equations can be normalized by noting that

$$b = 2\pi r$$

and defining the following non-dimensional parameters

$$s^* = \frac{s}{r_f} \qquad \dot{m}^* = \frac{\dot{m}}{\pi r_f^2 \rho_\infty u_\infty}$$

$$r^* = \frac{r}{r_f} \qquad \dot{m}_j^* = \frac{\dot{m}}{\pi r_f^2 \rho_\infty u_\infty} \tag{76}$$

$$\bar{u}^* = \frac{\bar{u}}{u_\infty} \qquad \rho_e^* = \frac{\rho_e}{\rho_\infty}$$

$$u_e^* = \frac{u_e}{u_\infty} \qquad \rho_d^* = \frac{\rho_d}{\rho_\infty}$$

The results are

$$\frac{d\bar{u}}{\bar{u}} + \frac{0.2r^*}{\dot{m}^*} \left\{ (\rho_e^* + \rho_d^*) \left(\bar{u}^* - \frac{u_e^*}{2} \right) + (\rho_e^* \rho_d^*)^{1/2} \frac{u_e^*}{2} \right. \tag{77}$$

$$\left. - \frac{u_e^*}{\bar{u}^*} \left[\rho_e^* \left(\bar{u} - \frac{u_e^*}{2} \right) + (\rho_e^* \rho_d^*)^{1/2} \frac{u_e^*}{2} \right] \right\} ds^* = 0$$

$$\frac{d\dot{m}^*}{\dot{m}^*} = \frac{0.2r^*}{\dot{m}^*} \left[\left(\rho_e^* + \rho_d^* \right) \left(\bar{u}^* - \frac{u_e^*}{2} \right) + (\rho_e^* \rho_\alpha^*)^{1/2} \frac{u_e^*}{2} \right] ds^* = 0 \tag{78}$$

Defining

$$a_1 = \bar{u}^* - \frac{u_e^*}{2} \tag{79}$$

$$b_1 = (\rho_e^* \rho_d^*)^{1/2}$$

$$c_1 = \rho_e^* + \rho_d^*$$

and substituting, we get

$$\frac{d\dot{m}^*}{\dot{m}^*} = \frac{0.2r^*}{\dot{m}^*}\left[b_1 u_e^* + a_1 c_1\right] ds^* \tag{80}$$

$$\frac{d\bar{u}^*}{\bar{u}^*} = -\frac{d\dot{m}^*}{\dot{m}^*} + \frac{0.2r^*}{\dot{m}^*}\frac{u_e^*}{\bar{u}^*}\left[\bar{\rho}_e^* a_1 + u_e^* \frac{b_1}{2}\right] ds^* \tag{81}$$

These equations have been integrated numerically by the second order Runge-Kutta method. Since the two equations are coupled, the two integrations must be carried out simultaneously. The basic recurrence formula of the method is

$$\bar{u}^*_{n+1} = \bar{u}^*_n + \left[\left(\frac{d\bar{u}^*}{ds^*}\right)_n + \frac{\left(\frac{d\bar{u}^*}{ds^*}\right)_n - \left(\frac{d\bar{u}^*}{ds^*}\right)_{n-1}}{2}\right]\Delta s^* \tag{82}$$

(See for example Reference 48, page 15). The method requires knowledge of the derivatives at n-1, and n in order to calculate $\bar{u}^*_{n+1}$. This produces a difficulty at the starting point, since there is no preceding point. This difficulty was overcome by computing the first point from the first order equation

$$\bar{u}^*_{n+1} = \bar{u}^* + \left(\frac{d\bar{u}^*}{ds^*}\right)_n \Delta s^* \tag{83}$$

using a very small value of .01 for Δs^*. The succeeding points were then computed from the second order equation, with the increments in s^* being gradually increased to a value of .08. This value was then

held constant for the remainder of the integration. The calculations were made for the following parametric values.

$M_\infty = 2.5$ $\qquad$ $\gamma_j = 1.4$

$\gamma_\infty = 1.4$ $\qquad$ $\theta_o = 60^o$

$M_{e_j} = 3.0$ $\qquad$ $\alpha = 15^o$

The details of determining the initial values for the velocity, enthalpy and concentration are contained in Appendix K. The results are shown in Figure 46 where $\bar{u}^*$ and $\dot{m}^*$ are plotted against s^*. s^* is measured from an origin located on the blunting sphere corresponding to $\theta_o = 60$ degrees. Note that the value $s^* = 4.25$ corresponds to the recompression point. The value of $\bar{u}^*$ and $\dot{m}^*$ have reached practically constant values long before this point is reached.

After the integration was completed, it was noticed that the differential equations could be somewhat simplified by slightly changing the definitions of the parametric a_1, b_1, and c_1. The proposed changes are as follows

$$A = \rho_e^* \left(\bar{u}^* - \frac{u_e^*}{2} \right) \tag{84}$$

$$B = \left(\rho_e^* \rho_d^* \right)^{1/2} \left(\frac{u_e^*}{2} \right)$$

$$C = 1 + \frac{\rho_d^*}{\rho_e^*}$$

Then

$$\frac{d\dot{m}^*}{\dot{m}^*} = \frac{0.2r^*}{\dot{m}^*} \left[2B + AC\right] ds^* \tag{85}$$

$$\frac{d\bar{u}^*}{\bar{u}^*} = -\frac{d\dot{m}^*}{\dot{m}^*} + \frac{0.2r^*}{\dot{m}^*} \frac{u_e^*}{\bar{u}^*} \left[A + B\right] ds^* \tag{86}$$

It is recommended that this notation be used in any future computer programs.

The velocity distribution across the mixing layer has some of the characteristics of a free jet into still air, since the mean velocity is greater than the external velocity in the early portion of the development of the free shear layer. On the other hand, since the internal velocity is zero, and the external velocity is finite, the profile will also be partially similar to that of a free shear layer. (Figure 47) The approach taken is to assume that the velocity profile is the sum of shear layer and free jet profiles. The relative importance of each function is then determined by substitution into the definition of $\bar{u}_*$.

The velocity profile for a pure shear layer is given by (see Ref. (49))

$$\frac{u}{u_e} = \frac{1}{2}\left[1 + \mathrm{erf}(\xi)\right] \tag{87}$$

and for jet flow into still air by

$$\frac{u}{u_{max}} = \mathrm{sech}^2(\eta) \tag{88}$$

where

$$\eta = \sigma \frac{y}{x}$$

$$\xi = k\eta$$

The velocity profile across the mixing layer is taken to be a superposition of a pure shear and jet flow profile.

$$\frac{u}{u_e} = \frac{1}{2}\left[1 + \text{erf}(k\eta)\right] + \lambda \,\text{sech}^2\eta \tag{89}$$

The constant k is determined by requiring that each term be within 5% of its limiting value at the same value of η. $\text{sech}^2\eta$ is within five-percent of its limiting value for η=2.2. This gives a value of

$$k = .52$$

Substituting into the definition of $\bar{u}/u_e$

$$\frac{\bar{u}}{u_e} = \frac{\int_{-\eta_o}^{\eta_o} \rho(u/u_e)^2\, dy}{\int_{-\eta_o}^{\eta_o} \rho(u/u_e)\, dy} \tag{90}$$

we get

$$\frac{\bar{u}}{u_e} = \left(\frac{\eta_o}{2} + \frac{1}{4}\int_{-\eta_o}^{\eta_o} (\text{erf}.52\eta)^2 d\eta + \frac{4}{3}\lambda^2 + 2\lambda\right)/(\eta_o + 2\lambda) \tag{91}$$

So that with $\eta_o = 2.2$, λ is determined by specifying $\bar{u}/u_e$. The velocity profile is plotted in Figure 47 for a value of $\bar{u}/u_e = 1.0$, which corresponds to the value at the wake neck. The jet effect persists even at this large downstream distance.

4.2.4.4 Enthalpy Variation in the Merged Shear Layer

A mean value of total enthalpy can be defined similar to the mean velocity as follows

$$\bar{H} = \frac{\int_{-\eta_o}^{\eta_o} \rho u H dy}{\int_{-\eta_o}^{\eta_o} \rho u dy} \tag{92}$$

The differential equation which defines the variation of $\bar{H}$ along the merged shear layer is expressed as follows (Ref. 47)

$$d\bar{H} + (\bar{H} - H_e) \frac{d\dot{m}_e}{\dot{m}} + (\bar{H} - H_d) \frac{d\dot{m}_d}{\dot{m}} = 0 \tag{93}$$

where H_e and H_d are the total enthalpies on the outside and inside of the merged shear layer respectively. The total enthalpy is normalized with respect to H_∞, so that

$$\bar{H}^* = \bar{H}/H_\infty, \tag{94}$$

$$H_e^* = H_e/H_\infty = 1,$$

$$H_d^* = H_d/H_\infty,$$

and substituting for $d\dot{m}_d$ and $d\dot{m}_e$, we get

$$\frac{d\overline{H}^*}{dS^*} = \frac{0.2r^*}{\dot{m}^*}\left[a_1(\rho_e^* + H_d^*\rho_d^*) + \frac{b_1 u_e^*}{2}(1 + H_d^*)\right] - \frac{\overline{H}^*}{\dot{m}^*}\frac{d\dot{m}^*}{dS^*} \tag{95}$$

where a_1 and b_1 have been previously defined. This equation was integrated in a way similar to the velocity equation. A value of $H_d^*=9$ was used, which is equivalent to $a_{o_j}/a_{o_e} = 3$ with $\gamma_j=\gamma_\infty$. The curve shown on Figure 48 follows the same general shape as the velocity curve and reaches an essentially constant value long before the wake neck is reached.

The enthalpy profile across the merged layer is obtained analogously to the velocity profile. The variation is assumed in the form.

$$H^* = (1 + H_d^*)/2 + (1 - H_d^*)/2 \text{ erf } (.52\eta) + \mu \text{ sech}^2\eta \tag{96}$$

Substitution of this equation into the definition of $\overline{H}^*$ gives a relationship between μ and $\overline{H}^*$. The profile is shown in Figure 47.

4.2.4.5 Variation of Jet Gas Concentration in the Merged Shear Layer

A mean value of jet gas concentration is defined as:

$$\overline{C} = \frac{\int_{-\eta_o}^{\eta_o} \rho u \, c \, dy}{\int_{-\eta_o}^{\eta_o} \rho u \, dy} \tag{97}$$

The differential equation which expresses the conservation of species is written as:

$$d\overline{C} + \overline{C}\,\frac{d\dot{m}_e}{\dot{m}} + (\overline{C} - C_d)\,\frac{d\dot{m}_d}{\dot{m}} = 0 \qquad (98)$$

This equation has been numerically integrated for the case of $C_d = 1$ (pure jet gas in the dead air region). The results are shown in Figure 49. Again there is little change in the rear section of the shear layer.

The concentration profile is obtained by assuming a form:

$$C = \frac{C_d}{2}\left[1 - \mathrm{erf}(.52\eta)\right] + \nu\ \mathrm{sech}^2\,\eta \qquad (99)$$

Substitution of this expression into the definition of $\overline{C}$ determines the constant ν. The profile is plotted in Figure 47 for the wake neck conditions. Similar to the enthalpy profile, there is very little wake effect evident.

4.2.5 Recirculation and Recompression Flow

As is indicated in Figure 42, gas from the dead air region is continually being entrained into the shear layer, both along the jet boundary and along the merged shear layer. The total rate of entrainment is symbolized by $\dot{m}_d$. At the same time, fluid from the merged shear layer will recirculate into the dead air region at the reattachment or wake recompression region at a rate $\dot{m}_r$. From mass conservation,

$$\dot{m}_d = \dot{m}_r \qquad (100)$$

From conservation of enthalpy, we can write

$$\dot{m}_d H_d = \dot{m}_r \overline{H}_r$$

or

$$H_d = \overline{H}_r \tag{101}$$

Similarly, from conservation of species

$$\dot{m}_d C_d = \dot{m}_r \overline{C}_r$$

or

$$C_d = \overline{C}_r$$

where $\overline{H_r}$ is a suitably averaged value of the total enthalpy of the recirculating fluid, and $\overline{C}_r$ a suitable value for the recirculating flow concentration. Considering Figure (47), there is some separation streamline which separates the fluid which recirculates from that which passes on downstream. This occurs at $\eta = \delta_r$. In the process of carrying out the various integrations, the dead air entrainment rate $\dot{m}_d$ and the total shear flow rate $\dot{m}$ have been computed. The value of δ_r is thus determined by the continuity equation

$$\frac{\dot{m}_d}{\dot{m}} = \frac{\int_{y_d}^{y_r} \rho u y dy}{\int_{y_d}^{y_e} \rho u y dy} \tag{102}$$

or in non dimensional form

$$\frac{\dot{m}_d^*}{\dot{m}^*} = \frac{\int_{\delta_d}^{\delta_r} \rho^* u^* \eta d\eta}{\int_{\delta_d}^{\delta_e} \rho^* u^* \eta d\eta} \tag{103}$$

Having determined δ_r by this means, it is then possible to determine δ from the relation

$$\dot{m}_d^* = 2 \left(\frac{s^*}{\delta}\right)^2 \int_{\delta_d}^{\delta_r} \rho^* u^* \eta d\eta$$

Then the appropriate value of $\overline{H}_r$ is

$$\overline{H}_r = \frac{\int_{\delta_e}^{\delta_r} \rho u H d\eta}{\int_{\delta_e}^{\delta_r} \rho u d\eta} \tag{104}$$

If we define

$$\overline{H}_\eta(\eta) = \frac{\int_{\delta_e}^{\eta} \rho u H d\eta}{\int_{\delta_e}^{\eta} \rho u d\eta} \tag{105}$$

so that

$$\overline{H}_\eta(\delta_d) = \overline{H}, \text{ then} \tag{106}$$

H_η is a weak function of η. This is because uH and u have profiles which are somewhat similar in shape. If we ignore this variation, it can be said that

$$H_d^* = \overline{H}_r^* \cong \overline{H}^* \tag{107}$$

We have already computed H_d^* to be 3.3 (Figure 48). Thus, as a first approximation, we use the asymptotic value from Figure 48

$$H_d^* \cong 3.3$$

To get a feel for the implication of this value consider that for

$$M_\infty = 2.5,$$

and $$\gamma_\infty = 1.4,$$

and $$T_\infty = 380^\circ R, \tag{108}$$

The free stream stagnation temperature is

$$T_{o_\infty} = 855^\circ R \tag{109}$$

so that

$$T_d = 2820^\circ R \tag{110}$$

$$T_d = 2360^\circ F$$

Thus the influx of cold air into the shear layer has cooled the jet with a total temperature of $7230^\circ F$ down to a dead air temperature of $2360^\circ F$.

An exactly equivalent analysis using the same arguments can be made for the gas concentration, so that to a first approximation we can conclude from Figure 49 that

$$C_d \tilde{=} \overline{C} = 0.31 \tag{111}$$

To obtain more exact value, these values of C_d and H_d^* should be put into the differential equations, and they should be reintegrated. The correction should be small however since C_d and H_d^* have only a very weak effect on the integration.

In addition to satisfying the conservation of mass, species and enthalpy in the recirculating region, the pressure rise at recompression must be also be satisfied. The pressure in the dead air region is determined by a modification of the analysis of Chapman[34] for laminar-separated regions using the data of Korst[35] for turbulent mixing layers. It is assumed that the retrorocket exhaust flow is

turbulent, both in the central core regions and along the jet boundary, and that this leads to a turbulent mixing layer accompanied by turbulent reattachment. D.R. Chapman developed a calculation scheme by which the dead-air pressure in a laminar-separated region may be determined. The essential mechanism considered was that there is a balance between the mass scavenged from the dead-air region by the mixing layer and the mass flow reversed back into the dead-air region by the pressure rise through the reattachment zone. For steady flow the dividing streamline at separation, as calculated from mixing layer theory, must be the dividing streamline at reattachment. If this were not the case, air would be either continually removed from or continually injected into the dead-air region, and the scavenged mass flux would not balance the reversed mass flux. In order for a particle along a streamline in the mixing layer to be able to overcome the pressure rise through the reattachment zone and to pass downstream, its total pressure P_t must be greater than the terminal static pressure P' at the end of the reattachment zone. The dead-air pressure is determined by requiring that the total pressure along the dividing streamline as it approaches the reattachment zone be equal to the terminal static pressure P'.

The equation for the dead-air pressure is

$$\frac{P_d}{P'} = \left[\frac{1+(1-\bar{u}_*^2)\frac{\gamma-1}{2} M_e^2}{1+\frac{\gamma+1}{2} M_e^2} \right]^{\gamma/\gamma-1} \tag{112}$$

where $\bar{u}_*$ is the ratio of the velocity along the dividing streamline to the velocity at the edge of the mixing layer and M_e is the Mach number at the outer edge of the mixing layer.

As noted by Chapman, for laminar mixing layers $\bar{u}_*$ is essentially a constant. We modified Chapman's analysis by using the turbulent $\bar{u}_*$ of Korst.[35] The variation of the turbulent $\bar{u}_*$ with exhaust layer Mach number M_ℓ is shown in Figure 50. M_e was assumed to be equal to M_ℓ, the Mach number of the mixing layer. This approach is only approximately applicable (limited to isoenergetic flow) to the problem of reattachment of the mixing layer to the aeroshell or recompression in the wake region and was used to obtain a very approximate idea of the resulting flow field geometries (Section 4.3), before the results for the mixing layer analysis became available.

An improved method for determining the pressure in the dead-air region is discussed in Reference 50 and is not limited to isoenergetic flow as the above analysis is. In the analysis of Hill and Luce, the Chapman's recompression conditions on the stagnating streamline is

$$P_t = P_e\left(1 + \frac{\gamma-1}{2} M_s^2\right)^{\gamma/\gamma-1} \tag{113}$$

where M_s is the Mach Number on the separating streamline and $P_e = P_d$. This is solved for the required kinetic energy

$$\frac{U_s^2}{2h_{t_s}} \frac{(\gamma-1)M_s^2/2}{1+(\gamma-1)M_s^2/2} = 1 - \left(\frac{P_e}{P_t}\right)^{\frac{\gamma-1}{\gamma}} \tag{114}$$

$$\text{But } h_t = h_c + (h_{t_e} - h_c)u^* \tag{115}$$

$$\text{and} \qquad u^* = u/u_e$$

Then substituting the expression for h_{t_s} and inverting, they obtain

$$\frac{h_c/h_{t_e} + (1-h_c/h_{t_e})u_s^*}{u_s^{*2}} = \frac{W_e^2}{1-\left(P_e/P_t\right)^{\frac{\gamma-1}{\gamma}}} \qquad (116)$$

where $W_e = u_e/V_m$

h_c = enthalpy of recirculating region.

In this equation the right hand side depends entirely on the external flow while the left hand side depends on the shear layer properties and is shown to be a function of the stream functions and the ratio of the injected to exterior enthalpies. A solution to the overall flow pattern is determined in an iterative manner. The Hill-Luce analysis simplifies to the Chapman analysis in the limit of isoenergetic-flows i.e., $h_c = h_{t_e}$.

4.3 COMPLETE SINGLE-JET FLOW PATTERN

In general, the overall field for the jet exhausting from an aeroshell into an oncoming stream must be determined in an iterative manner as follows:

1. Assume separated region pressure
2. Calculate jet flow and jet boundary location
3. Locate terminal shock on jet centerline
4. Determine interface geometry and mixing layer inclination
5. Compute growth of mixing layer

6. Locate separating streamline and compute recompression conditions at aeroshell surface or at wake neck region.

7. Evaluate the mass, enthalpy and concentration conservation equations for the separated region and merged mixing layer.

8. Iterate until pressure rise, conservation of mass, enthalpy and concentration are satisfied simultaneously in the recirculation region.

Since the analysis for the growth of the merged mixing layer was not finished until just before the interim report was written, sufficient time was not available to perform a series of calculations following this general procedure. However it was determined that the geometry of the flow field about aeroshell vehicles with a single retrorocket could be analyzed for all cases where reattachment occurs on the forward surface or shoulder of the aeroshell by a simplified analyses. The wake type flow regime is the only one which requires the general analysis in order to obtain the flow field geometry. However, the general analysis is required in all cases if the temperature and concentrations of jet gases in the recirculating region are to be determined.

We will now discuss some of the situations which may be analyzed by simplified methods. First, the maximum aeroshell opening that is compatible with attached turning shock waves at reattachment is found to be about thirty five degrees for a $M_\infty = 2.5$ free stream. For aeroshell opening angles below this maximum, (small aeroshell opening angles), the reattachment point moves in a continuous manner outward along the vehicle surface as the retrothrust coefficient increases from low C_T levels. For aeroshell opening angles greater than this angle (large aeroshell opening angles) the merged mixing layer does not possess enough energy to allow reattachment to occur on the forward surface of the aeroshell with attached turning shocks at reattachment. For this case with low and intermediate thrusting coefficients, reattachment always occurs at the shoulder of the vehicle and the flow

pattern is similar to the most common type of separated flow pattern observed in flow over spiked cone-cylinders[33] where reattachment occurs always on the shoulder of the vehicle. For large thrusting coefficients and large aeroshell opening angles, the shear layer does not reattach to the vehicle but passes around it forming a wake type flow and recompression of the mixing layer occurs in the wake neck region.

Secondly, an analysis is discussed which considers retrojet exhaust flows from vehicles with large aeroshell openings (cone semivertex angles of sixty degrees) and the magnitude of the thrusting coefficient is determined which separates reattachment at the shoulder flow (low and intermediate thrusting coefficients) from wake type flow (high thrusting coefficients). The fact that, for low and intermediate thrusting coefficients, reattachment always occurs at the vehicle shoulder provides a geometric constraint which is used to obtain permissible solutions for the flow field geometry. For the sixty degree aeroshell opening angle considered, the separation between the reattachment at the shoulder type flow from wake type flow occurs at a thrusting coefficient near one.

Thirdly, the flow geometry about aeroshells with small opening angles and small thrust coefficients (small enough to assure reattachment somewhere on the vehicle surface) is shown to be determined by applying the Chapman-analysis at the reattachment point. For an aeroshell opening angle of thirty degrees, it is found that the thrusting coefficient which separates reattaching flow from wake type flow has a magnitude of $C_T = 0.07$. Ways in which this calculation may be improved by treating the reattaching layer as a mixture of jet and atmospheric gases (Section 4.2.4) instead of just jet gas are discussed.

The relative geometry between an attaching mixing layer and the aeroshell vehicle is shown in Figure 51. The shear layer makes an angle α with respect to the jet centerline. The angle α is related to the dead-air pressure P_d/P_{o_f} through equations 10 or equation 19

depending on whether the free stream flow is supersonic or subsonic respectively. The relative angle between the local aeroshell surface and the mixing layer is $(\theta_v - \alpha)$. The flow geometry is similar to flow over a wedge, Figure 52. If the dead-air pressure, P_d/P_{o_f}, the mixing layer specific heat ratio, γ layer, and the free stream Mach number M_∞ are chosen, the angle, α, and Mach number, M_ℓ, of the mixing layer are determined. The maximum wedge angle, δ_{MAX}, for an attached oblique shock wave, is then determined from the relevant shock polar.

The maximum deflection angle for a specified mixing layer Mach number is given approximately by

$$\delta_{MAX} = \frac{4}{3\sqrt{3}(\gamma_{LAYER}+1)} \frac{(M_\ell^2 - 1)^{3/2}}{M_\ell^2} \tag{117}$$

But $$\delta_{MAX} = (\theta_{M_{MAX}} - \alpha) \tag{118}$$

So $$\theta_{M_{MAX}} = \delta_{MAX} + \alpha \tag{119}$$

The maximum vehicle surface angle $\theta_{V_{MAX}}$, for which the mixing layer at a fixed M_ℓ can be deflected parallel to the vehicle surface by an attached shock wave was evaluated from the shock polar, (γ=1.4) of Reference 51 and a free stream Mach number of $M_\infty = 2.5$. The variation of this maximum angle with dead-air pressure is shown in Figure 53. The mixing layer Mach number, M_ℓ, and the angle of the separated region, α, are also noted. Over the range of dead-air pressures considered, the maximum opening angle for attached shocks at reattachment is about thirty five degrees.

The magnitude of the thrusting coefficient which separates the regime of shear layer attachment at the vehicle shoulder (low and intermediate thrusting coefficients) from the regime of wake type flow for large aeroshell opening angles is found as follows. It is assumed that the mixing layer attaches to the shoulder of the

vehicle for low and intermediate thrusting coefficients as the flow rate varies. This is in contrast to vehicles with angles up to 35°, wherein the layer attaches to the vehicle at some intermediate point. The basic approach is to locate the center and diameter of the blunting sphere, and consider a tangent from the sphere to the vehicle shoulder. In this way a geometrical relationship exists between the slope of this line and jet and free stream conditions. From a balance of external pressures, an additional relationship is developed, between the slope of the tangent line and P_d/P_{o_f}. Combining the two relations we finally obtain P_d/P_{o_f} as a function of C_T, for a given jet and free stream conditions. The analysis is divided into two parts: $d_f/d_m < 1$, and $d_f/d_m > 1$, although the final results are presented as one continuous curve. For $d_f/d_m < 1$, the blunting sphere is less than the vehicle diameter, while for $d_f/d_m > 1$ it is larger than the vehicle diameter.

Geometrical Considerations, $d_f/d_m < 1$

The notation used is shown in Figure 54. The coordinates (x_f, y_f) of the tangent point on the blunting sphere can be written as

$$x_f = x_c + r_f \sin \alpha \tag{120}$$

$$y_f = r_f \cos \alpha \tag{121}$$

so that

$$\tan \alpha = (y_m - r_f \cos \alpha)/(x_c - x_m + r_f \cos \alpha) \tag{122}$$

Crossmultiplying, squaring, and solving the resultant quadratic equation we get

$$\sin \alpha = \left[(1+\bar{x}^2 - \bar{r}^2)^{1/2} - \bar{x}\,\bar{r}\right] /(1+\bar{x}^2) \tag{123}$$

where

$$\bar{x} = (x_c - x_m)/y_m \tag{124}$$

and

$$\bar{r} = r_f/y_m \tag{125}$$

Thus if x_c and r_f are known as functions of nozzle characteristics, α is determined directly. x_c is determined from Equation (34) of Section 4.2.3.4;

$$x_c/r_{e_j} = x_l/r_{e_j} - x/r_{e_j} \tag{126}$$

where

and

$$x/r_{e_j} = \left[(r_f/r_{e_j} - \delta/r_{e_j})^2 - (y_l/r_{e_j})^2\right]^{1/2} \tag{127}$$

and

$$\delta/r_{e_j} = \left\{(\rho_{e_j}/\rho_{o_j})(V_{e_j}/a^*)\,(r_{e_j}/y_l)\Big/\left(\frac{2}{\gamma_j+1}\right)^{\frac{1}{\gamma_j-1}}\right\}(P_{o_j}/P_{o_f}) \tag{128}$$

The radius (r_f) is determined in Section 4.2.3.1 and x_l and y_l are determined as discussed in Section 4.2.2.4. It was necessary to extend these curves to lower values of P_{e_j}/P_d for these calculations. The extensions are shown in Figures (55) and (56). The quantity x_m/r_{e_j} is calculated from

$$x_m/r_{e_j} = (1 - r_m/r_{e_j})/\tan\theta \tag{129}$$

The quantity P_{e_j}/P_d is calculated from

$$P_{e_j}/P_d = (P_{e_j}/P_{o_j})\,(P_{o_j}/P_{o_f})/(P_d/P_{o_f}) \tag{130}$$

where

$$P_{e_j}/P_{o_j} = \left(1 + \frac{\gamma_j - 1}{2} M_j^2\right)^{(\gamma_j - 1)\gamma_j} \tag{131}$$

Note that $\theta = \pi/2 - \alpha$ (132)

By holding P_{o_j}/P_d constant, curves of constant C_T may be generated in the $(P_d/P_{o_f}, \theta)$ plane as follows:

(1) Pick r_m/r_{e_j}, θ_v, M_j, γ_j, M_∞, γ_∞.

(2) Calculate x_m/r_{e_j} from (129).

(3) Calculate P_{e_j}/P_{o_j} from (131).

(4) Pick P_d/P_{o_f}, P_{o_j}/P_{o_f}.

(5) Find $(r_f/r_{e_j})^2/(P_{o_j}/P_{o_f})$ from Section 4.2.3.1.

(6) Calculate r_f/r_{e_j}.

(7) Calculate P_{e_j}/P_d from (130).

(8) Get x_l/r_{e_j} and y_l/r_{e_j} from Section 4.2.2.5.

(9) Calculate δ/r_{e_j} from (128).

(10) Calculate x/r_{e_j} from (127).

(11) Calculate x_c/r_{e_j} from (126).

(12) Calculate $\bar{x}$ and $\bar{r}$ from (124) and (125).

(13) Calculate $\sin\alpha$ from (123).

(14) Calculate θ from (132).

Geometric Considerations, $d_f/d_m > 1$

As the assumed values of P_{o_j}/P_{o_f} are increased, a point is reached where Equation (123) starts to give negative answers. This is equivalent to negative values of α, or in the equation:

$$\theta = 90^o - \alpha \tag{133}$$

$$\theta > 90^o \tag{134}$$

$$d_f/d_m > 1 \tag{135}$$

Thus the computational procedure for $\theta > 90^o$ is identical to that previously described. Before α was the angle of the conical portion of the interface. Now α is defined as the angle between the converging wake edge and the centerline and the equation for $\sin \alpha$ becomes just the negative of Equation 123. By this means, curves of constant C_T can be generated for $\theta > 90^o$.

Pressure Considerations, $d_f/d_m < 1$

In this regime, it has been shown (Section 4.23), that in the supersonic free stream Mach Number regime, the modified Newtonian pressure distribution agrees well with available experimental data. This distribution will therefore be used in conjunction with the geometrical constraints to determine equilibrium conditions. The equation is of the form:

$$P/P_{o_f} = \cos^2 \theta + P_\infty/P_{o_f} \sin^2 \theta \tag{136}$$

where θ is the Polar angle measured from the exhaust jet centerline.

Pressure Considerations, $d_f/dm > 1$

For values of θ greater than 90^o, it is assumed that the pressure reduces as a Prandtl-Meyer expansion thru an angle $(\theta - 90^o)$. In order to compute this expansion, it is necessary to know the Mach Number at the shoulder $(\theta = 90^o)$. This is computed from:

$$P_s/P_{o_f} = (P_s/P_\infty)(P_\infty/P_{o_\infty})(P_{o_\infty}/P_{o_f}) \tag{137}$$

where P_∞/P_{o_∞}, and P_{o_∞}/P_{o_f} are obtained from gas tables. P/P_∞ is obtained from the relation:

$$P_s/P_\infty = 1 + (\gamma/2)M_\infty^2 C_{p_s} \tag{138}$$

The C_p's at $\theta = 90^o$ are obtained from the experimental data of Reference (45). Using this data, the shoulder Mach Numbers have been computed and the results plotted in Figure (57). Knowing the shoulder Mach Number, values of P/P_{o_f} have been computed for various turning angles $(\theta - 90^o)$ and are shown in Figure (58).

For a specific free stream Mach Number, M_∞, the variation of pressure with angle α, ($\theta > 90$ degrees) is determined from Figure 58. If these results are combined with the modified Newtonian distribution for $\theta < 90$ degrees, a general pressure distribution curve is found.

An example calculation is made for

$M_\infty = 2.5$

$M_j = 3$

$\gamma_j = \gamma_\infty = 1.4$

$r_{e_j}/r_m = 0.2$

$\theta_v = 60^o$

The general pressure curve is shown in Figure 59. Curves of constant C_T, obtained from geometrical considerations, are superimposed on this figure also. The intersections represent possible equilibrium flow-conditions. The intersection point in Figure 59 for $C_T = 0.1$ is equivalent to a value of P_{e_j}/P_d of about one. Since the determination of x_1 and y_1 for this and lower values of P_{e_j}/P_d may be inaccurate, the value of $C_T = 0.1$ is considered to be a lower bound on the validity of this analysis. At $C_T = 0.5$, the diameter of the plume shoulder is equal to the diameter of the vehicle and $\alpha = 0$. This appears to be the maximum thrusting coefficient allowable to still have reattachment at the vehicle sholder. Constant thrusting coefficient curves are drawn for $C_T > 0.5$, under the assumption that reattachment to the vehicle shoulder still occurs for negative α's but this situation will most likely not be realized physically. From the permissible solutions (Figure 59), it is seen that the pressure in the constant pressure separated region will vary from $P_d/P_{o_f} = .30$ at $C_T = 0.1$ to $P_d/P_{o_f} = .1$ at $C_T = 0.5$.

Some conclusions concerning the pressure in the dead-air region, which completely surrounds the vehicle, for the wake type flow regime may be drawn from Figure 59. If it is assumed that a turning angle of 10^o-20^o is the maximum which will satisfy recompression requirements in the wake neck region, the pressure in the dead-air region will lie somewhere within the range $P_d/P_{o_f} = 0.05$ to $P_d/P_{o_f} = 0.025$.

Some calculations were made to determine the minimum value of the thrusting coefficient to assure wake type flow. Wake type flow (Figure 2) was said to exist if the mixing layer did not intersect the aeroshell shoulder as it converged toward the wake neck region. The geometry of the wake type flow region was determined as follows.

The pressure, P', downstream of the rearward compression point was calculated from the Chapman-Korst Theory (Section 4.25). At the rearward compression region, the mixing layer which makes an angle α with respect to the axis of symmetry is deflected parallel to it. From the relative geometry of the mixing layer and the axis of symmetry, the pressure downstream of the rearward compression point is determined from oblique shock relations. A solution existed when the pressure requirements from the Chapman-Korst analysis equaled those given by the oblique shock relations. Though the analysis (not given in this text) was approximate, it indicated that the thrusting coefficient had to be greater than one to assure that the mixing layer did not intersect the vehicle and the wake type flow existed.

Therefore the magnitude of the thrusting coefficient which separates the reattachment at the aeroshell shoulder flow from the wake type flow was calculated by approaching the value from below and from above. Approaching it from below, the maximum thrusting coefficient for reattachment at the vehicle shoulder was found to be $C_T = 0.5$. Approaching it from above, the minimum thrusting coefficient to assure wake type flow was found to be about $C_T = 1.0$. Therefore it is concluded from these approximate calculations that a magnitude of the thrusting coefficient near unity separates one flow regime from the other.

The flow pattern about an aeroshell vehicle with a small aeroshell opening angle, ($\theta_v = 30$ degrees) is shown in Figure 60 as the thrust coefficient is increased from low to intermediate values. This case was considered only because it provided a simple numerical test of the method and not because this particular geometry was of interest. It was noted earlier that for aeroshell vehicle opening angles less than thirty-five degrees, the reattachment of the exhaust layer to the aeroshell is accompanied by an attached oblique shock wave. The important point to be noted in these figures is that as the thrusting coefficient C_T is increased from low C_T levels, the reattachment point moves in a

continuous manner outward along the vehicle surface. For a particular magnitude of thrusting coefficient, (Intermediate Thrusting Coefficient) reattachment will occur at the shoulder of the aeroshell vehicle. For thrust coefficients greater than this value, reattachment of the exhaust layer to the aeroshell will no longer occur and wake type flow will exist. The flow field about an aeroshell with thirty degree opening angle, with a $M_{e_j} = 3.0$ retrorocket exhausting into an oncoming $M_\infty = 2.5$ stream is solved by applying a Chapman-Korst type analysis at the reattachment point.

The dead-air pressure is determined in the following manner. The ratio of the pressure downstream of reattachment to the shocked ambient pressure is calculated from the Chapman-Korst analysis (Section 4.2.5) for various values of dead-air pressure to shocked free stream pressure ratio. (Figure 61). From the relative geometry of the mixing layer and the aeroshell surface, the pressure rise, caused as the exhaust layer is deflected parallel to the aeroshell surface, is calculated from oblique shock relations. A solution exists when the pressure requirements of the Chapman-Korst analysis equal those given by the oblique shock relations. This occurs when $P_d/P_{o_f} = .20$, corresponding to $M_\ell = 1.69$ and $\alpha = 18.5$ degrees. The flow field is constructed from the knowledge of the dead-air pressure and inclination, α, of the mixing layer.

For these calculations it was assumed that the mixing layer specific heat ratio, γ, was 1.4, and that M_e in the Chapman-Korst analysis is equal to M_ℓ, the Mach Number of the mixing layer. The resulting geometry for the jet boundary, terminal shock and interface is shown in Figure 62 for three ratios of total jet to shocked free stream pressure. In each case, it is assumed that the aeroshell vehicle extends far enough downstream so that the mixing layer intersects the vehicle and a reattachment point (circle) exists.

When the thrusting coefficient was evaluated for each case, assuming that the vehicle base diameter (reference diameter) was equal to the diameter at the reattachment point, the magnitude of the thrusting coefficient was found to be $C_T = 0.07$. This indicates that the maximum C_T for reattachment of the mixing layer to the aeroshell shoulder (intermediate thrusting coefficient) is $C_T = 0.07$. Wake type flow exists for larger thrusting coefficients than this. This analysis may be improved by calculating the properties of the mixing layer as discussed in Section 4.2.4 and using the specific heat ratio, γ, appropriate to the layer which is composed of a mixture of free-stream and jet gases.

5.0 EXPERIMENTAL TEST PROGRAM

5.1 OBJECTIVES OF THE TEST PROGRAM

The objective of this section is to describe the test philosophy, to show where choices must be made and on what basis, and to make the choice if the evidence is clear-cut.

The purpose of the wind-tunnel test program of the Propulsive Re-entry Aerodynamics Study is to provide experimental results over a large range of the relevant parameters, to critically test and to verify or modify the analytic models being developed. Specifically, a realistic Mars entry configuration will be chosen, and its performance will be measured over an appropriate parameter range.

Currently, systematic information on the interaction of supersonic countercurrent large jet flow rates with an aeroshell from low subsonic to moderate supersonic speeds is not available. Therefore, in order to make the proper choices in the final vehicle design, it is necessary to know

1) the vehicle drag to optimize the propulsion system,

2) the pitching moments to define and optimize the control system and

3) the heating rate to minimize heat shield weight.

We plan to construct the models which will make these measurements possible.

5.2 RETROTHRUST SYSTEM FOR A MARS LANDER

The parameter which characterizes the interaction of a retrojet with a countercurrent stream is the thrusting coefficient, C_T, which has been defined as

$$C_T = \frac{T}{q_\infty A_m} = \frac{T}{\frac{1}{2}\rho_\infty V_\infty^2 A_m} \tag{139}$$

where T is the retrorocket thrust, q_∞ the free stream dynamic pressure, and A_m the aeroshell base area.

If gravity and drag are neglected and constant thrust is assumed, it is found that with a fuel expenditure equal to 20 percent of the vehicle weight, the change of vehicle velocity is 0.7 km/sec. (Section 3). This limits the vehicle ballistic coefficient β to 0.5 slugs/ft.^{2} or less and ignition altitude above the Mars surface to 5 km. or less, based on the entry trajectory calculations of Ref. 6 . If the vehicle change of mass is neglected.

$$V = V_o \sqrt{h/h_o} \tag{140}$$

where V_o and h_o are the velocity and altitude at retrorocket ignition, respectively. By using the information in Ref. 52 to calculate the sound speed, curves of C_T vs. M_∞ are obtained, which are shown in Figure 63.

It is assumed that the retrorocket maximum chamber pressure is 300 psi and that it is capable of a 12:1 throttling ratio. The ratio of the jet total pressure to the free stream total pressure, P_{o_j}/P_{o_∞}, as a function of M_∞ is shown in Fig. 64 for the two ignition altitudes (2.5 and 0.5 km) and for the two extremes of rocket power (i.e. full and minimum power).

The rocket thrust can also be defined by the following equation

$$T = C_F A^* P_{o_j} \tag{141}$$

where C_F is the thrust coefficient. Using this definition we obtain

$$\frac{d^*}{d_m} = (C_T q_\infty / C_F P_{o_j})^{1/2} \tag{142}$$

The values of d_j^*/d_m calculated for 300 psi chamber pressure and the flight conditions of Figure 63 are shown in Figure 65. These values are somewhat higher than those given in Table I which were supplied by the technical manager. However this is entirely consistent since the vehicle assumed there had a lower (than 0.5 slugs/ft^2) β and hence also lower ignition altitude.

To summarize, the retrorocket of a Mars entry configuration will be turned on at altitudes probably lower than 5 km, at free stream Mach number of 2.5 or less. Thus the 5 km ignition altitude curve of Fig. 63 represents an upper bound of C_T's to be simulated. The rocket will be maintained at full power during most of the descent, thus the P_{o_j} = 300 psi curve of Fig. 64 also represents an upper bound of P_{o_j}/P_{o_∞} to be simulated. The expected value of d_j^*/d_m from Fig. 65 is thus 0.026 or less.

5.3 FLOW REGIME CONSIDERATIONS

The analysis of the blunting sphere diameter and the slope of the interface between the jet and free stream have C_T as a parameter. The nozzle size (compared to the model) or nozzle area ratio are not formally involved. However the plume geometry obviously depends on P_{e_j}/P_d. If $P_{e_j} < P_d$, a normal shock will be required within the nozzle to match exit pressures. If $P_{e_j} \simeq P_d$, the "aerospike" configuration with a large shock stand-off distance will be encountered.

Since the plume geometry depends on other parameters as well, and since P_{e_j}/P_d is a complicated function of C_T, the task of defining the parameters for proper simulation seems a very complex one. However, P_d obviously depends on P_∞, and P_{e_j}/P_∞ varies linearly with $M_\infty^2 C_T$. Therefore the parameter $P_{e_j}/P_\infty M_\infty^2 C_T$ only depends on the nozzle parameters. In Fig. 66 is shown a plot of $P_{e_j}/P_\infty M_\infty^2 C_T$ vs. d^*/d_m for various nozzle area ratios. Lines of constant nozzle exit areas, d_e/d_m, are also shown.

TABLE I

REPRESENTATIVE MARS LANDER PARAMETERS

AEROSHELL CHARACTERISTICS

Diameter (D_A)	16.1 ft
Half-Angle	60^o
Nose Radius	0.1 D_A
Corner Radius	0.03 D_A

PROPULSION CHARACTERISTICS

Engine Circle Diameter	0.5 D_A
Maximum Chamber Pressure	250 psia
Expansion Ratio	40:1
Exit Diameter - 3 Engines	12.85 IN
1 Engine	22.25 IN
Thrust (Max-Min) - 3 Engines	1460-162 lbf
1 Engine	4380-486 lbd

The suggested nozzle configuration (Table I, $d_j^*/d_m = 0.0182$, and $A_e/A^* = 40$ is located on Figure 66 by a circular symbol. If we choose a different value of d^*/d_m, but keep the value of $P_{e_j}/P_\infty M_\infty{}^2 C_T$ the same (by changing A_e/A^*), we will have the same exit pressure for the different nozzle. Hence, by making the proper choice, we can match both C_T and P_{e_j}/P_∞, which means that we can simultaneously match the blunting sphere diameter and the plume geometry. Conversely, by changing $P_{e_j}/P_\infty M_\infty{}^2 C_T$ at constant d^*/d_m, we can investigate the effect of exit pressure on the plume geometry.

5.4 INVESTIGATION OF NASA WIND TUNNELS

For reasons which will be covered in detail in Section 5.5.1, the only wind tunnels of interest are large test section, variable density wind tunnels.

Mr. J. A. F. Hill visited the Ames Research Center on April 15, 1968. The 6' x 6' Supersonic Wind Tunnel would be available. Its performance characteristics are described in Reference 53 and summarized in Table II.

Mr. E. Wachsler visited the Langley Research Center on May 27, 1968. Because of their restricted Mach Number ranges, testing would have to be carried out partly in the 8' Pressure Transonic and partly in Test Section Number 1 of the Unitary Plan Wind Tunnel. Their performance characteristics are described in Reference 54 and summarized in Table II also.

The values of P_{o_j}/P_{o_∞} for the three Wind Tunnels,* as well as their Mach Number coverage, are shown in Figure 64. It can be seen that the P_{o_j}/P_{o_∞} ratio is higher for the Mars vehicle than can be simulated in any of the three tunnels.

---

* The operating characteristics of other wind tunnels are discussed in "National Wind Tunnel Summary" NASA, Washington, D. C., July 1961, AD 262 938. A summary of exhaust gas simulation capabilities of various wind tunnels is contained in Table I of "Wind Tunnel Testing Techniques for Integrated Airframe-Exhaust Nozzle Systems," Bonner, E., and Nixon, J. A., North American Rockwell Corporation Technical Report AFF DL-TR-68-94, July 1968, AD 8 36 259.

Table II. Wind Tunnel Characteristics

Wind Tunnel	Ames 6' Supersonic	Langley 8' Pressure Transonic	Langley Unitary Plan (Test Section 1)
Test Section	6' x 6'	7.1' x 7.1'	4' x 4'
Mach Number	.25, 0.6→2.2	0.2→1.3	1.47→2.15, 2.36→2.86
Minimum Total Pressure P_{o_∞} (atm)	0.3	0.25	0.27
Maximum Air Supply Pressure, P_{o_j} (psi)	3000	1500	1800
Jet Working Fluid other than air	yes	no	no
Schlieren	yes	yes (partly obstructed)	yes (partly obstructed)
Shadowgraph	yes	no	yes (partly obstructed)

We recommend that the Ames 6' Supersonic Wind Tunnel be chosen for testing because

1) it has a higher pressure air supply
2) the windows are unobstructed
3) jet working fluids other than air could be used
4) only 1 Wind Tunnel is involved, hence there would be no problems of model compatibility.

5.5 WIND-TUNNEL MODEL CONFIGURATION

5.5.1 Aeroshell Shape and Size

The shape of the aeroshell was suggested in Table I. The size of the model is set by the wind-tunnel test section size and the thrusting coefficient C_T. It was shown in Ref.24 that

$$\frac{d_f}{d_m} = 1.25\sqrt{C_T} \tag{143}$$

where d_f is the blunting sphere diameter. At transonic speeds the allowable tunnel blockage area is approximately 2 percent. Thus with a wind tunnel cross sectional area of 36 ft^2 and $C_T = 5$, the allowed value of $d_m = 4.1$ inches. It is planned that the model will be a 60^o half angle cone with a base diameter of 4 inches and a nozzle radius of 0.4 inches.

5.5.2 Nozzle Size and Area Ratios

5.5.2.1 Mars Lander Simulation

It is shown in Fig. 64 that even in the Ames wind-tunnel, it will not be possible to reach the values of P_{o_j}/P_{o_∞} experienced by the typical Mars lander. Therefore, to match in the wind-tunnel the vehicle C_T at full power, it will be necessary to have a larger than scaled throat. By using a throat area 5 times larger, the model C_T will match the vehicles C_T down to $M_\infty = 0.6$ for a

300 psi chamber pressure. If the rocket chamber pressure were 250 psi, the C_T can be matched for all Mach numbers. Therefore the throat size chosen is

$$\frac{d_j^*}{d_m} = 0.0182\sqrt{5} = 0.0407 \tag{144}$$

Of course values of C_T lower than the maximum can be easily obtained by throttling the jet air supply. For the configuration being considered, the useful range of C_T values is between the curves shown in Fig. 67.

In order to simulate the plume properly, the parameter $P_{e_j}/P_\infty M_\infty{}^2 C_T$ should be matched. In Fig. 66 a circle is shown for the lander configuration corresponding to $\frac{d_j^*}{d_m} = 0.0182$, $A_e/A^* = 40$, $\gamma_\infty = 1.304$ and $\gamma_j = 1.28$. To match $P_{e_j}/P_\infty M_\infty{}^2 C_T$ with $d_j^*/d_m = 0.0407$ and $\gamma_\infty = \gamma_j = 1.40$, we find $A_e/A^* = 10.80$. A drawing of the model is shown in Fig. 68. It is worth noting that the model nozzle has an exit area which is only 35% bigger than the exactly scaled value, while it allows us to simulate the thrusting coefficient and the plume geometry.

5.5.2.2 Flow Pattern Exploration

One of the objectives of the test program is to provide experimental data in areas where the validity of the assumptions of the analytical approach is questionable. It is desirable to keep the same thorat area, since this will give the same C_T range. If the nozzle area ratio is changed, the exit pressure at a given C_T will be different. Hence it will be possible to systemically examine how the plume geometry varies with $P_{e_j}/P_\infty M_\infty{}^2 C_T$.

We propose to test two other nozzle configurations with the same throat area, but with nozzle area ratios of 6.0 and 20.0, which correspond to values of $P_{e_j}/P_\infty M_\infty{}^2 C_T$ 2.5 times higher and lower

respectively than the Mars lander simulation configuration. The nozzle exit to model diameter ratios are 0.10 and 0.182 respectively, which seem quite reasonable.

5.5.2.3 Nozzle Shape

Large area ratio nozzles are generally not contoured since the gain in performance is very small while the construction difficulty is much greater. Straight 15^{o} half-angle conical nozzle contours have been chosen since they are typical of current construction practice.

5.5.2.4 Multi-Nozzle Configurations

It is probable that the Mars Lander will use a cluster of smaller retrorockets, rather than a single large one. In that case the flow pattern is more complex because of the mutual interaction of the jets, as well as the interactions with the counter current stream and the aeroshell. We plan to test two multiple nozzle configurations, which will have the same effective throat area and nozzle area ratios as the Mars lander simulation configuration (single nozzle).

The multiple jet configurations will consist of 3 nozzles, spaced 120^{o} apart on a jet centerline radius to model base radius of 0.5 and 0.8. Each nozzle will have a $d_j^*/d_m = 0.0235$ and an area ratio of 10.8. The nozzle contours will be straight 15^{o} half-angles cones. A drawing of the proposed model is shown in Fig. 69.

5.6 TEST PLAN

5.6.1 Model Types

It is desired to measure the pressure distribution, the drag and pitching moment, and the heating rate. In order to carry out these measurements, it will be necessary to construct three models, one for each type of measurement.

1) The pressure model will have approximately 12 taps, one of which will be in the base. The pressure measurements will indicate whether the flow is steady, the extent and boundaries of the dead-air region, and the minimum value of C_T at which the model will be fully immersed in the dead-air region.

2) The drag force and pitching moments will be measured with a force balance to be furnished by MITHRAS. Since the model drag variation is expected to be small compared to the thrust variation, the balance will be designed to measure the model aerodynamic drag force only, and not the jet thrust.

3) The heating rate and recovery temperature distribution will be measured with a thin-skinned model equipped with approximately 12 thermocouples. The hot air jet (~500° F, 0.72 lbs/sec, 3000 psia) will be cycled on and off at the appropriate rate. The jump in heating rate at the reattachment ring at moderate C_T and the heating rate near the aeroshell corner will be of particular interest.

5.6.2 Test Fluids and Parameter Range

The wind tunnel working fluid will be room temperature air. The Mach Number range will be from 0.25 to 2.5. The dynamic pressure will be 200 psf at transonic and supersonic speeds and lower at subsonic speeds.

The jet C_T will be varied from 0 (for tare readings) to 10. The jet working fluids will be room temperature air, hot (500° F) air and room temperature helium. The air heater will be furnished by MITHRAS. The jet working fluid will be hot air for the heating rate measurements, helium for the mixing studies, and room temperature air for most of the pressure, force and moment

measurements. The maximum jet mass flows will be 1.0, 0.72 and 0.34 lbs/sec for room temperature air, hot air and helium, respectively.

Most of the data will be taken at zero angle-of-attack, but $\alpha = 5^{o}$ and 10^{o} will be used, especially for the pitching moment measurements.

5.6.3 Data to be Taken

1) Wind Tunnel parameters
   a) Mach Number, M_{∞}
   b) Total Pressure, $P_{o_{\infty}}$
   c) Total Temperature, $T_{o_{\infty}}$

2) Jet Parameters
   a) Working fluid
   b) Total Pressure, P_{o_j}
   c) Total Temperature, T_{o_j}

3) Model Configuration
   a) single or multiple nozzle
   b) throat area, A_j^*
   c) nozzle area ratio, A_{e_j}/A_j^*
   d) angle of attack, α

4) Model Specific Measurements
   a) Pressure distribution along a ray, P(x)
   b) Drag force, D, and pitching moment C_M
   c) Temperature distribution as a function of time, T(x,t) The heating rate can be calculated at each thermocouple location from a knowledge of T(t).

5) Photographs

a) Schlieren and Shadow

The photographs will show the general features of the flow pattern. In particular they will show whether the flow is steady or not, the shock standoff distance, the diameter of the blunting sphere, the location of the mixing layer and its reattachment ring on the aeroshell, and the transition to the wake-type flow with the aeroshell completely immersed in the dead-air region.

6) Mixing

a) "Sniffing" with the MITHRAS Binary Gas Analyzer from an aft pressure tap when the jet fluid is helium will provide information on the mixing process at low and moderate C_T's.

5.7 TENTATIVE TEST SCHEDULE

The tentative test schedule for single nozzle configurations is shown in Table III and for multiple nozzles configurations in Table IV.

Table III. Proposed Wind Tunnel Test Program
Single Nozzle Configurations

Measured Quantity	A_e/A^*	d^*/d_m	r_c/r_m	Air Fluid	Mach No.	α	C_T
Pressure	20.	0.0407	0	Air	0.25 → 2.5	0^o	0-10.
	10.8	0.0407	0	Air	0.25 → 2.5	0^o	0-10.
	6.	0.0407	0	Air	0.25 → 2.5	0^o	0-10.
	10.8	0.0407	0	Air	0.25 → 2.5	$5-10^o$	0-2.
Force and Moments	20.	0.0407	0	Air	0.25 → 2.5	0^o	0-10.
	10.8	0.0407	0	Air	0.25 → 2.5	0^o	0-10.
	6.	0.0407	0	Air	0.25 → 2.5	0^o	0-10.
	10.8	0.0407	0	Air	0.25 → 2.5	$5-10^o$	0-2.
Heating Rate	20.	0.0407	0	500°F Air	0.25 → 2.5	0^o	0-2.
	10.8	0.0407	0	500°F Air	0.25 → 2.5	$0-10^o$	0-2.
	6.	0.0407	0	500°F Air	0.25 → 2.5	0^o	0-2.
Pressure and Mixing	10.8	0.0407	0	Helium	0.25 → 2.5	$0-10^o$	0-1.
Force and Moments	10.8	0.0407	0	Helium	0.25 → 2.5	$0-10^o$	0-1.

Table IV. Proposed Wind Tunnel Test Program
Multiple Nozzle Configurations

Measured Quantity	A_e/A^*	d^*/d_m	r_c/r_m	Jet Fluid	Mach No.	α	$C_T{}^*$
Pressure	10.8	0.0407	0.50	Air	0.25 → 2.5	0^o	0-10.
	10.8	0.0407	0.80	Air	0.25 → 2.5	0^o	0-10.
	10.8		0.50	Air	0.25 → 2.5	$5\text{-}10^o$	0-2.
	10.8	0.0407	0.80	Air	0.25 → 2.5	$5\text{-}10^o$	0-2.
Force and Moments	10.8	0.0407	0.50	Air	0.25 → 2.5	$0\text{-}10^o$	0-10.
	10.8	0.0407	0.80	Air	0.25 → 2.5	$0\text{-}10^o$	0-10.
Heating Rate	10.8	0.0407	0.50	500^oF Air	0.25 → 2.5	$0\text{-}10^o$	0-2.
	10.8	0.0407	0.80	500^oF Air	0.25 → 2.5	$0\text{-}10^o$	0-2.
Pressure and Mixing	10.8	0.0407	0.50	Helium	0.25 → 2.5	$0\text{-}10^o$	0-1.
	10.8	0.0407	0.80	Helium	0.25 → 2.5	$0\text{-}10^o$	0-1.
Force and Moments	10.8	0.0407	0.50	Helium	0.25 → 2.5	$0\text{-}10^o$	0-1.
	10.8	0.0407	0.80	Helium	0.25 → 2.5	$0\text{-}10^o$	0-1.

*Based on the throat area of all nozzles.

REFERENCES

1. Voyager Capsule Phase B, Final Report Vol. 1 - Summary Report No. F694, August 31, 1967. McDonnell Astronautics N67-40041.

2. Voyager Capsule Phase B, Final Report Vol. II - Capsule Bus System Part B1, Alternatives, Analyses, Selection, Report No. F694, August 31, 1967. McDonnell Astronautics N-67-40044.

3. Voyager Capsule Phase B, Final Report Vol. II - Capsule Bus System Part B2, Alternatives, Analyses, Selection, Report No. F694, August 31, 1967. McDonnell Astronautics N67-40045.

4. Voyager Capsule Phase B, Final Report Vol. I - Summary Report No. FR-22-103 Vol. I - Martin Marietta Corporation, Denver Division, August 31, 1967, N67-40442.

5. Voyager Capsule Phase B, Final Report Vol. II - Capsule Bus System Section I, Capsule Bus Report No. FR-22-103, Vol. II, Section I. Martin Marietta Corporation, Denver Division, August 31, 1967, N67-40443.

6. "Preliminary Payload Analysis of Automated Mars Sample Return Missions," Compiled and Written by J.C. Niehoff, AstroSciences Center of IIT Research Institute, Report No. M-13, Contract No. NASr-65(06), May 1967, N67-36556.

7. Hill, J.A.F. and Draper, J.S., "Analytical Approximation for the Flow from a Nozzle into a Vacuum," Engineering Note, Journal of Spacecraft and Rockets, 3, 10, October 1966, pp. 1552-1554.

8. Charwat, A.F., "Boundary of Underexpanded Axisymmetric Jets Issuing Into Still Air," AIAA Journal, Vol. 2, No. 1, January 1964 (pp. 161-163).

9. Finley, P.J., "The Flow of a Jet from a Body Opposing a Supersonic Freestream," Journal of Fluid Mechanics (1966), Vol. 26, Part 2 (pp. 337-368).

10. Finley, P.J., "Experiments on Jets Directed from Blunt Bodies Against a Supersonic Airstream," Ph.D. Thesis Cambridge University (1963).

REFERENCES (Continued)

11. Lopstoff, Mitchell, "Wing-Flow Study of Pressure-Drag Reduction at Transonic Speed by Projecting a Jet of Air from the Nose of a Prolate Spheroid of Fineness Ratio 6", NACA Research Memo RM L51E09; October 26, 1951.

12. Love, E.S., "The Effects of a Small Jet of Air Exhausting from the Nose of a Body of Revolution in Supersonic Flow," NACA Research RM L52119a, November 12, 1952.

13. Massachusetts Institute of Technology Naval Supersonic Laboratory, "An Experimental Study of a Window for an Infrared Seeker," Wind Tunnel Report 276, 1957.

14. Massachusetts Institute of Technology Naval Supersonic Laboratory, "Temperature Parameter Study of aWindow for an Infrared Seeker," Technical Report 341, 1958.

15. Watts, G.A., "An Experimental Investigation of a Sonic Jet Directed Upstream Against a Uniform Supersonic Flow," University of Toronto Technical Note No. 7, January 1956.

16. Charczenko, N. and Hennessey, K., "Investigation of a Retrorocket Exhausting from the Nose of a Blunt Body into a Supersonic Freestream," NASA Technical Note TN D-751, September 1961.

17. Peterson, V. and McKenzie, R., "Effects of Simulated Retrorockets on the Aerodynamic Characteristics of a Body of Revolution at Mach Numbers from 0.25 to 1.90," NASA Technical No. TN D-1300, May 1962.

18. Hayman, L.O. and McDearman, R.W., "Jet Effects On Cylindrical Afterbodies Housing Sonic and Supersonic Nozzles Which Exhaust Against a Supersonic Stream at Angles of Attach from 90^{o} to 180^{o}, NASA TN D-1016(1962)

19. Romeo, D. and Sterrett, J., "Exploratory Investigation of the Effect of a Forward-Facing Jet on the Bow Shock of a Blunt Body in a Mach Number 6 Freestream," NASA Technical Note TN D-1605, Feb., 1963.

20. Romeo, D. and Sterrett, J.R., "Flow Field for a Sonic Jet Exhausting Counter to a Hypersonic Mainstream," AIAA Journal, Vol. 3, No. 3; March 1965.

REFERENCES (Continued)

21. Keyes, J.W. and Hefner, J.N., "Effect of Forward-Facing Jets on Aerodynamic Characteristics of Blunt Configurations at Mach 6," Journal of Spacecraft and Rockets, Vol. 4, No. 4; April 1967.

22. MITHRAS, Inc., "Investigation of an Aerodynamic Spike in Hypersonic Flow," Airborne Instruments Lab. Rpt. No. 1198-1, Final for Contract AF04(694)-29, AD365190, (Confidential), June 1962.

23. Charwat, A.F., and Faulmann, D., "Investigation of the Flow and Drag Due to Control Jets Discharging Upstream into a Supersonic Flow," Delivered at Fifth Astronautical Fed. Cong., Warsaw, Poland; Sept. 7-12, 1964.

24. Good, R.E., Hill, J.A.F., "A Wind Tunnel Investigation of the Nitric Oxide-Oxygen Atom Reaction," MITHRAS Rpt. MC64-116-R2, 1966.

25. Sutton, E.P. and Finley, P.J., "The Flow of a Jet From The Nose of an Axisymmetric Body in a Supersonic Airstream," Archiwinn Mechaniki Stosowanej, 3, p. 781 (1964)

26. Finley, P.J., "Experiments On The Reattachment Of a Turbulent Axisymmetric Shear Layer," Aeronautical Quarterly, Nov. 1967.

27. Carlson, D.J., Project Engineer, "Solid Propellant Exhaust Radiation Studies," First Interim Report U-2573, Philco Res. Lab., April 1964.

28. Stitt, L.E., "Interaction of Highly Underexpanded Jets with Simulated Lunar Surfaces," NASA TN D-1095, Lewis Res. Center, December 1961.

29. Goethert, B.H., "Base Flow Characteristics of Missiles with Cluster-Rocket Exhausts," Aerospace Eng., March 1961, Starting page 29.

30. Wasko, R.A., "Heat Transfer to a Sphere with a Retrorocket Exhausting into a Freestream Mach 2.0 and 0.8," Lewis Res. Center, Cleveland, Ohio, Technical Note D-1535, November 1962.

31. Voyager Capsule Systems Constraints and Requirements Document PD606-4 Jet Propulsion Laboratory, Pasadena, California; May 18, 1967.

32. Harris, C.D., "Transonic Aerodynamic Investigation of Tension Shell and Blunted 100-Degree Conical Shapes For Unmanned Entry Vehicles," NASA TN D-3700 November 1966.

33. Wood, C.J., "Hypersonic Flow Over Spiked Cones," Journal of Fluid Mechanics, Vol. 12, Part 4. April 1962.

34. Chapman, D.R., Kuehn, D.M. and Larson, H.K., "Investigation of Separated Flows In Supersonic and Subsonic Streams With Emphasis On The Effect of Transition. NACA Report 1356, 1958.

35. Korst, H.H., "A Theory For Base Pressures In Transonic and Supersonic Flow," Journal of Applied Mechanics, December 1956.

36. Altshuler, S., Moe, M.M, Mohund, P., "The Electromagnetics of the Rocket Exhaust," Space Tech. Lab. Rpt. GM-TR-0165-00397, 1958.

37. Piesik, E.T., Koppang, R.R., Simkin, D.J., "Rocket Exhaust Impingement on a Flat Plate at High Vacuum," Journal of Spacecraft & Rockets, 3, 11, November 1966 (1650-1657).

38. Jarvinen, P.O., Hill, J.A.F., Draper, J.S., and Good, R.E., "High Altitude Rocket Plumes," Air Force Cambridge Research Laboratory Report AFCRL 66-656 Final Report, June 1966; Contract No. AF19(628)-4218. Also Mithras Division of Sanders Associates, Inc. Report MC 65-120-R3.

39. Jarvinen, P.O. and Draper, J.S., "Underexpanded Gas-Particle Jets," AIAA Journal, Vol.5, No. 4, April 1967, pp. 824-825.

40. Alden, H.L. and Habert, R.H., "Gas Dynamics Of High-Altitude Rocket Plumes," Air Force Cambridge Research Lab Report AFCRL-64-677 Final Report July 1964, Contract No. AF19(628)-3280. Also Mithras Division of Sanders Associates, Inc. Report MC 63-80-R1.

41. Luce, R.W. and Jarvinen, P.O., "An Approximate Method For Predicting Plume Sizes For Nozzle Flow Into Still Air," AIAA Journal, Vol. 6, No. 1; January 1968, pp. 182-183.

42. Love, E.S., Grigsby, C.E., Lee, L.P. and Woodling, M.J., "Experimental and Theoretical Studies of Azisymmetric Free Jets," NASA Technical Report TR R-6, 1959.

43. Andrews, E.H., Vick, A.R. and Craidon, C.B., "Theoretical Boundaries and Internal Characteristics Of Exhaust Plumes From Three Different Supersonic Nozzles," NASA Technical Note TND-2650, March 1965.

44. Jarvinen, P.O., Draper, J.S., and Carron, P.D., "High Altitude Rocket Plumes And Their Radar Observables," Air Force Cambridge Research Report, Final Report, February 1968, Contract No. AF19(628)-5912. Also Mithras Report MC 66-210-R1, Mithras Division of Sanders Associates.

45. Katz, J.R., "Pressure And Wave Drag Coefficients For Hemispheres, Hemisphere-Cones And Hemisphere Ogives," U.S. Naval Ordinance Test Station NAVORD Report 5849, China Lake, California, March 1958.

46. Robinson, R.C., Gombucci, B.J. and George, R.E., "Fluctuating Pressure On The Afterbodies Of Five Blunt Atmosphere Entry Vehicles," NASA TN D 4591, May 1968.

47. Shapiro, Ascher H., "The Dynamics and Thermodynamics of Compressible Fluid Flow," Vol. I, The Ronald Press Co., New York, 1953.

48. Kármán, Theodore von, and Biot, Maurice A. "Mathematical Methods in Engineering," First Edition, McGraw-Hill, New York, 1940.

49. Schlichting, Hermann. "Boundary Layer Theory," First Edition, McGraw-Hill, New York, 1955.

50. Hill, Jacques A. F., and Luce, Richard W., Wind-Tunnel Measurements of Turbulent Wake Cooling with Base Injection. MITHRAS, Inc., Report MC 64-85-R3, August 1966.

51. NACA Report 1135 "Equations, Tables and Charts for Compressible Flow by Ames Research Staff 1953.

52. Evans, D.E., Pitts, D.E., and Kraus, G.L., Venus and Mars Nominal Natural Environment for Advanced Manned Planetary Mission Programs, NASA SP-3016, Second Edition, 1967.

53. "Research Facilities Summary, Vol. II - Wind Tunnels, NASA Ames Research Center, December 1965.

54. Schaefer, W.T., Jr., "Characteristics of Major Active Wind Tunnels at the Langley Research Center," NASA TMX-1130, July 1965.

LOW AND INTERMEDIATE C_T, $\theta_v = 60°$

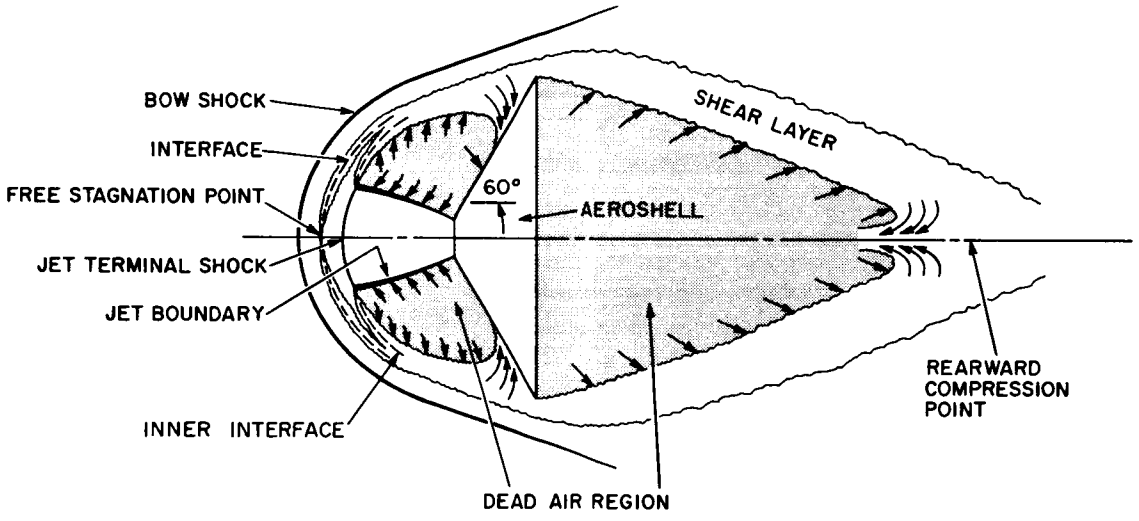

Figure 1. Low and intermediate C_T, $\theta_v = 60^o$.

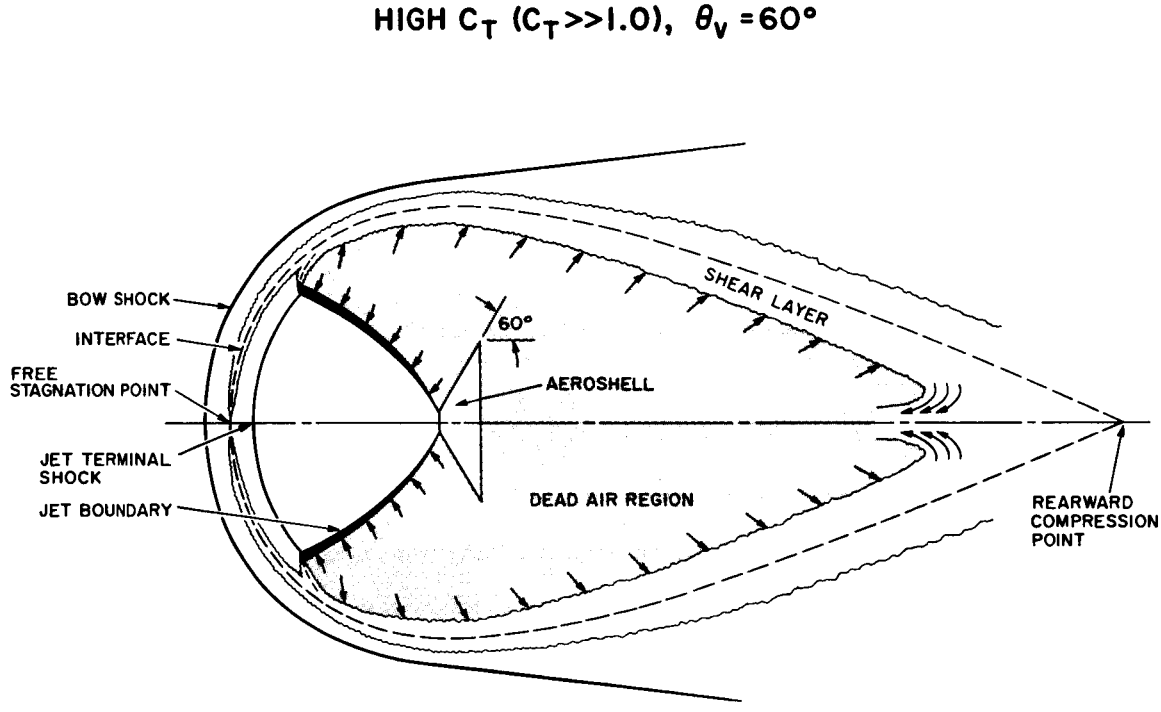

Figure 2. Flow field - high thrusting coefficient.

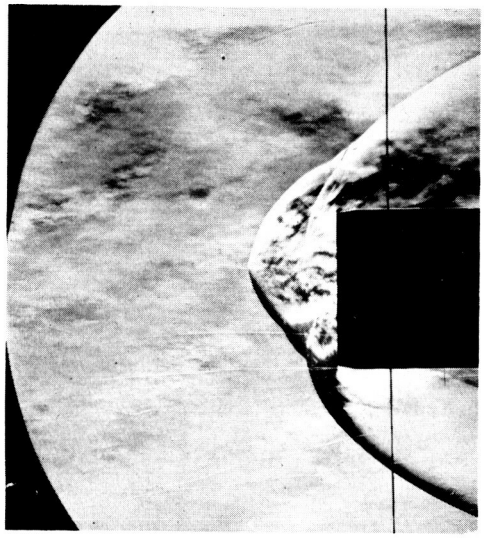

Figure 3. Schlieren photograph of Regime 1, $M = 3.5$, $C_T = 0.04$. Reference 13.

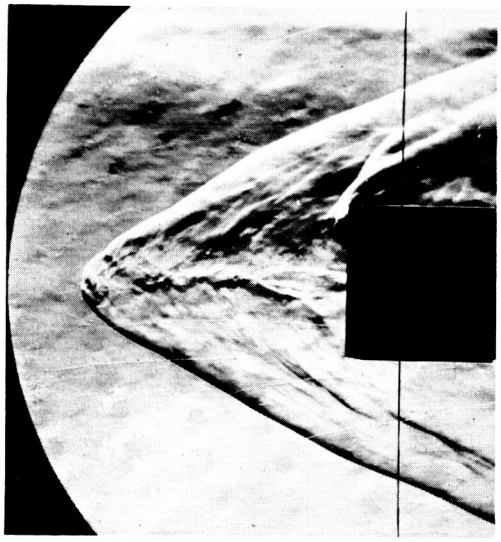

Figure 4. Schlieren photograph of Regime 2, $M = 3.5$, $C_T = 0.12$. Reference 13.

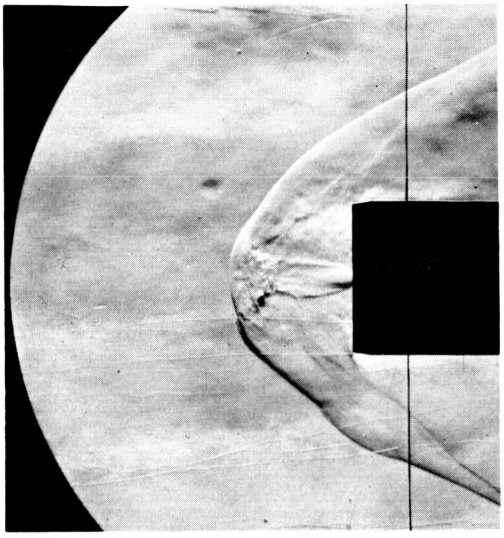

Figure 5. Schlieren photograph of Regime 3, M = 3.5, C_T = 0.28. Reference 13.

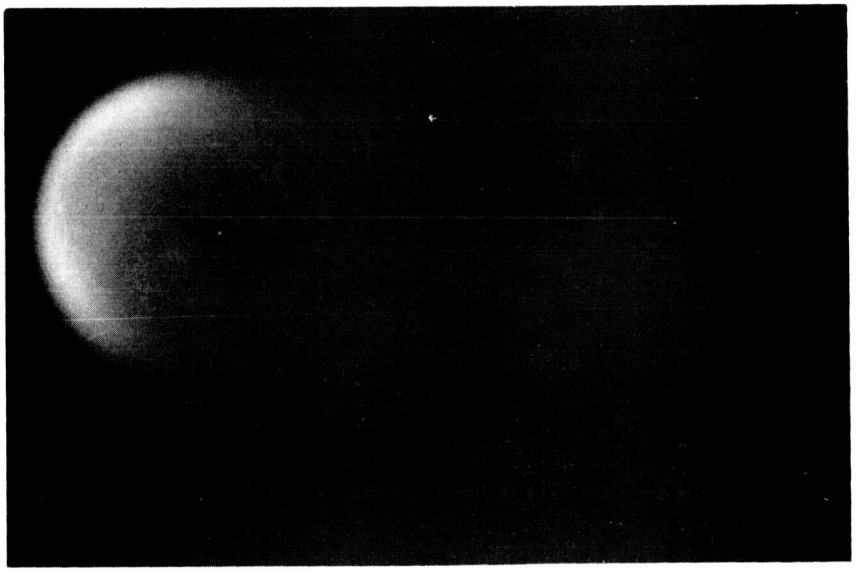

Figure 6. Nitric-oxide Glow photograph of Regime 4, M = 3.5, C_T = 109 Reference 24.

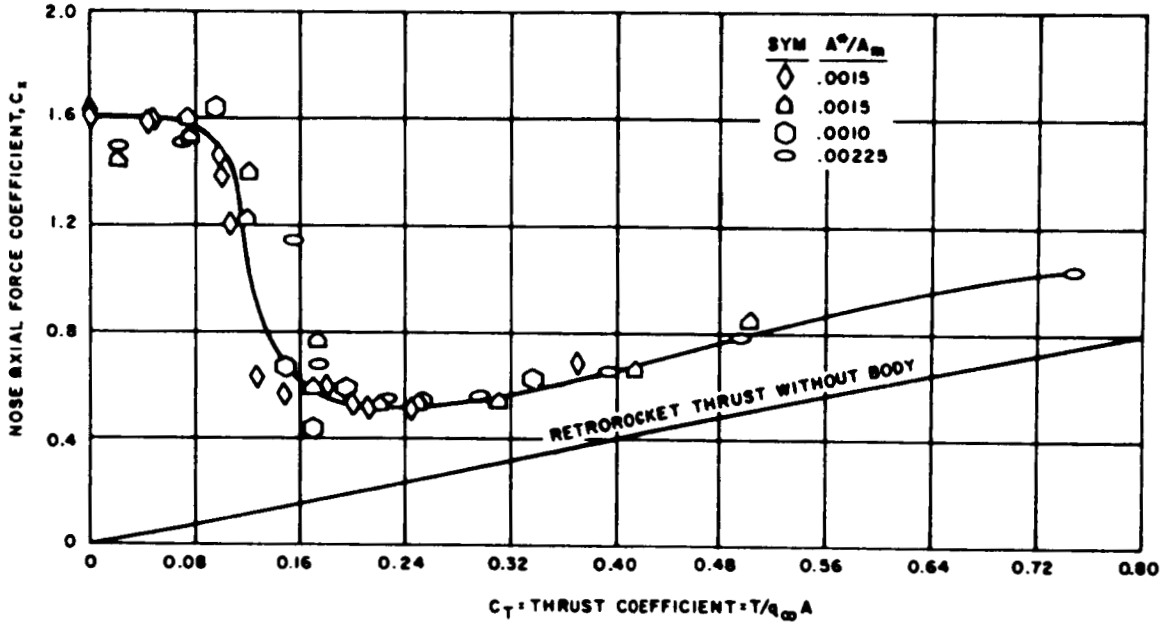

Figure 7. Total retroforce coefficient versus rocket thrust coefficient, M = 3.5 (Ref. 13).

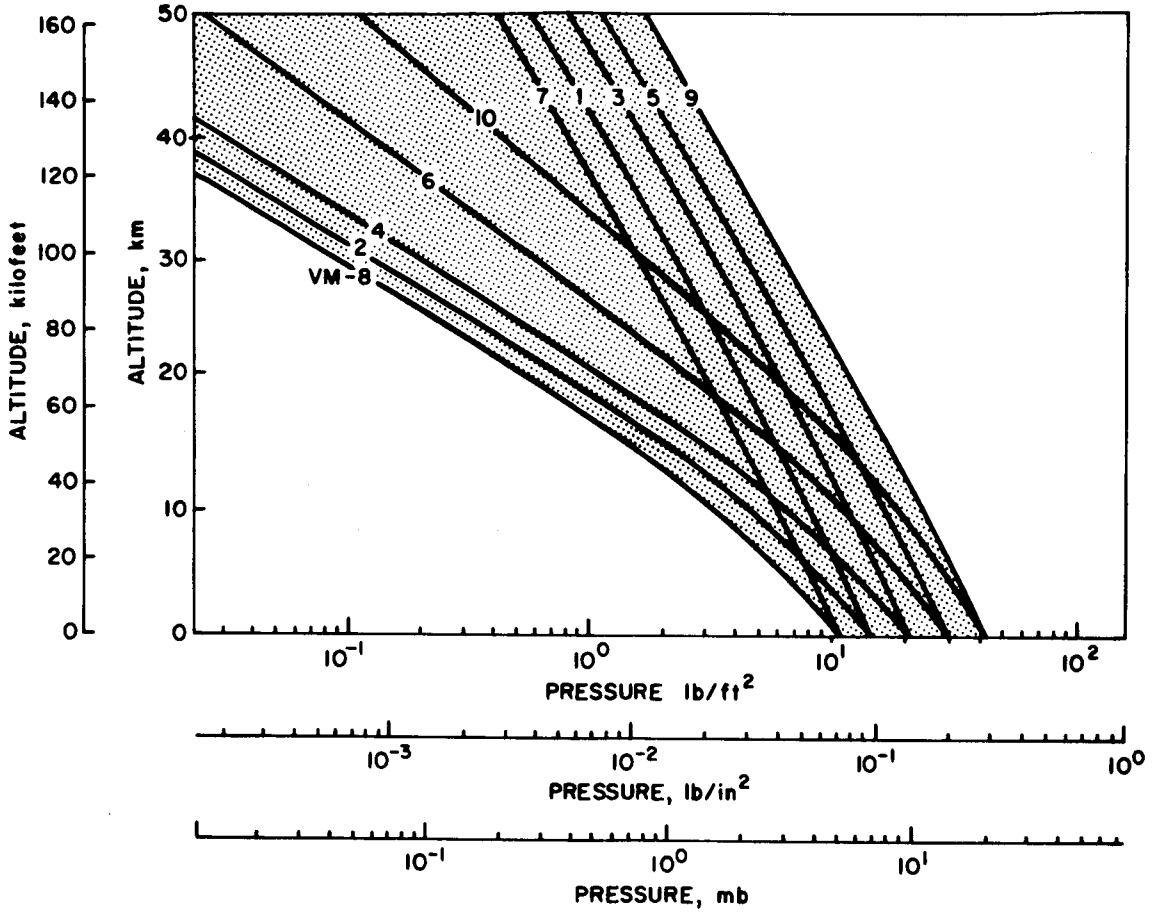

Figure 8. Atmospheric pressure - Models VM-1 through VM-10.

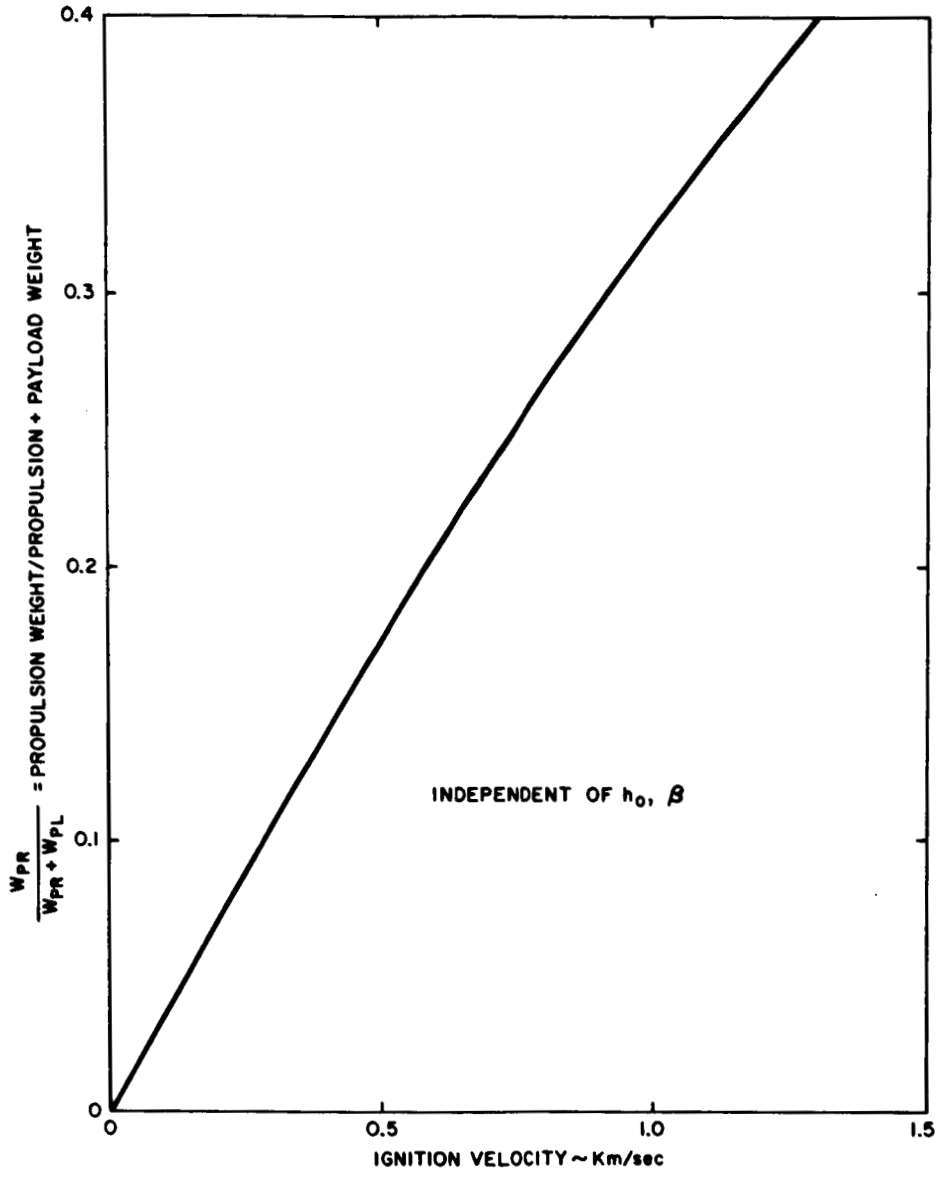

Figure 9. Propulsion system weight versus retrofire velocity.

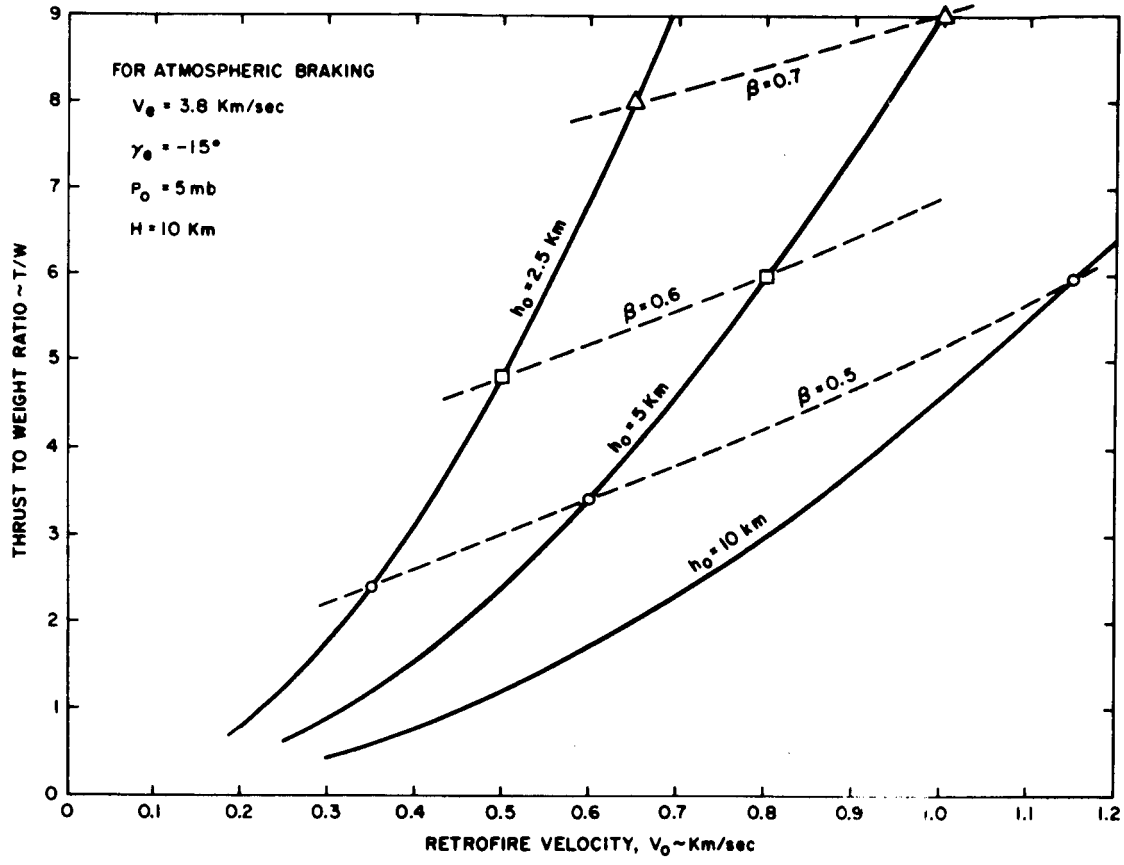

Figure 10. Thrust to weight ratio versus retrofire velocity.

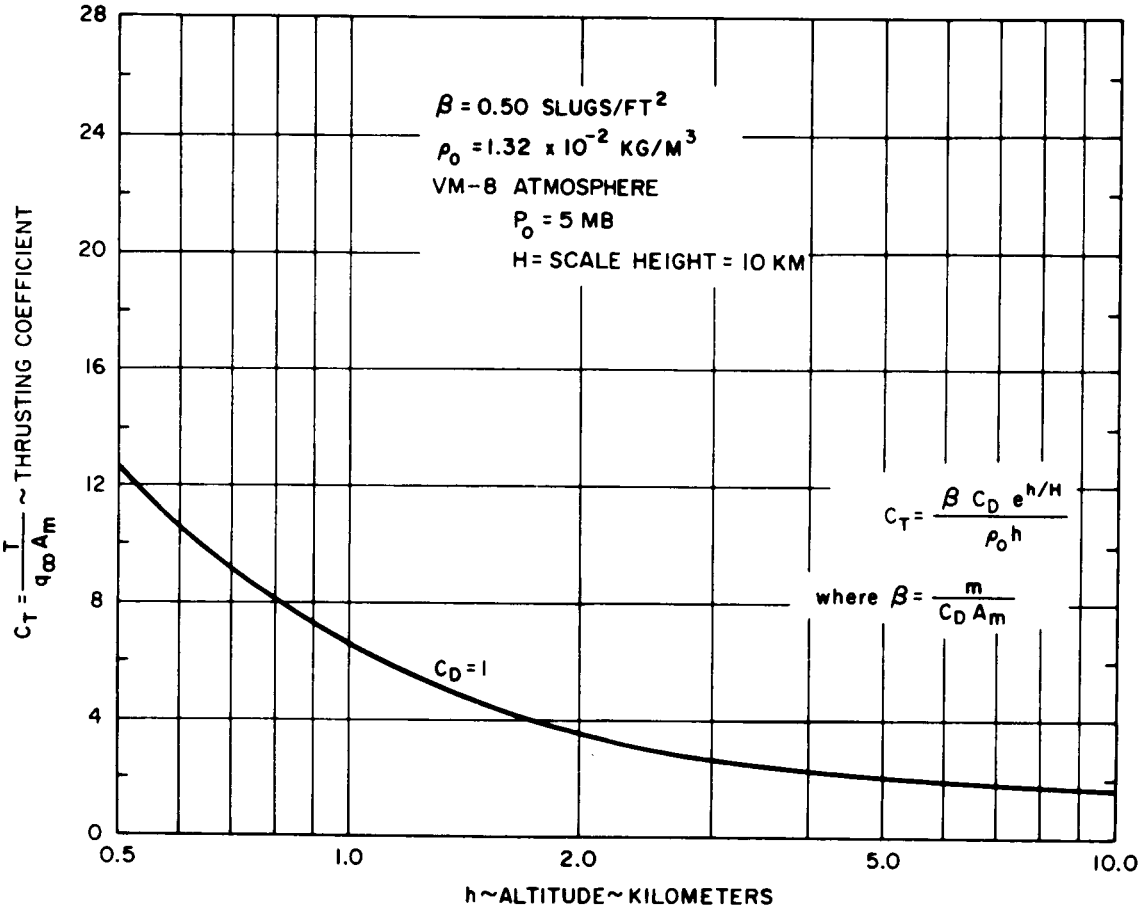

Figure 11. Retrorocket thrusting coefficient during MARS entry.

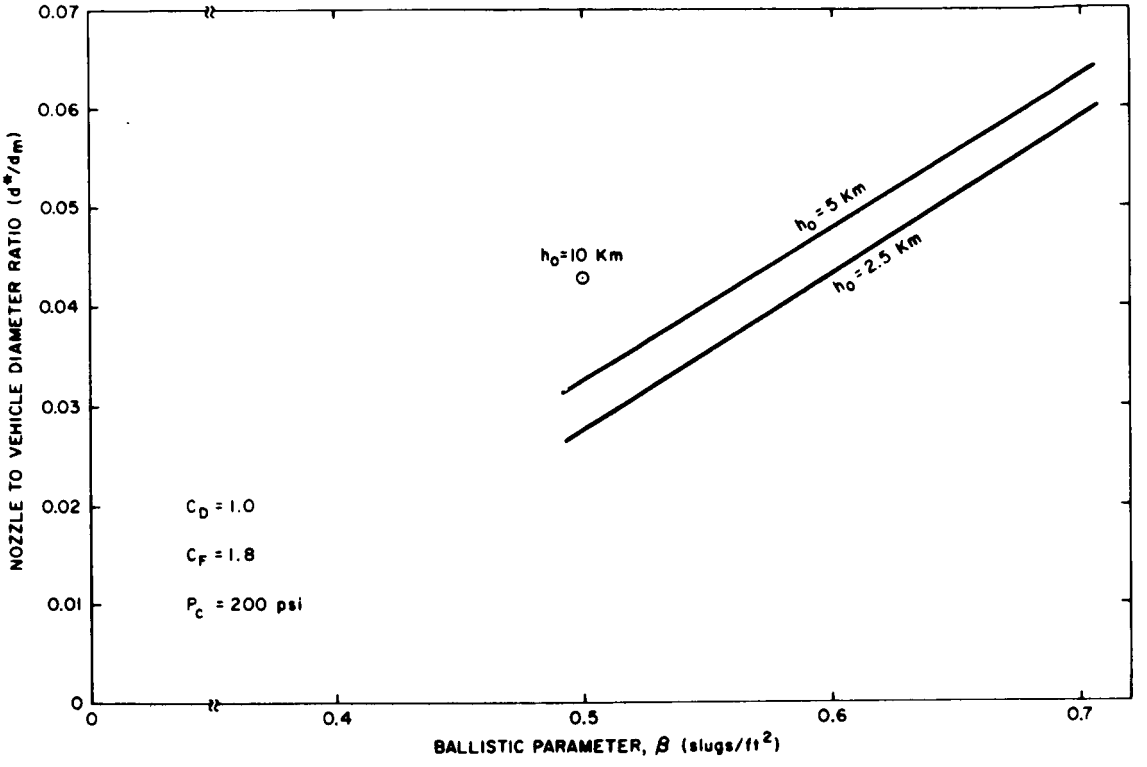

Figure 12. Nozzle size versus ballistic parameter.

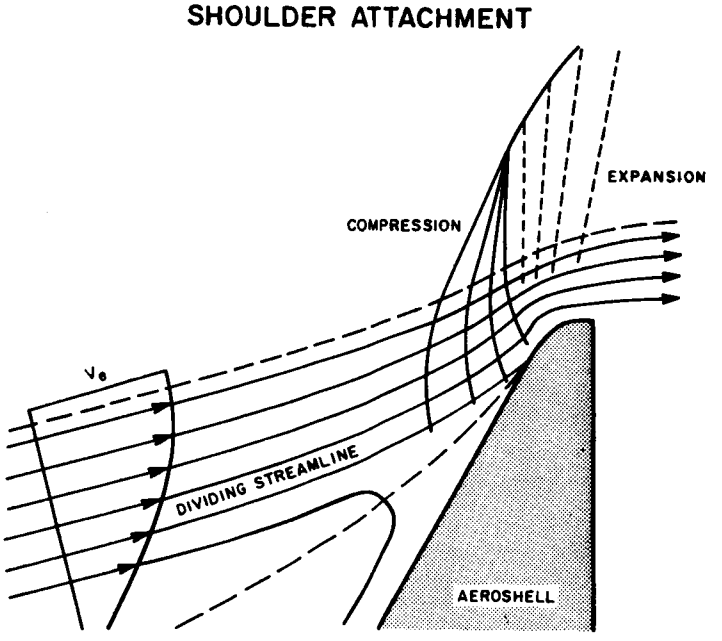

Figure 13. Aerodynamic features of shoulder attachment.

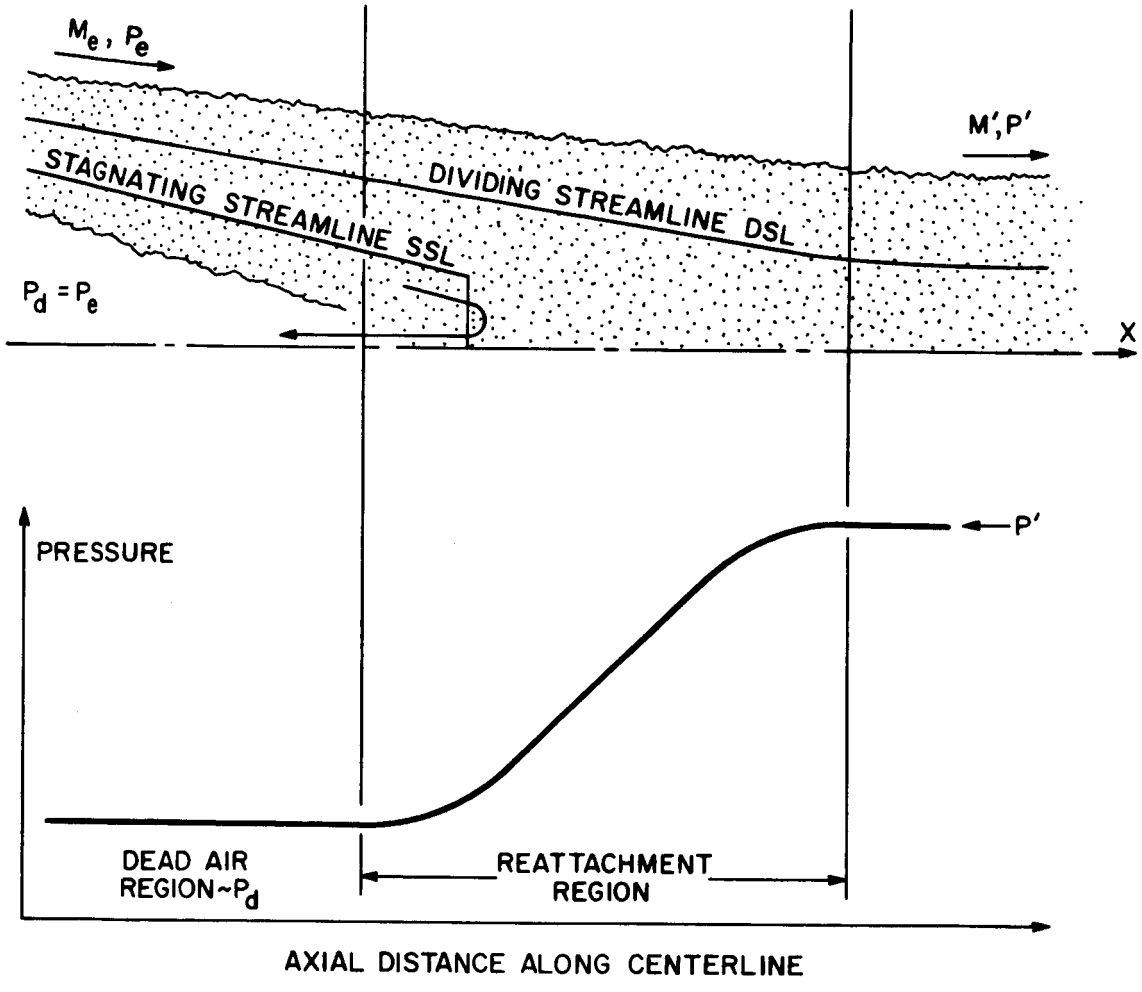

Figure 14. Wake neck recompression region.

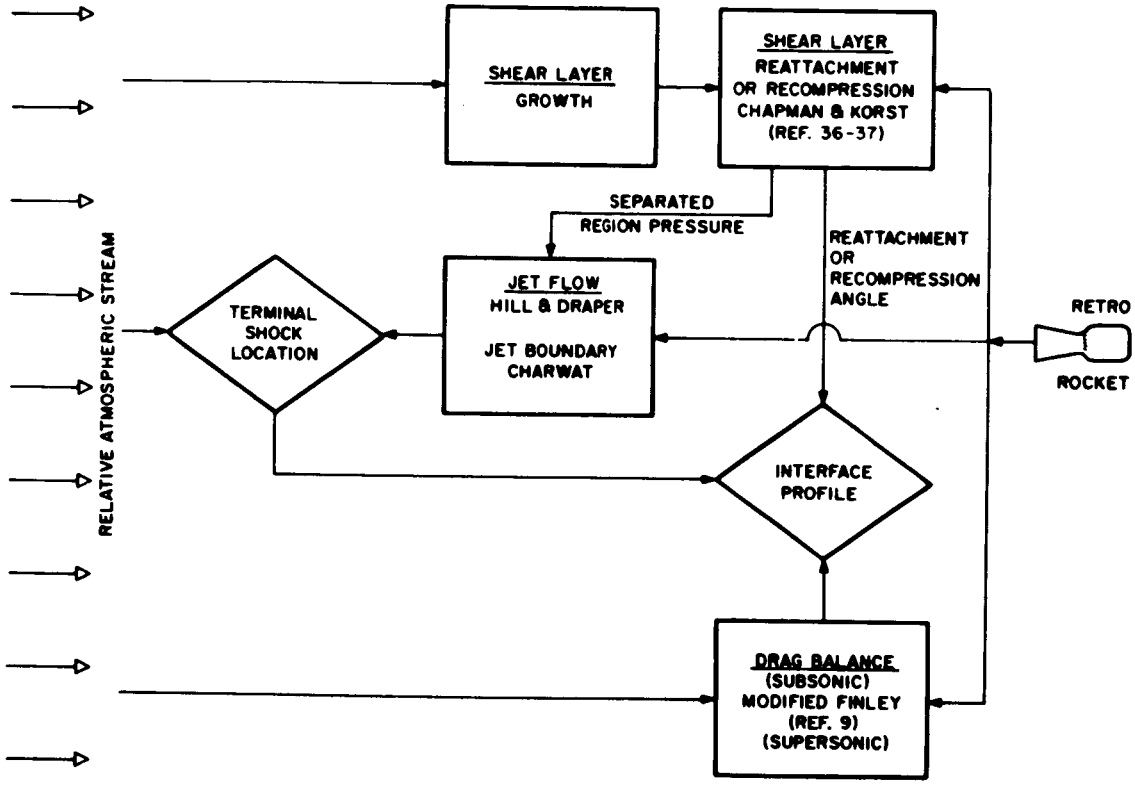

Figure 15. Schematic of analysis.

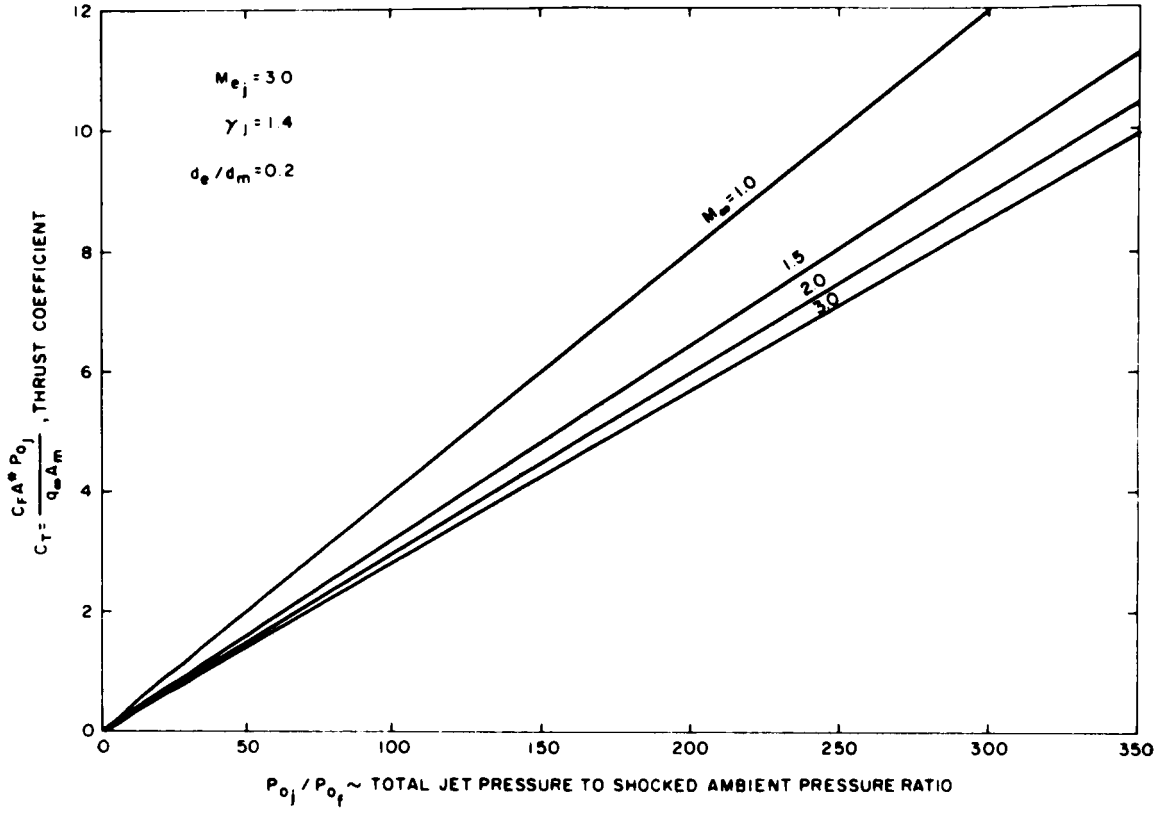

Figure 16. Variation of thrusting coefficient with P_{o_j}/P_{o_f} ratio.

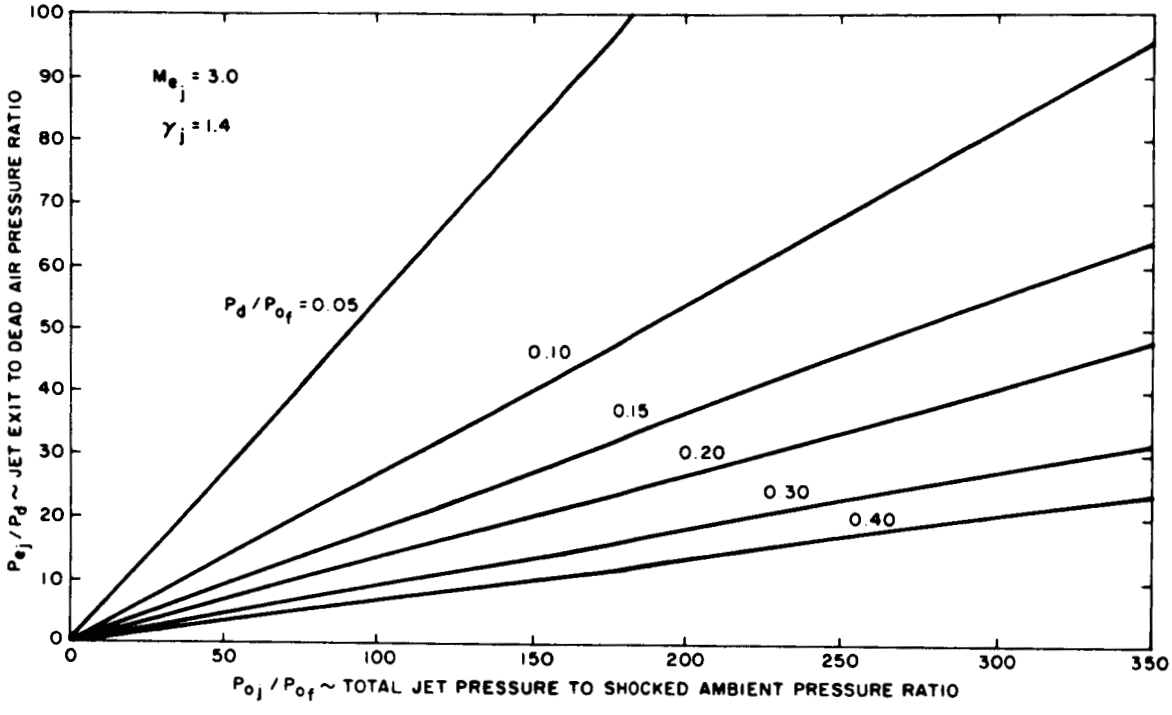

Figure 17. Jet exit to dead-air pressure ratio M_{e_j} = 3.0 γ_j = 1.4.

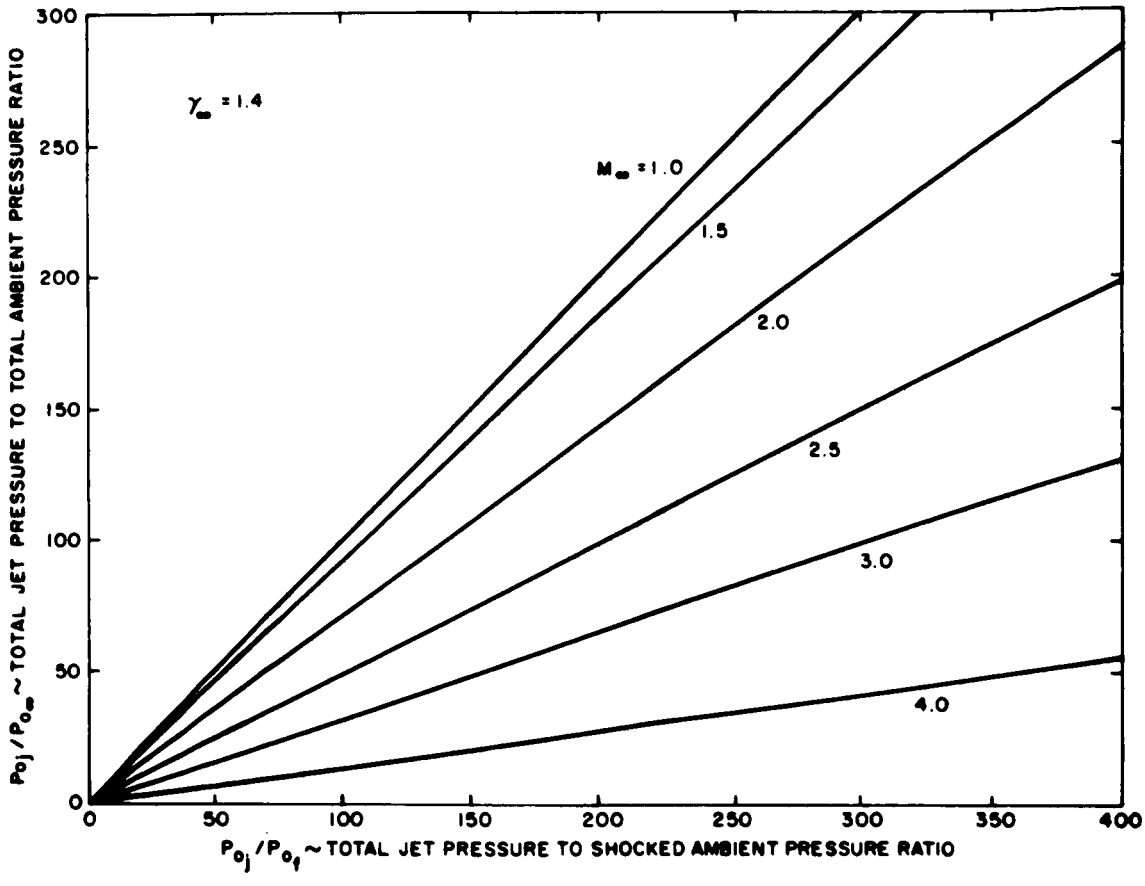

Figure 18. Total jet pressure to total ambient pressure ratio, $\gamma_\infty = 1.4$.

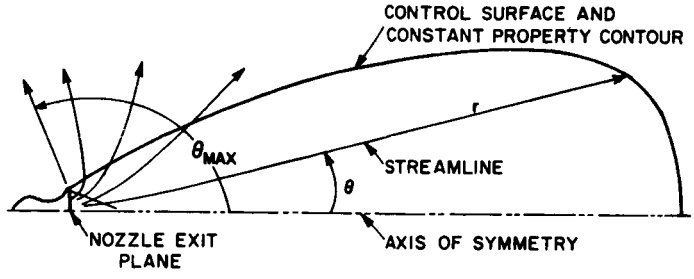

Figure 19. Schematic of flow pattern of a nozzle exhausting into vacuum.

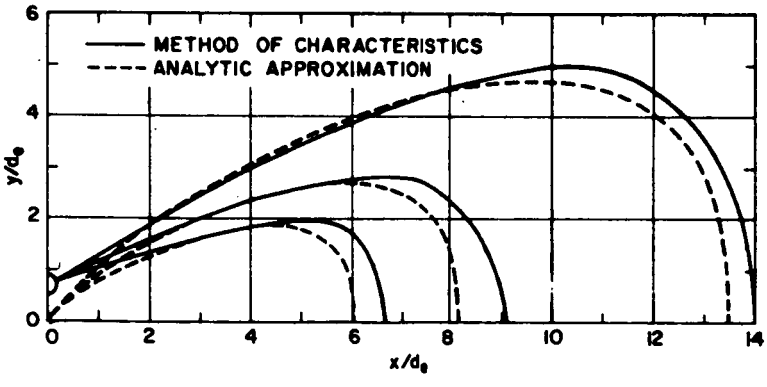

Figure 20. "Exact" and approximate constant-density contours for $A_e/A^* = 25$; $\gamma = 1.29$.

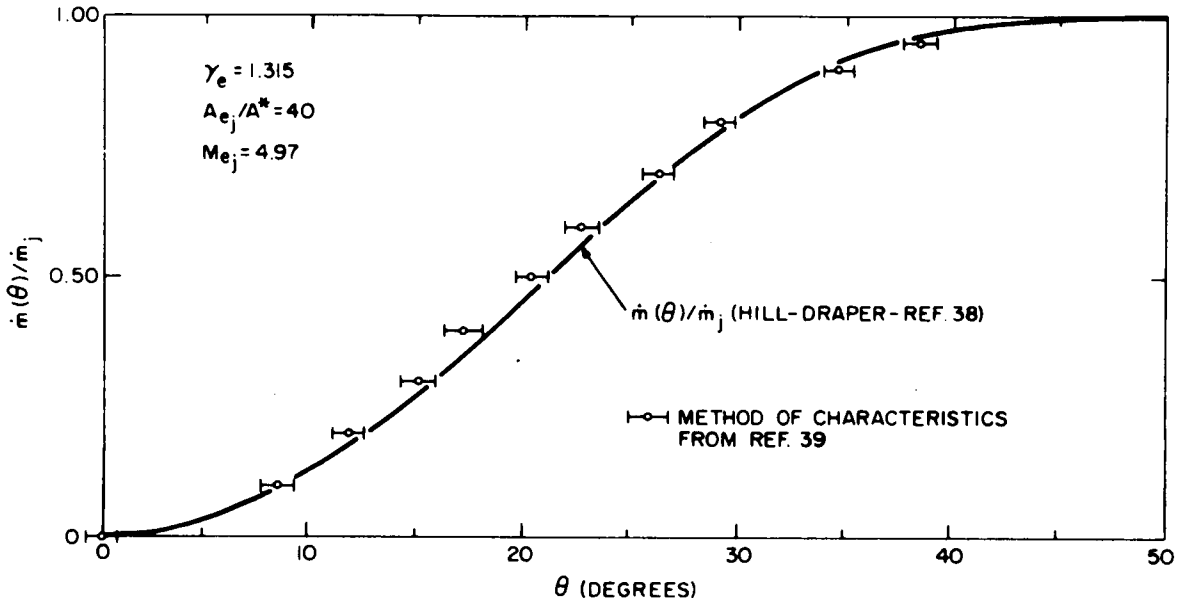

Figure 21. A jet mass flux distribution given by the method of characteristics and the Hill-Draper approximation.

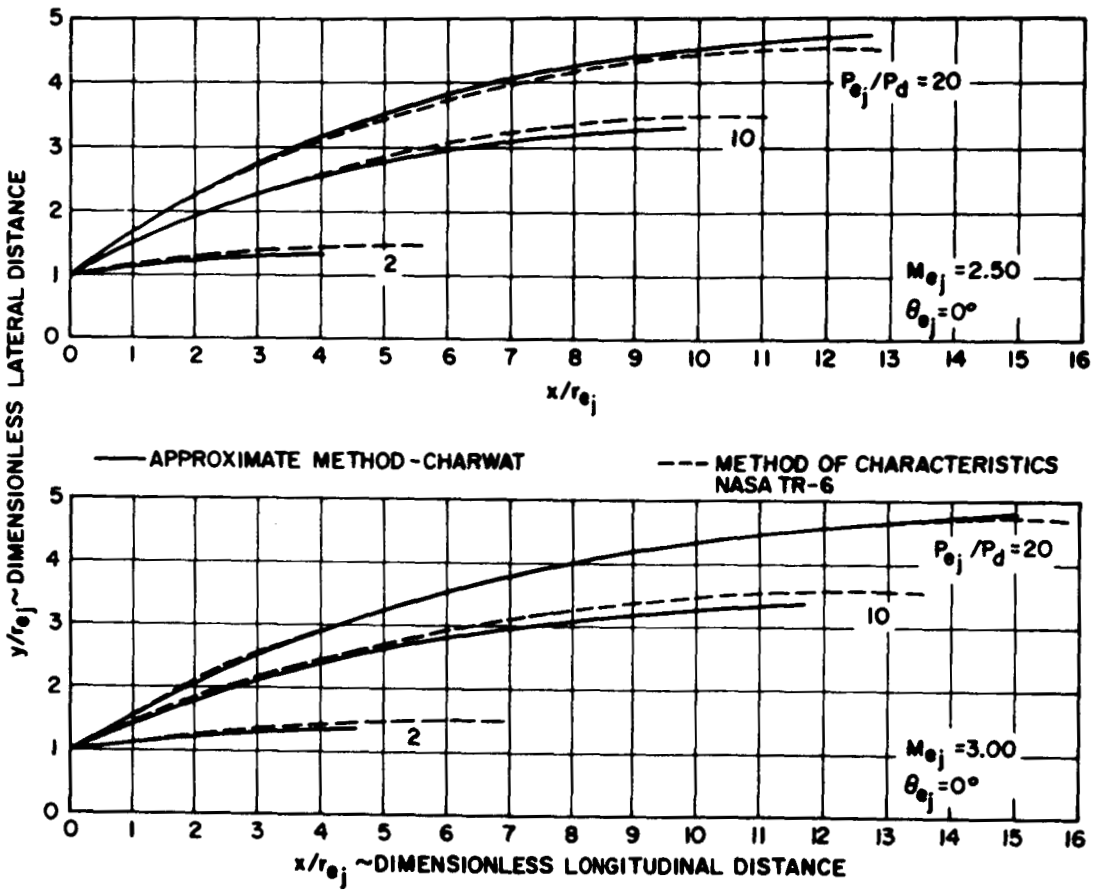

Figure 22. Comparison of Charwats' approximate method with method of characteristic solutions $\theta_{e_j} = \theta^{o}$, $M_{e_j} = 2.5$ and 3.0.

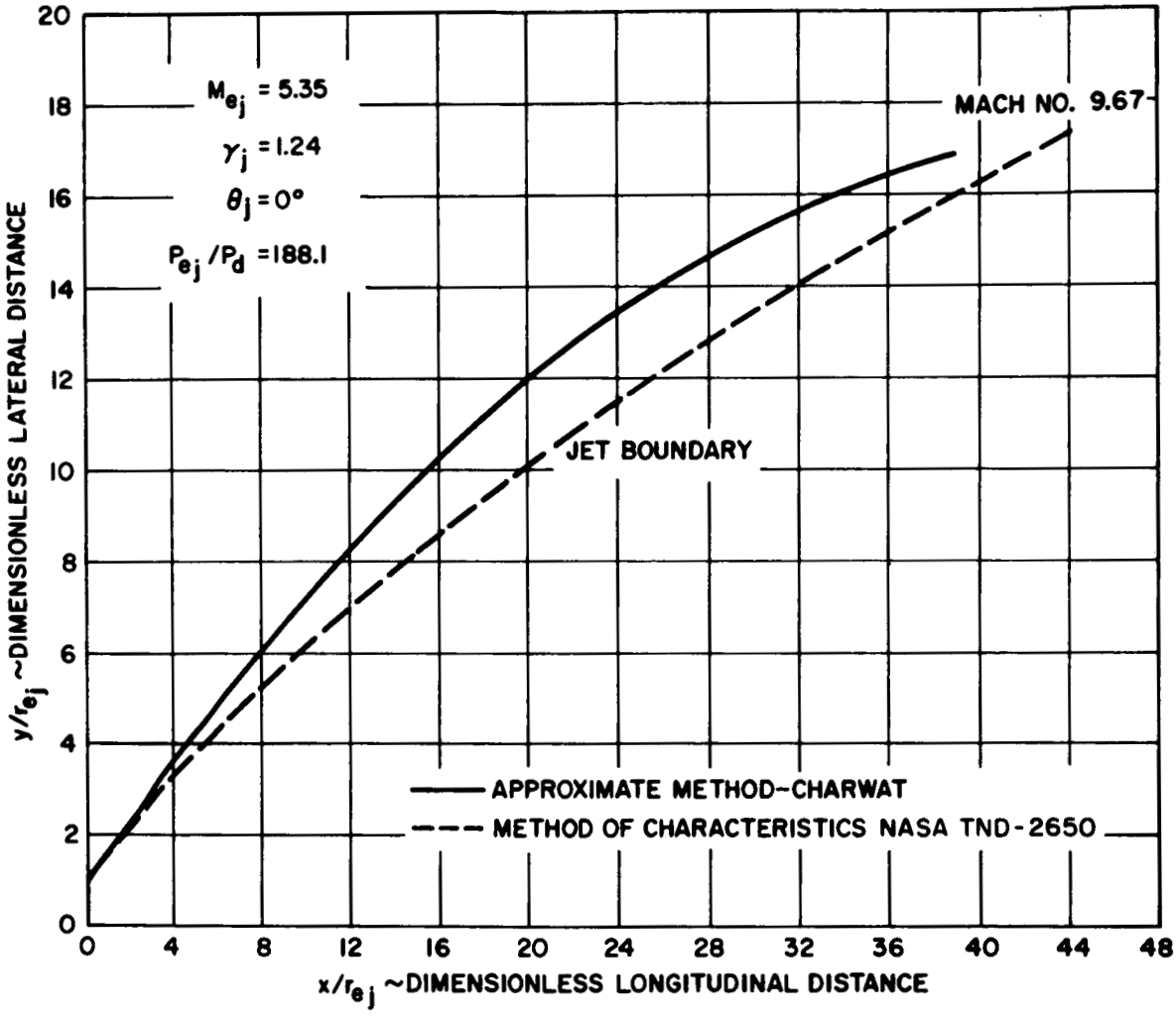

Figure 23. Comparison of approximate method with characteristic solutions, $\theta_{e_j} = 0^{\circ}$, $M_{e_j} = 5.35$, $= P_{e_j}/P_d = 188.1$.

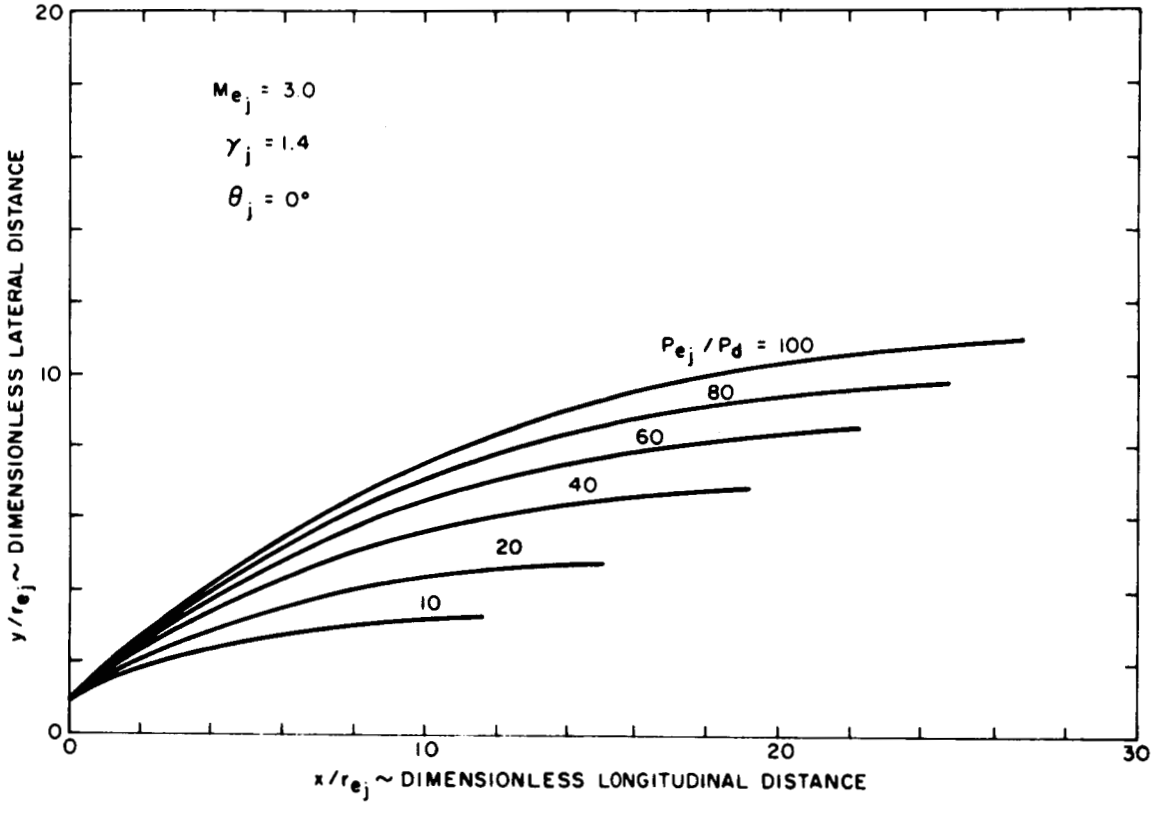

Figure 24. Jet boundary locations for study configuration $M_{e_j} = 3.0$, $\gamma_j = 1.4$, $\theta_j = 0^o$.

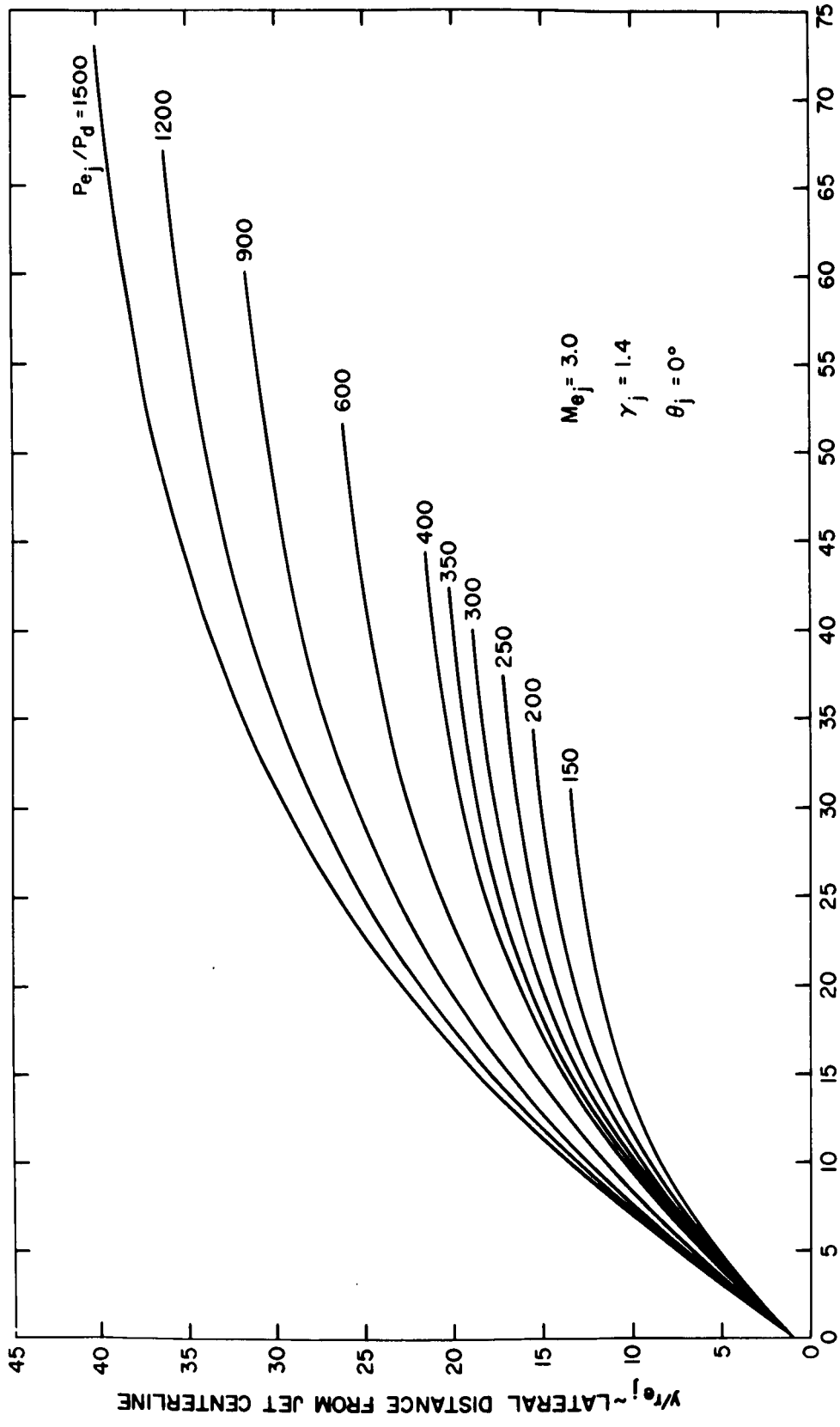

Figure 25. Jet boundary locations for study configuration, $M_{e_j} = 3.0$, $\gamma_j = 1.4$, $\theta_j = 0$.

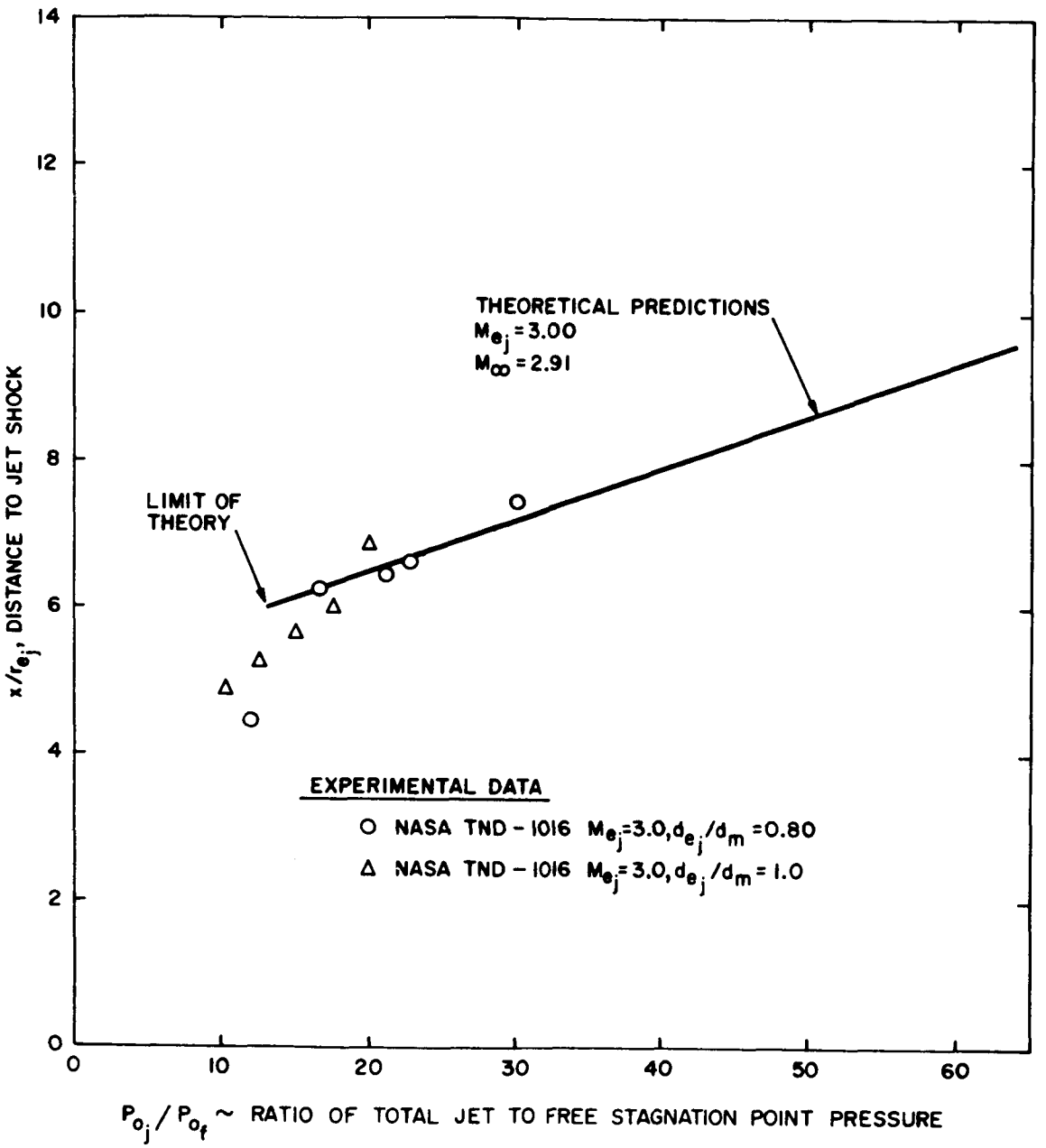

Figure 26. Comparison of theoretical location of jet shock with experimental data for jet into oncoming flow.

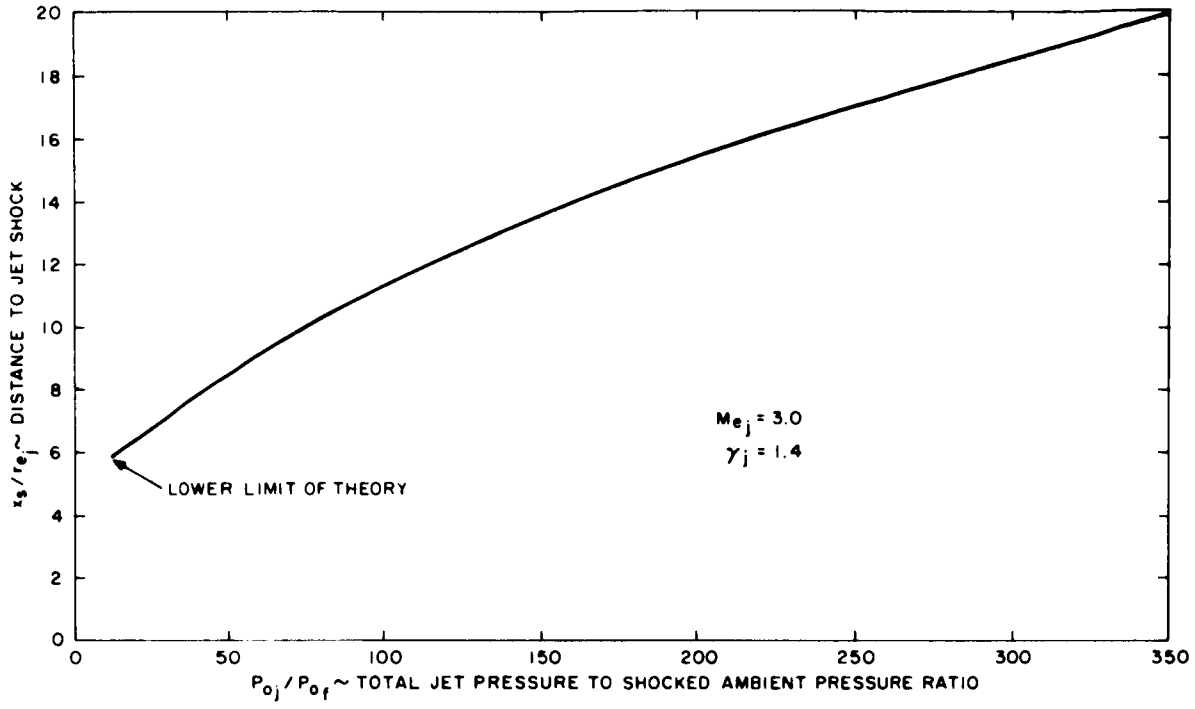

Figure 27. Jet terminal shock location.

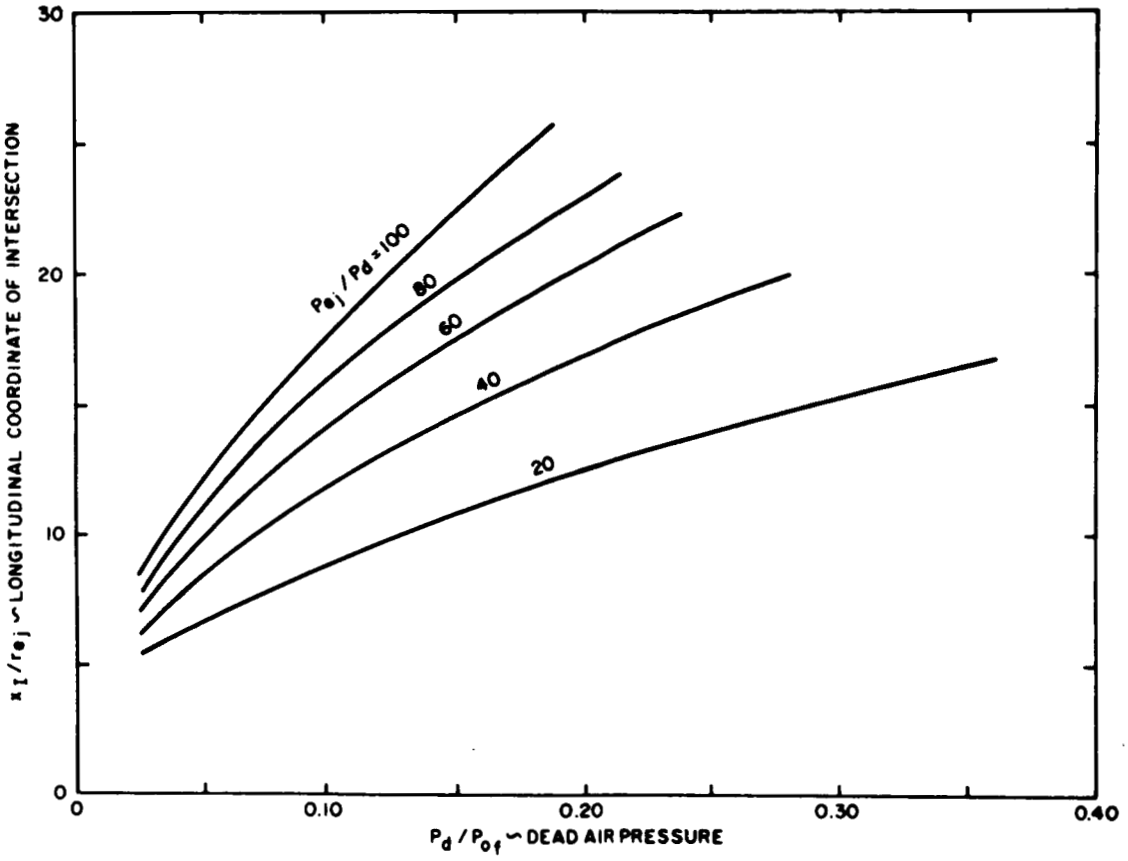

Figure 28. Longitudinal coordinate for intersection of jet boundary and terminal shock.

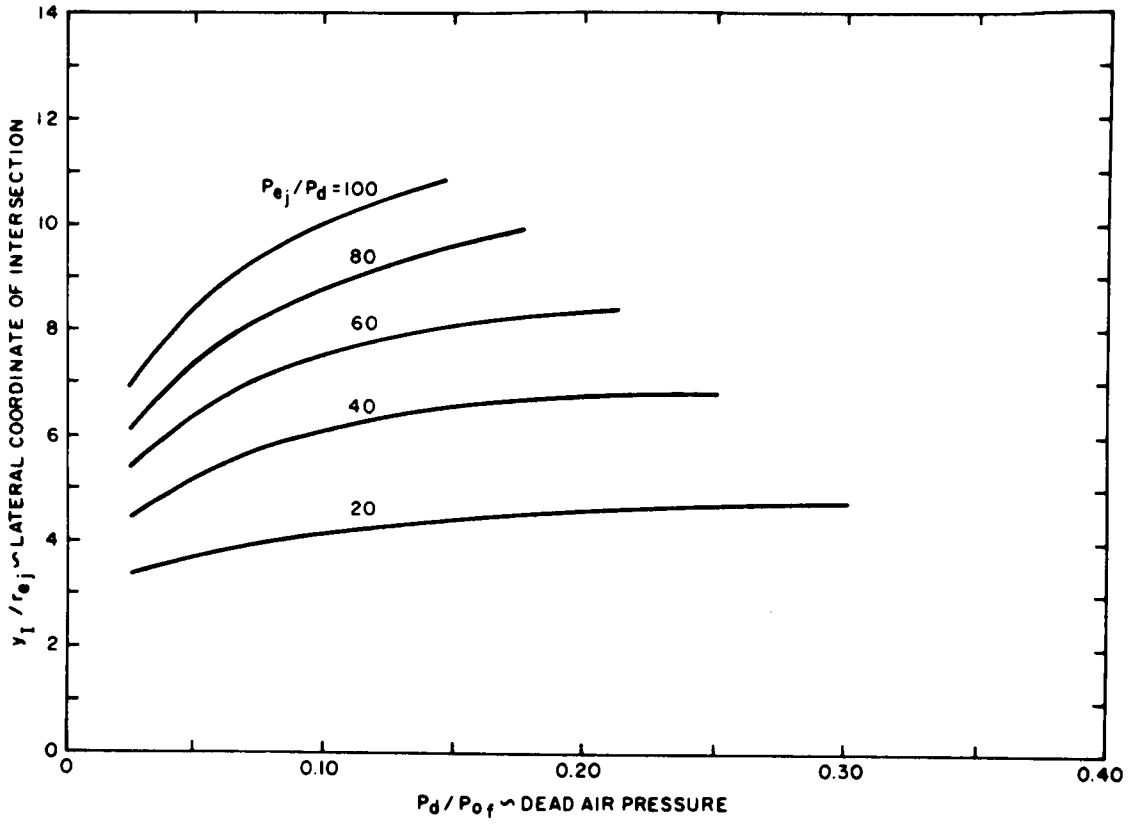

Figure 29. Lateral coordinate for interaction of jet boundary and terminal shock.

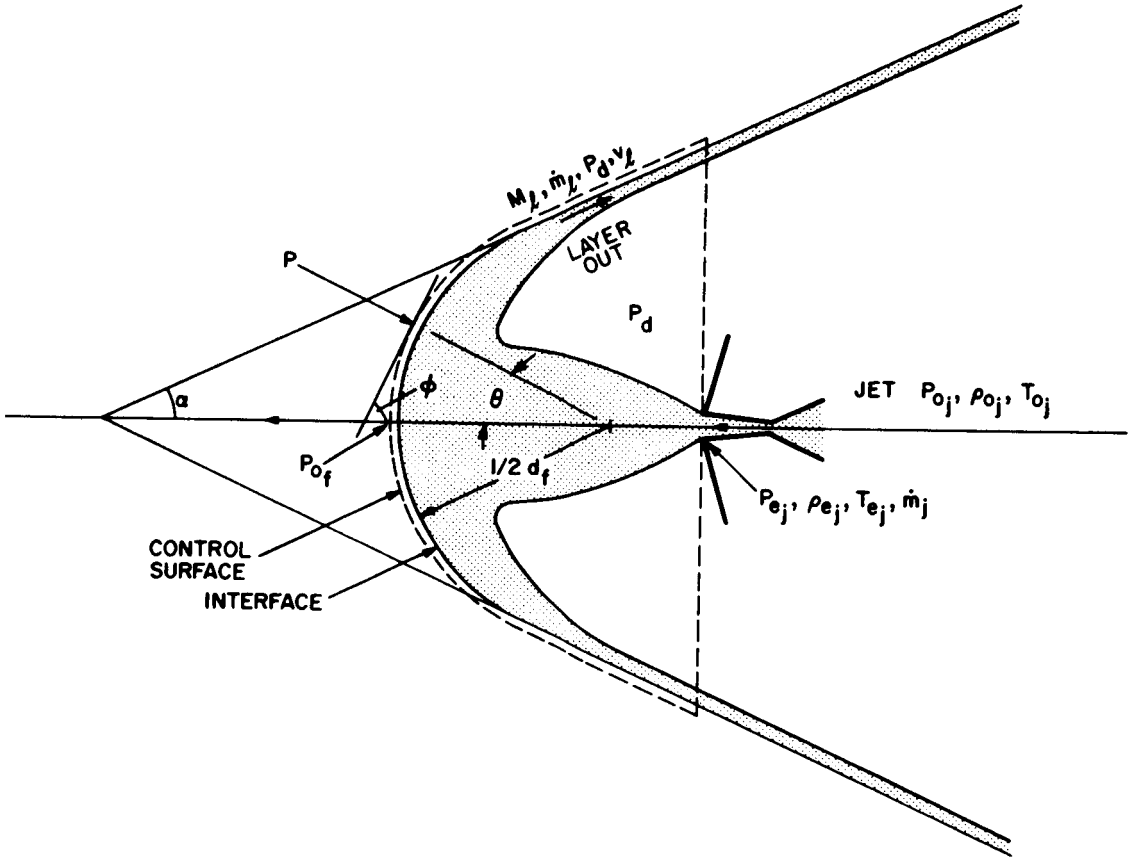

Figure 30. Control surface used for momentum balance.

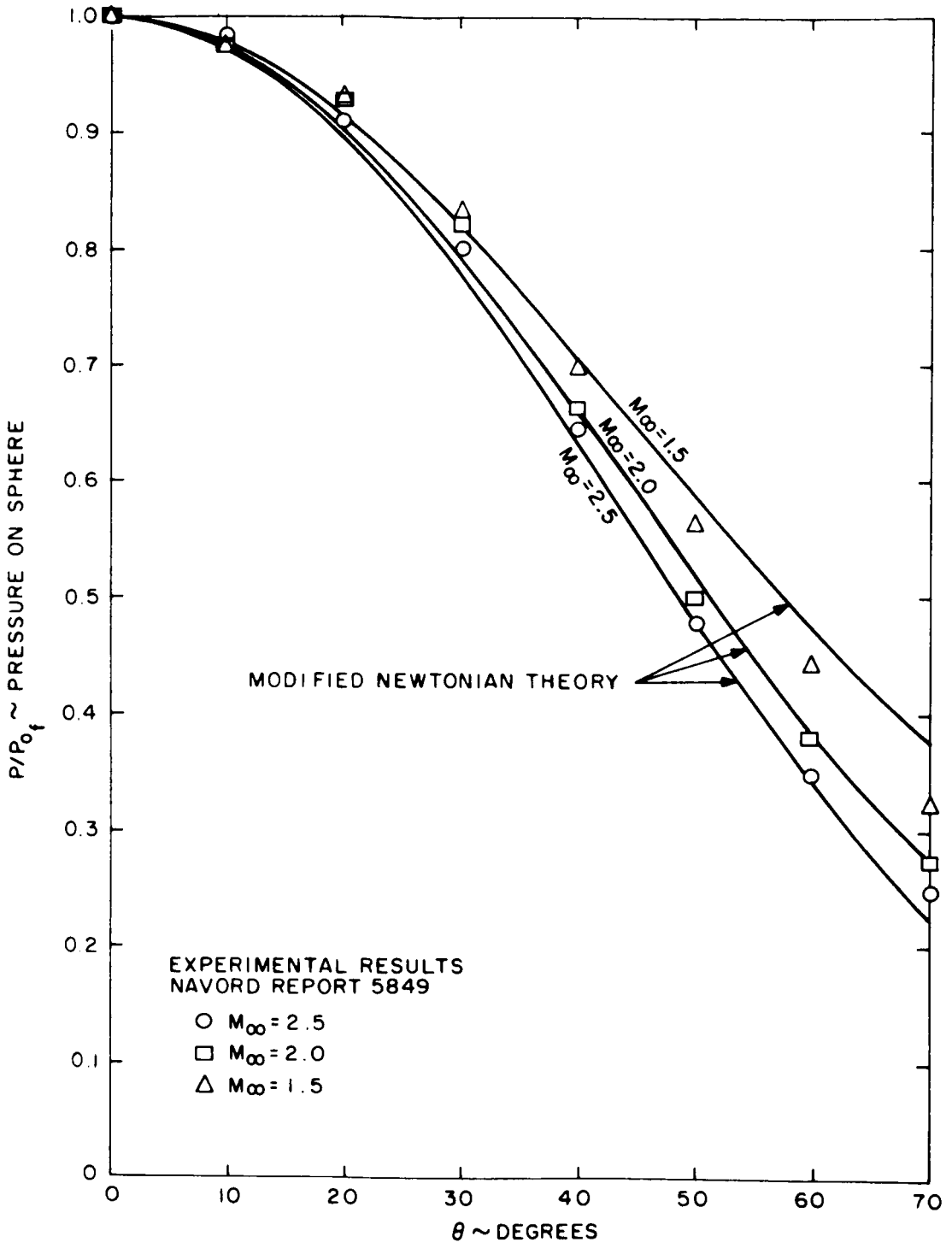

Figure 31. Pressure on spherical interface.

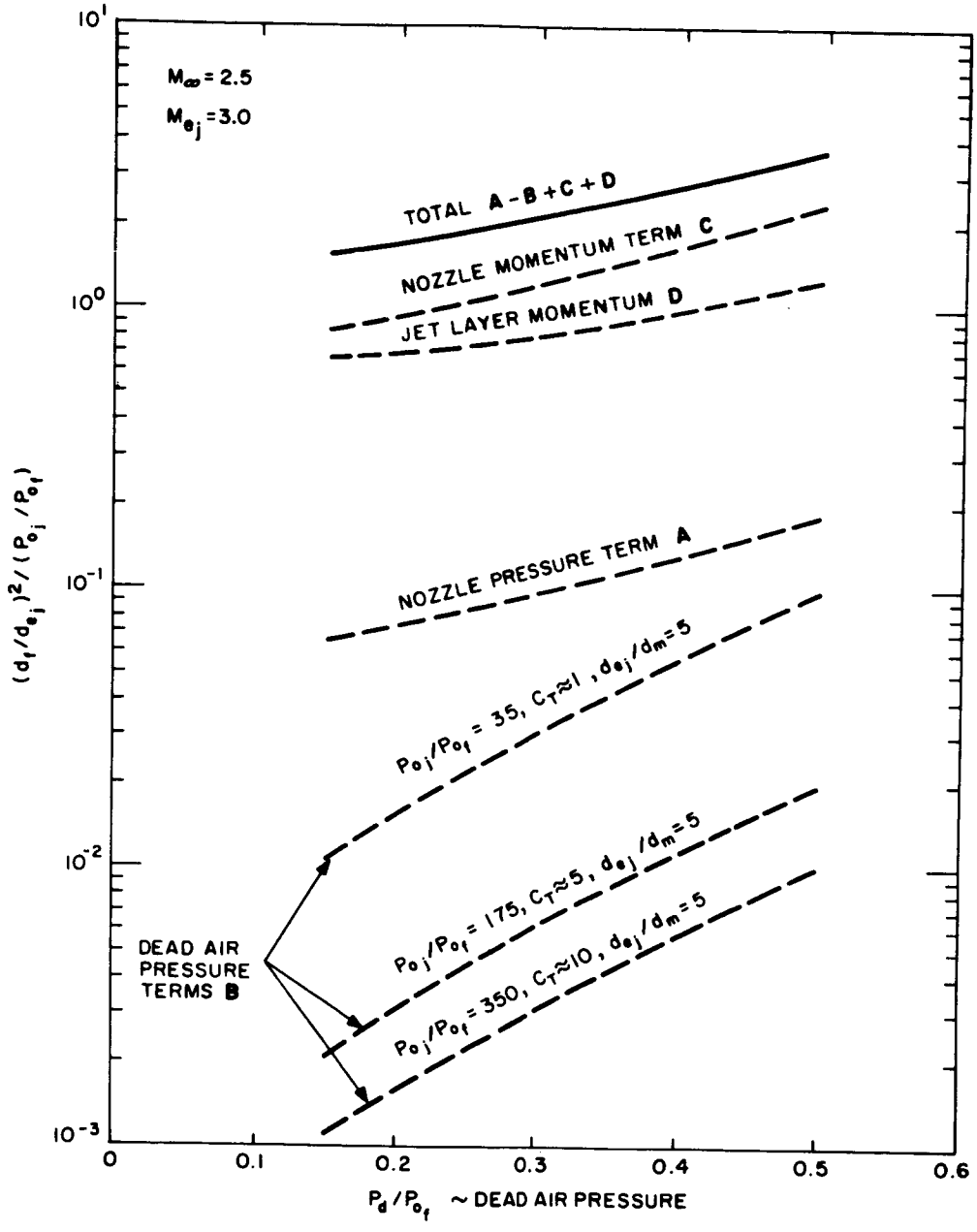

Figure 32. Diameter of blunting sphere, $M_\infty = 2.5$, $M_{e_j} = 3.0$.

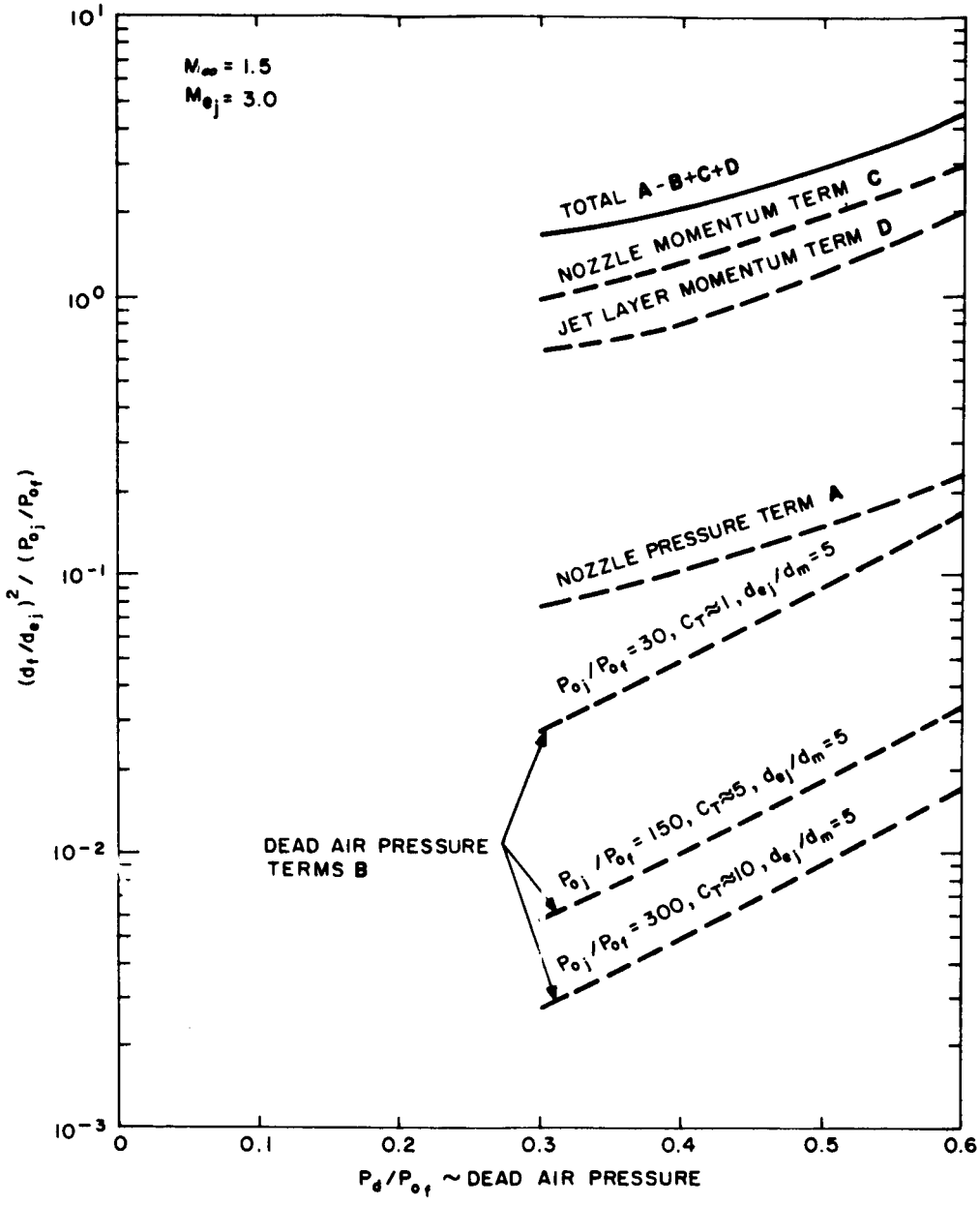

Figure 33. Diameter of blunting sphere, $M_\infty = 1.5$, $M_{e_j} = 3.0$.

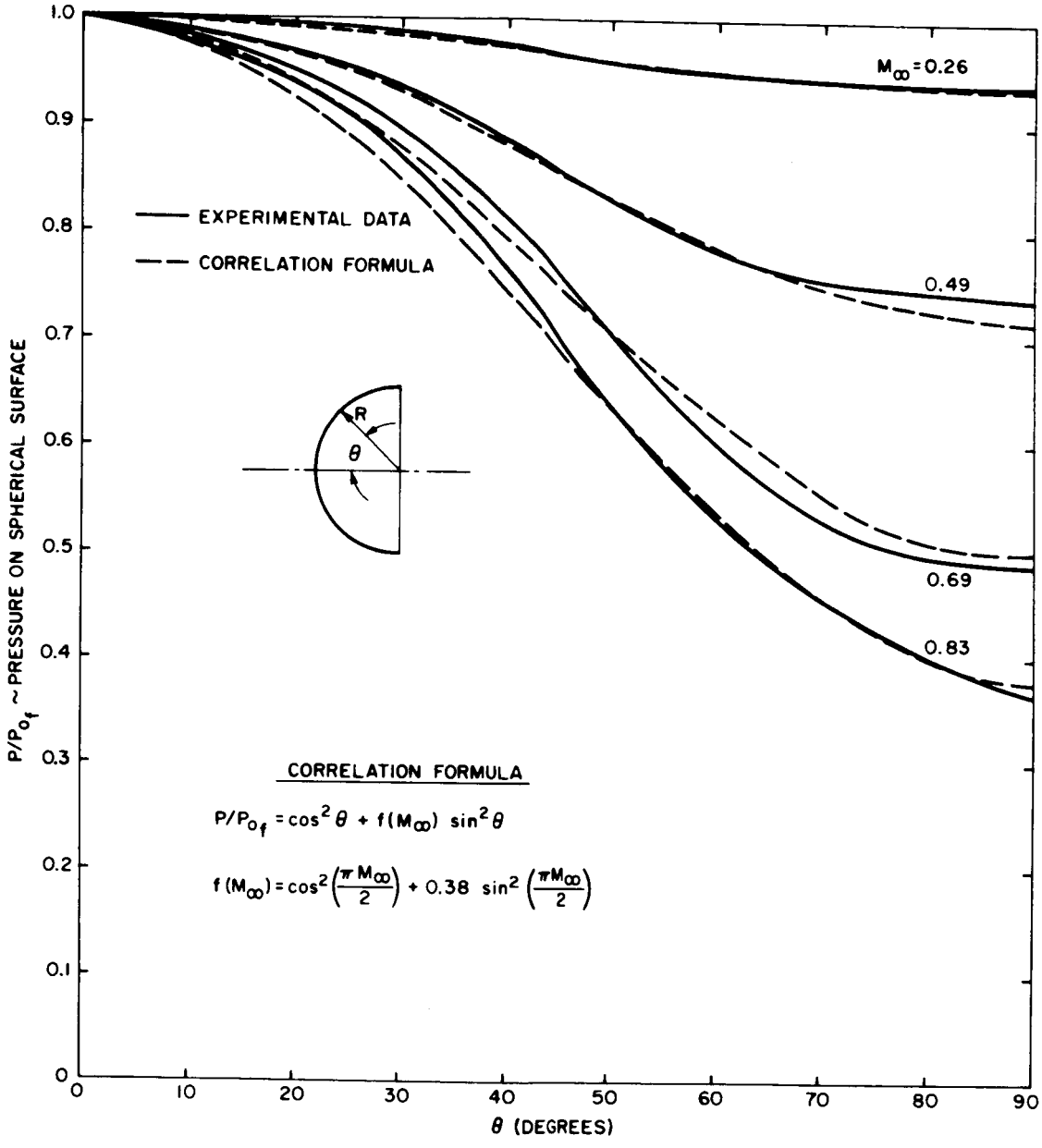

Figure 34. Subsonic pressure correlation.

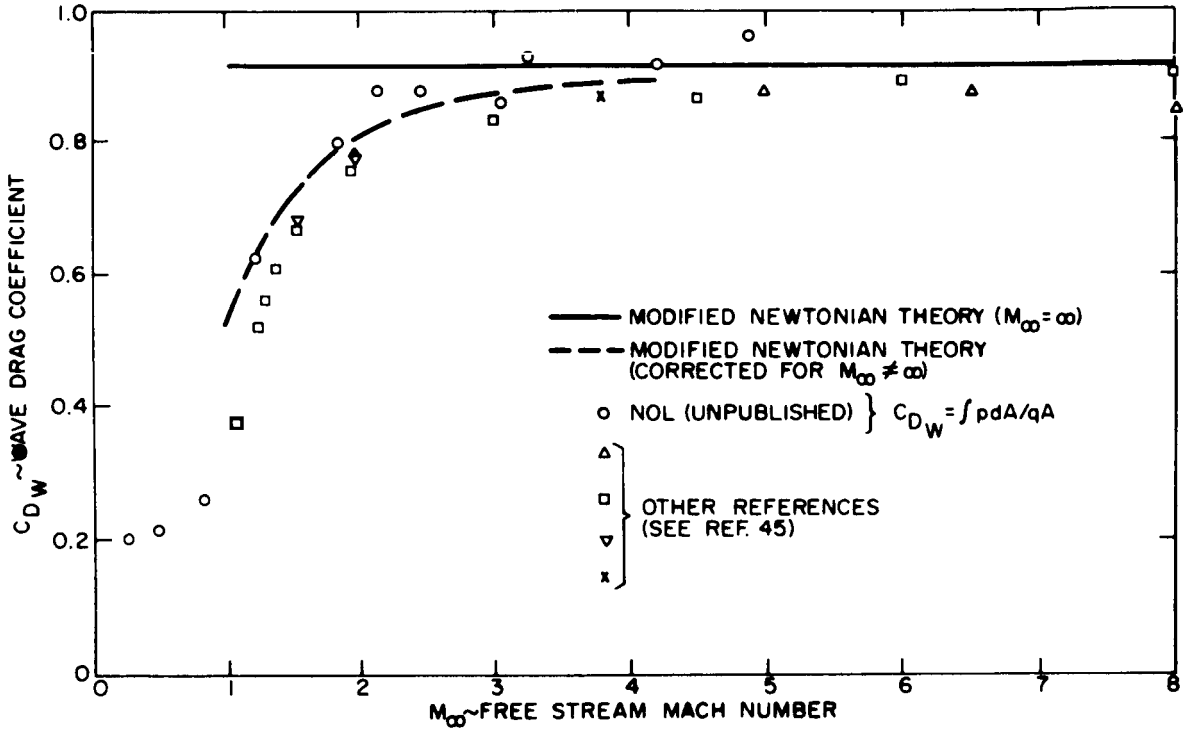

Figure 35. Wave drag coefficient for a hemisphere (Ref. 45).

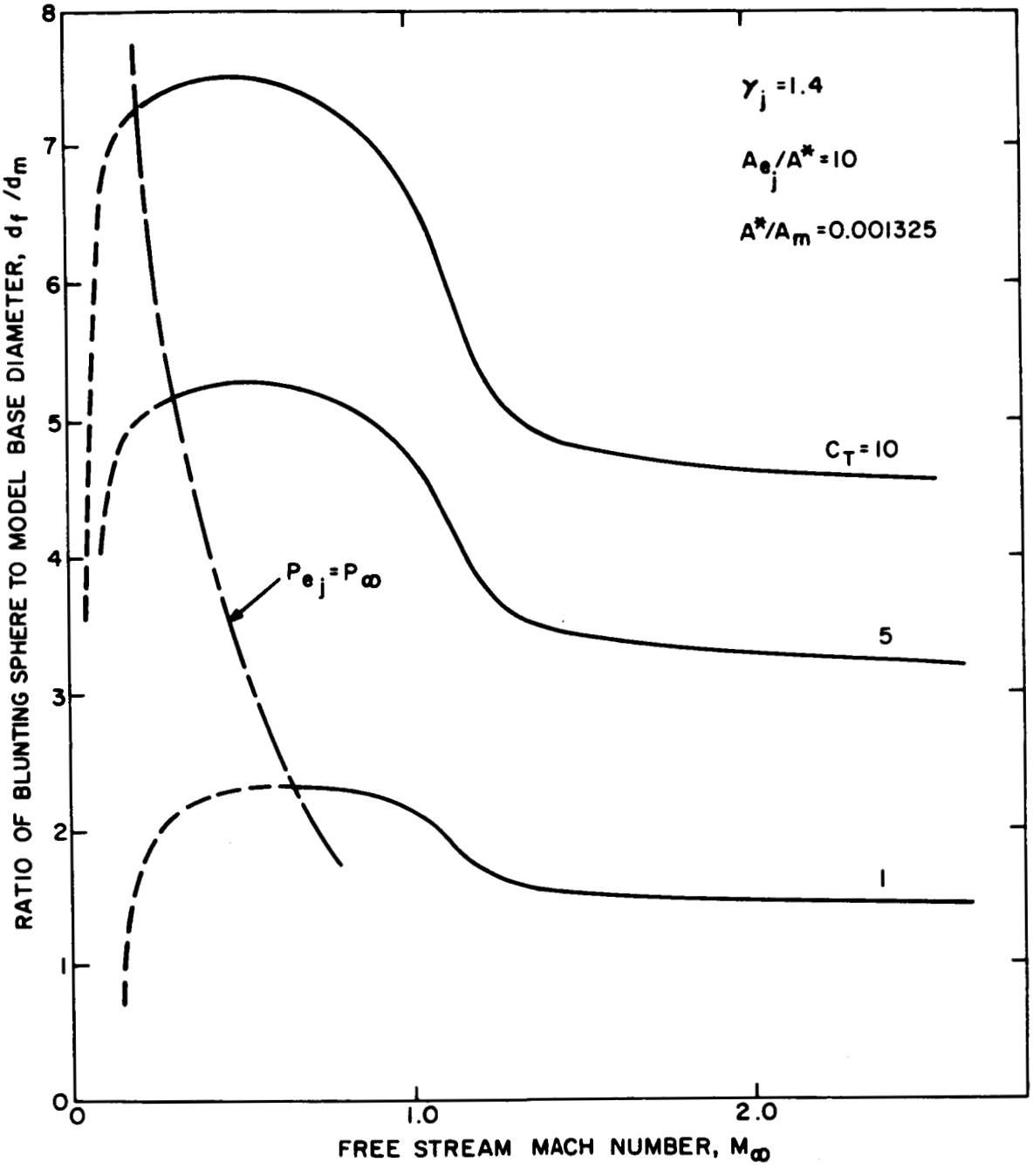

Figure 36. Variation of blunting sphere diameter with Mach number.

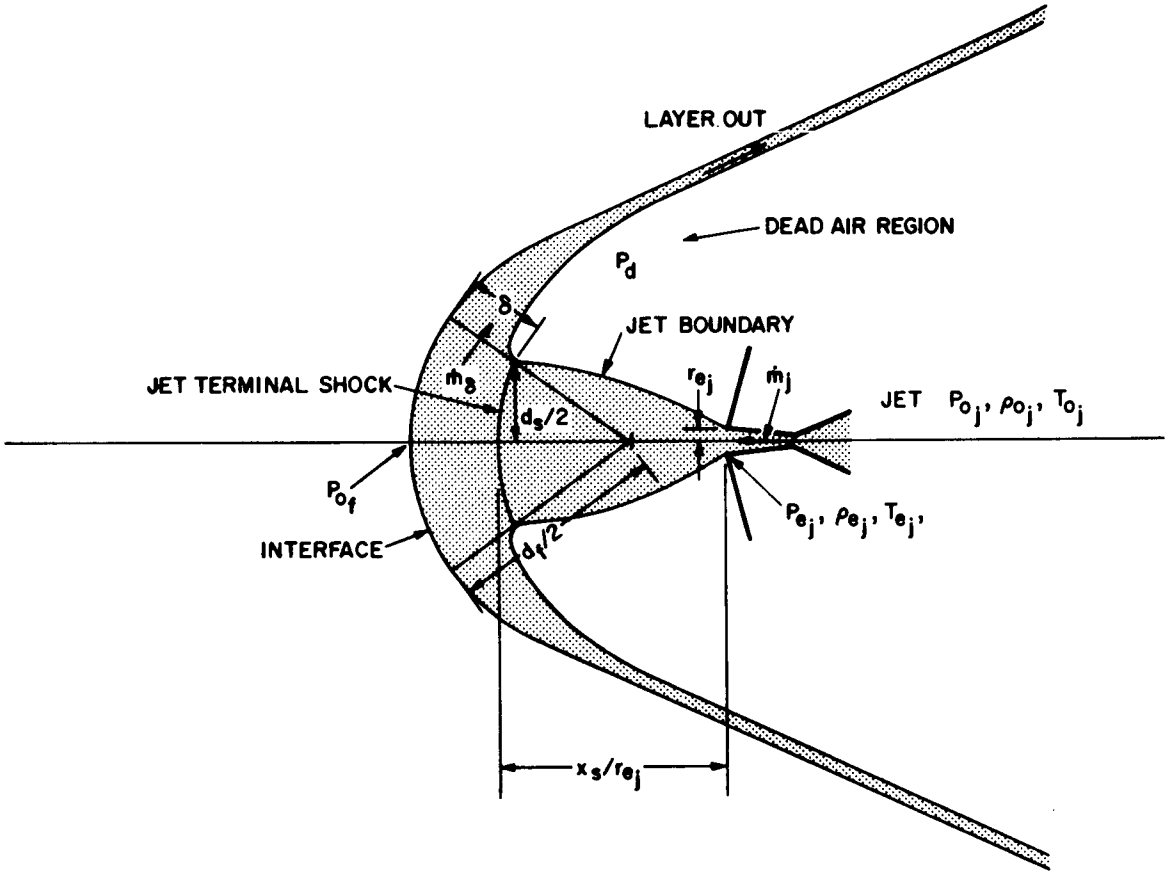

Figure 37. Mass balance geometry.

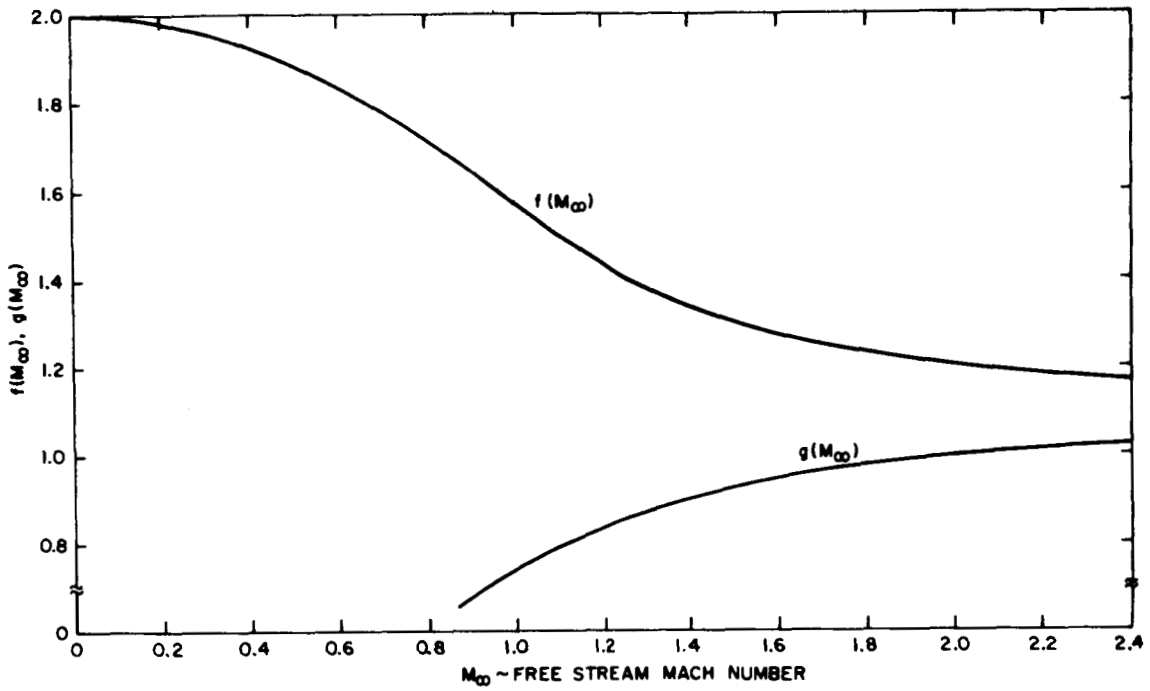

Figure 38. Pressure-ratio functions, $f(M_\infty)$, $g(M_\infty)$.

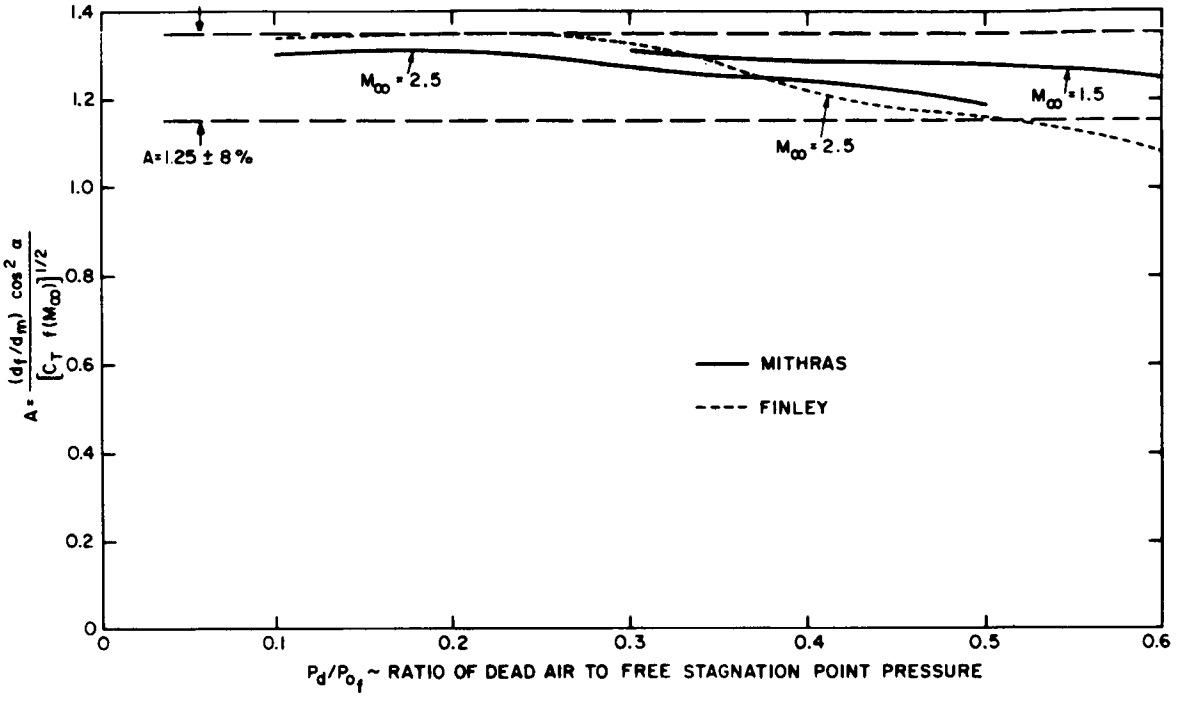

Figure 39. Correlation of blunting-sphere diameters.

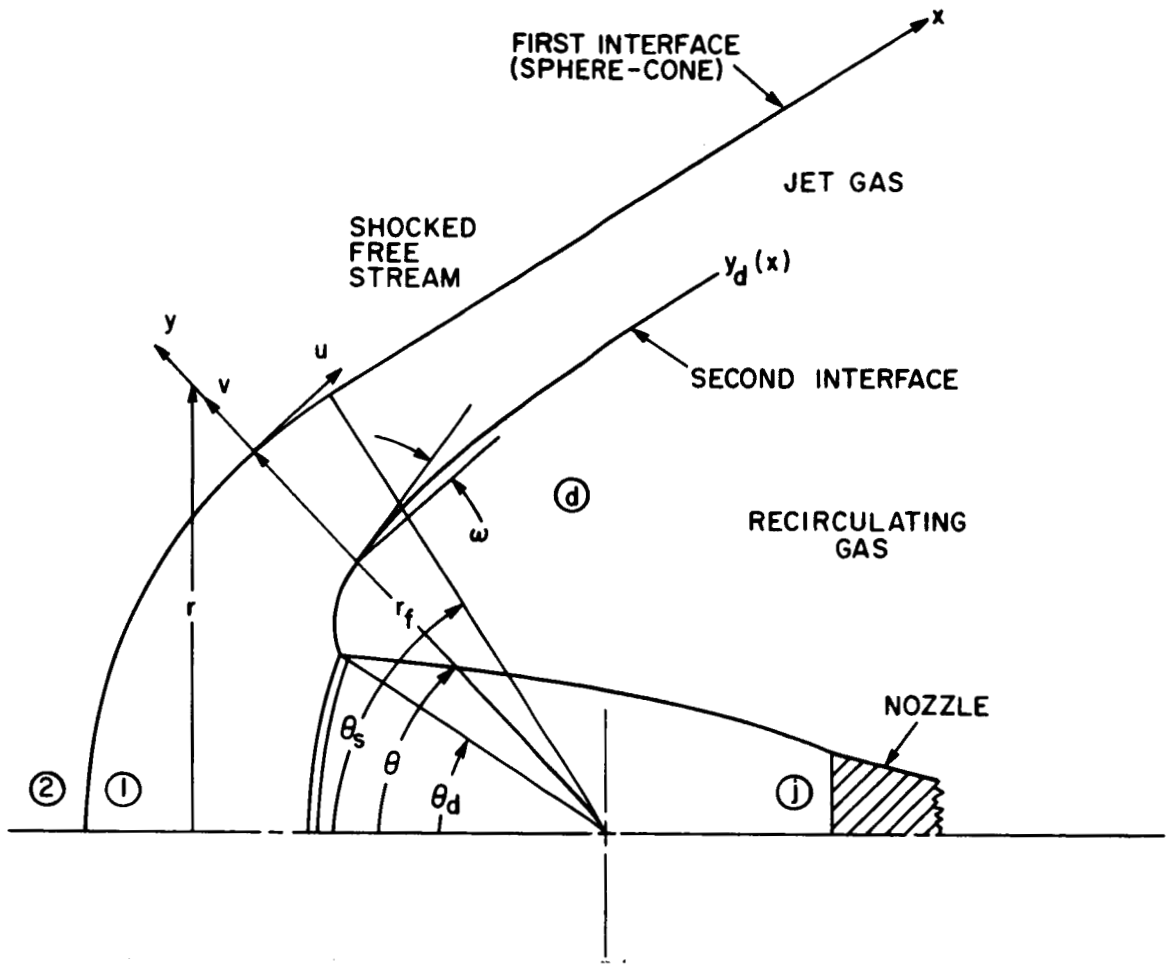

Figure 40. Geometry of interface location.

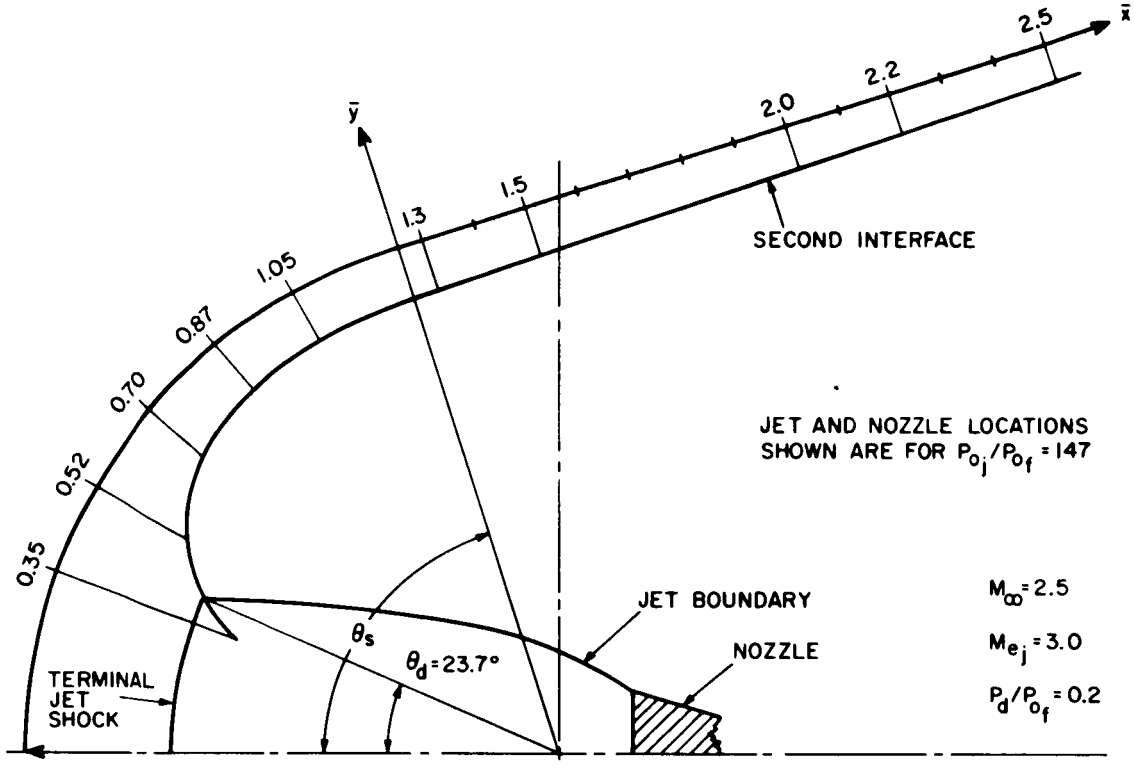

Figure 41. Location of second interface.

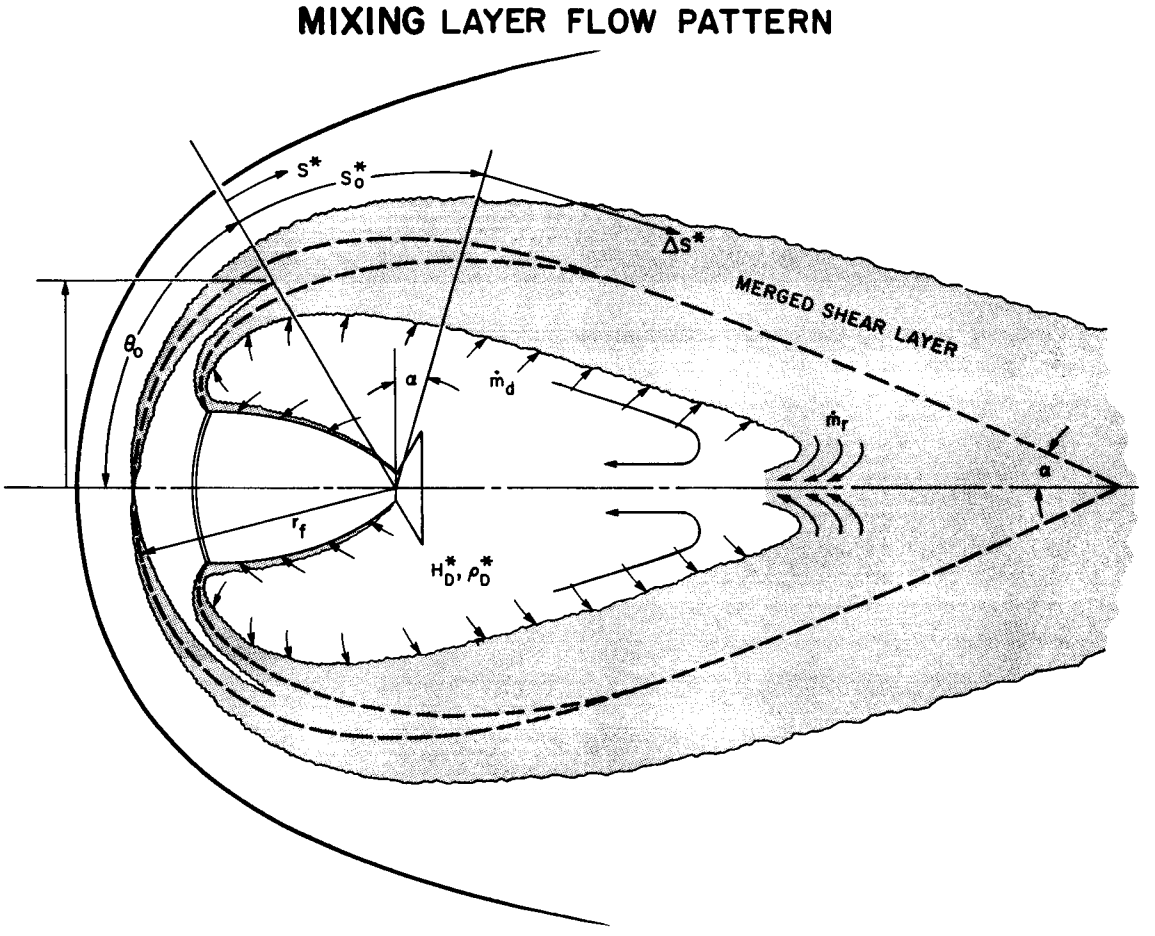

Figure 42. Mixing layer flow pattern.

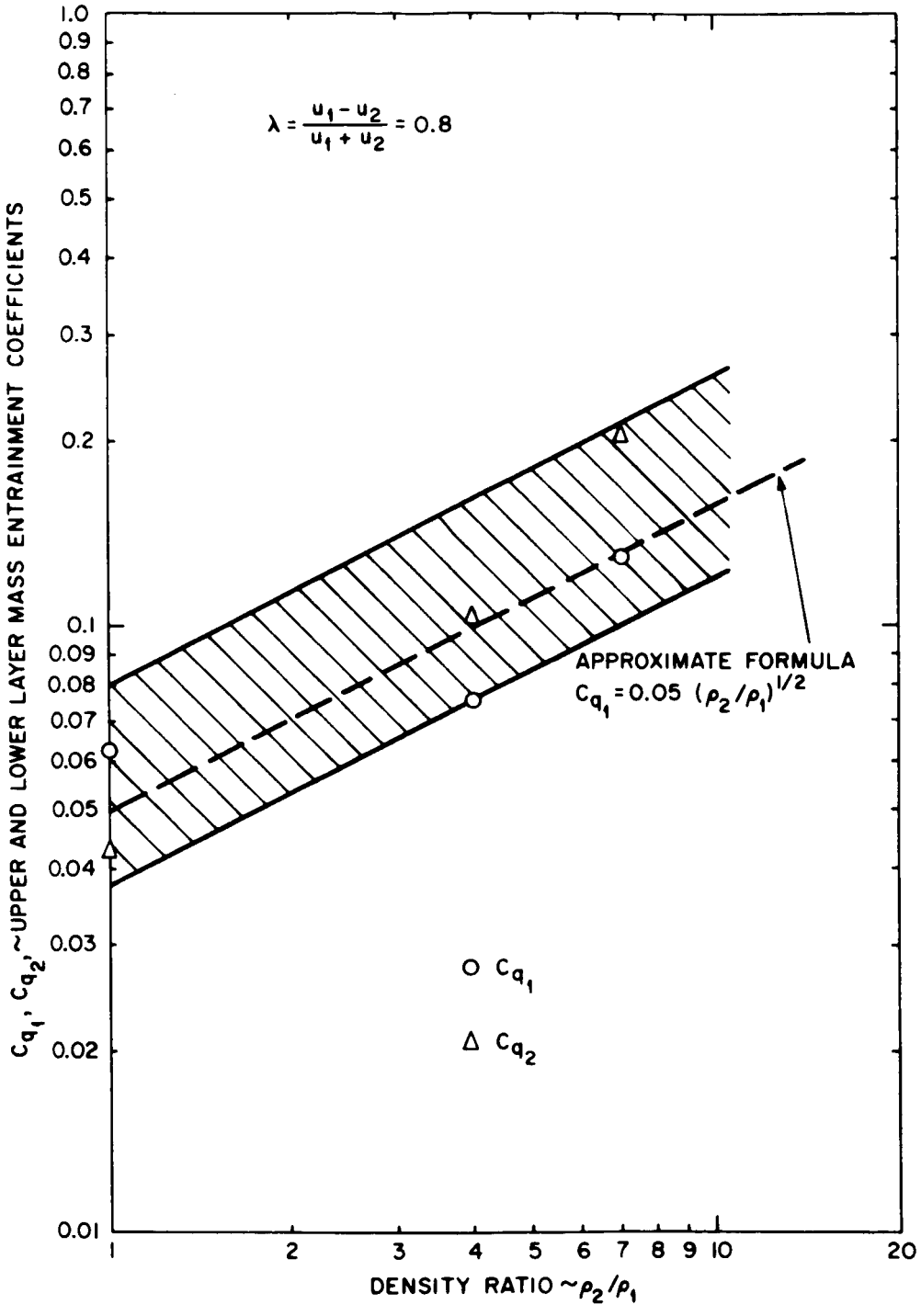

Figure 43. Mass entrainment coefficient as a function of density ratio for fixed velocity ratio.

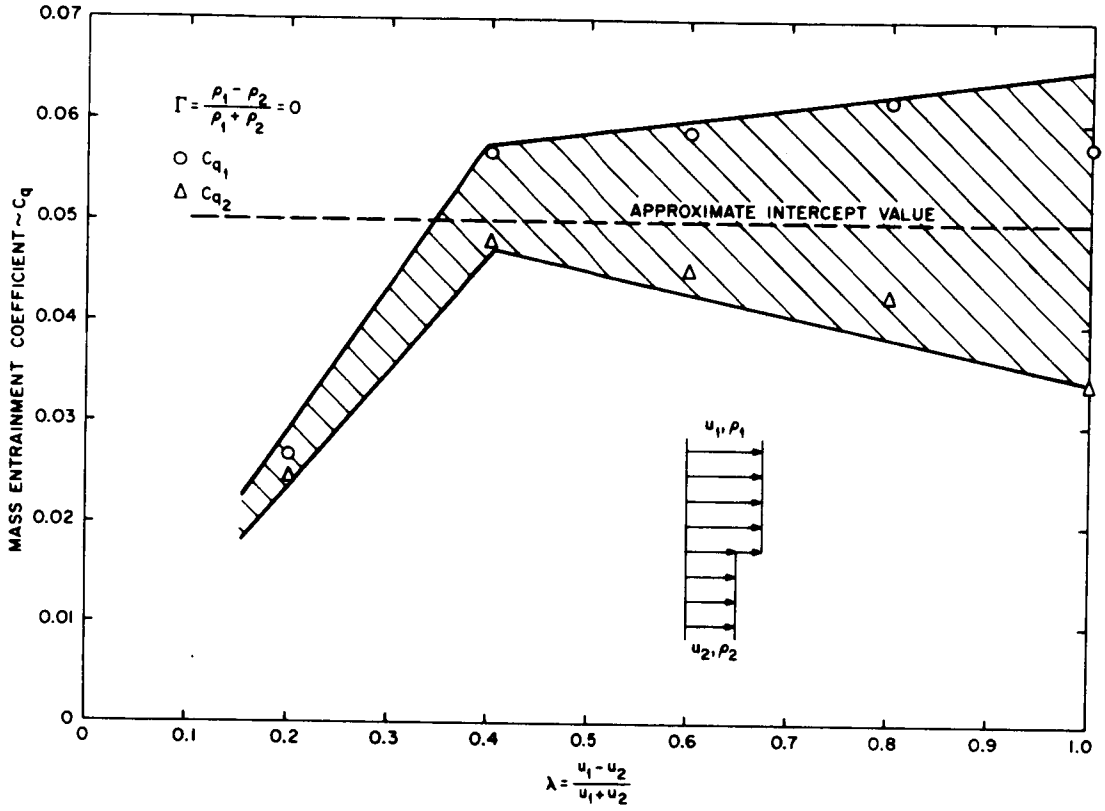

Figure 44. Mass entrainment coefficients as a function of velocity ratio for equal densities.

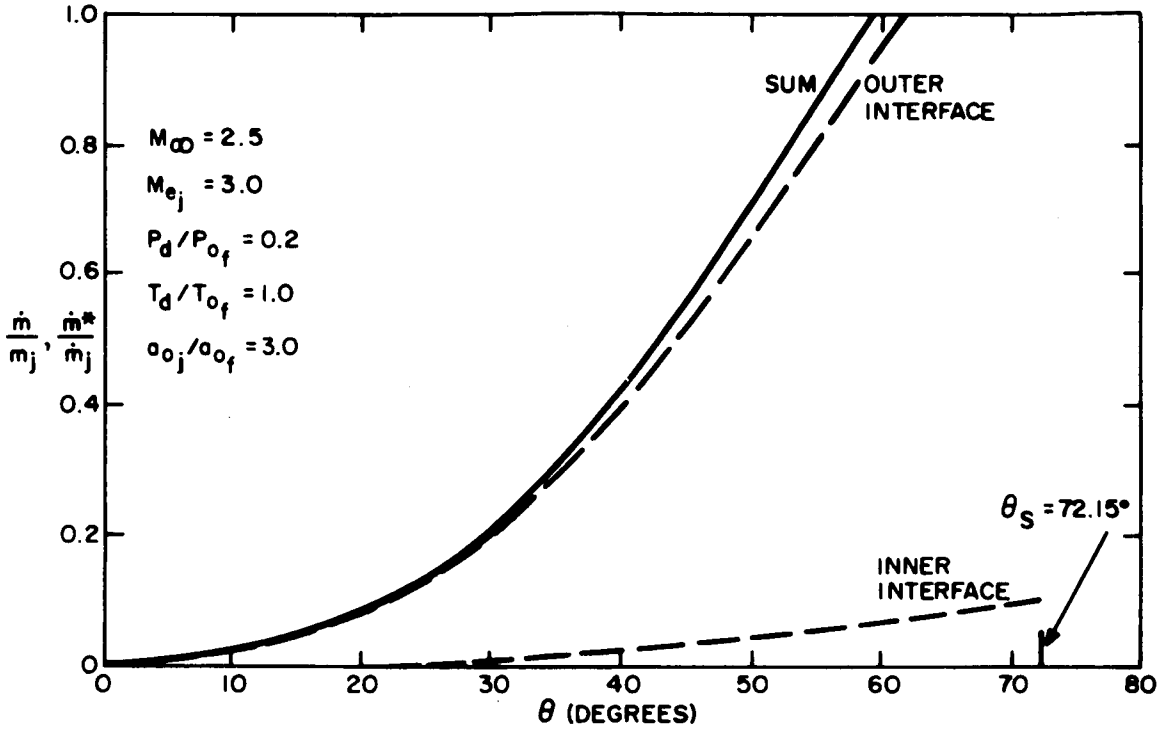

Figure 45. Ratio of entrained mass flux to jet mass flux.

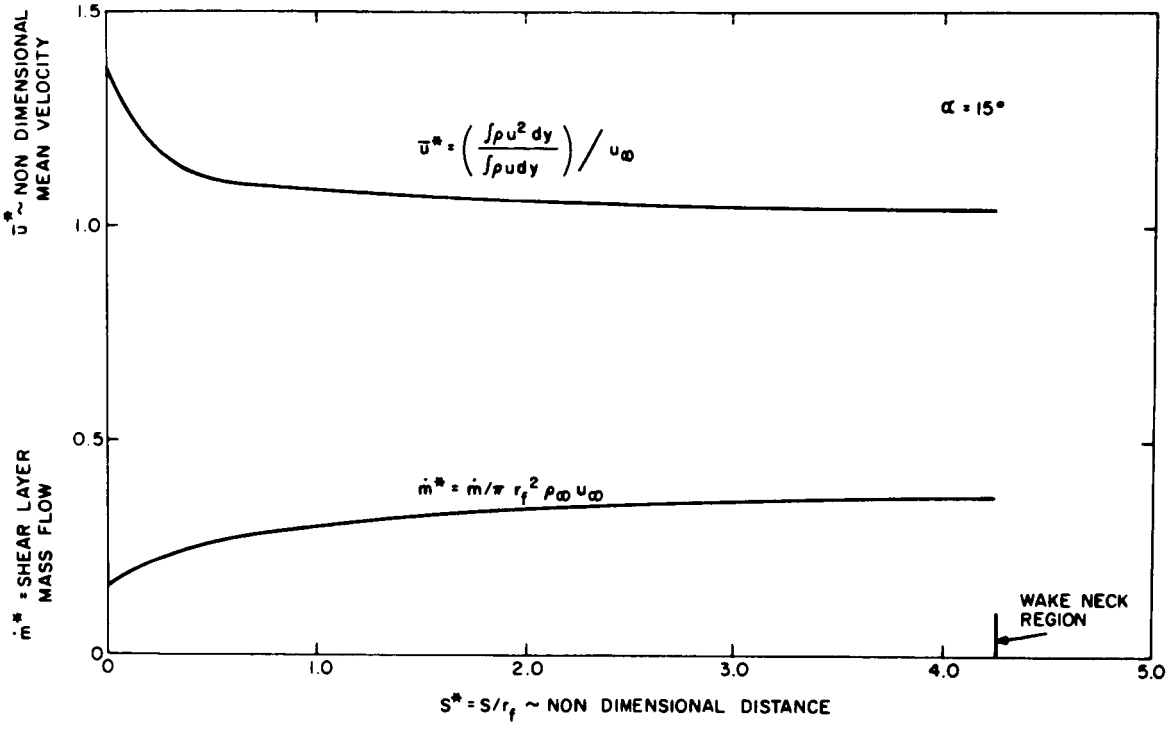

Figure 46. Variation of mean velocity and entrained fluid along the merged shear layer.

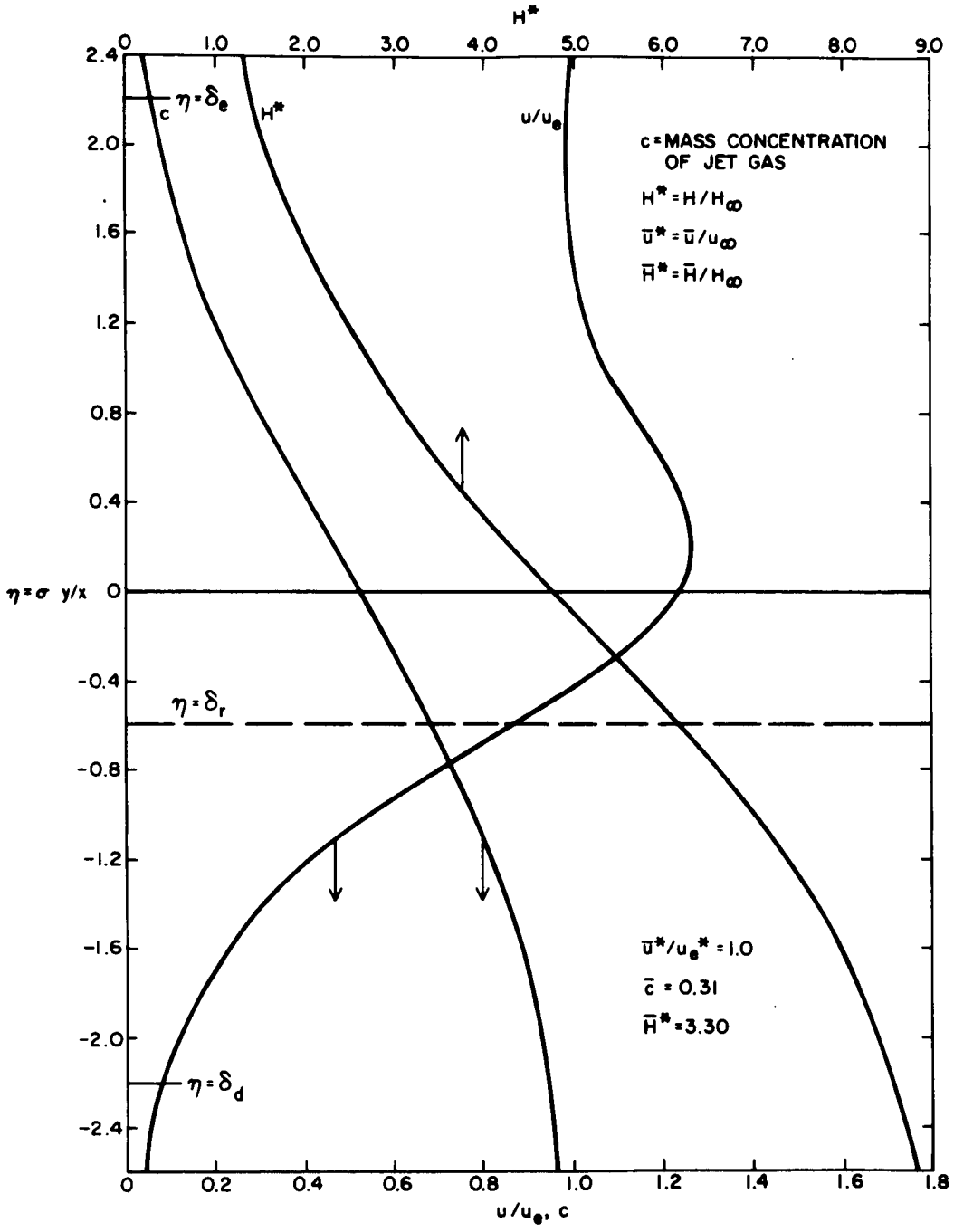

Figure 47. Velocity, enthalpy, and concentration profiles at Wake Neck.

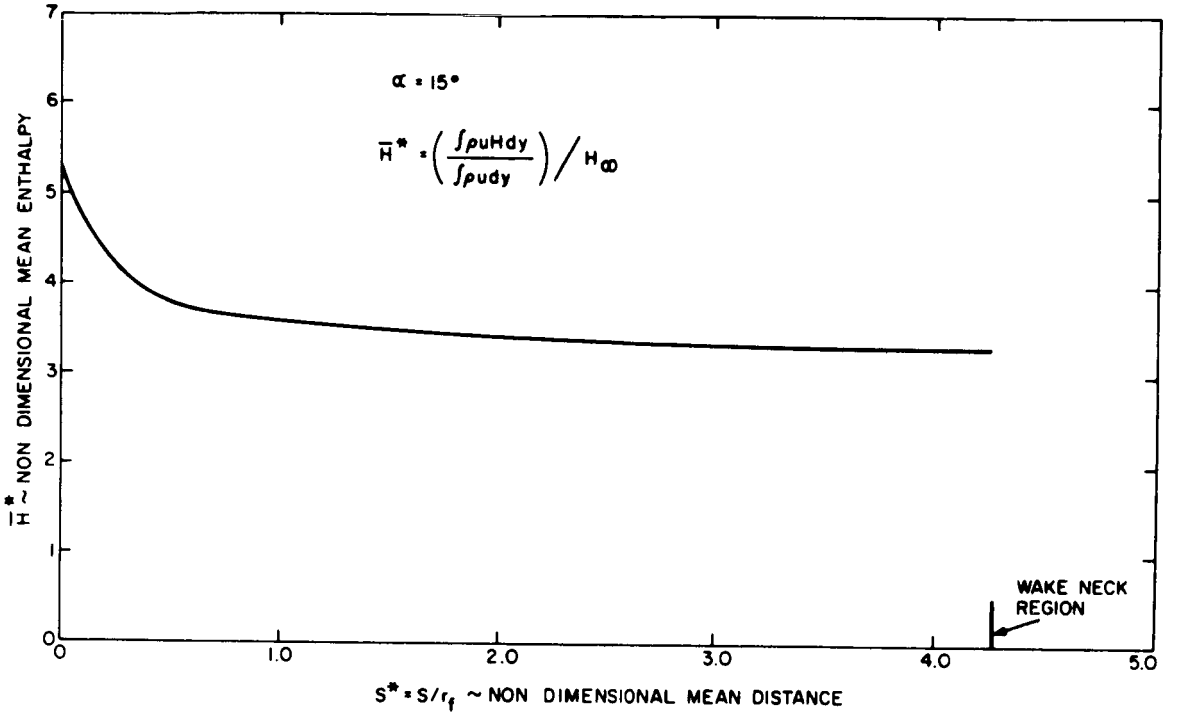

Figure 48. Variation of mean enthalpy along the merged shear layer.

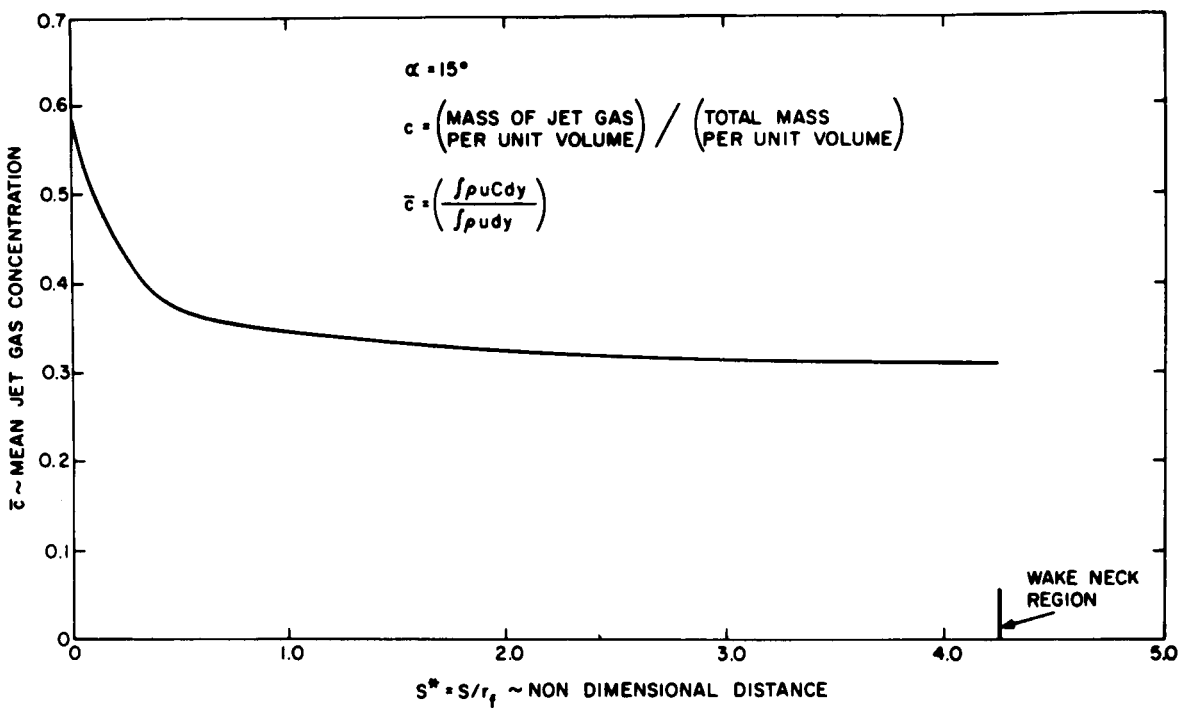

Figure 49. Variation of mean jet gas concentration along the merged shear layer.

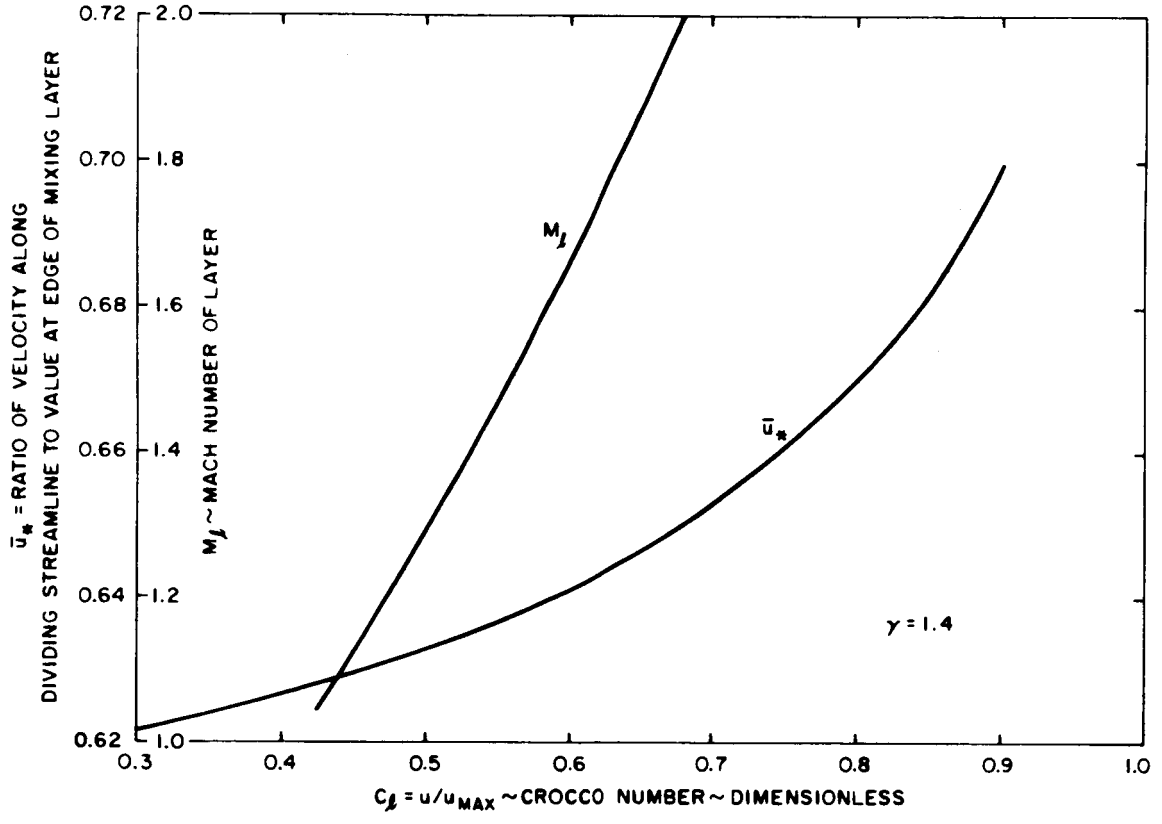

Figure 50. Korst's predictions applied to the turbulent exhaust layer.

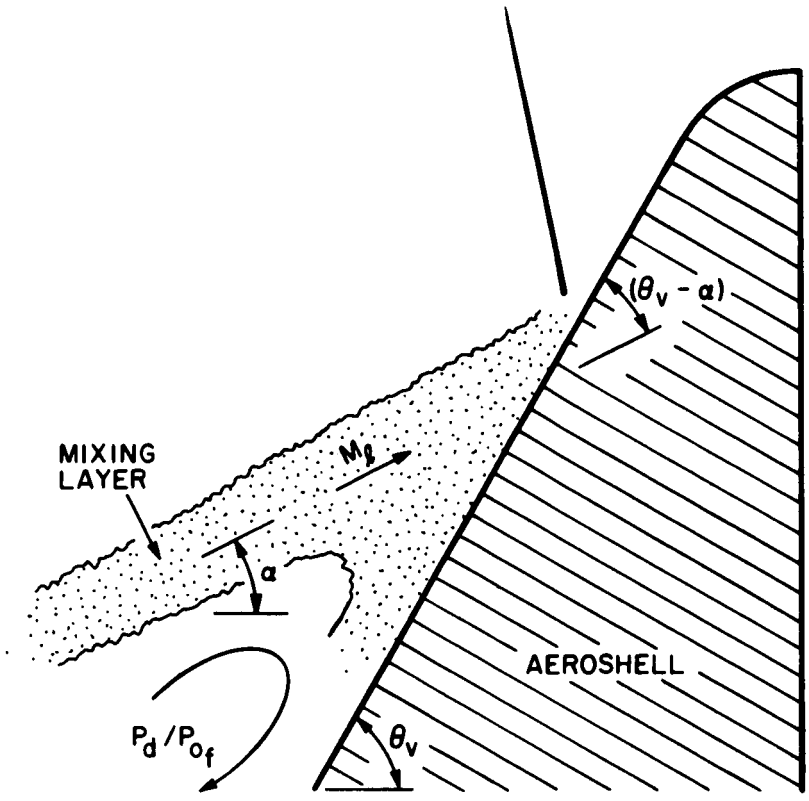

Figure 51. Relative geometry of mixing layer - aeroshell surface.

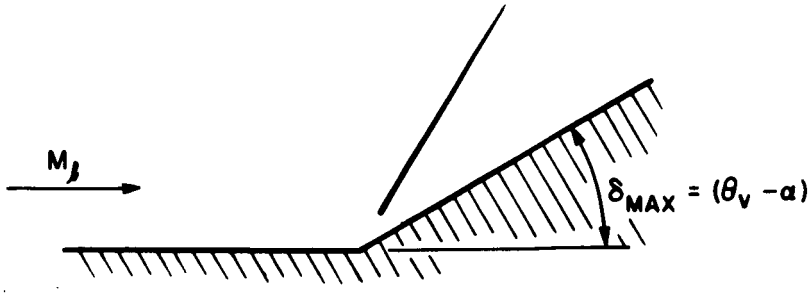

Figure 52. Equivalent flow.

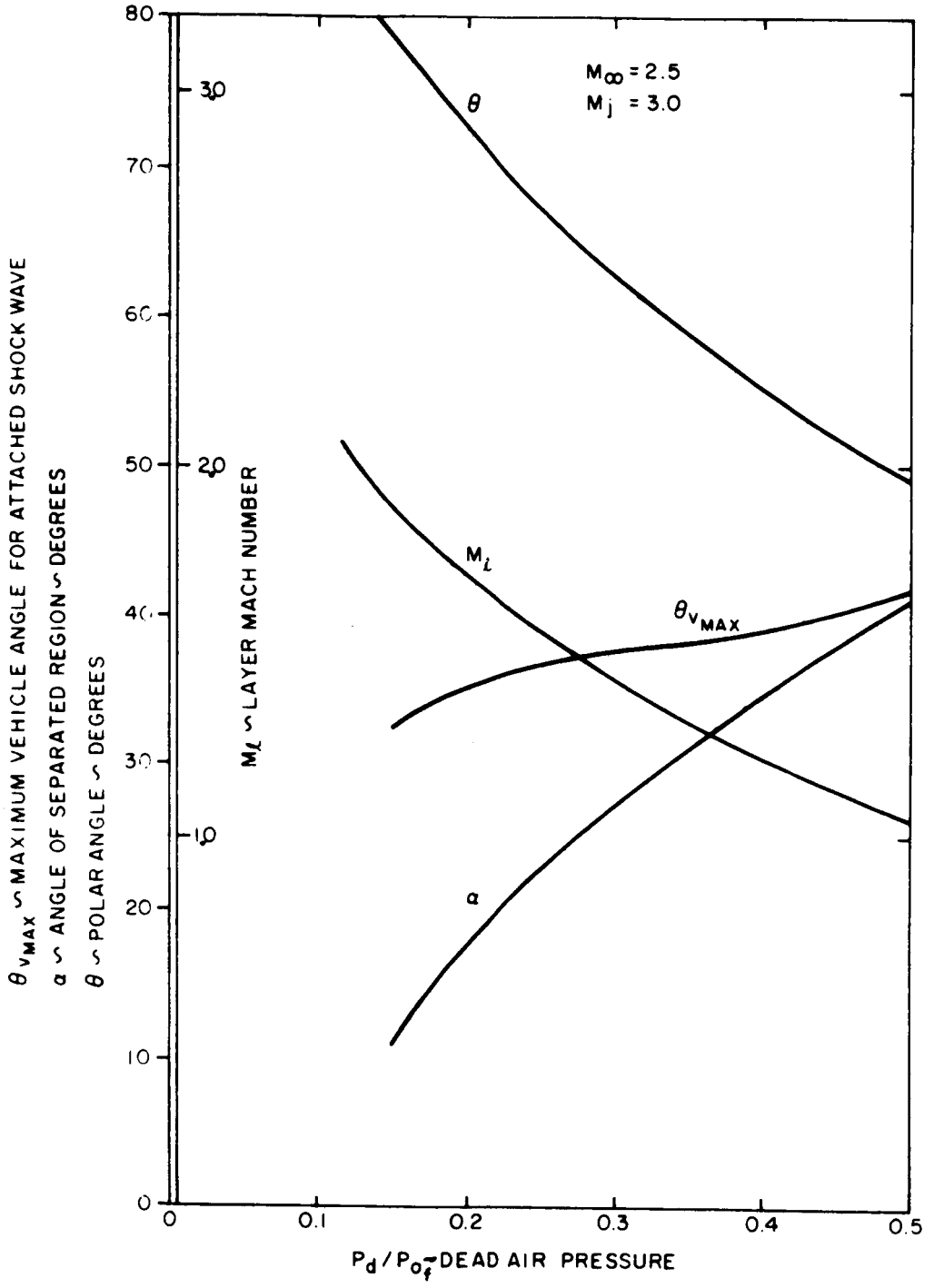

Figure 53. Characteristics of mixing layer.

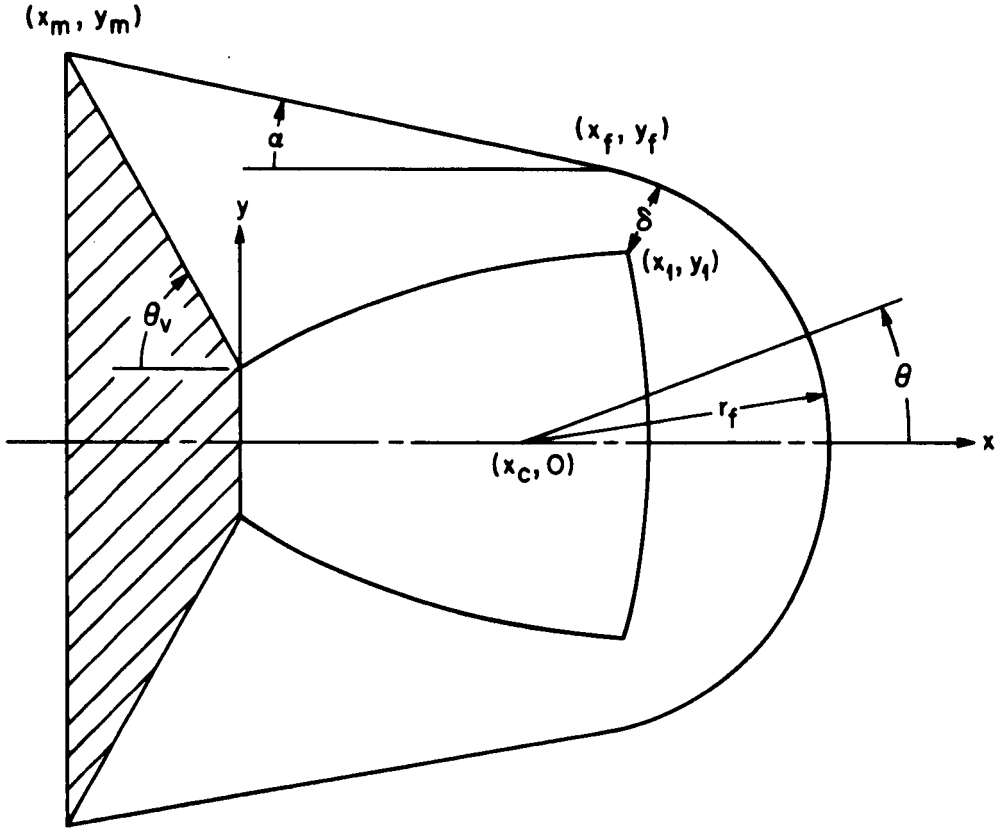

Figure 54. Geometry for shoulder attachment.

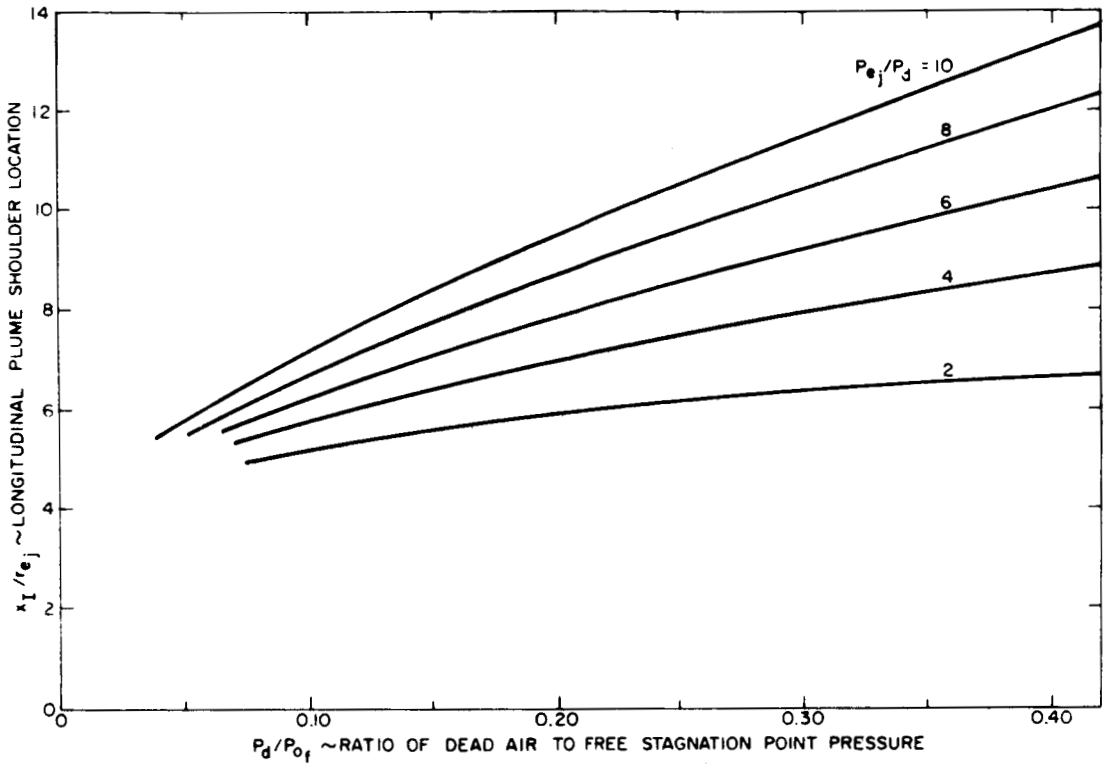

Figure 55. Longitudinal plume shoulder location.

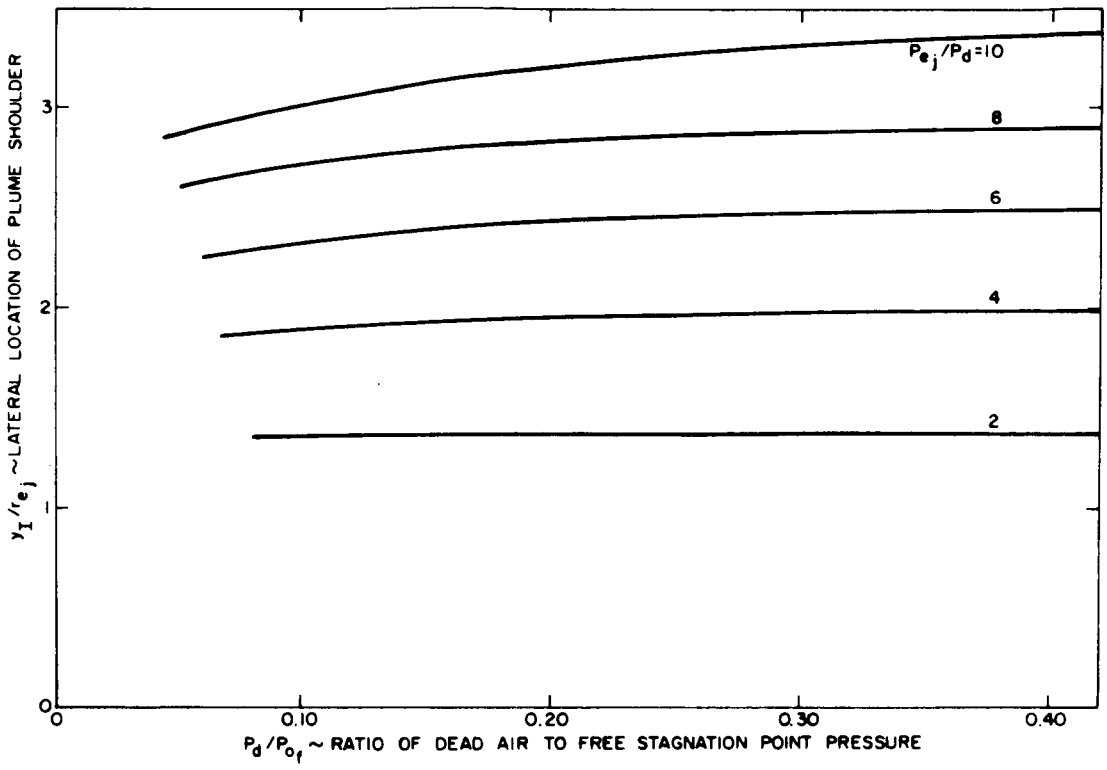

Figure 56. Lateral plume shoulder location.

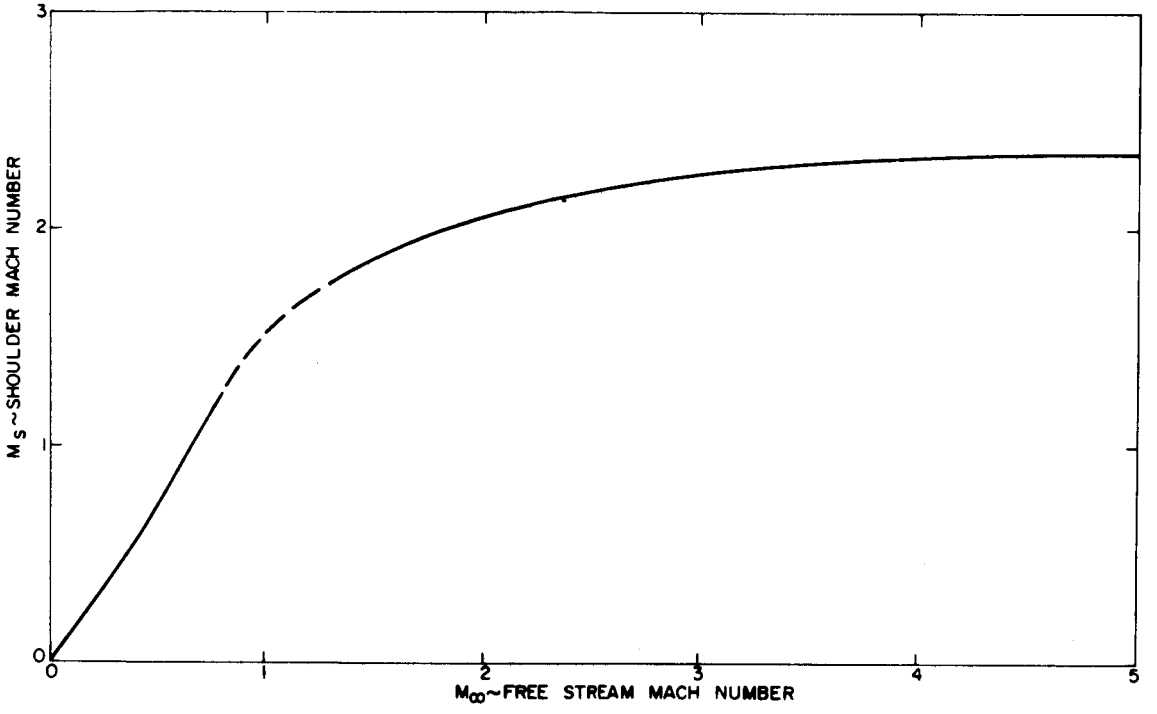

Figure 57. Variation of shoulder Mach number.

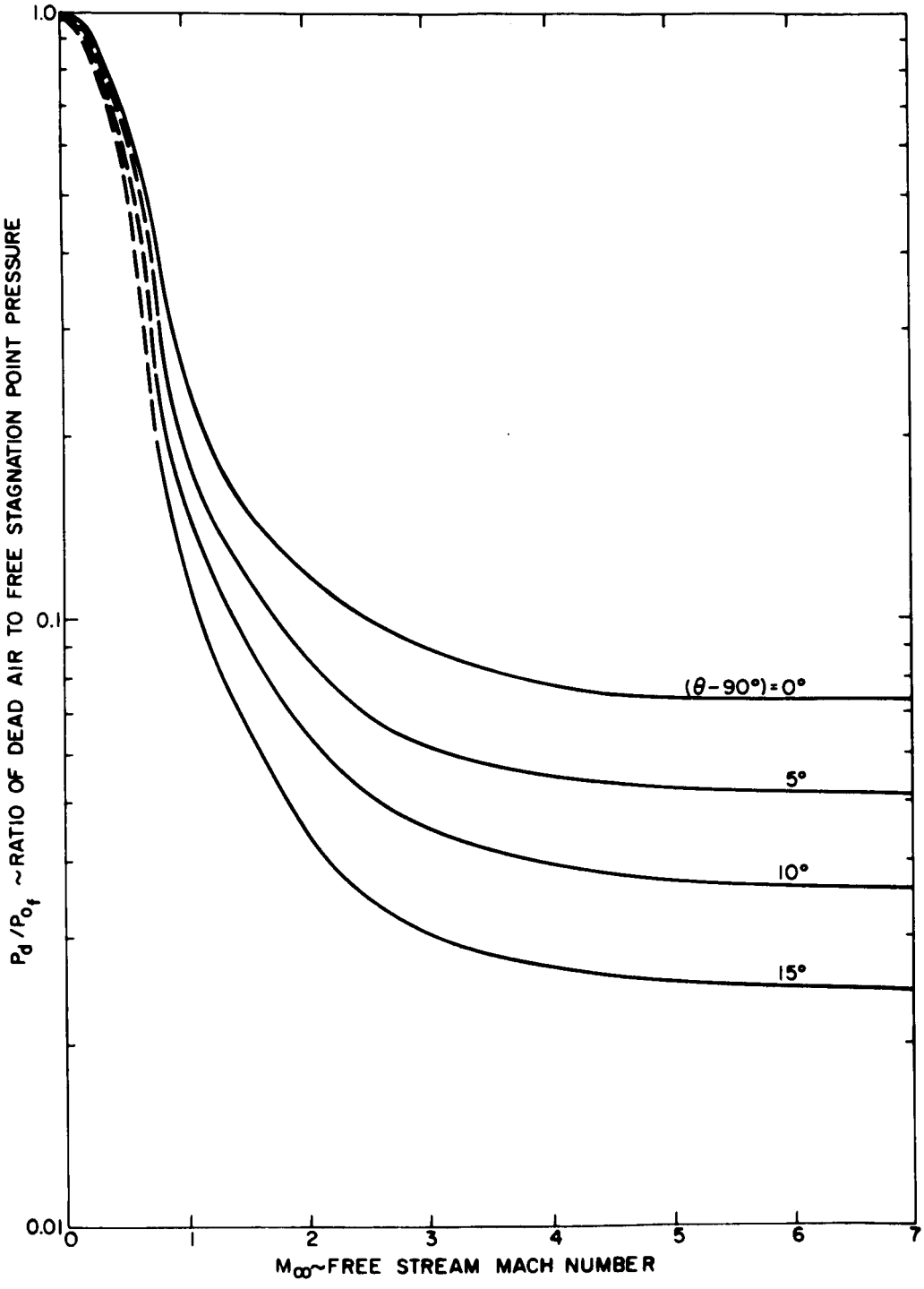

Figure 58. Pressure for various turning angles.

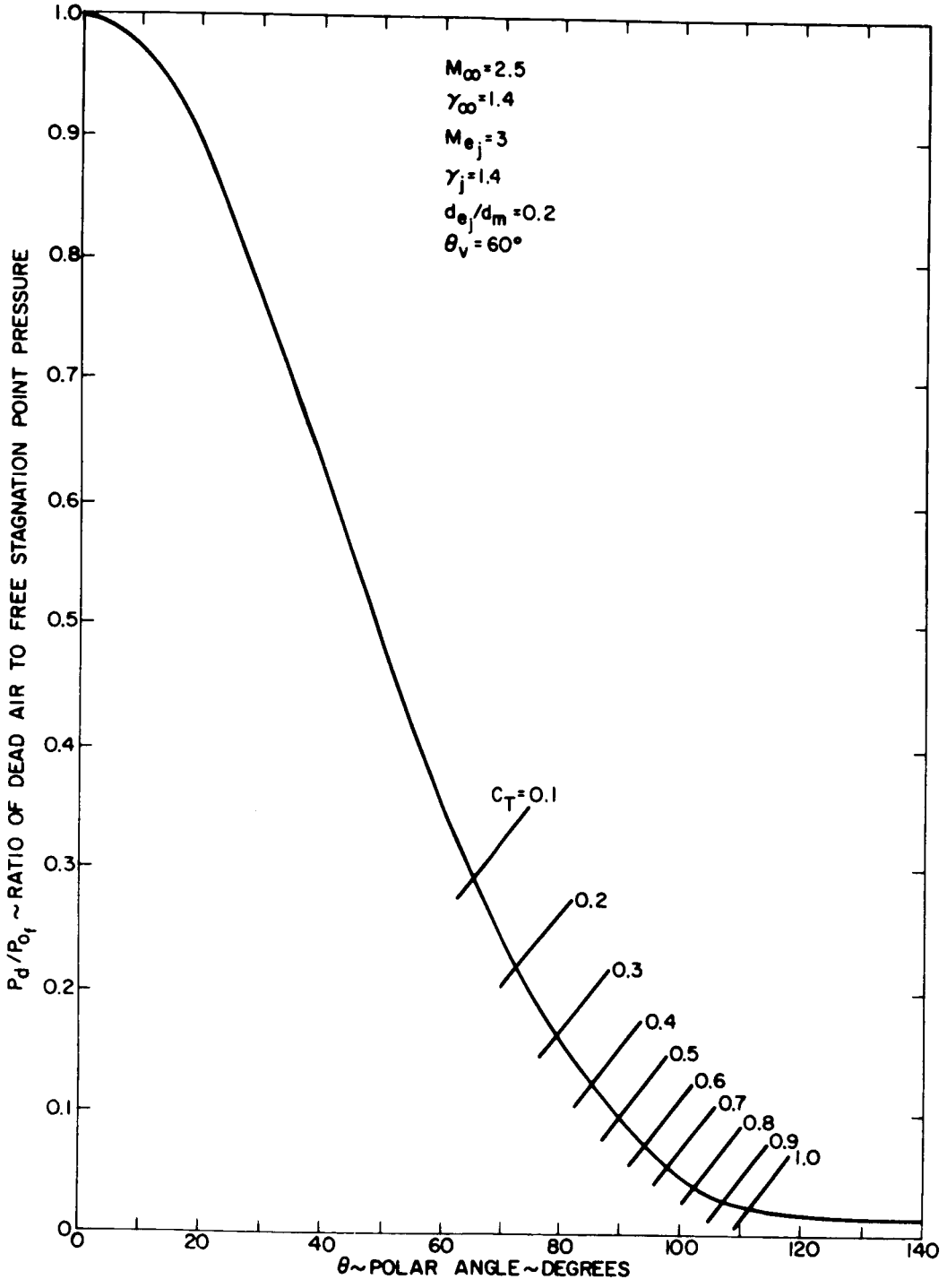

Figure 59. General pressure distribution.

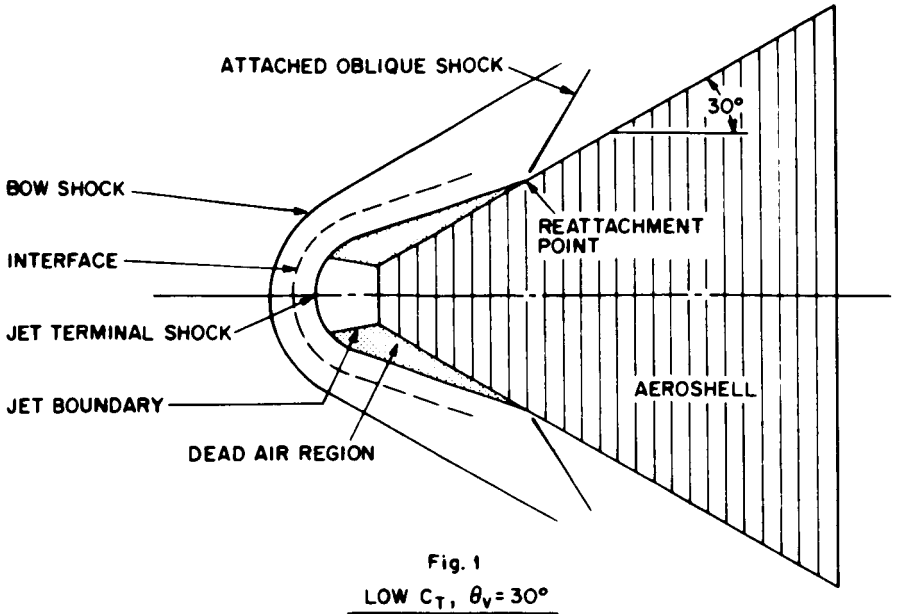

Fig. 1
LOW C_T, $\theta_v = 30°$

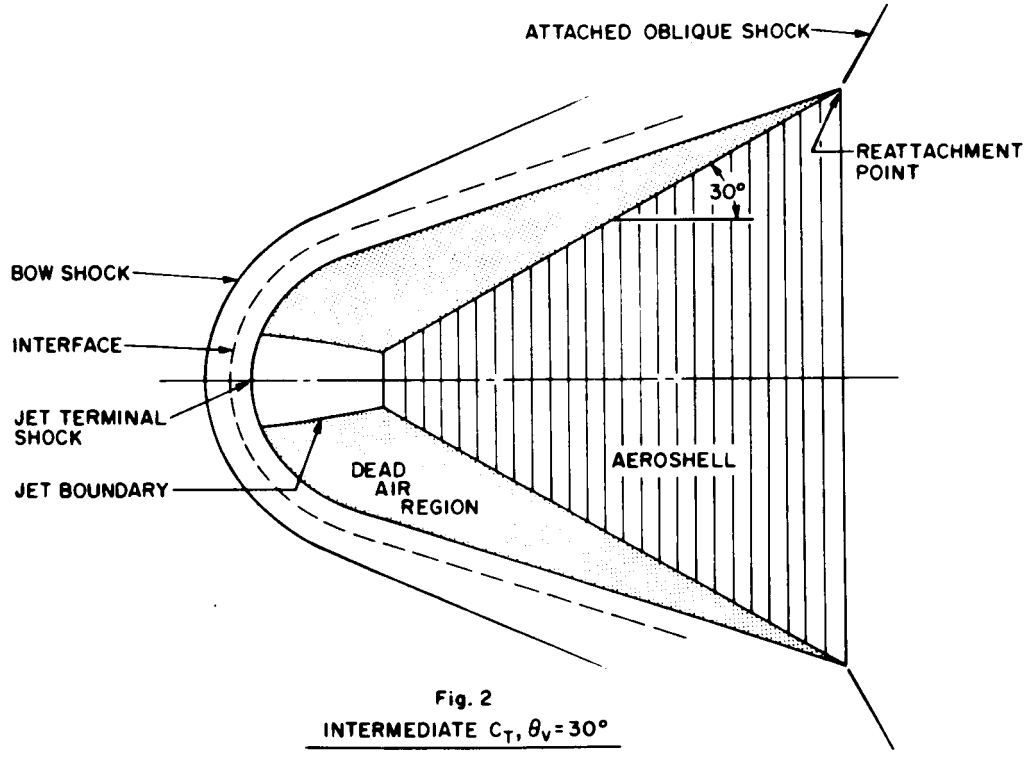

Fig. 2
INTERMEDIATE C_T, $\theta_v = 30°$

Figure 60. Flow geometry - small aeroshell openings.

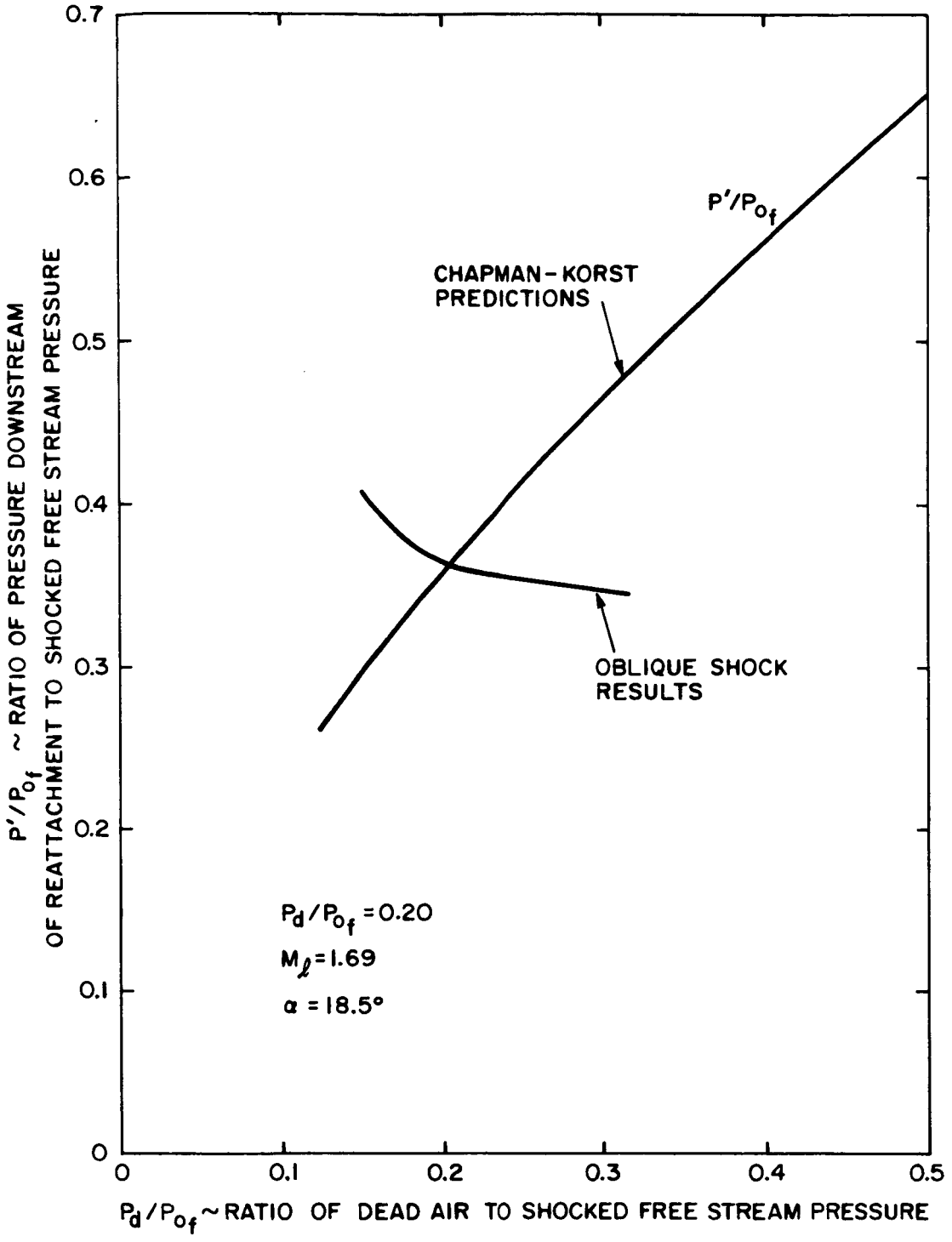

Figure 61. Solution for dead air pressure.

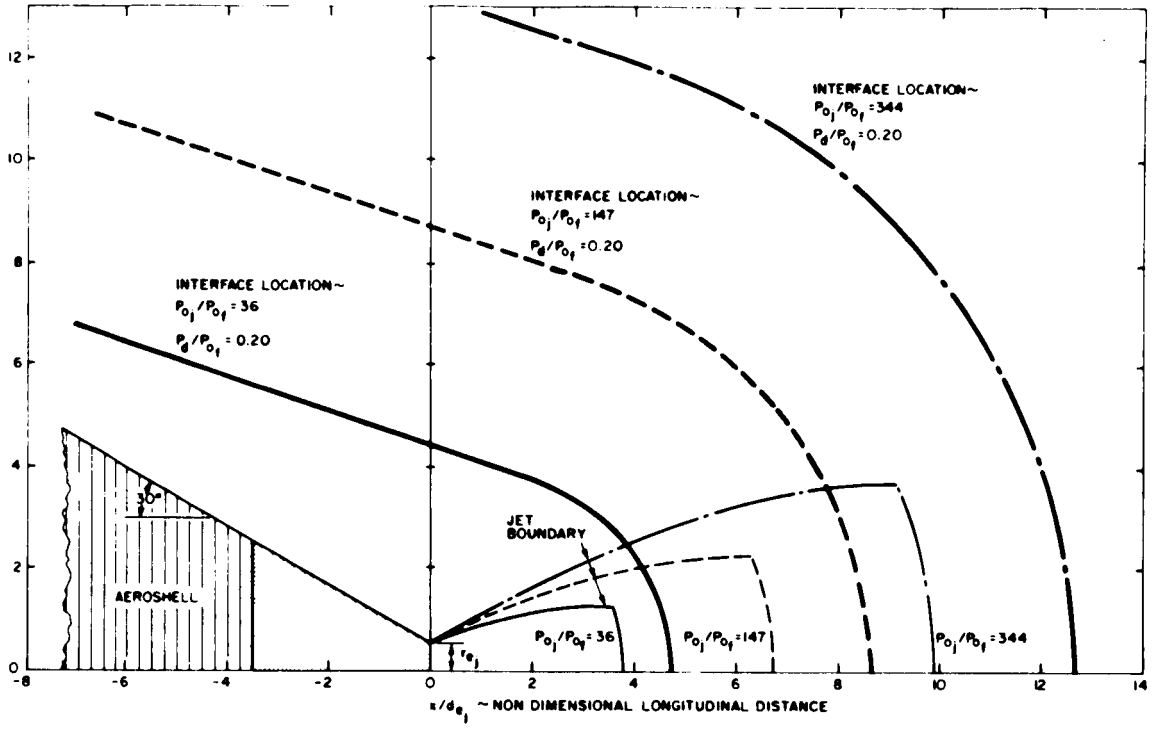

Figure 62. Superposition of three possible flow field configurations $\theta_v = 30^o$.

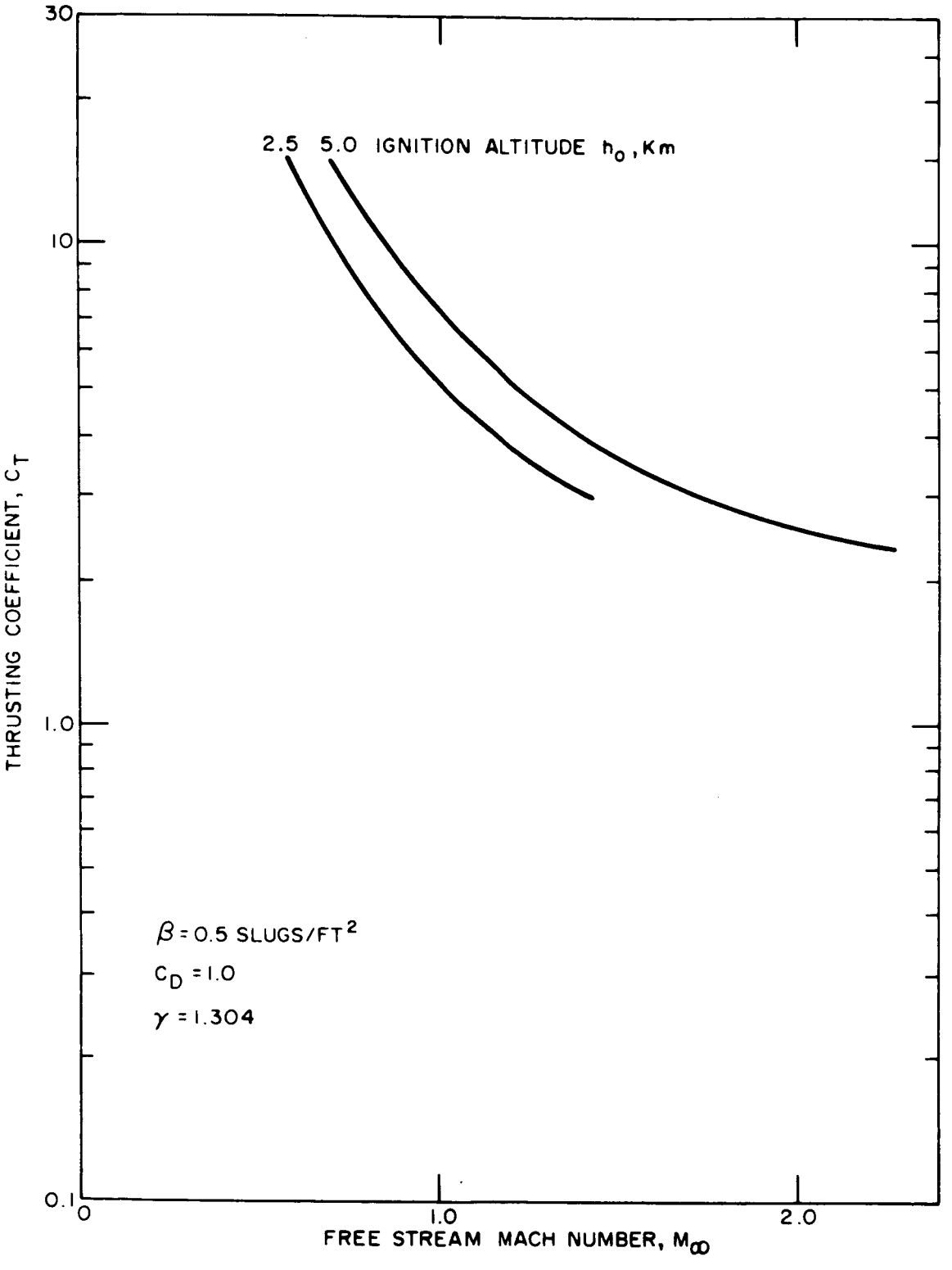

Figure 63. Terminal Landing Phase Mach number.

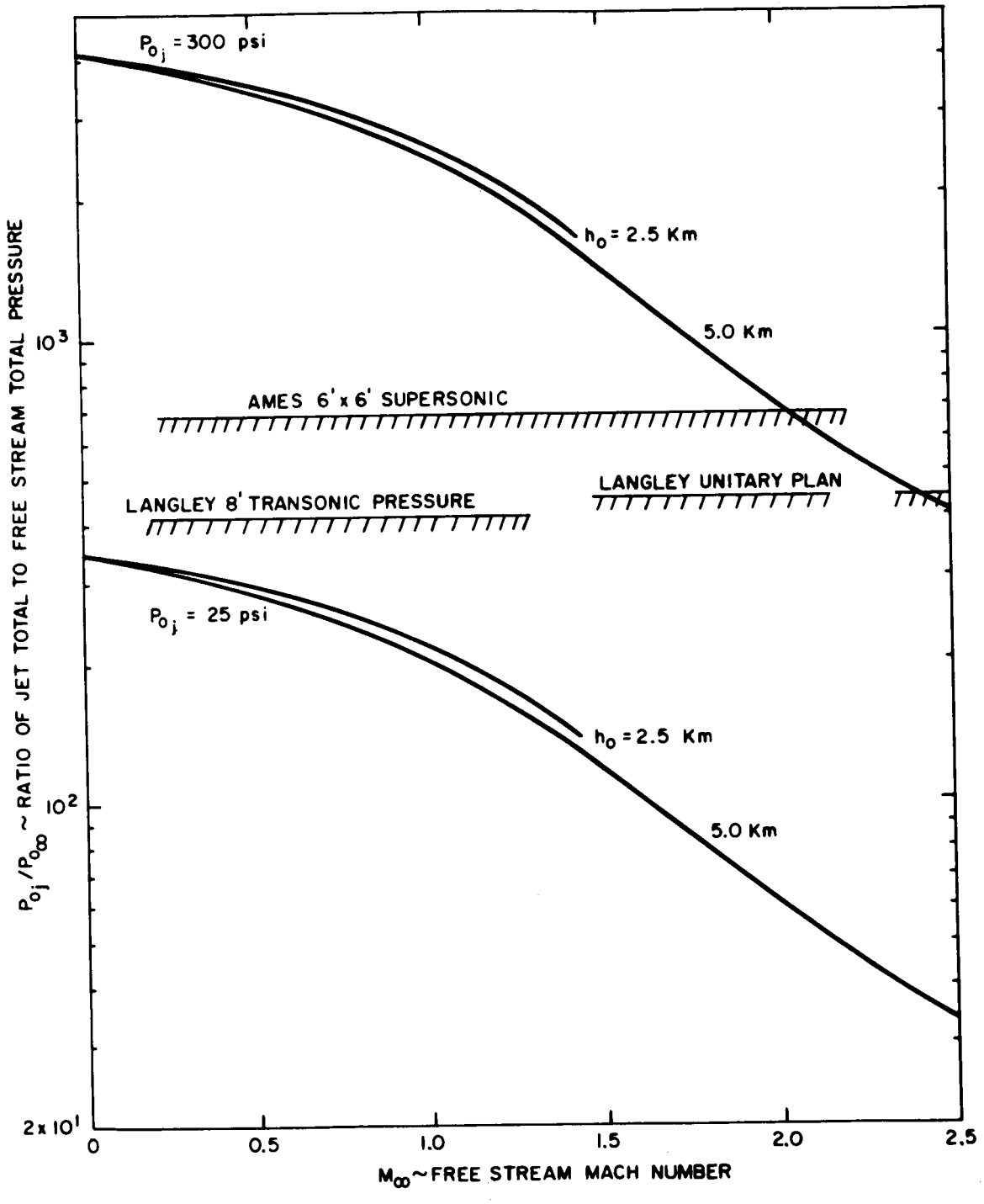

Figure 64. Mars Lander Retrorocket performance and wind tunnel simulation capabilities.

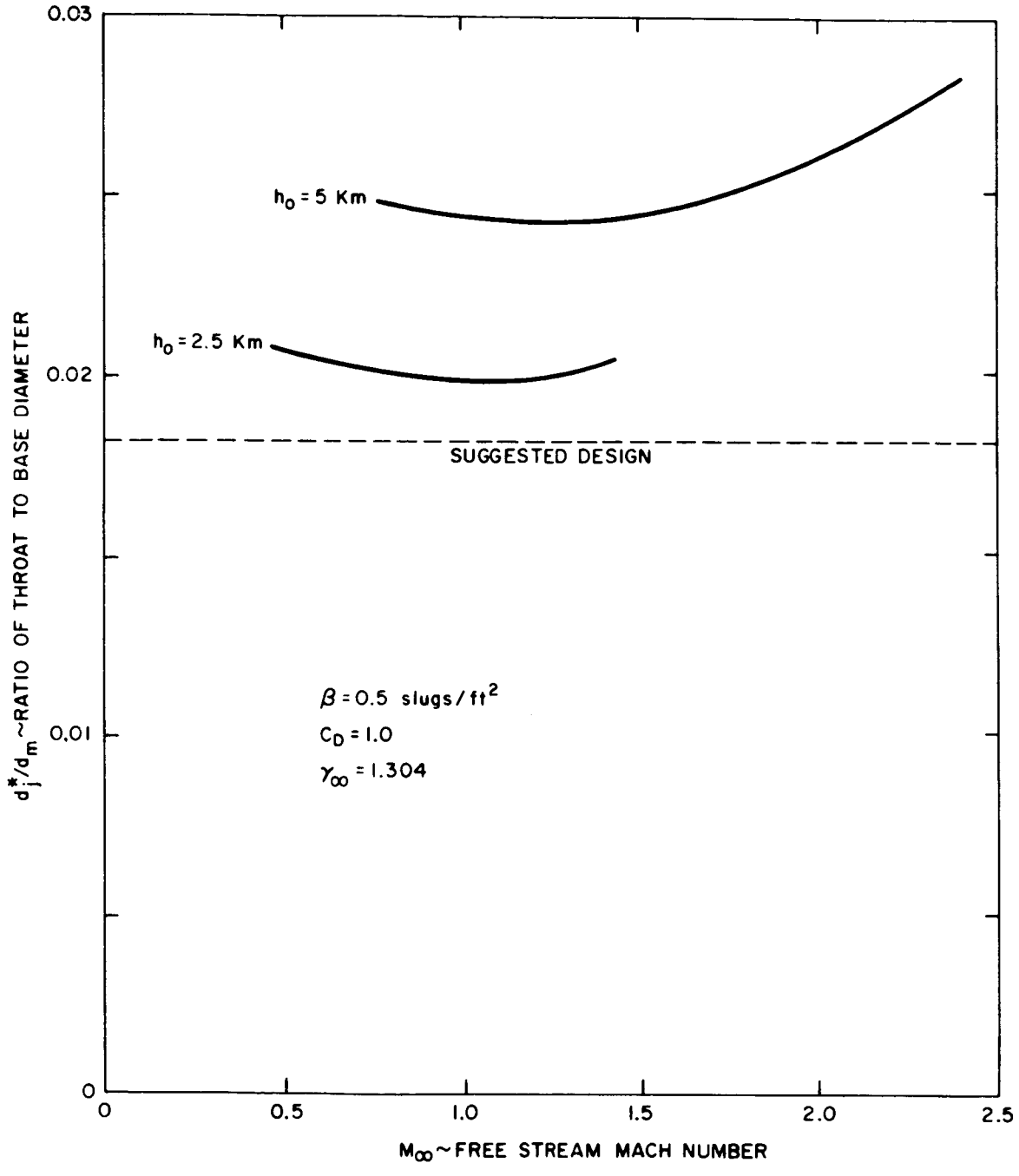

Figure 65. Throat sizing for Mars Lander.

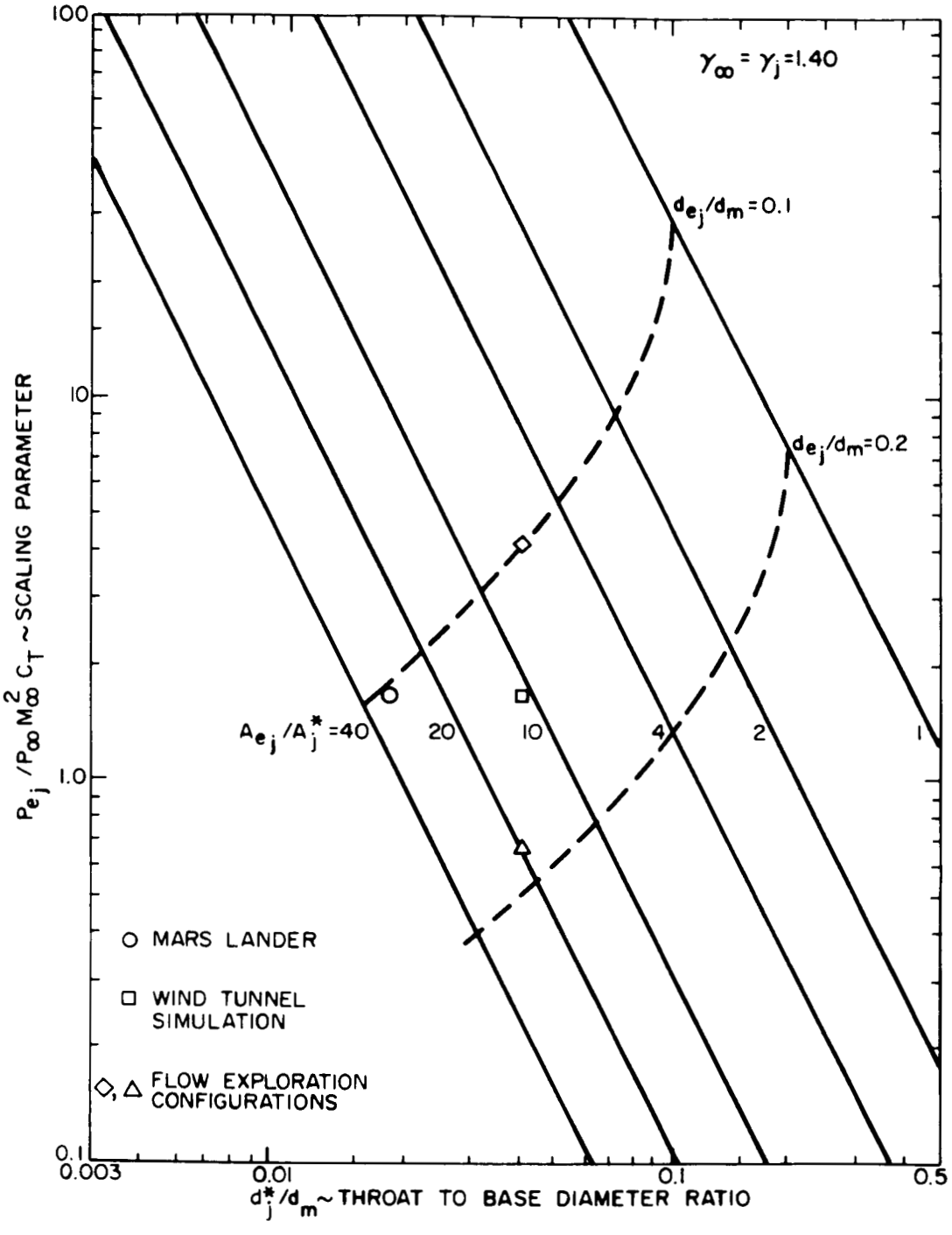

Figure 66. Nozzle throat and area ratio sizing.

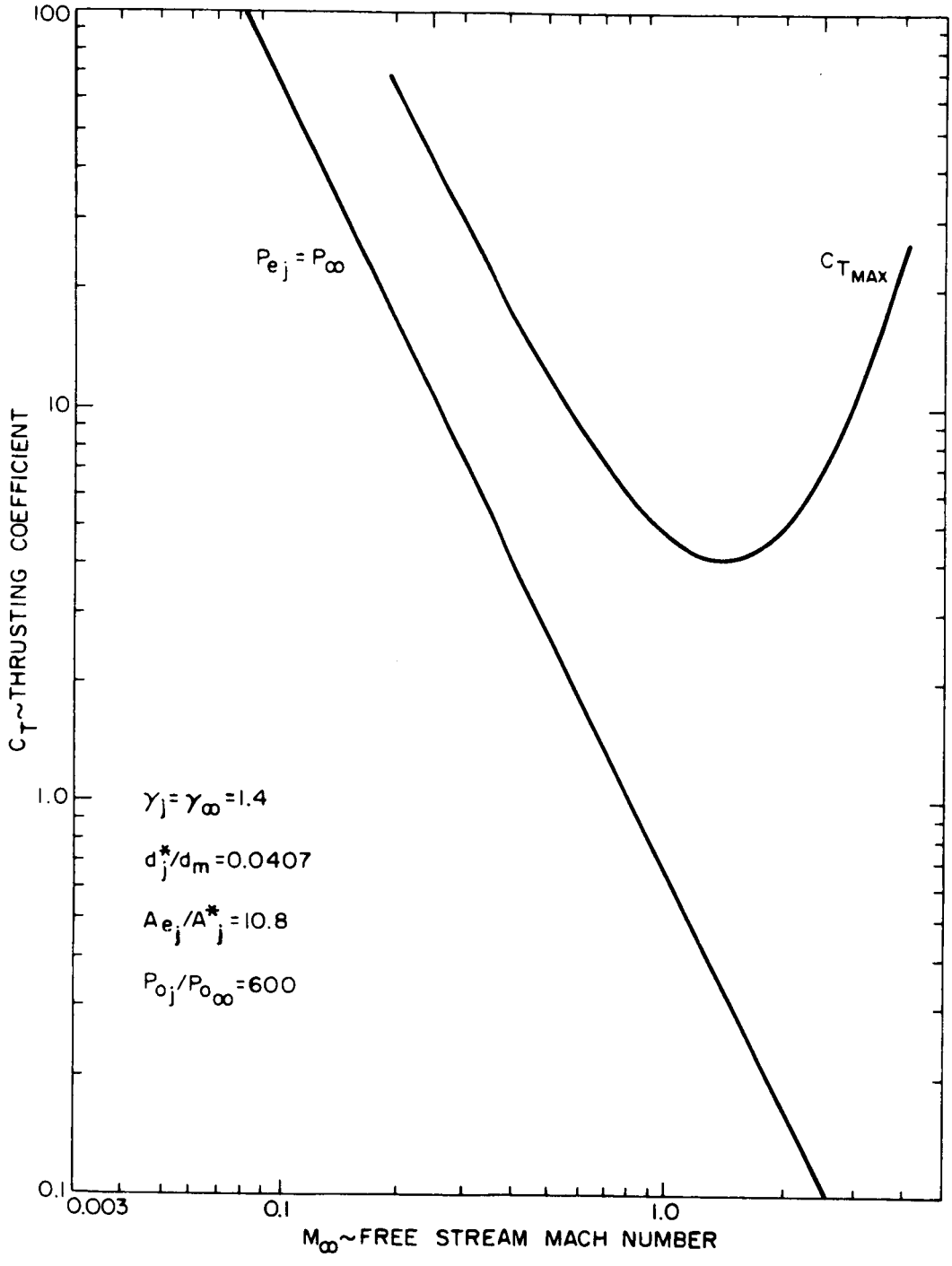

Figure 67. Useful range by throttling of the air supply is between the two curves for the wind-tunnel model simulating the Mars Lander configuration.

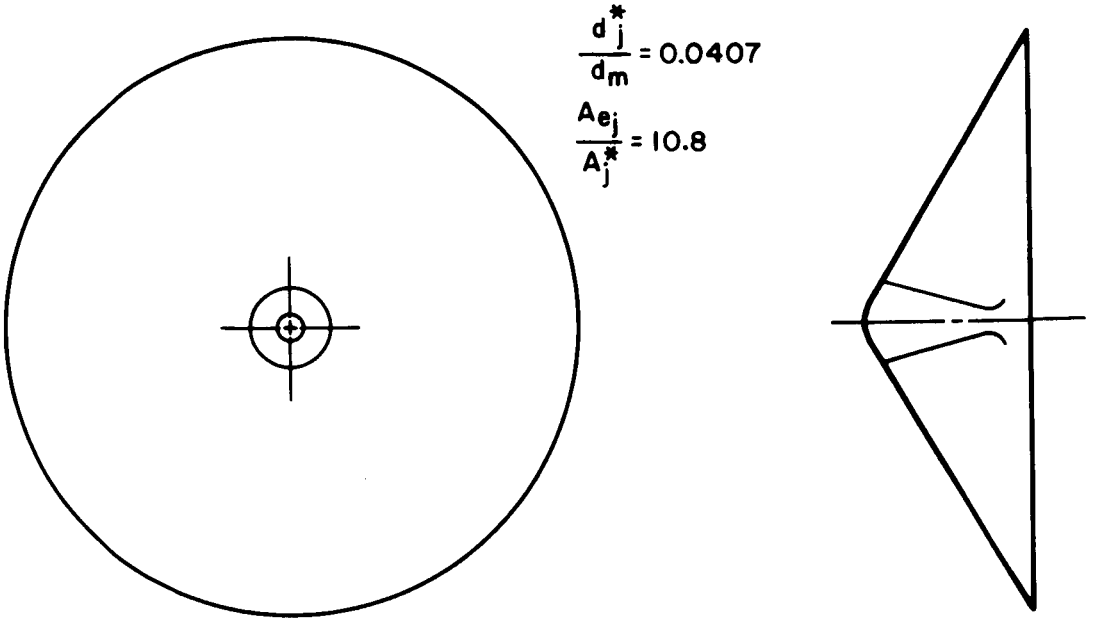

Figure 68. Single nozzle wind-tunnel model simulating the Mars Lander configuration.

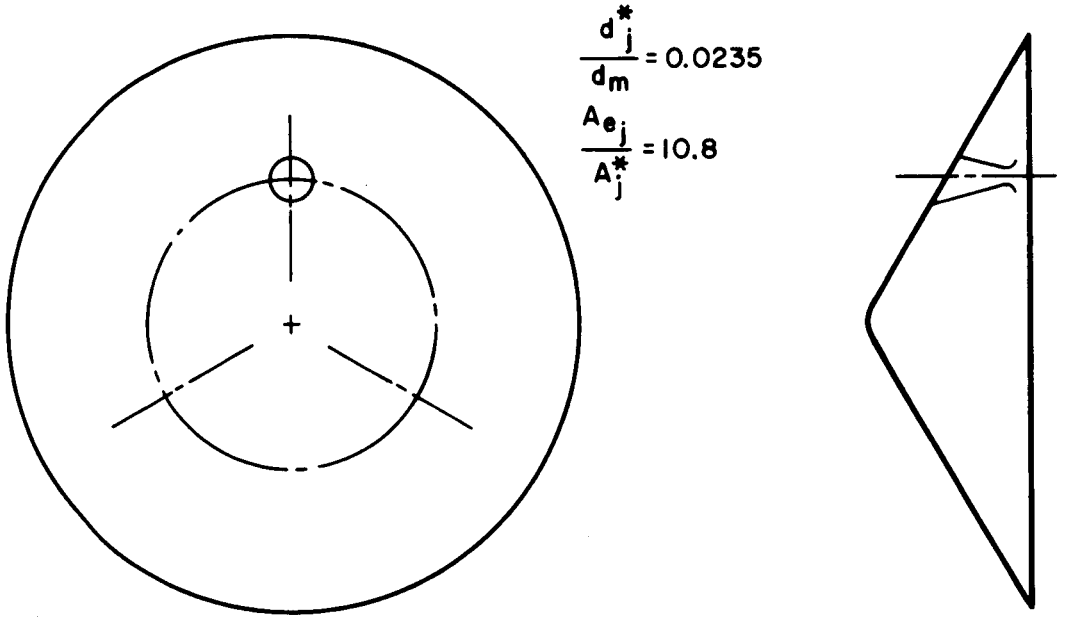

Figure 69. Multiple nozzle wind-tunnel model simulating the Mars Lander configuration.

APPENDIX A

RELATED REFERENCES

A.1 FOREWARD FACING JETS INTO ONCOMING STREAM

1. Lopstoff, M., "Wingflow Study of Pressure Drag Reduction at Transonic Speed by Projecting a Jet of Air from the Nose of a Prolate Spheroid of Fineness Ratio 6," NACA RML 51E09 (1951).

2. Love, E. S., "The Effects of a Small Jet of Air Exhausting from the Nose of a Body of Revolution in Supersonic Flow," NACA RM L52119a (1952).

3. Stalder, J. R. and Inouye, M., "A Method of Reducing Heat Transfer to Blunt Bodies by Air Injection," NACA RM A56B27a (1956).

4. Watts, G. A., "An Experimental Investigation of a Sonic Jet Directed Upstream Against a Uniform Supersonic Flow," UTIA TN No. 7 (1956).

5. Massachusetts Institute of Technology Naval Supersonic Laboratory, "An Experimental Study of a Window for an Infrared Seeker," Wind Tunnel Report 276, 1957.

6. Ferri, A. and Bloom, M., "Cooling by Jets Directed Upstream in Hypersonic Flow," WADC TN 56-382 (1957). AD97232

7. Massachusetts Institute of Technology Naval Supersonic Laboratory, "Temperature Parameter Study of a Window for an Infrared Seeker." Technical Report 341, 1958.

8. MacMahon, H. M., "An Experimental Study of the Effect of Mass Injection at the Stagnation Point of a Blunt Body, "GALCIT Hypersonic Research Project Memo No. 42 (1958).

9. Lam, S. H., "Interaction of a Two-Dimensional Inviscid Incompressible Jet Facing a Hypersonic Stream," AFOSR TN 59-274 (1959). AD212708.

10. Eminton, E., "Orifice Shapes for Ejecting Gas at the Nose of a Body in Two Dimensional Flow," Royal Aircraft Establishment (Farnborough). Technical Note No. Aero 2711, August, 1960

11. Warren, C. H. E., "An Experimental Investigation of the Effect of Ejecting a Coolant Gas at the Nose of a Bluff Body," J. Fluid Mech. 8, p. 400 (1960).

12. Charczenko, Nickolai and Hennessey, Katherine, "Investigation of a Retrorocket Exhausting from the Nose of a Blunt Body into a Supersonic Free Stream," NASA Technical Note TN D-751. September, 1961.

13. MITHRAS, Inc., "Investigation of an Aerodynamic Spike in Hypersonic Flow," Airborne Instruments Lab. Rpt. No. 1198-1, Final for Contract AF04(694)-29, AD365190, (Confidential) June, 1962.

14. Peterson, Victor and McKenzie, Robert, "Effects of Simulated Retrorockets on the Aerodynamic Characteristics of a Body of Revolution at Mach Numbers from 0.25 to 1.90." NASA Technical Note TN D-1300, May, 1962.

15. Hayman, L. O. and McDearmon, R. W., "Jet Effects on Cylindrical Afterbodies Housing Sonic and Supersonic Nozzles Which Exhaust Against a Supersonic Stream of Angles of Attack from 90° to 180°," NASA TN D-1016 (1962).

16. Wasko, Robert A., "Heat Transfer to a Sphere with a Retrorocket Exhausting into a Free Stream; Mach 2.0 and 0.8," NASA TN D-1535, November, 1962.

17. Hill, J. A. F., and Lorah, L. D., "Flow Pattern Study and Mixing Flow Analysis of an Aerospike in Hypersonic Flow," (U) AD 360 563, Airborne Instruments Lab. Report 1198 TN2. January, 1962. (Confidential)

18. Baron, J. R. and Alzner, E., "An Experimental Investigation of a Two Layer Inviscid Shock Cap due to Blunt Body Nose Injection," J. Fluid Mech. 15, p. 442, (1963).

19. Romeo, David and Sterrott, James, "Exploratory Investigation of the Effect of a Forward-Facing Jet on the Bow Shock of a Blunt Body in a Mach Number 6 Free Stream," NASA Technical Note TN D-1605, February, 1963.

20. Finley, P.J., "Experiments on Jets Directed from Blunt Bodies against a Supersonic Airstream," Ph.D. Thesis, Cambridge University (1963).

21. Tucker, L. M., "An Experimental Investigation of Contoured Nose Orifices with Ejection at Free-Stream Mach Numbers of 1.86 and 4.3, "Royal Aircraft Establishment TN Aero 2923 (November, 1963).

22. Charwat, A. F. and Allegre, J., "Interaction of a Supersonic Stream and a Transverse Supersonic Jet, "AIAA J. 2, p. 1965, (1964).

23. Lorah, L. D., Hill, J. A. F., "Development of Improved Cooling Systems for High-Performance Missiles (U)". NAVWEPS Report 8041, NOTS TP 3034, MITHRAS Rpt. MC 61-2, April, 1964. (Confidential.)

24. Wang, C. Y., "Contours for Stagnation Point Mass Injection in Hypersonic Flow," AIAA J. 2, 178-179 (1964).

25. Sutton, E. P. and Finley, P. J., "The Flow of a Jet from the Nose of an Axisymmetric Body in a Supersonic Airstream." Archiwinn Mechaniki Stosowane, J. 3, p. 781 (1964).

26. Sutton, E. P. and Finley, P. J., "The Flow of a Jet from the Nose of an Axisymmetric Body in a Supersonic Airstream", Aeronautical Research Council ARC 25689.

27. Charwat, A. F. and Faulman, D., "Investigation of the Flow and Drag due to Control Jets Discharging Upstream into a Supersonic Flow," Proceedings XVth International Astronautical Congress, Warsaw, 1964.

28. Gilles, S. E. and Kallis, J. M., "Penetration Distance of Retrocket Exhaust Plumes into Oncoming Stream," Aerospace Report No. TDR-26-9 (4181)-2, SSD-TDR-64-23, Aerospace Corporation, El Segundo, California, May, 1964.

29. Romeo, David and Sterrett, James, "Flow Field for Sonic Jet Exhausting Counter to a Hypersonic Mainstream, " AIAA, 3, 544-546, March, 1965.

30. Gollnick, A. F., Jr., "Experiments on Blunt Body Flows with Central Injection, "Massachusetts Institute of Technology, Aerophysics Lab., TR 105, Air Force Office of Scientific Research 65-1149 (May, 1965).

31. Finley, P., "The Flow of a Jet from a Body Opposing a Supersonic Free Stream," J. Fluid Mech., 26, 337-368 (1966).

32. Good, R. E., Hill, J. A. F., "A Wind Tunnel Investigation of the Nitric Oxide-Oxygen Atom Reaction," Mithras Rpt. MC 64-116-R2, 1966.

33. Wuest, W., "Approximate Determination of the Flow Field on a Profile with Nose Blowing and Supersonic Free Stream," Deutsche Luft and Raumfohrt Report 66-09, 1966.

34. Wuest, W., "The Flow on Airfoil with Blowing From a Nose Slot." NASA TTF-10, 906. National Aeronautics and Space Administration, May, 1967.

35. Cassanova, R. A., "Flow Field of a Sonic Jet Exhausting Counter To a Low Density Supersonic Stream" AEDC-TR-67-149, Aerospace Environmental Facility, Arnold Air Force Station, Tennessee October 1967 AD 659372.

36. Keyes, J. and Hefner, J. N. "Effect of Forward-Facing Jets on Aerodynamics Characteristics of Blunt Configurations at Mach 6. Journal of Spacecraft and Rockets., April 1967, p. 533.

37. Foreman, K. M., "The Interaction of a Retrorocket Exhaust Plume with the Martian Air Environment," Grummen Research Department Memorandum RM-354, Geo-Astrophysics Section, Grummen Aircraft Engineering Corporation, Bethpage, New York, February, 1967.

38. Hefner, J. N. and Keyes, J. W., "Drag Characteristics of Several Blunt Configurations Utilizing Forward-Facing Jets at a Mach Number of 6." Langley Working Paper LWP-379. Langley Research Center, Langley Station, Hampton, Virginia. National Aeronautics and Space Administration, March, 1967.

A.2 INTERACTION OF A TRANSVERSE JET WITH THE FREE STREAM AND THE USE OF JETS FOR THRUST VECTOR CONTROL

1. Ferrari, C., "Interference Between a Jet Issuing Laterally from a Body and the Enveloping Free Stream," Johns Hopkins University, Bumblebee Series Report No. 286 (1959). AD 226477

2. Vinson, P. W., Amick, J. L. and Liepman, H. P., "Interaction Effects Produced by Jets Exhausting Laterally Near Base of Ogive-Cylinder Model in Supersonic Main Stream," NASA Memo 12-5-58W (1959)

3. Amick, J. L. and Hayes, P. B., "Interaction Effects of Side Jets Issuing From Flat Plates and Cylinders Aligned with a Supersonic Stream," WADD TR 60-329 (1960). AD 245 328.

4. Cubbison, R. W., Anderson, B. H., and Ward, J. J., "Surface Pressure Distributions with a Sonic Jet normal to Adjacent Flat Surfaces at Mach 2.92 to 6.4", NASA TND-580, Lewis Research Center, Cleveland, Ohio, February, 1961.

5. Rao, G. V. R., "Recent Developments in Rocket Nozzle Configuration", ARS Journal, November, 1961.

6. Romeo, D. J. and Sterrett, J. R., "Aerodynamic Interaction Effects Ahead of a Sonic Jet Exhausting Perpendicularly from a Flat Plate into a Mach Number 6 Free Stream," NASA TN D-743 (1961).

7. Wu, J. M., Chapkis, R. L., and Mager, A., "Approximate Analysis of Thrust Vector Control by Fluid Injection," ARS J. 31, p. 1677 (1961).

8. Gagnon, R., "Thrust Vector Control of Plug Nozzles", Final Report on AF Contract No. 61-115, January, 1962. AD 357 944

9. Dahm, T. J., "The Development of an Anology to Blast-Wave Theory for the Prediction of Interaction Forces Associated with Giseors Secondary Injection into a Supersonic Stream", VIDYA Technical Note 9166-TN-3, May, 1964. VIDYA Research and Development, Palo Alto, California.

10. Harold, R. E., "An Investigation of the Interaction of a Secondary Air Jet with a Supersonic Air Stream," Boeing Document D2-20494-1. The Boeing Company, Seattle, Washington, 1964.

11. Charwat, A. F. and Allegre, J., "Interaction of a Supersonic Stream and a Transverse Supersonic Jet", AIAA Journal Vol. 2, No. 11, November 1964, p. 1965-1972.

12. Peake, D. J., "The Pressures on a Surface Surrounding a Jet Issuing Normal to a Mainstream," Aeronautical Report LR-4-10 National Research Council of Canada, Ottowa, 1964.

13. Katzen, E. D. and Kaatari, G. E., "Flow Around Blunt Bodies Including Effects of High Angles of Attack, Nonequilibrium Flow, and Vapor Injection," AIAA Entry Technology Conference Proceedings, AIAA Publication CP-9 (1964).

14. Zukoski, E. E. and Spaid, F. W., "Secondary Injection of Cases into a Supersonic Flow", AIAA J. 2, p. 1689 (1964).

15. Evers, J. L., "A Study of the Bow Shocks Induced by Secondary Injection into Supersonic and Hypersonic streams." Technical Note 29 von Karmon Institute for Fluid Dynamics, Rhode-Saint-Genese, Belgium. 1965.

16. Brookbury, L. J. S. and Wood, M. N., "The Static Pressure Distribution Around a Circular Jet Exhausting Normally from a Plane Wall into an Airstream," Ministry of Aviation, Aeronautical Research Council Current Papers, CP No. 882, 1965.

17. Ting, L. and Ruger, C. J., "Oblique Interaction of a Jet into a Stream," AIAA Journal Vol. 3, No. 3, March, 1965, pp. 534-536.

18. Reichenau, D. E. A., "Interference of Cold and Hot Rocket Exhaust Issuing Normal to the Airstream from a Flat Plate at Free Stream Mach Numbers From 0.6 to 1.4." AEDC-TR-66-127, A484682, Arnold Engineering Development Center, Arnold Air Force Station, Tennessee, June, 1966.

19. Lee, C. C., "A Review of Research on the Interaction of a Jet with an External Stream," Technical Note R-184, March, 1966. Research Laboratories Brown Engineering Company, Inc., Huntsville, Alabama, 1967.

20. Schetz, J. A. Hawkins, P. F., and Lehman, H., "Structure of Highly Underexpanded Transverse Jets in a Supersonic Stream" AIAA Journal Vol. 5, No. 5, May, 1967, pp. 882-884

21, Hsia, H. T. S., "Equivalence of Secondary Injection to a Blunt Body in Supersonic Flow", AIAA Journal Vol. 4, No. 10, October, 1966, pp.1832-1834.

22. Abbott, W. A., "Studies of Flow Fields Created by Vertical and Inclined Jets when Stationary or Moving over a Horizontal Surface." Ministry of Aviation Aeronautical Research Council, Current Papers, CP No. 911, 1967.

A.3 INTERACTION OF A JET WITH A SURFACE

1. Stitt, L. E., "Interaction of Highly Underexpanded Jets with Simulated Lunar Surfaces", NASA TN D-1095, December, 1961.

2. Eastman, D. W., and L. P. Radtke, 'Flow Field of an Exhaust Plume Impinging on a Simulated Lunar Surface," AIAA J., Vol. 1, No. 6, pp. 1430-1431, June, 1963. Roberts, L., "The Action of a Hypersonic Jet on a Dust Layer, "Inst. Aerospace Sci., paper No. 63-50, 1963.

3. Vick, A. R. and Adrews, E. H., Jr., 'Investigation of Highly Underexpanded Exhaust Plumes Impinging upon a Perpendicular Flat Surface," NASA TN D-3269, February, 1966.

4. Eastman, D. W. and J. P. Bonnema, 'Flow Field of a Highly Underexpanded Jet Impinging on a Surface," AIAA J., Vol. 4, No. 7, pp. 1302-1303, July, 1966.

5. Clark, L. V., 'Free Jet Impingement Normal to a Curved Surface in a Vacuum, " NASA Technical Note NASA TN D-3920, National Aeronautics and Space Administration, Washington, D.C., April, 1967.

APPENDIX B

RETROJET OPERATING CONDITIONS

B.1 SIMPLIFIED EQUATION OF MOTION

If we assume that the trajectory has become vertical before retrorocket firing and neglect the force of gravity and drag, the equation of motion is simply

$$-m\, dv/dt = T \tag{B-1}$$

In terms of specific impulse I_s

$$dm/dt = -\, T/gI_s$$

so that the instantaneous mass is

$$m = m_o - (T/gI_s)t \tag{B-2}$$

Equation (1) may then be written

$$-\frac{dv}{dt} = \frac{T}{m_o - (T/gI_s)t}$$

$$= g\frac{T}{W_o}\left[\frac{1}{1 - (T/W_oI_s)t}\right]$$

which has the integral

$$V = V_o + gI_{sp}\, \ell n \left(1 - \frac{T}{WI_s}\, t\right) \qquad (B-3)$$

This may be integrated again for the height variation with time.

$$h_o - h = V_o t - gI_s\left[\left(\frac{WI_s}{T} - t\right) \ell n \left(1 - \frac{I}{WI_s}\, t\right) + t\right] \qquad (B-4)$$

B.2 PROPELLANT WEIGHT AND THRUST

Let t_b be the total burn time. The final mass is

$$m_f = m_o - Tt_b/gI_s$$

The mass ratio

$$\frac{m_p}{m_o} = \frac{m_o - m_f}{m_o} = \frac{Tt_b}{WI_s} \qquad (B-5)$$

Substituting in equation (3) for $V = O$ at $t = t_b$ we obtain

$$\ell n \left(1 - \frac{m_p}{m_o}\right) = - V_o/gI_s$$

or $$\boxed{\frac{m_p}{m_o} = 1 - e^{-V_o/gI_s}} \qquad (B-6)$$

and the burning time is

$$t_b = \frac{WI_s}{T} \frac{m_p}{m_o} \tag{B-7}$$

Substituting in equation (4) for h = O at t = t_b yields the thrust/weight ratio

$$\frac{T}{W} = \frac{I_s}{h_o} \left\{ V_o \frac{m_p}{m_o} - gI_s \left[\frac{m_p}{m_o} + \left(1 - \frac{m_p}{m_o} \right) \ell n \left(1 - \frac{m_p}{m_o} \right) \right] \right\} \tag{B-8}$$

B.3 THRUST COEFFICIENT AND NOZZLE AREA

The thrust coefficient is defined as

$$C_T = \frac{T}{qA}$$

and the ballistic parameter as

$$\beta = \frac{W}{gC_D A} \qquad \text{slugs/ft.}^2$$

At the retrofire altitude we may write

$$C_T = \frac{2gC_D\beta}{\rho V_o^2} \quad \frac{T}{W} \tag{B-9}$$

where ρ as a function of h_o must be obtained from a suitable model of the Martian atmosphere.

For those cases of interest where the propulsion system expenditure is small (i.e. less than twenty percent), a constant mass analysis may be used. Under this assumption, the thrust is

$$T = \frac{1/2 m V_o^2}{h_o} \tag{B-10}$$

where h_o is the ignition altitude

and V_o is the velocity at ignition.

From conservation of energy,

$$V = \sqrt{V_o^2 - \frac{2}{m} T (h_o - h)} \tag{B-11}$$

For an exponentially varying atmospheric density

$$\rho = \rho_o e^{-h/H} \tag{B-12}$$

where ρ_o is the surface density

H is the atmospheric scale height

h is the height above the surface.

Therefore,

$$C_T = \frac{T}{q_\infty A_m} = \frac{T}{1/2 \rho V^2 A_m} = \frac{1/2 m V_o^2 / h_o}{(1/2 \rho V^2 A_m)} \tag{B-13}$$

Substituting Equations (11) and (12) into (13).

$$C_T = \frac{me^{+h/H}}{\rho_o h A_M} = \frac{m}{C_D A_m} \frac{C_D e^{h/H}}{\rho_o h} = \frac{\beta C_D e^{h/H}}{\rho_o h} \qquad \text{(B-14)}$$

where $\beta = \frac{m}{C_D A}$

The variation of thrust coefficient with altitude is found to be independent of ignition altitude, h_o, and initial velocity V_o.

The nozzle area may also be computed from the thrust/weight ratio since

$$\frac{T}{W} = \frac{C_F P_c A^*}{\beta g C_D A}$$

We get the simple result

$$\frac{A^*}{A} = \frac{\beta g C_D}{P_c C_F} \frac{T}{W} \qquad \text{(B-15)}$$

APPENDIX C

RELATIONSHIP BETWEEN JET AND FREE-STREAM CONDITIONS

The following expressions were used to construct figure 16:

$$C_T = \frac{C_F A_j^* P_{o_j}}{q_\infty A_m} = \frac{C_F}{\left(\frac{\gamma_\infty}{2} P_\infty M_\infty^2\right)} \frac{A_j^*}{A_{e_j}} \frac{A_{e_j}}{A_m} \frac{P_{o_j}}{P_{o_f}} P_{o_f} \tag{C-1}$$

and

$$C_T = \frac{2 C_F}{\gamma_\infty M_\infty^2} \left(\frac{A_j^*}{A_{e_j}}\right)\left(\frac{d_{e_j}}{d_m}\right)^2 \left(\frac{P_{o_j}}{P_{o_f}}\right)\left(\frac{P_{o_f}}{P_\infty}\right) \tag{C-2}$$

where

$\frac{A_j^*}{A_{e_j}}$ follows from choices for γ_j and M_{e_j}, (C-3)

$\frac{d_{e_j}}{d_m}$ from choice of ratio of nozzle exit to vehicle, diameter ratio (C-4)

$$\frac{P_{o_f}}{P_\infty} = \frac{\left(\frac{\gamma_\infty + 1}{2} M_\infty^2\right)^{\gamma_\infty/(\gamma_\infty - 1)}}{\left(\frac{2\gamma_\infty}{\gamma_\infty + 1} M_\infty^2 - \frac{\gamma_\infty - 1}{\gamma_\infty + 1}\right)^{1/(\gamma_\infty - 1)}}, \tag{C-5}$$

and

$\frac{P_{o_j}}{P_{o_f}}$ is free variable. (C-6)

Figure 17 was constructed from the following relationships

$$\left(\frac{P_{e_j}}{P_d}\right) = \left(\frac{P_{e_j}}{P_{o_j}}\right) \left(\frac{P_{o_j}}{P_{o_f}}\right) \left(\frac{P_{o_f}}{P_d}\right) \tag{C-7}$$

where

$$\frac{P_{e_j}}{P_{o_j}} = \left(1 + \frac{\gamma_j - 1}{2} M_{e_j}^2\right)^{-\left(\frac{\gamma_j}{\gamma_j - 1}\right)} \tag{C-8}$$

and

$$\frac{P_{o_j}}{P_{o_f}} \text{ and } \frac{P_d}{P_{o_f}}, \text{ are free variables.} \tag{C-9}$$

For Figure 18

$$\frac{P_{o_j}}{P_{o_\infty}} = \left(\frac{P_{o_j}}{P_{o_f}}\right) \left(\frac{P_{o_f}}{P_\infty}\right) \left(\frac{P_\infty}{P_{o_\infty}}\right) \tag{C-10}$$

where

$$\frac{P_{o_f}}{P_\infty} \text{ from equation C-5,} \tag{C-11}$$

$$\frac{P_\infty}{P_{o_\infty}} = \left(1 + \frac{\gamma_\infty - 1}{2} M_\infty^2\right)^{-\left(\frac{\gamma_\infty}{\gamma_\infty - 1}\right)}, \tag{C-12}$$

and

$$\frac{P_{o_j}}{P_{o_f}} \text{ is a free variable.} \tag{C-13}$$

In the course of the present investigation it was necessary to interpret Finleys data in terms of the retrorocket thrust coefficient C_T. This is accomplished as follows:

The thrust coefficient C_T can be expressed as:

$$C_T = \frac{C_F A^* P_{o_j}}{q_\infty A_m} \quad , \tag{C-14}$$

$$C_T = 2 C_F \, (P_{o_f}/P_\infty) \, (P_{o_j}/P_{o_f}) \, (d_{e_j}/d_m)^2 \, / \, \gamma_\infty M_\infty^2 (A_{e_j}/A_j^*) , \tag{C-15}$$

or $$C_T = K(\gamma_\infty, M_\infty) \, C_F (P_{o_j}/P_{o_f}) \, (d_{e_j}/d_m)^2 \, / \, (A_{e_j}/A_j^*) \tag{C-16}$$

where

$$K = 2(P_{o_f}/P_\infty) \, / \, \gamma_\infty M_\infty^2 = P_{o_f}/q_\infty \tag{C-17}$$

The function K is plotted against M_∞ for $\gamma_\infty = 1.4$ in Figure C-1. It can be seen that in the supersonic regime, K is essentially constant. This is the region of Finleys data, ie$M_\infty = 2.5$. The thrust coefficient is thus proportional to

$$(P_{o_j}/P_{o_f}) \, (d_{e_j}/d_m)^2 \quad , \tag{C-18}$$

where the proportionality constant depends on the engine characteristics. Figure C-2 shows C_T plotted against

$$P_{o_j}/P_{o_f}$$

for various values of d_m/d_{e_j}. The curves are for $\gamma_j = 1.4$ and $M_{e_j} = 1.0$.

Finley (Ref. 9) defines a force coefficient C_f as

$$C_f = T/A_m P_{o_f}$$

To convert his data which is plotted against $\sqrt{C_f}$ to the C_T notation used in this report we can write

$$C_T = C_f(P_{o_f}/q_\infty) \qquad \text{(C-19)}$$

$$= K\, C_f$$

From Figure C-1 in the supersonic range

$$C_T \cong 2\, C_f \qquad \text{(C-20)}$$

or Figure C-1 may be used directly.

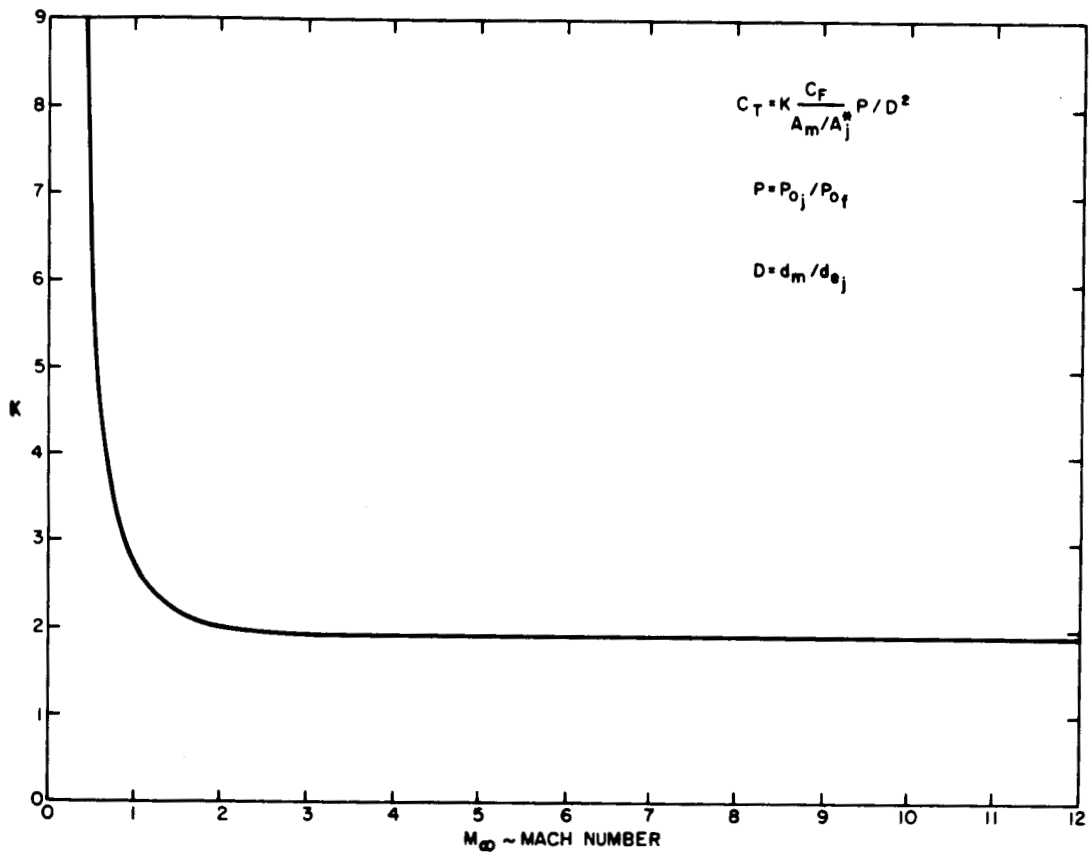

Figure C-1. Variation of K with mach number.

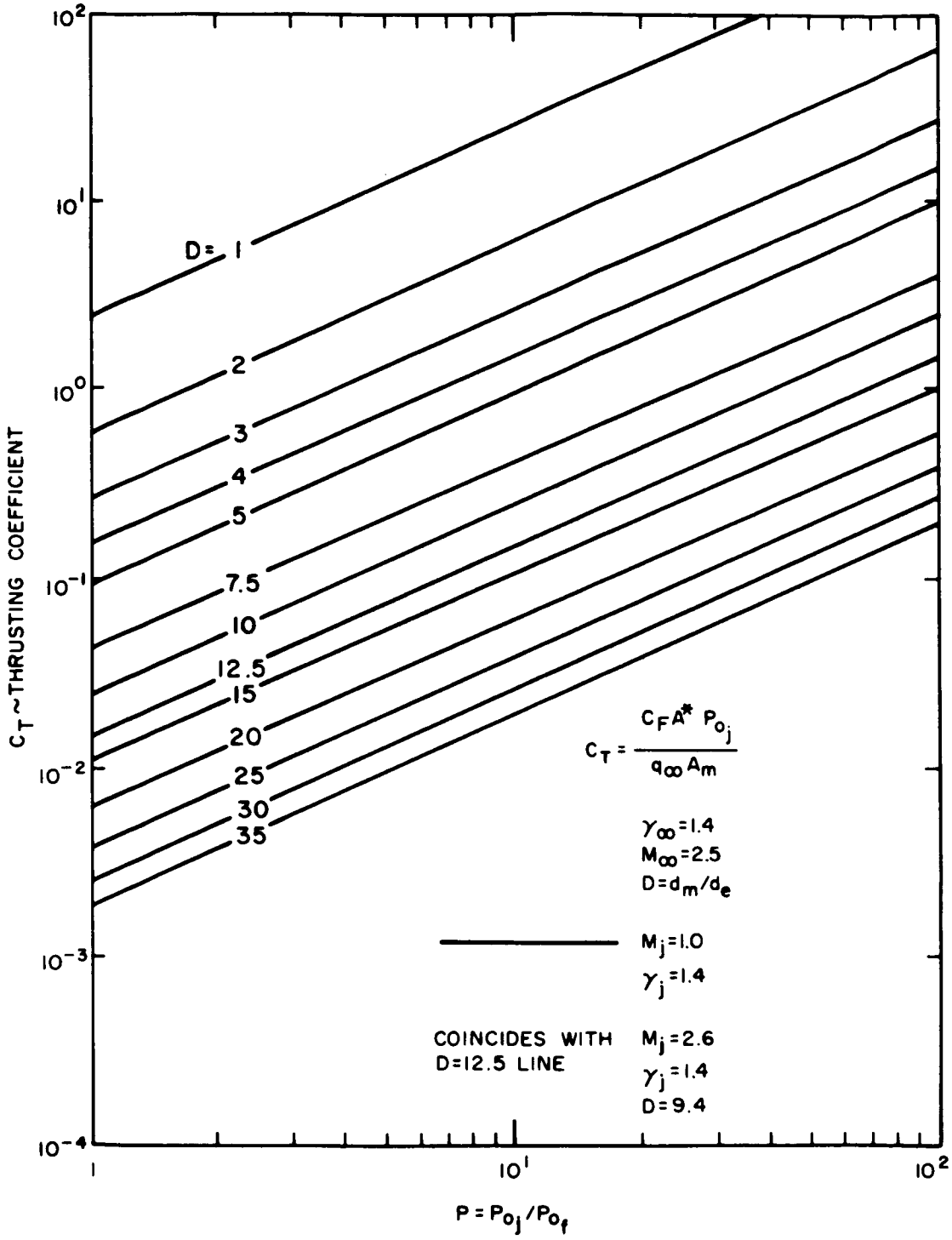

Figure C-2. Thrusting coefficient - sonic jet.

APPENDIX D

DETERMINATION OF THE JET BOUNDARY

As discussed in the text, the method of Charwat (Ref. 8) was used in computing the contours of the jet boundaries. The method starts by assuming a Prandtl-Meyer expansion to ambient pressure and isentropic flow along the boundary. Since the pressure is constant and P_t is constant, then Mach number and associated properties such as A^* are constant. The flow is made determinant by writing

$$d(P/P_t) = \frac{\partial(P/P_t)}{\partial(A/A_j^*)} \frac{dA}{A_j^*} + \frac{\partial(P/P_t)}{\partial\theta} d\theta = 0 \quad , \tag{D-1}$$

$$\frac{dA}{A_j^*} = 2\left(\frac{A_{e_j}}{A_j^*}\right)\left(\frac{r}{r_{e_j}}\right) \quad d\left(\frac{r}{r_{e_j}}\right) \quad , \tag{D-2}$$

and $$\frac{\partial(P/P_t)}{\partial\theta} = \frac{\gamma_j M^2 (P/P_t)}{(M^2-1)^{1/2}} \tag{D-3}$$

A function ψ is defined which is constant along the jet boundary. It is expressed as follows, using isentropic flow relations

$$\psi = \frac{2}{\gamma_j+1} \frac{(M^2-1)^{1/2}}{M^2(A/A_j^*)_M} \left(\frac{A}{A_j^*}\right)_{M_j} \tag{D-4}$$

After integration, Eqs. D-1 through D-4 yield the following relation

$$\theta - \theta_o = \psi\left[1 - (r/r_{e_j})^2\right] \qquad \text{where} \qquad \text{(D-5)}$$

θ_o is the initial expansion angle at the edge of the nozzle which is known in terms of the Prandtl-Meyer Function and nozzle divergence half angle at the exit

$$\theta_o = \nu_M + \nu_{M_{e_j}} + \theta_j \qquad \text{(D-6)}$$

From equation D-5, the shape of the jet boundary in generalized coordinates is determined.

$$X = \int_{1/\rho_o}^{R} \cot\left[\phi(1-R^2)\right]dR \qquad \text{(D-7)}$$

where

$$X = x/(r_{e_j}\rho_a)\ ,\ R = r/(r_{e_j}\rho_a)$$

$$\rho_a = r_a/r_j = \left[1 + (\theta_o/\psi)\right]^{1/2}$$

$$\phi = \psi\rho_a^2 = (\psi + \theta_o)$$

The shape of the boundary is determined from equation D-7 once ϕ and ρ_a are specified. ϕ and ρ_a contain the influence of the four physical parameters M_{e_j}, θ_j, (P/P_{e_j}) and γ_j.

Comparisons of Charwat's method with method of characteristic solutions were made in Figures 22 and 23. Some additional comparisons are made in Figures D-1 through D-4. A comparison of jet boundary shapes calculated with Charwat's approximate method and method of characteristic solutions[43] are shown in Figures D-1 and D-2 for $M_{e_j} = 5.35$ and $\gamma_j = 1.24$, zero nozzle divergence angle and $P_{e_j}/P_d = 9.8$ and 31.9 respectively. A comparison of the approximate jet boundary method with characteristic solutions[42] were also made to test the method as the nozzle divergence angle is varied. Figures D-3 and D-4. Good agreement is obtained at a pressure ratio of $P_{e_j}/P_d = 10$ for nozzle divergence angles from zero to fifteen degrees (Figure D-3). However at the higher pressure ratio $P_{e_j}/P_d = 100$ and a nozzle divergence angle of 20.66 the approximate method does not compare as favorably with the method of characteristic solutions[43]. Figure D-4. Other comparisons at high pressure ratios and large divergence angles could not be made due to a lack of method of characteristic solutions.

We have found that the approximate method is suitable for calculations over the pressure ratios of interest and the desired degree of accuracy (10 percent) for nozzles with zero divergence angle, and properly accounts for variations in nozzle divergence angle at low pressure ratios. The approximate method at high pressure ratios and large nozzle divergence angles give reasonable results but its overall suitability for these conditions can only be judged when a comparison of the theoretical method is made with experimental results in Phase II.

For the range of parameters of interest in the present investigation, the jet terminal shock location x_s/r_{e_j} varies from 6 to 20 for $M_{e_j} = 3.0$, $\gamma_j = 1.4$. It can be shown that the normalized distance to the jet terminal shock, x_s/r_{e_j}, decreases with increasing

jet exit Mach number for P_{o_j}/P_{o_f} held constant. Thus the longitudinal variation of the terminal shock wave location will be less for a $M_{e_j} = 5.35$ nozzle than for a $M_{e_j} = 3.0$. Therefore, when evaluating the comparison of the method of characteristics solution with the approximate calculations, our attention should be concentrated on the $x_s/r_{e_j} \leq 20$ longitudinal distance region.

The results of the jet boundary calculation are used in two places in the analysis. First, the jet boundary is used in conjunction with the terminal shock location to determine the plume shoulder location (Section 4.2.2.4). Secondly, it is used in the calculation of the mass entrained along the jet boundary. (Section 4.2.5).

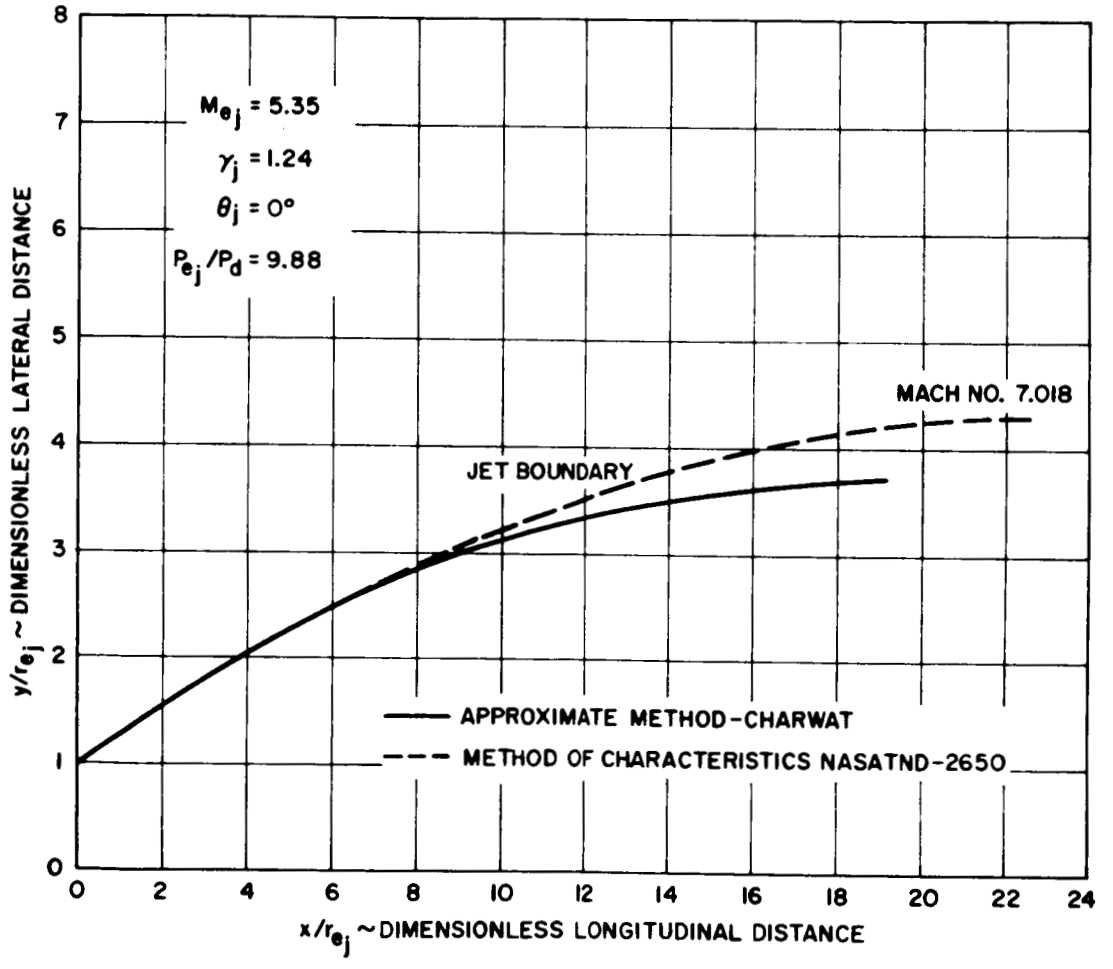

Figure D-1. Comparison of approximate method with characteristic solutions $\theta_{e_j}=0^{o}$ $M_{e_j}=5.35$ $P_{e_j}/P_d=9.88$.

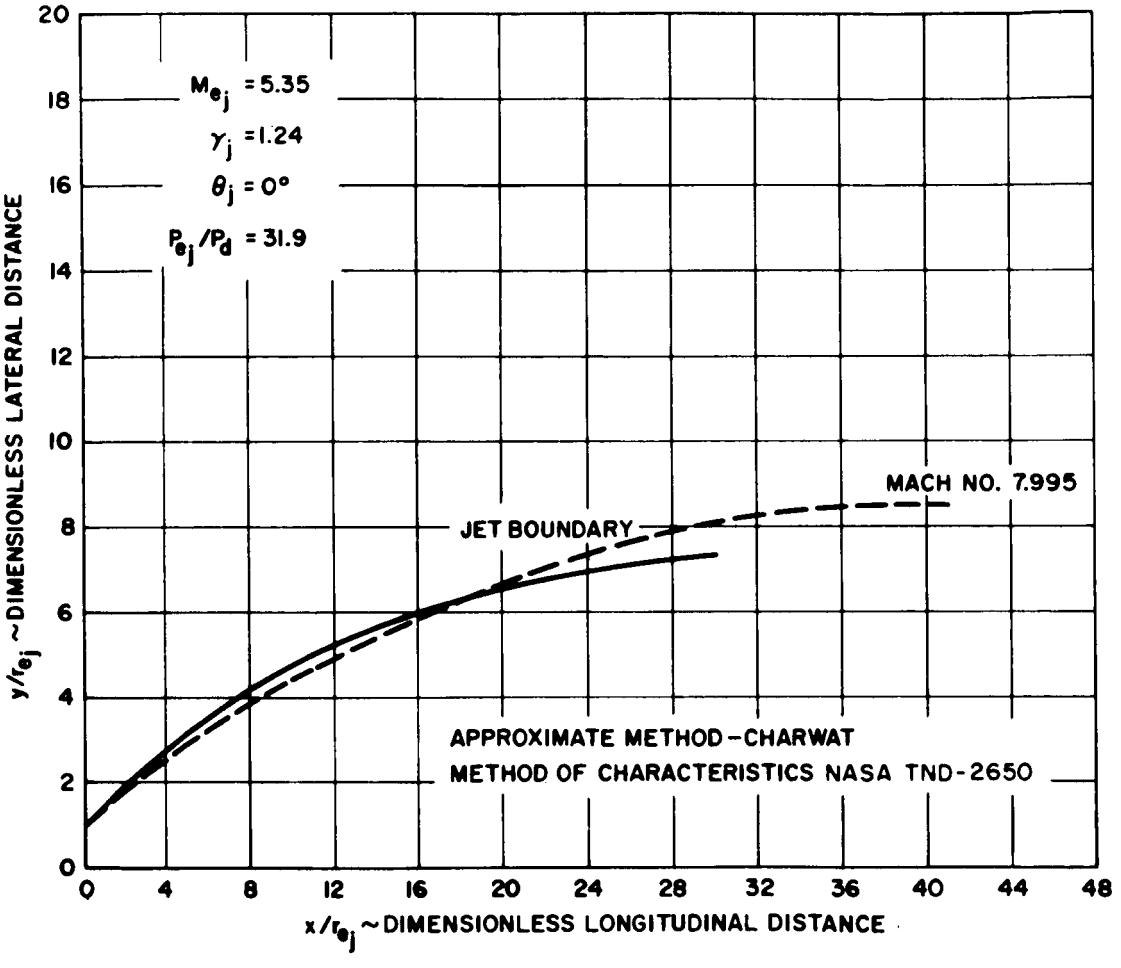

Figure D-2. Comparison of approximate method with characteristic solutions $\theta_{e_j}=0^{\circ}$ $M_{e_j}=5.35$ $P_{e_j}/P_d=31.9$.

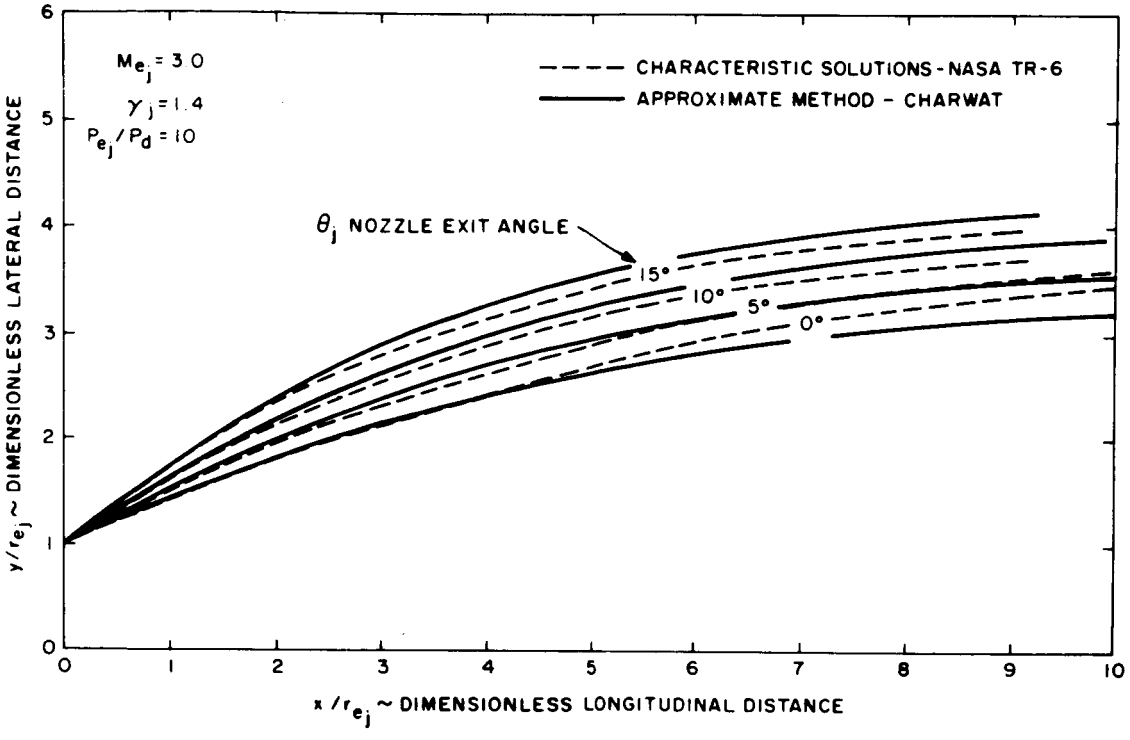

Figure D-3. Comparison of approximate and exact solutions with variations in nozzle divergence angle $P_{e_j}/P_d = 10$.

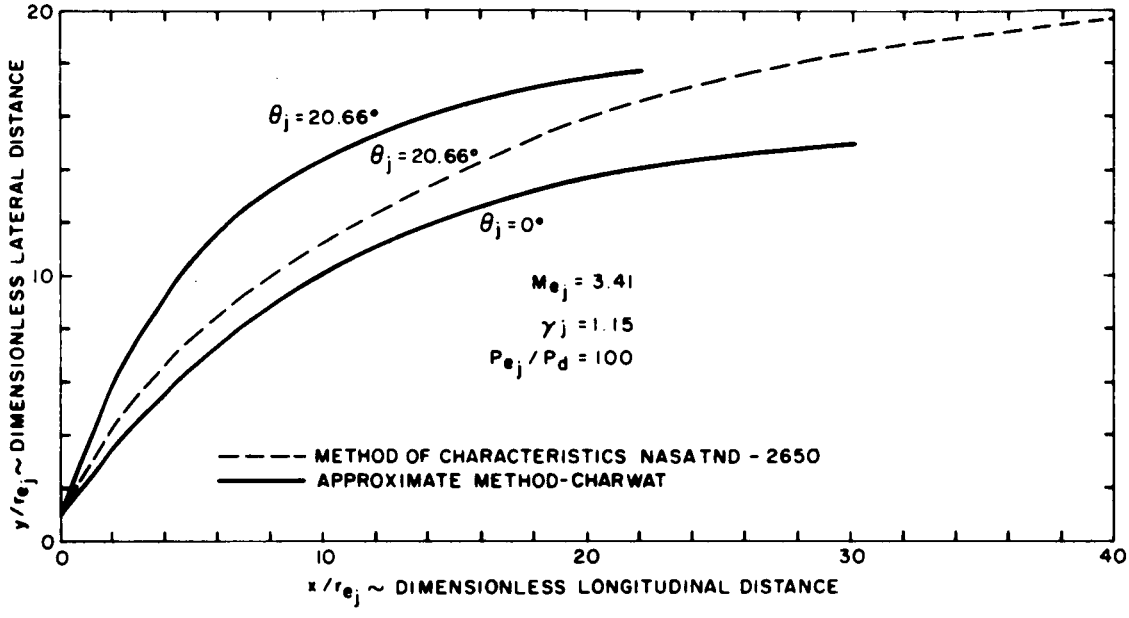

Figure D-4. Jet boundary comparison at large pressure ratio and nozzle divergence angle.

APPENDIX E

THE JET TERMINAL SHOCK LOCATION

The jet terminal shock location on the centerline of the retrorocket is positioned so that the stagnation pressure of the shocked free stream gas, $P_{o_{f_\infty}}$ is equal to the recovered stagnation pressure of the jet, $P_{o_{f_j}}$, at the free stagnation point.

The density and Mach number decay along the centerline is determined from the Hill-Draper[E-1] analytical approximations for flow from a nozzle into a vacuum.

The relationship between longitudinal distance and density is

$$\frac{x_1}{r_j^*} = \left\{ \left(\frac{2}{\gamma_j + 1} \right)^{1/\gamma_j - 1} \frac{\lambda_j}{\sqrt{\pi}} \frac{C_j^*}{C_j} \frac{\rho_{o_j}}{\rho_{1_j}} \right\}^{1/2} \tag{E-1}$$

The local Mach number is found to be

$$M_j = \left(\frac{2}{\gamma_j - 1} \right)^{1/2} \left\{ \left(\frac{\rho_{o_j}}{\rho_{1_j}} \right)^{\gamma_j - 1} - 1 \right\}^{1/2} \tag{E-2}$$

where

$$\lambda_j = \left\{ \sqrt{\pi} \left(1 - C_{F_j} / (C_j C_{F_{MAX}}) \right) \right\}^{-1} \tag{E-3}$$

$$C_j = V_j / V_{max} \tag{E-4}$$

where V_{max} is the limiting velocity of the jet flow.

$$C_{F_{MAX}} = \frac{2\gamma_j}{\sqrt{\gamma_j^2 - 1}} - \left[\frac{2}{\gamma_j + 1}\right]^{1/\gamma_j - 1} \tag{E-5}$$

$$C_{F_j} = \sqrt{\frac{2\gamma_j^2}{\gamma_j - 1}\left[\frac{2}{\gamma_j+1}\right]^{\frac{\gamma_j+1}{\gamma_j-1}}\left[1 - \left\{\frac{P_{e_j}}{P_{o_j}}\right\}^{\frac{\gamma_j-1}{\gamma_j}}\right] + \frac{A_{e_j}}{A_j}\frac{P_{e_j}}{P_{o_j}}} \tag{E-6}$$

The relationship between the free stream total pressure and the recovered stagnation pressure downstream of the bow shock (assuming supersonic free stream conditions) is

$$\frac{P_{o_\infty}}{P_{o_{f_\infty}}} = \left(\frac{2\gamma_\infty}{\gamma_\infty + 1} M_\infty^2 - \frac{\gamma_\infty - 1}{\gamma_\infty + 1}\right)^{1/(\gamma_\infty - 1)} \left(\frac{(\gamma_\infty - 1)M_\infty^2 + 2}{(\gamma_\infty + 1) M_\infty^2}\right)^{\gamma_\infty/(\gamma_\infty - 1)} \tag{E-7}$$

and between the jet total pressure and the recovered stagnation pressure

$$\frac{P_{o_j}}{P_{o_{f_j}}} = \left(\frac{2\gamma_j}{\gamma_j + 1} M_j^2 - \frac{\gamma_j - 1}{\gamma_j + 1}\right)^{1/(\gamma_j - 1)} \left(\frac{(\gamma_j - 1)M_j^2 + 2}{(\gamma_j + 1)M_j^2}\right)^{\gamma_j/(\gamma_j - 1)} \tag{E-8}$$

Comparisons of theoretical predictions for the location of the terminal shock for supersonic jets into oncoming streams with experimental data of Hayman and McDearman are discussed in Section 4.2.2.3. The preceding analysis has also been applied to the problem of locating the terminal shock in exhaust flows from sonic nozzles into oncoming supersonic streams. A comparison of the predictions of the Hill-Draper model for the centerline Mach number variation downstream of the nozzle exit plane with the method of

characteristic solutions of Owen and Thornhill[E-2] is made in Figure E-1. The Hill-Draper Method predicts a Mach number variation which is always within about 10 percent of the method of characteristic calculations. A comparison of the location of the terminal shock as predicted with the analysis and the experimental results of Romeo and Sterrett[E-3] for a sonic jet into an oncoming M = 6.0 stream is made in Figure E-2. The approximate results are within 10 per cent of the experimental results. It should be noted that Romeo and Sterrett found that the terminal shock location correlated as a function of $P_{o_j}/P_{o_{f_j}}$ or $P_{o_j}/P_{o_{f_\infty}}$.

REFERENCES

E-1 Hill, J.A. F.H. and Draper, J.S., "Analytical Approximation For the Flow From a Nozzle Into a Vacuum", Journal of Spacecraft and Rockets. Vol. 3, No. 10, October 1966, pp. 1552-1554.

E-2 Owen, P.L. and Thornhill, C.K., "The Flow In an Axially-Symmetric Supersonic Jet from a Nearly Sonic Orifice Into a Vacuum", A.R.E. Report 30/48, September 1948.

E-3 Romeo, D.J. and Sterrett, J.R., "Flow Field for a Sonic Jet Exhausting Counter to a Hypersonic Mainstream", AIAA Journal, Vol. 3, No. 3, March 1965, pp. 544-546.

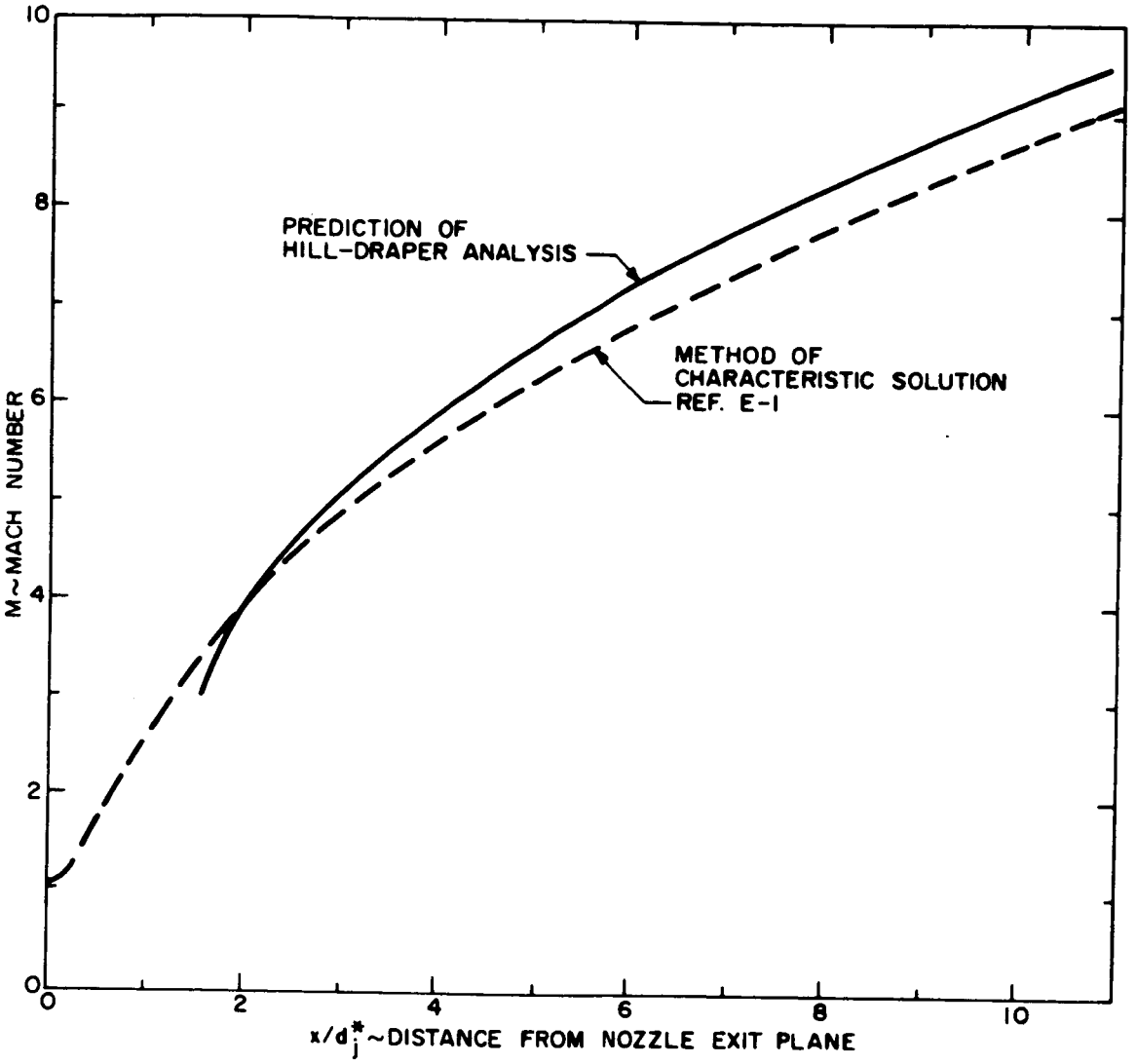

Figure E-1. Comparison of prediction of Hill-Draper model for centerline Mach number variation with method of characteristic solutions - sonic jet.

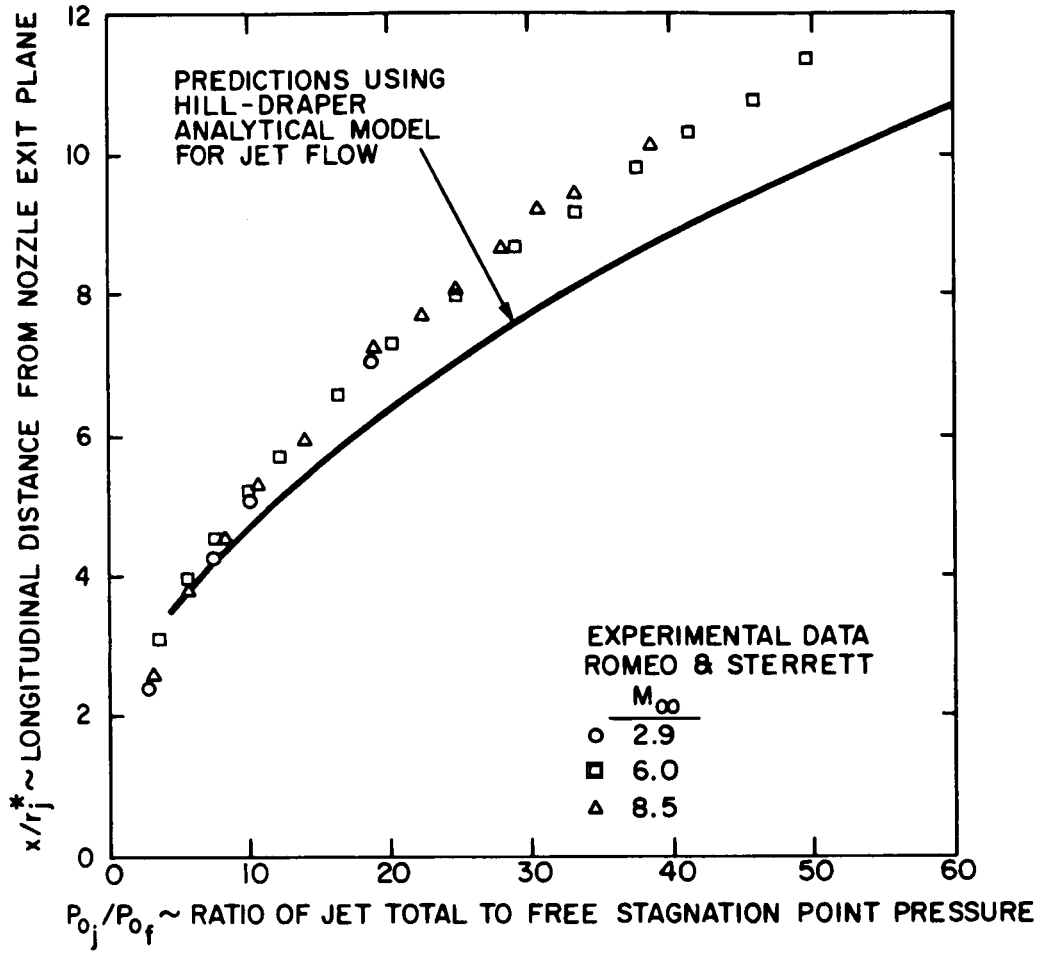

Figure E-2. Terminal shock location - sonic jet into counter current.

APPENDIX F

VARIATION OF BLUNTING SPHERE DIAMETER WITH MACH NUMBER

The flow geometry is shown in Figure 30. We assume that the (axial) jet velocity is brought to a standstill against P_{o_f}, the free stream pitot pressure, and that the jet/free-stream interface is a hemisphere. Then the jet momentum leaving the control volume is also axial and its total pressure is P_{o_f}.

For momentum balance in the control volume, the drag on the hemisphere must equal the change of jet momentum entering and leaving the control volume. The jet momentum entering is simply the jet thrust corrected for the finite back pressure. Hence,

$$D = T + \dot{w} V_\ell \tag{F-1}$$

or

$$C_D q_\infty A_f = \dot{w} V_j + A_e P_{e_j} - A_e P_d + \dot{w} V_\ell \tag{F-2}$$

where A_f is the blunting sphere base area, $\dot{w}$ is the jet mass flow, V_j and V_ℓ are the jet velocity in the nozzle exit plane and hemisphere corner respectively, and P_{e_j} and P_d are the jet pressure inside and outside of the nozzle exit plane respectively.

Reference F.1 is a compilation of experimental drag coefficients for hemispheres. To be consistent with their definition, we must assume that the base pressure is P_∞. This is a good assumption when the hemisphere is the nosecap of a long cylinder. Recent experimental

data on blunt entry shapes[F-2] has shown that the dead air or base pressure is slightly less than P_∞. For the isolated hemisphere we will use $P_d/P_\infty = 1.0$.

The vacuum thrust of the jet is given as

$$T = \dot{w} V_j + A_e P_{e_j} \tag{F-3}$$

Using the continuity equation

$$\dot{w} = \rho_j A_e V_j, \tag{F-4}$$

the definition of sound speed

$$a_j^2 = \frac{\gamma_j P_{e_j}}{\rho_j} \tag{F-5}$$

and Mach number

$$M_j = V_j/a_j, \tag{F-6}$$

we obtain

$$T = \dot{w} V_j \left(1 + \frac{P_{e_j}}{\rho_j V_j^2}\right) = \dot{w} V_j \left(1 + \frac{a_j^2}{\gamma_j V_j^2}\right) = \dot{w} V_j \left(1 + \frac{1}{\gamma_j M_j^2}\right) \tag{F-7}$$

Therefore, the momentum balance equation becomes

$$C_D q_\infty A_f = \dot{w} V_j \left(1 + \frac{1}{\gamma_j M_j^2} + \frac{V_\ell}{V_j}\right) - A_e P_\infty \tag{F-8}$$

or

$$C_D \frac{A_f}{A_m} = \frac{\dot{w}V_j}{q_\infty A_m} \left(1 + \frac{1}{\gamma_j M_j^2} + \frac{V_\ell}{V_j} \right) - \frac{A_e}{A_m} \frac{P_\infty}{q_\infty} \qquad \text{(F-9)}$$

where A_m is the base area.

The thrusting coefficient C_T is defined as

$$C_T = \frac{T}{q_\infty A_m} = \frac{\dot{w}V_j}{q_\infty A_m} \left(1 + \frac{1}{\gamma_j M_j^2} \right) \qquad \text{(F-10)}$$

Therefore,

$$C_D \frac{A_f}{A_m} = C_T + \frac{C_T}{1 + \frac{1}{\gamma_j M_j^2}} \cdot \frac{V_\ell}{V_j} - \frac{A_e}{A_m} \frac{P_\infty}{q_\infty} \qquad \text{(F-11)}$$

Since

$$q_\infty = 1/2 \, \rho_\infty V_\infty^2 = \frac{\gamma}{2} P_\infty M_\infty^2 \qquad \text{(F-12)}$$

we obtain

$$C_D \frac{A_f}{A_m} = C_T \left(1 + \frac{V_\ell / V_j}{1 + \frac{1}{\gamma_j M_j^2}} \right) - \frac{A_e}{A_m} \frac{2}{\gamma_\infty M_\infty^2} \qquad \text{(F-13)}$$

By assuming that the jet mass flow is isentropically accelerated from its stagnation pressure P_{o_f} to the corner static pressure P_∞, we

can find the jet layer Mach number by interpolating in Ref. F.3 or by rearranging

$$\frac{P_{o_f}}{P_\infty} = \left(1 + \frac{\gamma_j - 1}{2} M_\ell^2\right)^{\gamma/\gamma-1} \tag{F-14}$$

to obtain

$$M_\ell = \left(\frac{(P_{o_f}/P_\infty)^{\frac{\gamma_j - 1}{\gamma_j}} - 1}{\frac{\gamma_j - 1}{2}} \right)^{1/2} \tag{F-15}$$

By neglecting the mixing of the jet and free stream

$$a_{o_j} = a_{o_\ell} \tag{F-16}$$

and

$$a_j^* = a_\ell^*$$

Therefore

$$\frac{V_\ell}{V_j} = \frac{V_\ell / a_\ell^*}{V_j / a_j^*} \tag{F-17}$$

Since we know the values of M_ℓ from above and M_j, we can find V_ℓ/a^* and V_j/a^* tabulated in Ref. F.3.

The final expression then is

$$\frac{A_f}{A_m} = \frac{d_f^2}{d_m^2} = \frac{C_T}{C_D}\left(1 + \frac{(V_\ell/a^*)/(V_j/a^*)}{1 + \frac{1}{\gamma_j M_j^2}}\right) - \frac{A_e}{A_m}\,\frac{2}{C_D \gamma_\infty M_\infty^2} \qquad \text{(F-18)}$$

If M_∞ is supersonic, the back pressure term is small. For a given nozzle, V_j/a^* is fixed. If M_j is supersonic, $\frac{1}{\gamma_j M_j^2} < 1$ and

$$\frac{d_f}{d_m\sqrt{C_T}} \approx \frac{1}{\sqrt{C_D}}\left(1 + \frac{V_\ell}{a^*}\,\frac{a^*}{V_j}\right)^{1/2} \qquad \text{(F-19)}$$

Since V_ℓ/a^* changes slowly with M_∞

$$\frac{d_f}{d_m}\sqrt{\frac{C_D}{C_T}} = K \qquad \text{(F-20)}$$

where K is a weak function of M_∞ and M_j.

REFERENCES

F.1 Katz, J.R., "Pressure and Wave Drag Coefficients for Hemisphere, Hemisphere-Cones and Hemisphere-Ogives," U.S. Naval Ordnance Test Station, NAVORD Report 5849, March 1958.

F.2 Robinson, R.C., Gombucci, B.J., and George, R.E., "Fluctuating Pressures On The Afterbodies of Fine Blunt Atmosphere Entry Vehicles," NASA TN D 4591, May 1968.

F.3 Ames Research Staff, "Equations, Tables and Charts for Compressible Flow," NACA TR 1135, 1953.

APPENDIX G

LOCATION OF THE CENTER OF THE BLUNTING SPHERE, $M_\delta \neq 1.0$

For specific M_∞ and M_{e_j}, and for a given P_d/P_{o_f}, the diameter of the blunting sphere has been determined by a momentum balance in Section 4.2.3.1. In Section 4.2.3.2, the location of the center of the blunting sphere was determined by assuming chocked flow in an annulus running from the edge of the jet to the interface. In this Appendix it is shown that this assumption can be relaxed with negligibly small effect on the blunting sphere center location.

Referring to Figure (G-1), x_i/d_{e_j}, y_i/d_{e_j}, and d_f/d_{e_j} are known for a specific situation. Then continuity requires:

$$\left\{2\pi y_1 + \pi d_f \sin\theta_d\right\} \frac{\delta}{2} (\rho_1 u_1) = \dot{m}_j \tag{G-1}$$

In this equation, it has been assumed that the effective density is ρ_1, the density just inside the first interface, and from the geometry of Figure (G-1)

$$(d_f/2 - g) \sin\theta_d = y_1 \tag{G-2}$$

Dividing (G-1) by $d_{e_j}^2 P_{o_j} a_{o_j}$, and (G-2) by d_{e_j}, and combing the equations, it is possible to show that:

$$\sin\theta_d \left\{1 - 4\left(\frac{d_{e_j}}{d_f}\right)^2 \left(\frac{y_1}{d_{e_j}}\right)^2 / \sin^2\theta_d\right\} = \left[\left(\frac{d_{e_j}}{d_f}\right)^2 (P_{o_j}/P_{o_f})\right] \cdot \frac{(P_{e_j}/P_{o_j}) M_{e_j} \sqrt{T_{o_j}/T_{e_j}}}{(P/P_{o_f}) M_1 \sqrt{T_{o_j}/T_1}} \tag{G-3}$$

The ratio P_e/P_{o_f} as a function of θ_d is determined by the modified Newtonian expression, and M_e and T_e/T_{o_j} from the isentropic flow tables. If equation (G-3) is multiplied by $\sin\theta_d$, it can be written in the following form.

$$\sin^2\theta_d - \left[\left(\frac{d_{e_j}}{d_f}\right)^2\left(\frac{P_{o_j}}{P_{o_f}}\right)\right] \cdot \frac{(P_{e_j}/P_{o_j})M_{e_j}\sqrt{T_{o_j}/T_{e_j}}}{(P/P_{o_f})M_1\sqrt{T_{o_j}/T_1}} \sin\theta_d$$

$$-4\left(\frac{d_{e_j}}{d_f}\right)^2 (y/d_{e_j})^2 = 0 \qquad \text{(G-4)}$$

This is simply a quadratic equation, so that $\sin\theta_d$ can be solved for explicitly. This calculation has been made for:

$$M_\infty = 2.5,\ M_{e_j} = 3.0$$

$$P_d/P_{o_f} = .2,\ P_{o_j}/P_{o_f} = 36,\ 147,\ 144$$

The value of θ_d varies very little and is approximately 25°. Once θ_d has been determined, the location of the center of the blunting sphere is determined directly by the relation:

$$x_c/d_{e_j} = x_1/d_{e_j} - y/d_{e_j} \cot\theta_d \qquad \text{(G-5)}$$

The results of these calculations are shown in Figure (G-2), where the corrected blunting spheres are superimposed on the results of Section 4.2.3. It can be seen that the change is quite small.

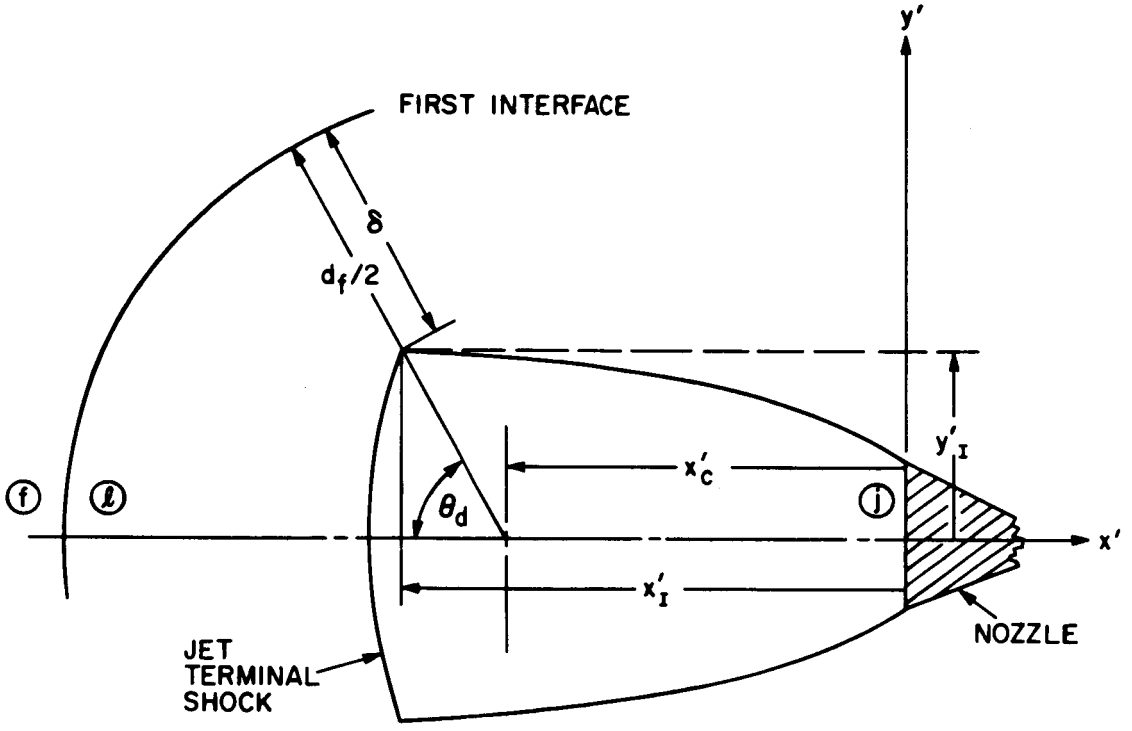

Figure G-1. Geometry for locating center of blunting sphere.

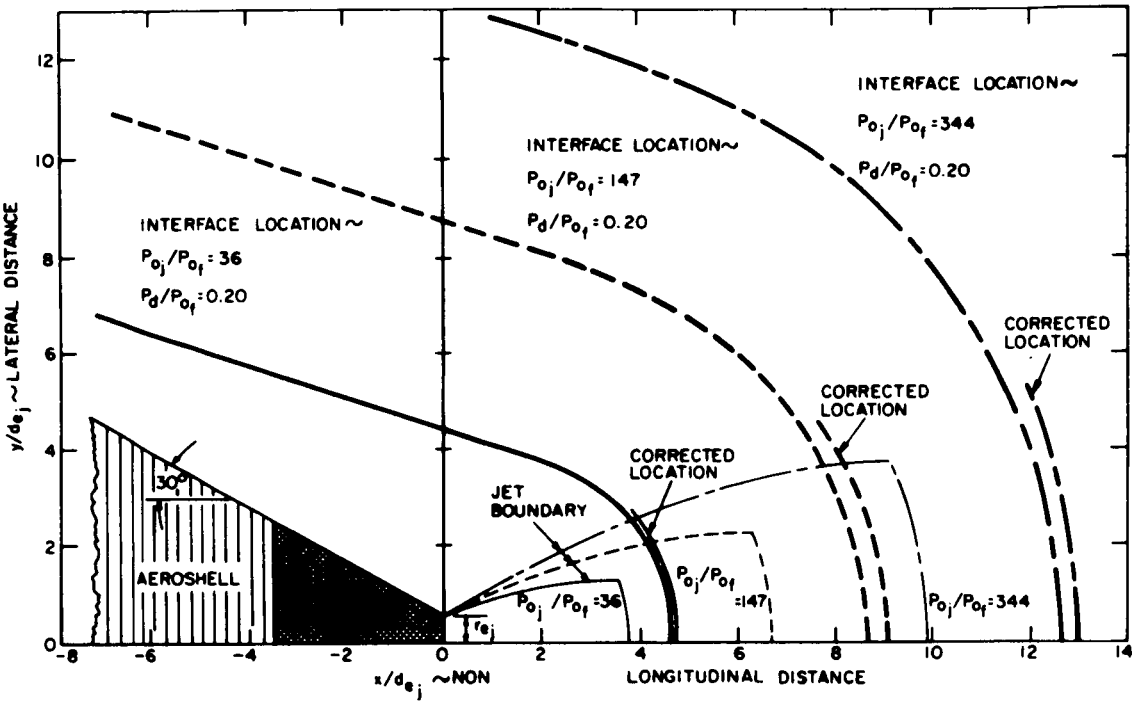

Figure G-2. Superposition of three possible flow field configurations, $\theta_v = 30^o$.

APPENDIX H

MASS ENTRAINMENT RATE FOR HETEROGENEOUS TURBULENT MIXING

Consider the turbulent mixing of two parallel streams of different density moving at different velocities, as shown in the sketch below.

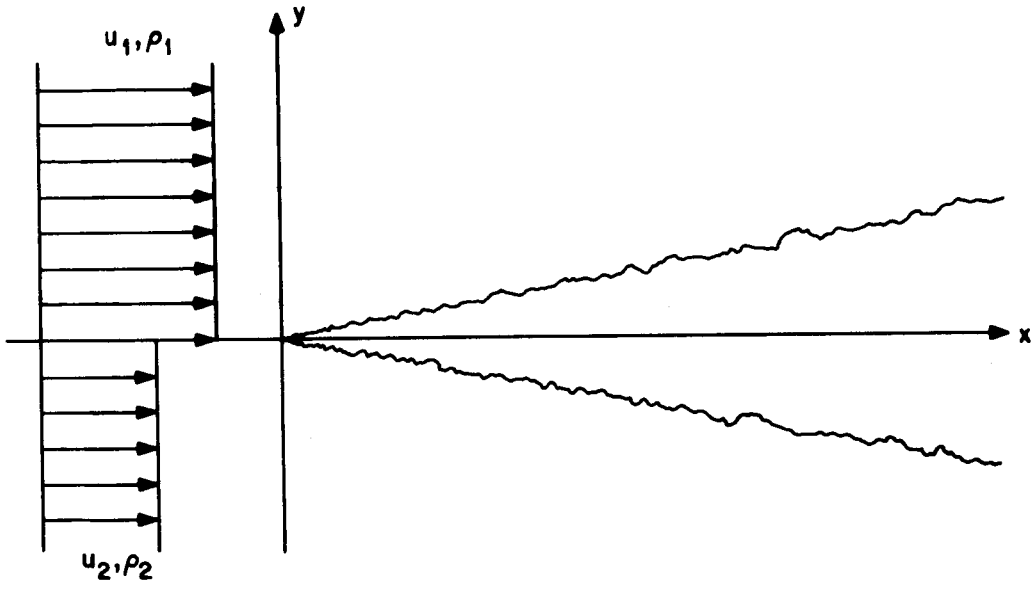

Both fluids are assumed to be incompressible. This problem has been studied by several authors. The most recent treatment of it appears in References H-1 and H-2, where due account has been taken of the displacement of the dividing streamline in the turbulent mixing region. A history of previous solutions to the problem is given in Reference H-1. The purpose of this Appendix is to compute the rate of mass entrainment of the external fluid by turbulent region.

Assuming that the pressure gradient in the x-direction is zero, the turbulent boundary layer equations admit a self-similar

solution in which,

$$\rho = \rho\ (\xi)$$

$$u = u\ (\xi)$$

$$v = v\ (\xi)$$

where $\xi = (\sigma y)/x$

and σ is a constant to be determined experimentally. (The notation will correspond to that of References H-1 and H-2). Letting ξ_o denote the value of ξ at which the stream function is zero; i.e., the location of the dividing streamline, consider mass balance for the control volume shown below.

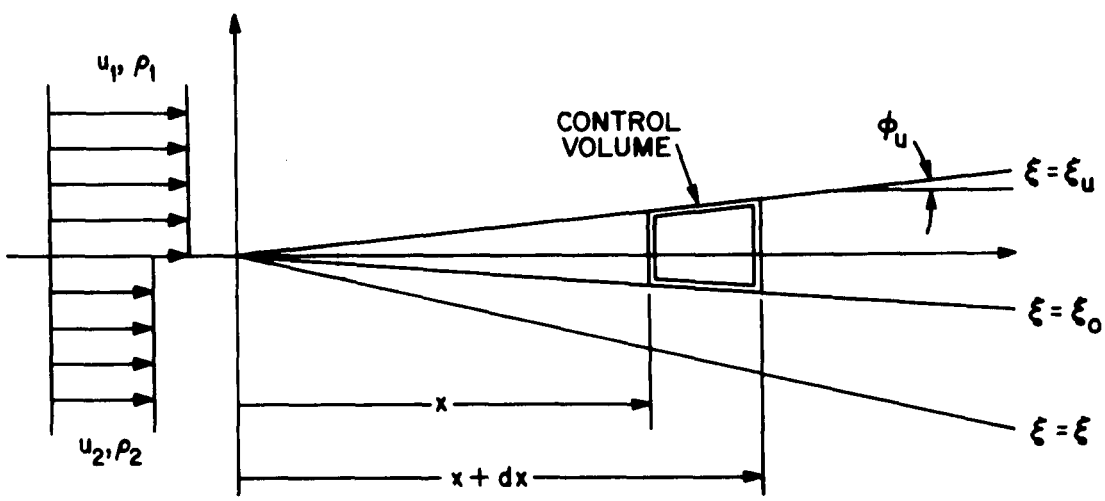

Defining $d\dot{m}_1$ to be the difference in mass flow between a station at x and a station at (x + dx) for the upper portion of the mixing layer,

$$d\dot{m}_1 = \int_{y_o(x+dx)}^{y_u(x+dx)} \rho\ (x+dx, t)u(x+dx_1 t)dt - \int_{y_o(x)}^{y_u(x)} \rho\ (x_1 t)u(x_1 t)\ dt \qquad \text{(H-1)}$$

$$\dot{dm}_l = \rho(\xi_u)\,[u(\xi_u)\,\sin\phi_u - v(\xi_u)\,\cos\phi_u]\,\frac{dx}{\cos\phi_u} \tag{H-2}$$

$$\dot{dm}_l = \rho(\xi_u)\,[u(\xi_u)\,\tan\phi_u - v(\xi_u)]\,dx \tag{H-3}$$

so,

$$\frac{\dot{dm}_l}{dx} = \rho(\xi_u)\,[u(\xi_u)\,\tan\phi_u - v(\xi_u)] \tag{H-4}$$

Defining the mass entrainment coefficient for the upper fluid as

$$C_{q_l} \equiv \frac{1}{\rho_l u_l}\,\frac{\dot{dm}_l}{dx} \tag{H-5}$$

Equation (H-4) gives,

$$C_{q_l} = \frac{\rho(\xi_u)}{\rho_l u_l}\,\left[u(\xi_u)\,\frac{\xi_u}{\sigma} - v(\xi_u)\right] \tag{H-6}$$

For a turbulent Schmidt number equal to unity, the "velocity function" is defined in terms of the self-similar dependent variable $F(\xi)$, by the expression,

$$\psi = U \times F(\xi) \tag{H-7}$$

(See Reference H-1, Section III-4).

where

$$U = \frac{u_1 + u_2}{2}$$

$$u = \frac{\partial\psi}{\partial y} \tag{H-8}$$

$$v = -\frac{\partial\psi}{\partial x}$$

Equation H-6 may then be written in the form

$$C_{q_1} = \frac{1}{1+\lambda} \frac{\rho(\xi_u)}{\rho_1} F(\xi_u) \tag{H-9}$$

where

$$\lambda = \frac{u_1 - u_2}{u_1 + u_2} \tag{H-10}$$

Similarly, a mass entrainment coefficient may be defined for the lower portion of the mixing layer as

$$C_{q_2} = \frac{1}{\rho_1 u_1} \frac{d\dot{m}_2}{dx} \tag{H-11}$$

Then considering a control volume below the stagnation streamline, conservation of mass leads to the following expression for C_{q_2}:

$$C_{q_2} = - \frac{\rho(\xi_u)}{\rho_1} \left(\frac{1}{1+\lambda}\right) F(\xi_u) \tag{H-12}$$

In Reference H-2, a transformation found by Von Karman which will reduce the differential equation and boundary conditions for the turbulent dependent variable F to those for a laminar variable f is given. This transformation is: (Reference H-1, p. 56, Equations III-4.23).

$$\frac{df}{d\eta} = \frac{\sigma}{1+\lambda} \frac{dF}{d\xi} \tag{H-13}$$

$$\eta = 2\sqrt{1+\lambda}\,\xi \tag{H-14}$$

or, as derived from these two:

$$F = \frac{\sqrt{1+\lambda}}{2\sigma} f \tag{H-15}$$

Cq_1 and Cq_2 for turbulent mixing may then be obtained in terms of f and η as tabulated in Reference H-1. Also, as discussed in Section III-5 of Reference H-1, for large magnitudes of η,

$$f(\eta) \sim \eta_u - (\eta_o + \alpha) \text{ as } \eta \to +\infty \tag{H-16a}$$

$$f(\eta) \sim \left(\frac{1-\lambda}{1+\lambda}\right)(\eta_2-\eta_o) - \beta \text{ as } \eta \to -\infty \tag{H-16b}$$

where η_o denotes the location of the dividing streamline for laminar mixing. It will now be assumed that η_u and η_ℓ correspond to the upper and lower edges of the mixing layer. The upper and lower edges of the mixing region are defined as those values of η for which either

$$u_u = u_1 - (.05)(u_1-u_2) \tag{H-17a}$$

$$u_1 = u_2 + (.05)(u_1-u_2) \tag{H-17b}$$

or

$$\rho_u = \rho_1 + (.05)(\rho_2-\rho_1) \tag{H-18a}$$

$$\rho_2 = \rho_2 - (.05)(\rho_2-\rho_1) \tag{H-18b}$$

whichever is larger. Using Equations (H-14) through (H-16), Equations (H-9) and (H-12) may then be written in the forms:

$$Cq_1 = \left(\frac{1-\Gamma}{1+\Gamma}\right)\left[\frac{1}{2\sigma\sqrt{1+\lambda}}\right]\left(\frac{\rho}{\rho_2}\right)_u\left[\eta_u-\eta_o-\alpha\right] \tag{H-19a}$$

$$Cq_2 = -\left(\frac{1-\Gamma}{1+\Gamma}\right)\left[\frac{1}{2\sigma\sqrt{1+\lambda}}\right]\left(\frac{\rho}{\rho_2}\right)_2\left[\left(\frac{1-\lambda}{1+\lambda}\right)(\eta_2-\eta_o)-\beta\right] \tag{H-19b}$$

Values of η_o, α and ρ are tabulated in Reference H-1 for different values of λ and Γ, and η_u, η_ℓ, may be interpolated from velocity and density profiles which are also tabulated in Reference H-1. The choice of η_u, η_ℓ is governed by definitions H-17 or H-18. Several values of σ have been measured by Baker and Weinstein, and are tabulated in Reference H-2. The results of carrying out the indicated computations for Cq_1 and Cq_2 using informations from References H-1 and H-2, for one value of λ and three values of Γ are noted in Figure 43 of the main text. Figure 44 shows the variation of mass entrainment coefficients with velocity ratio, for the special case of homogeneous mixing $\rho_2 = \rho_1$.

The approximate formula chosen for the mass entrainment coefficient (i.e. $Cq = 0.05\ (\rho_2/\rho_1)^{1/2}$) contains no constants whose values have to or can be chosen later from the results of the wind tunnel tests. We have tried to develop a self-consistent theory without adjustable constants. Therefore if any differences between experimental results and theoretical predictions are found, they result directly from the choices made for the elements contained in the theoretical analysis.

REFERENCES

H-1 Baker, R. L., and Weinstein, H., "Analytical Investigation of the Mixing of Two Parallel Streams of Dissimilar Fluids," NASA CR-956 - January, 1968.

H-2 Baker, R. L., and Weinstein, H., "Experimental Investigation of the Mixing of Two Parallel Streams of Dissimilar Fluids," NASA CR-957, January, 1968.

APPENDIX I

FLUID ENTRAINMENT BY THE OUTER INTERFACE MIXING REGION

This Appendix describes the computation of the fraction of the jet mass flux which is entrained by the mixing layer at the jet-shocked gas interface. Figure (I-1) depicts the geometry of the problem.

The x, y coordinate system is located along the inviscid interface, which is assumed to be a portion of a sphere. It will be assumed that the mass flux per unit length entrained by the mixing region is locally equal to the two-dimensional mass flux per unit span for constant-pressure mixing. Then,

$$\frac{d\dot{m}_1^*}{2\pi r(x)} = d\dot{m}_1 = \rho_1 u_1 C_{q_1} dx$$

where

$\dot{m}_1^*$ = mass flux in axisymmetric, variable-pressure case

$\dot{m}_1$ = mass flux per unit span in two-dimensional, constant-pressure case

C_{q_1} = two-dimensional mass entrainment coefficient

ρ_1, u_1 = local values of density and velocity ($u_1 > u_2$) at a given x.

The portion of the jet mass flux which has been entrained by the mixing region will then be

$$\frac{\dot{m}_1^*}{\dot{m}_1} = \frac{2\pi}{\dot{m}_j} \int_o^x r(x)\, \rho_1 u_1 C_{q_1} dx \qquad \text{(I-1)}$$

The variation of C_{q_1} with velocity ratio u_2/u_1 and density ratio ρ_2/ρ_1, computed in Section 4.2.4.1 will be approximated by

$$C_{q_1} = (.05)\,(\rho_2/\rho_1)^{1/2} \tag{I-2}$$

Since for this hemispherical interface

$$x = d_f/2$$

Equation I-1 may be written as

$$\frac{\dot{m}_1}{\dot{m}_j} = \frac{(.10)\,\pi\,(d_f/2)^2}{\dot{m}_j} \int_o^\theta \rho_1 u_1 \left(\frac{\rho_2}{\rho_1}\right)^{1/2} \sin\theta\, d\theta \tag{I-3}$$

where Equation I-2 has been used.

As discussed in Section 4.2.3.3, the radius $d_f/2$ is related to the vacuum thrust of the rocket

$$\left(\frac{d_f}{2}\right)^2 = \frac{T}{p_{o_{f_\infty}} \cos^4\alpha \; 1-p_\infty/p_{o_{f_\infty}}}$$

and the vacuum thrust to the jet mass flux by

$$T = \dot{m}_j V_j \left[1 + \frac{1}{\gamma_j M_{e_j}^2}\right]$$

Substituting in Equation (I-3)

$$\frac{\dot{m}_1^*}{\dot{m}_j} = \frac{(.10)\pi}{\cos^4\alpha} \left\{ \frac{1 + \frac{1}{\gamma_j M_{e_j}^2}}{1 - \frac{p_\infty}{p_{o_{f_\infty}}}} \right\} \frac{V_j}{p_{o_{f_\infty}}} \int_o^\theta \rho_1 u_1 \left(\frac{\rho_2}{\rho_1} \right)^{1/2} \sin\theta \, d\theta \quad \text{(I-4)}$$

Now, continuity of pressure across the interface requires that

$$P_{o_2} = P_{o_1}$$

i.e.

$$p_{o_{f_\infty}} = p_{o_{f_j}}$$

and then it is possible to write Equation (I-4) in the form

$$\frac{\dot{m}_1^*}{\dot{m}_j} = \frac{(.314)\,\gamma_j}{\cos^4\alpha} \left\{ \frac{1 + \frac{1}{\gamma_j M_{e_j}^2}}{1 - \frac{p_\infty}{p_{o_{f_\infty}}}} \right\} \frac{V_j}{a_{o_1}} \int_o^\theta \frac{\rho_1 u_1}{\rho_{o_1} a_{o_1}} \left(\frac{\rho_2}{\rho_1} \right)^{1/2} \sin\theta \, d\theta \quad \text{(I-5)}$$

where a denotes the speed of sound. Writing the integrand in terms of Mach number, temperature ratio and pressure ratio

$$\frac{\dot{m}_1^*}{\dot{m}_j} = \frac{(.314)\gamma_j}{\cos^4\alpha} \left\{ \frac{1 + \frac{1}{\gamma_j M_{e_j}^2}}{1 - \frac{p_\infty}{p_{o_{f_\infty}}}} \right\} \left(\frac{V_j}{a_{o_1}} \right) \left(\frac{a_{o_1}}{a_{o_2}} \right) I(\theta) \quad \text{(I-6)}$$

where

$$I(\theta) = \int_o^{\theta} M_1 \left(\frac{p_1}{p_{o_{f_j}}} \right) \sqrt{\frac{T_{o_1}}{T_1}} \sin\theta \, d\theta \qquad \text{(I-6a)}$$

Note that since

$$\frac{p_1}{p_{o_{f_j}}} (x) = \frac{p_2}{p_{o_{f_\infty}}} (x)$$

the Mach number and temperature ratio must also be equal on both sides of the interface.

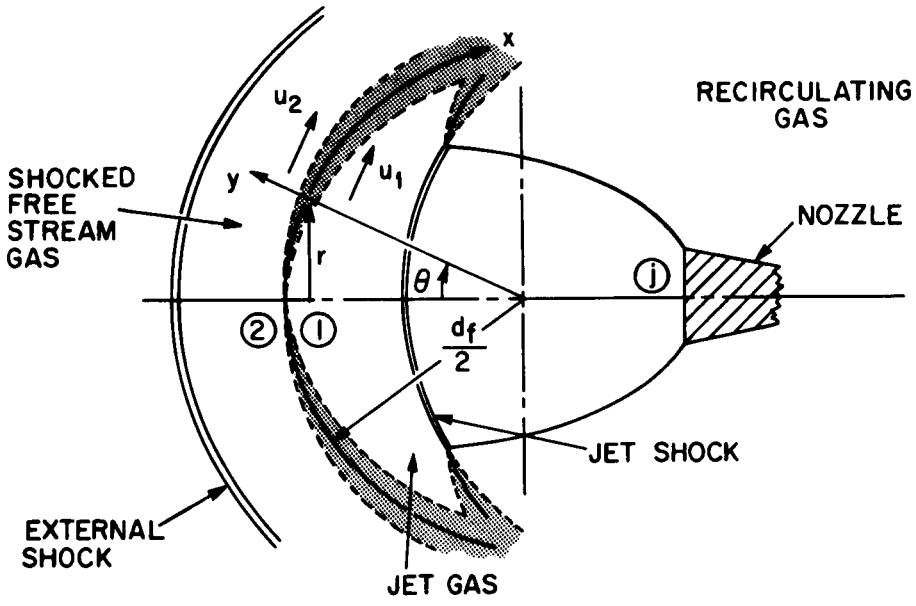

Figure I-1. Mixing layer geometry.

APPENDIX J

FLUID ENTRAINMENT BY THE INNER INTERFACE

This Appendix describes the computation of the fraction of the jet mass flux which is entrained by the mixing layer at the jet-recirculating flow interface. The sketch below depicts the geometry of the problem.

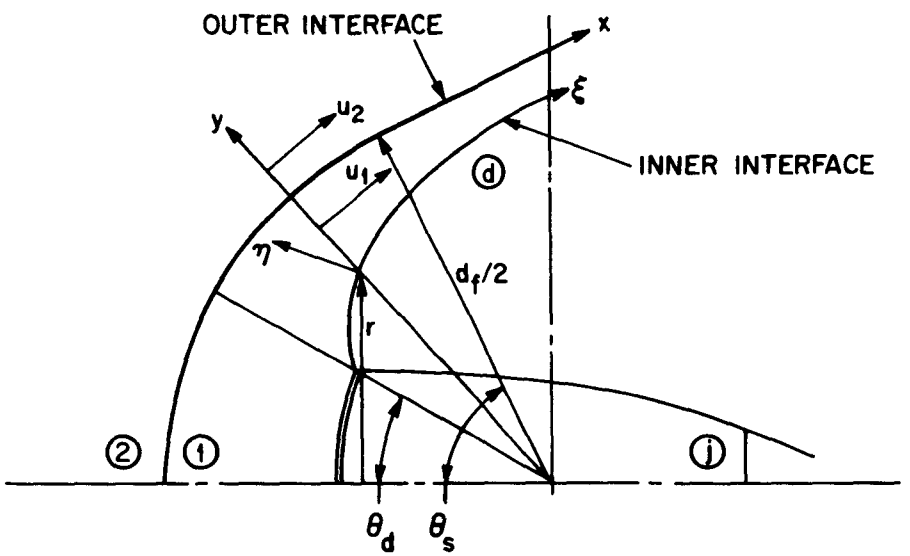

Fluid Entrainment by the Inner Interface

As discussed in Section 4.2.4.1, it is assumed that the rate of mass entrainment per unit circumference is locally equal to the rate of mass entrainment per unit span for two-dimensional, constant pressure mixing. Then,

$$\frac{\dot{m}}{\dot{m}_j} = \frac{2\pi}{\dot{m}_j} \int_o^{\xi} r(\xi)\, \rho_1 u_1\, C_{q_1}\, d\xi \qquad \text{(J-1)}$$

where $\dot{m}$ represents the mass flux which has been entrained at a given location ξ along the inner interface. Note that Equation (J-1) assumes that all flow variables are constant along the jet layer. This is not strictly true, since then the pressure will not be continuous across the inner interface.

Now, for $\theta < \theta_s$

$$r = (d_f/2 + y_d) \sin\theta \tag{J-2}$$

(where y_d is negative), and

$$d\xi = d\theta \left[(d_f/2 + y_d)^2 + \left(\frac{dy_d}{d\theta} \right)^2 \right]^{1/2} \tag{J-3}$$

The right-hand side of Equation (J-1) is normalized by dividing numerator and denominator by

$$\left(\frac{d_f}{2} \right)^2 \rho_{o_1} a_{o_1}$$

Then,

$$\frac{\dot{m}}{\dot{m}_j} = \frac{2\pi \left(\frac{d_f}{2} \right)^2}{(\dot{m}_j/\rho_{o_1} a_{o_1})} \int_o^{\xi} \bar{r} \left(\frac{\rho_1 u_1}{\rho_{o_1} a_{o_1}} \right) C_{q_1} \, d\xi \tag{J-4}$$

where, for $\bar{x} \leq \theta_s$

$$\bar{r} = \frac{r}{d_f/2} = (1 + \bar{y}_d) \sin \bar{x} \tag{J-5a}$$

$$d\bar{\xi} = d\bar{x} \left[(1 + \bar{y}_d)^2 + \left(\frac{d\bar{y}_d}{d\bar{x}} \right)^2 \right]^{1/2} \tag{J-5b}$$

$$\left(\bar{x} = \frac{x}{d_f/2} , \; \bar{y} = \frac{y}{d_f/2} \right)$$

The mass entrainment coefficient will in this case have the form

$$C_{q_1} = (.05)\sqrt{\frac{\rho_d}{\rho_1}} \tag{J-6}$$

(See Section 4.2.4.1) Then Equation (J-4) may be written as:

$$\frac{\dot{m}}{\dot{m}_j} = (.10)\left[\left(\frac{d_f}{d_{e_j}}\right)^2 \left(\frac{p_{o_1}}{p_{o_j}}\right)\right]\left[\frac{\sqrt{T_j/T_{o_j}}}{M_j(p_j/p_{o_j})}\right]$$

$$\cdot \left[\left(\frac{p_d}{p_{o_j}}\right)\left(\frac{p_{o_j}}{p_{o_1}}\right)\left(\frac{T_{o_j}}{T_d}\right)\right]^{1/2} \int_o^{\bar{\xi}} \bar{r}\, M_1 \sqrt{\frac{p_1}{p_{o_1}}}\, d\xi \tag{J-7}$$

The distance $\bar{y}_d$ between the outer and inner interfaces has been calculated in Section 4.2.3.4. There it is shown that for $\bar{x} \leq \theta_s$

$$\bar{y}_d = -1 + \sqrt{1 - F(\bar{x})} \tag{J-8a}$$

where

$$F(\bar{x}) = \frac{(.1608)}{\sin \bar{x}\left[(.4305) + M_1(p_1/p_{o_1})\sqrt{T_{o_1}/T_1}\right]} \tag{J-8b}$$

We now consider a particular case just to try out the calculation scheme and not because this case is of particular interest.

$M_\infty = 2.5 \qquad M_j = 3.0$

$p_d/p_{o_1} = .20$

Differentiating Equation (J-8a):

$$\frac{d\bar{y}_d}{d\bar{x}} = -\frac{1}{2} \frac{(dF/d\bar{x})}{\sqrt{1-F(\bar{x})}} \qquad (J-9)$$

$F(\bar{x})$ was plotted and $(dF/d\bar{x})$ measured graphically. Equations (I-5a, b) may then be used in the integrand of (J-7) to evaluate $\dot{m}/\dot{m}_j$ as a function of $\bar{x}$. *When carrying out the integration with respect to $\bar{x}$, it must be noted that the lower limit of integration will be

$$\bar{x}_d = \theta_d$$

In evaluating the constant part of Equation (J-7), it was assumed that

$$T_{o_j} = T_d$$

There is some dependence of Equation (J-7) on the ratio

$$p_{o_j}/p_{o_1},$$

since this ratio appears in the constant in (J-7), and the lower limit $\bar{x}_d$ also depends on (p_{o_j}/p_{o_1}). For the specific cases

$$p_{o_j}/p_{o_1} = 36, 147, \text{ and } 344$$

p_1/p_{o_1} is again assumed to be given by the Newtonian expression

$$p_1/p_{o_1} = \cos^2\bar{x} + \frac{p_d}{p_{o_{f_j}}} \sin^2\bar{x}$$

were again chosen, but it was found that all these cases led to almost identical numerical results.

The equations of Appendix I were written in a form resembling Equation (J-7); i.e.,

$$\frac{\dot{m}^*}{\dot{m}_j} = (.10)\left[\left(\frac{d_f}{d_j}\right)^2 \left(\frac{p_{o_1}}{p_{o_j}}\right)\right] \cdot \left[\frac{\sqrt{T_j/T_{o_j}}}{M_j(p_j/p_{o_j})}\right] \cdot$$

$$\cdot\left(\frac{a_{o_j}}{a_{o_2}}\right) \int_o^{\bar{x}} \left[\frac{p_1}{p_{o_1}} M_1 \sqrt{\frac{T_{o_1}}{T_1}}\right] \sin \bar{x}\, d\bar{x} \qquad \text{(J-10)}$$

As in Section 4.2.4.1, it was assumed that

$$\frac{a_{o_j}}{a_{o_2}} = 3.$$

APPENDIX K

INITIAL CONDITION FOR MERGED MIXING LAYER

The initial value of $\bar{u}_*$ for starting the streamwise integration is obtained by a momentum balance in the upstream area where the two shear layers are merging. Figure (K-1) shows the geometry of the situation, with the control volume indicated. Equating the incoming and outgoing momentum flux, we get:

$$u_e \dot{m}_j + u_\ell \dot{m}_j = 2\dot{m}_j \bar{u} \tag{K-1}$$

or

$$\bar{u}_* = \frac{1}{2} u_{e*} (1 + u_\ell / u_e) \tag{K-2}$$

but

$$u_\ell / u_e = M_\ell / M_e \; a_\ell / a_e \tag{K-3}$$

$$= a_{o_\ell} / a_{o_e}$$

so that with the assumption that for a typical retrojet:

$$a_{o_j} / a_{o_f} = 3 \tag{K-4}$$

we get

$$\bar{u}^* = 2 u_e^* \tag{K-5}$$

as the starting value for the integration. The starting value for the integration of the total enthalpy $\bar{H}^*$ is determined in a similar way to that for the velocity $\bar{u}^*$. Referring to Figure (K-1) again, we can write an

energy balance in the form:

$$\dot{m}\bar{H}^* = \dot{m}_j H_j^* + \dot{m}_i H_d^* + \dot{m}_o H_\infty^* \qquad \text{(K-6)}$$

Referring to Figure (45), it can be seen that at $\theta = 60^o$,

$$\dot{m}_i/\dot{m}_j \cong .07 \qquad \text{(K-7)}$$

$$\dot{m}_o/\dot{m}_j \cong .93$$

So that:

$$\bar{H}^* = \frac{1}{2} H_j^* + .035\, H_d^* + .465 \qquad \text{(K-8)}$$

In the numerical calculations, with $a_{o_j}/a_{o_f} = 3$, it was assumed that $a_{o_d} = a_{o_j}$, so that

$$H_j^* = H_d^* = 9 \qquad \text{(K-9)}$$

which gives

$$\bar{H}^* = 5.275$$

To determine the starting value for the mass concentration integration, an equation was written expressing conservation of species from the control volume shown in Figure (K-1).

$$\dot{m}\bar{C} = \dot{m}_j + \dot{m}_i C_d \qquad \text{(K-10)}$$

so that with the assumption of $C_d = 1$, and with same ratio $\dot{m}_i/\dot{m}_j$ which was assumed in the enthalpy calculations:

$$\bar{C} = 0.57 \qquad \text{(K-11)}$$

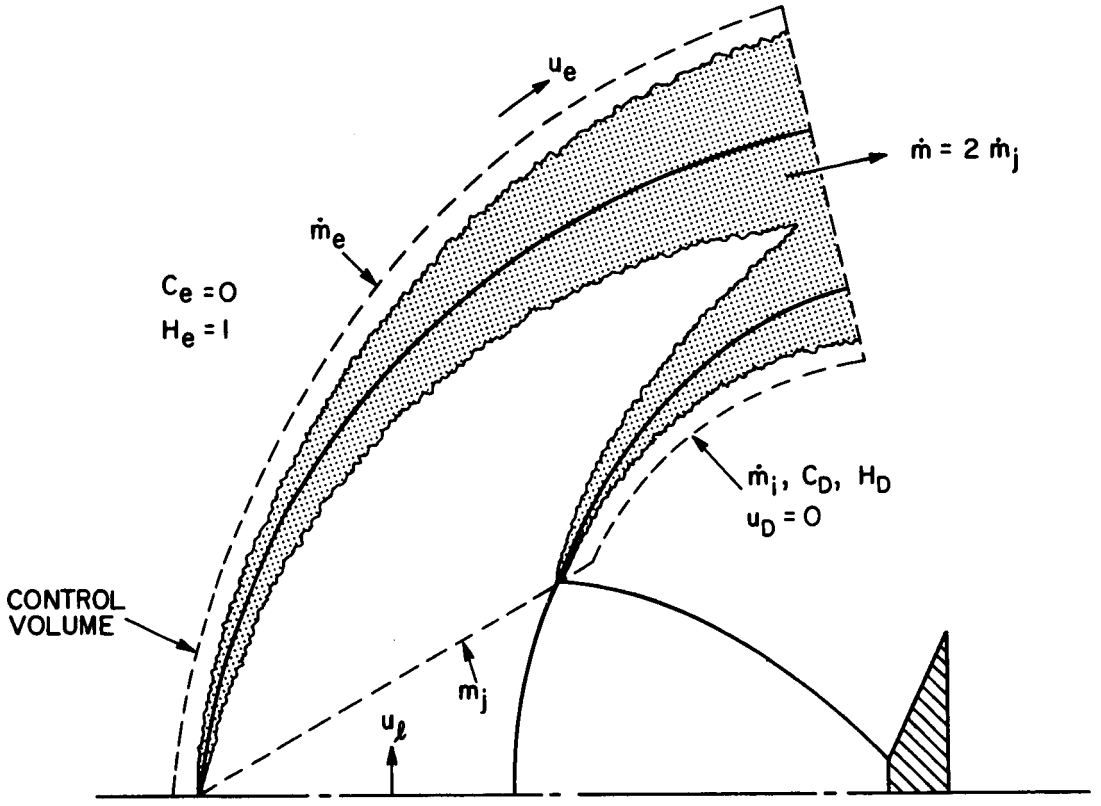

Figure K-1. Initial Condition Geometry.

APPENDIX L

JET MOLECULAR WEIGHT EFFECT

The assumptions have been frequently made in this report in order to obtain realistic numerical examples that:

$$a_{o_j}/a_{o_f} = 3 \tag{L-1}$$

$$\gamma_j = \gamma_\infty \tag{L-2}$$

It is reasonable to ask then whether the results are sufficiently general to cover jets with molecular weights different than the ambient molecular weights. This analysis demonstrates that this is the case for the enthalpy calculations. We can write:

$$(a_{o_j}/a_{o_f})^2 = \frac{R_J T_{o_j}}{R_\infty T_{o_\infty}} = 9 \tag{L-3}$$

and

$$H_j/H_\infty = \frac{C_{P_j} T_{o_j}}{C_{P_\infty} T_{o_\infty}} \tag{L-4}$$

From the perfect gas relations:

$$C_{P_j}/C_{P_\infty} = \left(\frac{\gamma_j R_j}{\gamma_j - 1}\right) \Big/ \left(\frac{\gamma_\infty R_\infty}{\gamma_\infty - 1}\right) \tag{L-5}$$

so that with $\gamma_j = \gamma_\infty$:

$$C_{P_j}/C_{P_\infty} = R_j/R_\infty \qquad \text{(L-6)}$$

and therefore:

$$H_j/H_\infty = 9 \qquad \text{(L-7)}$$

APPENDIX M

DISTRIBUTION LIST FOR FINAL REPORT

Contract NAS7-576

Copies	Recipient	Designee
4	Chief, Liq. Prop. Technology, RPL NASA Washington, D.C. 20546	(x)
1	Director, Launch Vehicles and Propulsion, SV NASA Washington, D.C. 20546	(x)
1	Director, Advanced Manned Missions, MT NASA Washington, D.C. 20546	(x)
1	Director, Mission Analysis Division NASA Ames Research Center Moffett Field, California 24035	(x)
	Jet Propulsion Laboratory 4800 Oak Grove Dr. Pasadena, Calif. 91103	(x)
5	Mr. Hartwell R. Long (Technical Manager)	
1	NASA Pasadena Office 4800 Oak Grove Drive Pasadena, California 91103	(x)
1	Contracting Officer	(x)
1	Office of Technical Information and Patent Matters	(x)
20	NASA Scientific + Technical Information Facility P.O. Box 33 College Park, Maryland 20740	(x)

NASA Field Centers

1	Marshall Space Flight Center Huntsville, Alabama, 35812	Keith Chandler
2	Ames Research Center Moffett Field, California 94035	Harold Hornby

Copies	Recipient	Designee
2	Goddard Space Flight Center Greenbelt, Maryland 20771	Merland L. Moseson Code 620 Dan Grant
2	Jet Propulsion Laboratory California Institute of Technology 4800 Oak Grove Drive Pasadena, California 91103	Henry Burlage, Jr. Propulsion Div.
2	Langley Research Center Langley Station Hampton, Virginia 23365	Dr. Floyd L. Thompson Director Kenneth Pierpont
2	Lewis Research Center 21000 Brookpark Road Cleveland, Ohio 44135	Dr. Abe Silverstein Director I. A. Johnsen
2	Marshall Space Flight Center Huntsville, Alabama 35812	Hans G. Paul Code R-P+VED Werner Voss R-P and VE-PM
2	Manned Spacecraft Center Houston, Texas 77001	Dr. Robert R. Gilruth Director G. Thibodaux
2	John F. Kennedy Space Center NASA Cocoa Beach, Florida 32931	Dr. Kurt H. Debus
1	NASA Test Facility Propulsion Engineering Office White Sands, New Mexico	I. D. Smith Staff Chemist
	Government Installations	
1	Aeronautical Systems Divison Air Force Systems Command Wright-Patterson Air Force Base Dayton, Ohio 45433	D. L. Schmidt Code ASRCNC-2
1	Air Force Missile Development Center Holloman Air Force Base New Mexico 88330	Maj. R. E. Bracken Code MDGRT

Copies	Recipient	Designee
1	Air Force Missile Test Center Patrick Air Force Base, Florida	L. J. Ullian
1	Air Force Systems Divison Air Force Unit Post Office Los Angeles 45, California 90045	Col. Clark Technical Data Center
2	AFFTC (FTBPP-2) Edwards AFB, California 93523	Myrtle C. Jones
1	Arnold Engineering Development Center Arnold Air Force Station Tullahoma, Tennessee 37388	Dr. H. K. Doetsch
1	Bureau of Naval Weapons Department of the Navy Washington, D.C. 20546	J. Kay RTMS-41
1	Defense Documentation Center Headquarters Cameron Station, Building 5 5010 Duke Street Alexandria, Virginia 22314 Attn- TISIA	
1	Headquarters, U.S. Air Force Washington 25, D.C. 20546	Col. C. K. Stambaugh AFRST
1	Picatinny Arsenal Dover, New Jersey 07801	I. Forsten, Chief Liquid Propulsion Laboratory, SMUPA-DL
2	Air Force Rocket Propulsion Laboratory Research and Technology Division Air Force Systems Command Edwards, California 93523	RPRR/MR. H. Main K. Rimer
1	U.S. Atomic Energy Commission Technical Information Services Box 62 Oak Ridge, Tennessee 37830	A. P. Huber Oak Ridge Gaseous Diffusion Plant (ORGDP) P.O. Box P

Copies	Recipient	Designee
1	U.S. Army Missile Command Redstone Arsenal Alabama 35809	Dr. Walter Wharton
1	U.S. Naval Ordnance Test Station China Lake California 93557	Code 4562 Chief, Missile Propulsion Div.
	CPIA	
1	Chemical Propulsion Information Agency Applied Physics Laboratory 8621 Georgia Avenue Silver Spring, Maryland 20910	P. Martin
	Industry Contractors	
1	Aerojet-General Corporation P.O. Box 296 Azusa, California 91703	L. F. Kohrs
1	Aerojet-General Corporation P.O. Box 1947 Technical Library, Bldg 2015, Dept. 2410 Sacramento, California 95809	R. Stiff
1	Aeronutronic Divison Philco Corporation Ford Road Newport Beach, California 92663	Mr. N. Stern Dr. Stanley Byron
1	Aerospace Corporation 2400 East El Segundo Boulevard P.O. Box 95085 Los Angeles, California 90045	Mr. M. J. Russi
1	Air Research Mfg. Co. 9851 Sepulveda Blvd Los Angeles, Calif. 90045	Mr. C. S. Coe
1	Arthur D. Little, Inc. 20 Acorn Park Cambridge, Massachusetts 02140	E. Karl Bastress

Copies	Recipient	Designee
1	Astropower Laboratory McDonnell-Douglas Aircraft Co., Inc. 2121 Paularino Newport Beach, California 92663	Dr. George Moc Director, Research
1	Astrosystems International, Inc. 1275 Bloomfield Avenue Fairfield, New Jersey 07007	A. Mendenhall
1	Atlantic Research Corporation Edsall Road and Shirley Highway Alexandria, Virginia 22314	A. Scurlock
1	Beech Aircraft Corporation Boulder Divison Box 631 Boulder, Colorado 80302	J. H. Rodgers
1	Bell Aerosystems Company P.O. Box 1 Buffalo, New York 14240	J. Flanagan
1	Bendix Systems Division Bendix Corporation 3300 Plymouth Road Ann Arbor, Michigan 48105	John M. Brueger
1	Boeing Company P.O. Box 3707 Seattle, Washington 98124	J. D. Alexander
1	Brown Engineering Co., MS-190 Research Park Huntsville, Alabama 35807	W. J. Tomme
1	Missile Divison Chrysler Corporation P.O. Box 2628 Detroit, Michigan 48231	John Gates
1	Wright Aeronautical Division Curtiss-Wright Corporation Wood-Ridge, New Jersey 07075	G. Kelley

Copies	Recipient	Designee
1	Missile and Space Systems Divison McDonnell-Douglas Aircraft Co., Inc. 3000 Ocean Park Boulevard Santa Monica, Calif. 90406	R. W. Hallet Chief Engineer Advanced Space Tech.
1	Aircraft Missiles Division Fairchild Hiller Corporation Hagerstown, Maryland 21740	J. S. Kerr
1	General Dynamics Convair Division 5001 Kearny Villa Road P.O. Box 1628 San Diego, Calif. 92112	E. R. Peterson V.P., Research and Eng. F. P. Boynton
1	Missile and Space Systems Center General Electric Company Valley Forge Space Technology Center P.O. Box 8555 Philadelphia, Pa.	F. Mezger
1	Advanced Engine + Technology Dept. General Electric Company Cincinnati, Ohio 45215	D. Suichu
1	Grumman Aircraft Engineering Corp. Bethpage, Long Island New York 11714	Joseph Gavin
1	Honeywell, Inc. Aerospace Div. 2600 Ridgway Rd. Minneapolis, Minn.	Mr. Gordon Harms
1	Hughes Aircraft Co. Aerospace Group Centinela and Teale Streets Culver City, Calif.	E. H. Meier V.P. and Div. Mgr. Research and Dev. Div.
1	Walter Kidde and Company, Inc. Aerospace Operations 567 Main Street Bellevile, New Jersey	Mr. R. J. Hanville Dir. of Research Engr.

Copies	Recipient	Designee
1	Ling-Temco-Vought Corporation Astronautics P.O. Box 5907 Dallas, Texas 75222	Garland Whisenhunt J. W. Arnold
1	Lockheed Missiles and Space Co. Attn- Technical Information Center P.O. Box 504 Sunnyvale, California 94088	Y. C. Lee
1	Lockheed Propulsion Company P.O. Box 111 Redlands, California 92374	H. L. Thackwell
1	The Marquardt Corporation 16555 Saticoy Street Van Nuys, Calif. 91409	Warren P. Boardman, Jr.
1	Baltimore Division Martin Marietta Corporation Baltimore, Maryland 21203	John Calathes (3214)
1	Denver Division Martin Marietta Corporation P.O. Box 179 Denver, Colorado 80201	J. D. Goodlette (A-241) A. J. Kullas
1	Orlando Division Martin Marietta Corp. Box 5837 Orlando, Florida	Mr. J. Ferm
1	McDonnell Aircraft Corporation P.O. Box 516 Municipal Airport St. Louis, Missouri 63166	R. A. Herzmark
1	Rocket Research Corporation 520 South Portland Street Seattle, Washington 98108	Foy McCullough, Jr.
1	Space + Information Systems Division North American Rockwell, Inc. 12214 Lakewood Blvd Downey, California 90241	H. Storms F. G. Etheridge

Copies	Recipient	Designee
1	Rocketdyne (Library 586-306) North American Rockwell, Inc. 6633 Canoga Avenue Canoga Park, Calif. 91304	E. B. Monteath
1	Northrop Space Laboratories 3401 West Broadway Hawthorne, California 90250	Dr. William Howard
1	Reaction Motors Division Thiokol Chemical Corporation Denville, New Jersey 07832	Arthur Sherman Mr. Robert Gere
1	Republic Aviation Corporation Farmingdale Long Island, New York	Dr. William O'Donnell
1	Space General Corporation 9200 East Flair Avenue El Monte, California 91734	C. E. Roth
1	Stanford Research Institute 333 Ravenswood Avenue Menlo Park, California 94025	Lionel Dickinson
1	TRW Systems One Space Park Redondo Beach, Calif. 90278	Mr. D. Lee
1	TAPCO Divison TRW, Incorporated 23555 Euclid Avenue Cleveland, Ohio 44117	P. T. Angell
1	Thiokol Chemical Corporation Huntsville Division Huntsville, Alabama 35807	John Goodloe
1	United Technology Center 587 Methilda Avenue P.O. Box 358 Sunnyvale, California 94088	B. Adelman
1	Florida Research and Development Pratt and Whitney Aircraft United Aircraft Corporation P.O. Box 2691 West Palm Beach, Florida 33402	R. J. Coar

Copies	Recipient	Designee
1	Vickers, Inc. Box 302 Troy, Michigan	
1	Sunstrand Aviation 2421 11th Street Rockford, Illinois 61101	Mr. R. W. Reynolds
1	Hamilton Standard Division United Aircraft Corp. Windsor Locks, Conn. 06096	Mr. R. Hatch
1	Sandia Corporation P.O. Box 5000 Albuquerque, New Mexico	Dr. J. K. Cole
1	AVCO Corporation AVCO Space Systems Division Lowell Industrial Park Lowell, Massachusetts 01851	Dr. B. L. Reeves
1	Consolidated Engineering Technology Corp. 188 Whisman Road Mountain View, Calif. 94040	Dr. R. Anderson
1	G.V.R. Rao and Associates 14827 Ventura Boulevard Sherman Oaks, Calif. 91403	G.V.R. Rao
1	Lockheed Missles and Space Co. Huntsville Research and Engineering Center 4800 Bradford Drive Huntsville, Alabama	R. J. Prozan
1	Cornell Aeronautical Laboratory, Inc. Buffalo, New York 14221	Dr. J. G. Hall